

# Integrated Sinc Method for Composite and Hybrid Structures

Wesley C. H. Slemm

Dissertation submitted to the Faculty of the  
Virginia Polytechnic Institute and State University  
in partial fulfillment of the requirements for the degree of

Doctor of Philosophy  
in  
Aerospace Engineering

Rakesh K. Kapania, Chair  
Romesh C. Batra  
Michael K. Philen  
Alan J. Brown  
Mayuresh J. Patil

June 4, 2010  
Blacksburg, Virginia

Keywords: Interlaminar Stresses, Cohesive Zone Modeling, Numerical Indefinite Integration, Integrated Sinc Method, Local Petrov-Galerkin Method, Collocation Method, Meshless Methods, Composite Materials, Functionally Graded Materials, Hybrid Materials

Copyright 2010, Wesley C. H. Slemm

# Integrated Sinc Method for Structural Mechanics Applications

Wesley C. H. Slemph

(ABSTRACT)

Composite materials and hybrid materials such as fiber-metal laminates, and functionally graded materials are increasingly common in application in aerospace structures. However, adhesive bonding of dissimilar materials makes these materials susceptible to delamination. The use of integrated Sinc methods for predicting interlaminar failure in laminated composites and hybrid material systems was examined. Because the Sinc methods first approximate the highest-order derivative in the governing equation, the in-plane derivatives of in-plane strain needed to obtain interlaminar stresses by integration of the equilibrium equations of 3D elasticity are known without post-processing. Interlaminar stresses obtained with the Sinc method based on Interpolation of Highest derivative were compared for the first-order and third-order shear deformable theories, the refined zigzag beam theory and the higher-order shear and normal deformable beam theory. The results indicate that the interlaminar stresses by the zigzag theory compare well with those obtained by a 3D finite element analysis, while the traditional equivalent single layer theories perform well for some laminates.

The philosophy of the Sinc method based on Interpolation of Highest Derivative was extended to create a novel weak form based approach called the Integrated Local Petrov-Galerkin Sinc Method. The Integrated Local Petrov-Galerkin Sinc Method is easily utilized for boundary-value problem on non-rectangular domains as demonstrated for analysis of elastic and elastic-plastic plane-stress panels with elliptical notches. The numerical results showed excellent accuracy compared to similar results obtained with the finite element method.

The Integrated Local Petrov-Galerkin Sinc Method was used to analyze interlaminar debonding of composite and fiber-metal laminated beams. A double-cantilever beam and a fixed-ratio mixed mode beam were analyzed using the Integrated Local Petrov-Galerkin Sinc Method and the results were shown to correlate well with those by the finite element method. An adaptive Sinc point distribution technique was implemented for the delamination analysis which significantly improved the methods accuracy for the present problem. Delamination of a GLARE, plane-strain specimen was also analyzed using the Integrated Local Petrov-Galerkin Sinc Method. The results correlate well with 2D, plane-strain analysis by the finite element method, including interlaminar stresses obtained by through-the-thickness integration of the equilibrium equations of 3D elasticity.

## Dedication

*To the Almighty God Father, and His Son Jesus Christ;  
To my loving wife Sarah L. Slep,  
To my first son Campbell C. Slep whose birth is imminent,  
To my brothers Charles H. Slep, III, Andrew C. H. Slep, and W. C. Hunter Slep.  
To my parents Jean and Charles Slep.*

*“Through physical phenomenon the greatness of God is seen;  
however, unless understanding that physical phenomenon helps our fellow man,  
we cannot be satisfied.”  
-Wesley C. H. Slep*

## Acknowledgment

I would like to thank my adviser Prof. Rakesh K. Kapania for his constant support and patience, invaluable guidance and excellent suggestions. Also I would like to thank Dr. Sameer B. Mulani for the numerous discussions we have had on both technical and non-technical issues. Both of them have met with me on a regular basis to discuss and refine the theoretical and computational aspects of this research. I would like to thank Richard K. Bird and Kim S. Bey for conversations regarding this thesis. I take this opportunity to also thank Prof. Romesh Batra, Prof. Michael K. Philen, Prof. Alan J. Brown, and Prof. Mayuresh J. Patil for serving on my committee and for the technical suggestions to this dissertation.

This research has been sponsored, in part, by the Army Research Office through the National Defense Science and Engineering Graduate Fellowship.

My friends have contributed considerably by supporting me and helping me in the last four years. I would like to extend my thanks particularly to Jason Twedt, Pankaj Joshi, Sunny Muhammed, Karen Scott, Will Walker, Chris Emory, and Nathaniel Verano. I would also like to thank my friends in Hampton, VA during the last seven months while I was at NASA Langley Research Center. Special thanks to Nathan DeHart, Laura Carmines, Steadman Knight, and Lindsay Kleinow and the men and women of St. Luke's United Methodist Church.

I thank my family who has given me infinite moral support and encouragement over the years. I cannot begin to thank my parents enough for everything they have done for me. I certainly owe them a sincere debt of gratitude for teaching me the value and pleasure of hard work.

I thank my loving wife Sarah Slep whose infinite love, patience, and hard work have made this dissertation possible and insured my sanity in the process.

# Contents

<b>Abstract</b>	<b>ii</b>
<b>Dedication</b>	<b>iii</b>
<b>Acknowledgment</b>	<b>iv</b>
<b>Table of Contents</b>	<b>v</b>
<b>List of Figures</b>	<b>ix</b>
<b>List of Tables</b>	<b>xvi</b>
<b>1 Introduction</b>	<b>1</b>
1.1 Composite and Hybrid Material Systems in Flight Vehicles . . . . .	1
1.2 Traditional Fiber-Matrix Composites . . . . .	2
1.2.1 Failure Criteria . . . . .	3
1.2.2 Micromechanical Models . . . . .	4
1.2.3 Matrix Cracking . . . . .	4
1.2.4 Delamination Analysis . . . . .	5
1.3 Other Hybrid materials . . . . .	6
1.4 Accurate Stress Computation in Composites . . . . .	8
1.5 Review of Sinc Numerical Methods . . . . .	10
1.6 Scope of this Dissertation . . . . .	13
<b>2 ESL Composite Plate Theories</b>	<b>17</b>
2.1 Interlaminar Stresses . . . . .	21
2.2 Beam Theory Reduction . . . . .	24
2.2.1 Plane-Stress Beams . . . . .	25
2.2.2 Plane-Strain Beams . . . . .	27
<b>3 Sinc Numerical Methods</b>	<b>29</b>
3.1 Numerical Indefinite Integration . . . . .	32
3.2 Basics . . . . .	34
3.3 Integrated Sinc Basis Function . . . . .	36
3.3.1 Problems Involving only First-Order Derivatives . . . . .	36
3.3.2 Problems Involving only First- and Second-Order Derivatives . . . . .	41

<b>4</b>	<b>SIHD</b>	<b>45</b>
4.1	One-Dimensional BVPs . . . . .	45
4.1.1	Composite Timoshenko Beam . . . . .	48
4.2	2D BVPs . . . . .	57
4.2.1	Classical Laminated Composite Plate . . . . .	62
4.3	Summary and Conclusions . . . . .	65
<b>5</b>	<b>Composite Beam Analysis with SIHD</b>	<b>68</b>
5.1	Laminated Beams . . . . .	68
5.2	FGM Beams . . . . .	75
5.2.1	Numerical Integration of Interlaminar Stresses in FGM . . . . .	75
5.2.2	FGM Beam Results . . . . .	79
5.3	Summary and Conclusions . . . . .	81
<b>6</b>	<b>Refined Beam Theories</b>	<b>94</b>
6.1	HOSNDT . . . . .	96
6.2	Refined Zigzag . . . . .	101
6.3	Numerical Results . . . . .	104
6.3.1	Material A . . . . .	104
6.3.2	Material B . . . . .	107
6.4	Summary and Conclusions . . . . .	111
<b>7</b>	<b>ILPGSM</b>	<b>113</b>
7.1	Basis Functions . . . . .	114
7.2	Formulation of 2D Elasto-Static Problems . . . . .	115
7.2.1	Domain transformation . . . . .	117
7.2.2	Essential Boundary Conditions . . . . .	120
7.2.3	Integration Scheme . . . . .	121
7.3	Analysis of a 1D, Tapered, Axial Bar . . . . .	121
7.4	Analysis of a 2D, Timoshenko Cantilever Beam . . . . .	129
7.5	Conclusions . . . . .	135
<b>8</b>	<b>Notched Panels</b>	<b>138</b>
8.1	Analysis Method . . . . .	140
8.1.1	Domain Decomposition by “Isoparametric” Mapping . . . . .	140
8.1.2	Incremental-Iterative Approach . . . . .	143
8.2	Numerical Results for Elastic Notched Panel . . . . .	151

8.2.1	J-Integral . . . . .	154
8.2.2	Comparison of Additional Domain Decomposition . . . . .	157
8.3	Numerical Results for Elastic-Plastic Notched Panel . . . . .	160
8.3.1	Circular Notch . . . . .	161
8.3.2	Elliptical Notch . . . . .	165
8.3.3	J-integral . . . . .	168
8.4	Summary and Conclusions . . . . .	170
<b>9</b>	<b>Delamination by ILPGSM</b>	<b>171</b>
9.1	Rate Independent CZM . . . . .	174
9.2	Delamination Kinematics . . . . .	178
9.3	Principle of Virtual Work . . . . .	180
9.3.1	Internal Virtual Work . . . . .	180
9.3.2	External Virtual Work . . . . .	190
9.3.3	Essential Boundary Conditions . . . . .	191
9.4	Mode I DCB . . . . .	191
9.4.1	Finite Element Analysis . . . . .	192
9.4.2	Numerical Results . . . . .	193
9.5	Adaptive Sinc Point Distribution . . . . .	197
9.5.1	Comparison of DCB Results by Adaptive and Standard ILPGSM . .	200
9.6	FRMM . . . . .	202
9.6.1	Numerical Results for FRMM Delamination . . . . .	203
9.7	Delamination of GLARE Specimen . . . . .	204
9.8	Summary and Conclusions . . . . .	214
<b>10</b>	<b>Conclusion and Future Work</b>	<b>217</b>
10.1	Merits and Demerits . . . . .	218
10.2	Basis Function Improvement . . . . .	220
10.3	FE Smoothing by the Integrated Basis . . . . .	224
10.4	Dynamic Analysis . . . . .	226
10.5	Final Remarks . . . . .	229
	<b>Bibliography</b>	<b>230</b>
	<b>Appendices</b>	<b>260</b>
A	Fourth-Order Basis . . . . .	260
B	Governing Equations of ESL Beam Theories . . . . .	266

C	Solving the Bickford Beam Problem using SIHD . . . . .	268
D	Analytic solution for the tapered bar problem. . . . .	274
E	Mixed Finite Element Formulation . . . . .	275
F	Analytical Solution for Infinite Elliptical Panel . . . . .	277
G	Stress Integration Procedure for Perfectly Plastic and Kinematic Hardening Materials . . . . .	279
H	Numerical Results - Elastic, Elliptical Notched Panels . . . . .	285
I	Numerical Results - Elastic-plastic, Circular and Elliptical Notched Panels .	287
J	Numerical Results - FRMM Composite Specimen . . . . .	289



# List of Figures

2.1	Geometry of a laminated composite plate. The thickness dimension has been exaggerated to illustrate the layers and mid-plane. In general $a \gg h$ and $b \gg h$ . . . . .	22
3.1	Plot of the Sinc function for $-10 \leq x \leq 10$ . . . . .	29
3.2	Transformation from $t \in (0, 1)$ onto the real line $\tau \in (-\infty, \infty)$ . . . . .	30
3.3	Approximation of the example function with various choices of mesh size using $N = 10$ or 21 Sinc points. . . . .	35
3.4	Error of Sinc approximation for various mesh size choices. . . . .	36
4.1	Flowchart of the SIHD method. (LW: Li and Wu's approach, Present: The alternative approach.) . . . . .	49
4.2	Deflection and rotation results for $h = \alpha/N$ , $\alpha = 1$ , and $N = 100$ . (LW - Li and Wu, P - Present) . . . . .	51
4.3	Histogram of Sinc point distribution within the domain using $N = 100$ and $h = 1/N$ . (LW - Li and Wu, P - Present) . . . . .	52
4.4	Histogram of Sinc point distribution within the domain using $N = 100$ and $h = \alpha/N$ . (LW - Li and Wu, P - Present) . . . . .	52
4.5	Deflection and rotation results for $h = \alpha/N$ , $\alpha = 3$ , and $N = 100$ . (LW - Li and Wu, P - Present) . . . . .	53
4.6	Convergence of SIHD for increasing number of Sinc points with $h = 1/N$ . (LW - Li and Wu, P - Present) . . . . .	55
4.7	Convergence of SIHD for increasing number of Sinc points with $h = 3/N$ . (LW - Li and Wu, P - Present) . . . . .	55
4.8	Error versus Sinc span, $\alpha$ , with $N = 20$ for a $[0^\circ/90^\circ/0^\circ]$ graphite/epoxy Timoshenko beam. . . . .	56
4.9	Normalized plate deflection and error in the deflection for a classical laminated composite plate using $\alpha = 1$ and $N = 20$ . . . . .	63
4.10	Normalized plate deflection and error in the deflection for a classical laminated composite plate using $\alpha = 3$ and $N = 20$ . . . . .	63
4.11	Convergence of displacement and stresses for increasing number of Sinc points with $\alpha = 1, 2$ , and 3 for a classical laminated composite plate. . . . .	64
4.12	Error versus Sinc span, $\alpha$ , with $N = 20$ for a classical laminated composite plate. . . . .	65
5.1	FE mesh for $[0/90/0]$ graphite/epoxy laminated composite beam. . . . .	70

5.2	Fringe plots of stress components in simply-supported laminated beam with length-to-thickness ratio of $a/h = 5$ . . . . .	72
5.3	Longitudinal and transverse normal stress components at beam center for simply-supported laminated beam with $a/h = 5$ . . . . .	83
5.4	Transverse shear and normal stress components at $x = 0, 0.1a$ for simply-supported laminated beam with $a/h = 5$ . . . . .	84
5.5	Fringe plots of stress components in simply-supported laminated beam with length-to-thickness ratio of $a/h = 10$ . . . . .	85
5.6	Longitudinal and transverse normal stress components at beam center for simply-supported laminated beam with $a/h = 10$ . . . . .	86
5.7	Transverse shear and normal stress components at $x = 0, 0.1a$ for simply-supported laminated beam with $a/h = 10$ . . . . .	87
5.8	Fringe plots of stress components in simply-supported laminated beam with length-to-thickness ratio of $a/h = 20$ . . . . .	88
5.9	Longitudinal and transverse normal stress components at beam center for simply-supported laminated beam with $a/h = 20$ . . . . .	89
5.10	Transverse shear and normal stress components at $x = 0, 0.1a$ for simply-supported laminated beam with $a/h = 20$ . . . . .	90
5.11	Geometry of a plate with functionally graded core that was considered in the present analysis. . . . .	91
5.12	Through-the-thickness material volume fraction variation for functionally graded sandwich composite beam. . . . .	91
5.13	Longitudinal and transverse normal stress components at beam center for functionally graded sandwich beam with $p = 1, 2, 4, \infty$ . . . . .	92
5.14	Transverse shear and transverse normal stress components at $x = 0, 0.1a$ for functionally graded sandwich beam with length-to-thickness ratio of $a/h = 20$ . . . . .	93
6.1	Definition of beam geometry and coordinate system. . . . .	97
6.2	Longitudinal and transverse normal stress components at $x = 0.5$ for simply supported laminated beam with Material A. . . . .	105
6.3	Transverse shear and normal stress components at $x = 0, 0.1a$ for simply supported laminated beam with Material A. . . . .	106
6.4	Longitudinal and transverse normal stress components at $x = 0.5$ for simply supported laminated beam with Material B. . . . .	109
6.5	Transverse shear and normal stress components at $x = 0, 0.1a$ for simply supported laminated beam with Material B. . . . .	110
7.1	Diagram of physical and computational domain for the ILPGSM. . . . .	116

7.2	Local Petrov-Galerkin subdomains in the computational domain. The dots indicate centers of the given subdomain. The “x’s” indicate Sinc points within the computational domain. . . . .	119
7.3	Displacement and stress obtained with $N = 10$ (21 Sinc points) and the ILPGSM using the Lagrange multiplier method to impose essential boundary conditions for $\delta = 0.01$ . Results are compared with the analytic solution. . .	124
7.4	Displacement and stress obtained with $N = 20$ (41 Sinc points) and the ILPGSM method using the Lagrange multiplier method to impose essential boundary conditions for $\delta = 0.0001$ . Results are compared with the analytic solution. . . . .	125
7.5	Numerical error of the displacement and stress for tapered axial bar with taper ratio of 101:1 and increasing number of Sinc points. . . . .	127
7.6	Numerical error of the stress verses number of degrees of freedom and computational time for axial bar with taper ratio of 101:1. . . . .	128
7.7	Numerical error of the displacement and stress for tapered axial bar with taper ratio of 10,001:1 and increasing number of Sinc points. . . . .	129
7.8	Numerical error of the stress verses number of degrees of freedom and computational time for axial bar with taper ratio of 10,001:1. . . . .	130
7.9	Boundary conditions and dimensions of the Timoshenko cantilever problem.	130
7.10	Contours of displacement and stress in the Timoshenko cantilever obtained by the ILPGSM with the Sinc-2 basis function ( $N = 10$ ). The essential boundary conditions are imposed by the Lagrange multiplier method. . . . .	132
7.11	Numerical error of the displacements and stresses with increasing number of Sinc points. Numerical result are compared with the SIHD method, a displacement-based $C^0$ FEA, and a mixed FEA. . . . .	134
7.12	Numerical error of displacement and stress verse computational time and number of degrees of freedom for solution from ILPGSM with the Sinc-2 basis function and Lagrange multiplier method, a displacement-based $C^0$ FEA, and a mixed FEA. . . . .	136
8.1	Domain transformation using Lagrange interpolation polynomials. . . . .	141
8.2	Dimensions and loading for a notched plane-stress panel. . . . .	142
8.3	Domain decomposition and transformation onto two rectangular domains with boundary contours $\Gamma_1$ , $\Gamma_2$ and $\Gamma_3$ indicated. . . . .	142
8.4	Four subdomain decomposition and transformation onto four rectangular domains. . . . .	143

8.5	Displacement contours for a panel with a circular notch by ILPGSM and the analytic solution. . . . .	152
8.6	Contours of von Mises stress for a panel with a circular notch by ILPGSM and by the analytic solution. . . . .	153
8.7	Displacement contours for a panel with an elliptical notch with aspect ratio $r_2/r_1 = 10$ by ILPGSM and the analytic solution. . . . .	153
8.8	Contours of von Mises stress for a panel with an elliptical notch with aspect ratio of 10 by ILPGSM and the analytic solution. . . . .	154
8.9	Von Mises stress along $x_1 = 0$ in the vicinity of the hole. . . . .	155
8.10	Path dependence of J-integral for elliptical hole . . . . .	156
8.11	Paths on which the J-integral was computed and averaged for the elliptical notch with aspect ratio of 5. . . . .	156
8.12	Comparison of J-integral by ILPGSM with the analytic solution. J-integral given in units of $N/m$ . . . . .	157
8.13	Comparison of % error in displacement and stresses from ILPGSM with 2 and 4 subdomains. . . . .	158
8.14	Comparison of error in stress component, $\sigma_{11}$ from solution with two and four subdomains. The two subdomain solution had 7,396 DOF and the four subdomain solution had 7,688 DOF. . . . .	159
8.15	Converged FEA mesh and ILPGSM Sinc point distribution for elastic-plastic plane-stress panel with circular notch. . . . .	162
8.16	Displacement of the point $(a, 0)$ verses applied tension load. The onset of plasticity occurs at about 130 MPa. . . . .	163
8.17	Von Mises stress and plastic strain for panel with circular notch. Load step 1 - 100 MPa, 2 - 130 MPa, 3 - 150 MPa, 4 - 200 MPa, 5 - 250 MPa, 6 - 300 MPa and 7 - 340 MPa. . . . .	163
8.18	Growth of plastic zone with increasing applied load by ILPGSM and FEA. The red and blue contours indicates yielded material from the FEA and ILPGSM respectively. . . . .	164
8.19	Displacement of the point $(a, 0)$ verses applied tension load. The onset of plasticity occurs at about 36 MPa. . . . .	165
8.20	Von Mises stress and plastic strain for panel with elliptical notch of aspect ratio of five ( $r_2/r_1 = 5$ ). Load step 1 - 100 MPa, 2 - 130 MPa, 3 - 150 MPa, 4 - 200 MPa, 5 - 250 MPa, 6 - 300 MPa and 7 - 340 MPa. . . . .	166

8.21	Growth of plastic zone with increasing applied load by ILPGSM and FEA for elliptical notch with aspect ratio of five ( $r_2/r_1 = 5$ ). The red and blue contours indicates yielded material from the FEA and ILPGSM respectively.	167
8.22	Comparison of contours of von Mises stress by ILPGSM and FEA for panel with elliptical hole. . . . .	168
8.23	Comparison of contours of $u_1$ and $u_2$ by ILPGSM and FEA for panel with elliptical hole. . . . .	169
8.24	Comparison of J-integral computed by ILPGSM and ABAQUS FEA. J-integral given in units of $N/m$ . . . . .	170
9.1	Cohesive damage evolution laws for traction-separation behavior in ABAQUS.	173
9.2	Exponential cohesive damage evolution laws. . . . .	173
9.3	Exponential cohesive law through a loading and unloading cycle. . . . .	177
9.4	Undeformed and deformed geometries of two stacked Timoshenko beams with deformation kinematics indicated. . . . .	179
9.5	Delamination kinematics with layer-wise plate theory. . . . .	179
9.6	Deformation of cohesive layer with cohesive mid-surface indicted. . . . .	182
9.7	Applied forces and moments to top and bottom sublaminates. . . . .	190
9.8	Loading configurations for (a) double cantilever beam (DCB) and (b) fixed ratio mixed mode (FRMM) delamination. . . . .	191
9.9	Finite element mesh for aluminum double cantilever beam with boundary conditions indicated. . . . .	193
9.10	Comparison of deformed shape of aluminum DCB by ILPGSM and ABAQUS plane-strain FEA. An amplification factor of 3 was used to illustrate the results.	195
9.11	Comparison of normal traction in adhesive layer by ABAQUS COH2D4 elements and by ILPGSM with cohesive zone modeling. ( $T = 1,200$ s corresponds to $\bar{w} = 1$ mm, $T = 2,400$ s corresponds to $\bar{w} = 2$ mm, $T = 3,600$ s corresponds to $\bar{w} = 3$ mm, and $T = 4,800$ s corresponds to $\bar{w} = 4$ mm) . . .	196
9.12	Reaction force history for mode I loading of adhesively bonded double cantilever beam. . . . .	196
9.13	Two-subdomain adaptive Sinc point distribution approach . . . . .	198
9.14	Reaction force history for the aluminum DCB using the a single Sinc point distribution and using the adaptive Sinc point distribution with two subdomains.	200
9.15	Shear force in the top sublaminate for single subdomain analysis and adaptive Sinc point distribution. . . . .	202

9.16	Reaction force history for a FRMM specimen of a $[0^\circ]_s$ composite beam. Comparison is made with a 2D plane-strain analysis with ABAQUS cohesive finite elements. The ILPGSM results were obtained using the adaptive Sinc point distribution approach with $N = 50$ (1,249 DOF). . . . .	204
9.17	Layup of GLARE 3-3/2-0.4 with dimensions [1]. The dimensions, loading, and boundary conditions of the plane-strain specimen considered in this analysis are given. . . . .	205
9.18	Illustration of resin-rich region between the aluminum layer and the glass fiber-epoxy in which delamination is expected to occur. . . . .	206
9.19	Reaction force history of GLARE specimen with 10 mm initial delamination between top aluminum and composite layers. Results were obtained using an ABAQUS plane-strain FEA and ILPGSM with $N = 60$ . . . . .	209
9.20	Deformation of GLARE specimen with increasing applied opening displacement.	210
9.21	Traction components in the cohesive layer between the top aluminum and composite layers in a GLARE 3-3/2-0.4 plane-strain specimen. . . . .	211
9.22	Fringe plots of stress in a GLARE 3-3/2-0.4 beam with an applied load of 3 mm. . . . .	213
9.23	Through-the-thickness distributions of bending stress in GLARE 3-3/2-0.4 plane-strain specimen with applied displacements of 3.0 mm. . . . .	214
9.24	Through-the-thickness distributions of transverse shear and transverse normal stress in GLARE 3-3/2-0.4 plane-strain specimen with applied displacements of 3.0 mm. . . . .	215
10.1	Gibbs phenomenon associated with Sinc approximation for a function $y = 5$ .	221
10.2	Comparison of basis function presented in Chapter 3 and basis function developed in this chapter for simple 1D BVP. Results were obtained using $\alpha = 2.0$ .	224
10.3	Pointwise numerical error in $f(x)$ found by SIHD with $N = 10$ or 21 Sinc points over the domain. . . . .	225
10.4	Patch over which FE results could be smoothed with the integrated Sinc basis to obtain the interlaminar stresses through the thickness of a composite shell element. . . . .	225
E.1	Four node FE used in both the displacement based $C^0$ and the mixed FEM with node numbering convention indicated. . . . .	275
F.1	Geometry definition form infinite tensioned panel with elliptic notch. . . . .	277
H.1	Displacement contours for a panel with a elliptical notch with aspect ratio $r_2/r_1 = 5$ by ILPGSM. . . . .	285

H.2	Contours of Von Mises stress for a panel with an elliptical notch with aspect ratio of 5. . . . .	286
H.3	Von Mises stress along $x_1 = 0$ in the vicinity of the hole for aspect ratio of 5.; the analytic solution being valid for infinite domain. . . . .	286
I.1	Comparison of contours of Von Mises stress by ILPGSM and FEA for panel with circular hole. . . . .	287
I.2	Comparison of contours of $u_1$ and $u_2$ by ILPGSM and FEA for panel with circular hole. (1- 150 MPa, 2-250 MPa, 3 - 340 MPa applied load) . . . . .	288
J.1	Comparison of deformed shape of a $[0]_s$ FRMM composite specimen obtained by the ILPGSM and a FEA. The deformation is shown utilizing an amplification factor of 3. . . . .	290
J.2	Comparison of traction components in the cohesive layer of a $[0]_s$ FRMM composite specimen by ILPGSM and a FEA. . . . .	291

## List of Tables

4.1	Material properties for the AS4-3502 composite material. . . . .	50
4.2	Summary table of unknowns in the SIHD method for analysis of a classical laminated composite plate. . . . .	59
5.3	Material properties for a typical graphite/epoxy lamina. . . . .	69
5.4	L2 norm of displacements between fine and coarse mesh solution of graphite-epoxy, laminated beams. . . . .	70
5.5	FE mesh sizes for $[0^\circ/90^\circ/0^\circ]$ , graphite/epoxy, laminated composite beams. .	70
5.6	L2 norm of displacements between fine and coarse mesh solution for sandwich beam with functionally graded core. . . . .	80
5.7	FE mesh size for sandwich beam with functionally graded core. . . . .	80
6.8	Material properties for a graphite/epoxy lamina (A) and a fictitious orthotropic lamina with extremely different shear moduli (B). . . . .	104
6.9	L2 norm of displacements between fine and coarse mesh solution for laminated beam with material configuration B. . . . .	108
8.10	Elastic-plastic material properties for a generic aluminum alloy. . . . .	160
8.11	L2 norm of displacements between fine and coarse mesh solution for notched elastic-plastic panels. . . . .	161
9.12	Material properties for aluminum alloy for mode I delamination. . . . .	192
9.13	Material properties for LESA adhesive for mode I delamination. . . . .	192
9.14	Comparison of computational time by the single subdomain and by the two-subdomain adaptive Sinc point distribution procedure for aluminum DCB. . . . .	201
9.15	Material properties for composite material for FRMM delamination. . . . .	203
9.16	Material properties for cohesive layer used for FRMM specimen. . . . .	203
9.17	Material properties for GLARE constituents. . . . .	207
9.18	Material properties for cohesive layer. . . . .	207



# 1 Introduction

## 1.1 Composite and Hybrid Material Systems in Flight Vehicles

The term *hybrid* is used to describe material systems which are derived from unlike sources or composed of adhesively bonded dissimilar materials. The potential benefits of using hybrid material systems are that combining dissimilar materials could result, if done carefully, in the creation of a hybrid which has the best properties of both components (worst of both if not done carefully). Accordingly, the new hybrid material systems may fill a gap in capabilities that was otherwise not achievable by standard materials. Kromm *et al.* [2] describe hybrid materials as “a combination of two or more materials in a predetermined geometry and scale, optimally serving a specific engineering purpose.” The definition of Kromm *et al.* could apply to any combination of materials indicating everything from metal alloys to fiber/matrix composites; however, in industry typically the term hybrid refers to new innovative material systems and not standard fiber/matrix composites. Examples of hybrid material systems include particulate composites [3, 4, 5, 6, 7, 8], sandwich structures with foam core [9, 10, 11, 12, 13, 14], fiber-metal laminates [15, 16, 17, 18, 19, 20, 21], and a wide variety of nanocomposites [22, 23, 24, 25, 26]. In aerospace engineering, generally speaking, the desire for low weight conflicts with the necessity for stiff, strong, and tough structures. While aluminum alloys have been the standard in aircraft design for years, increasing percentages of composite materials are being used for design. Today hybrid material systems have become widespread throughout aerospace structures including the Airbus A380 and the Boeing 787 dreamliner.

Fiber-matrix composites have been used in aircraft structures for quite some time. In 1967, composites were first successfully flown in a flight test [27]. A left-hand, inboard, airflow director door constructed of boron fiber-reinforced plastic was included in a test plane. Composite materials use in military aircraft have been widespread now for many

years. The B-2, F/A-18E/F, F-22, V-22, and AV-8B were each composed of over twenty percent composite material [28]. Composite materials used in design of the F-15, F-100, AV-8B, F-18, and C-130 wing structures resulted in 11-23% weight savings over a baseline metal structure [28]. Today's commercial aircraft are also being constructed primarily of composite. The Airbus A380 and the Boeing 787 boast about 50% composite material by volume. The Airbus A380 is composed of large GLARE ("GLASS-REINFORCED," a fiber-metal hybrid) panels as the upper fuselage skin material [20, 21]. Some carbon fiber reinforced plastics are used in the tail of the aircraft and engine casings as well. The Boeing 787 uses carbon fiber reinforced epoxy laminated and sandwich composites in much of the airframe structure. Carbon-fiber laminates make up the fuselage and wing panels and carbon sandwich panels are used in the engine casings and tail skin.

## 1.2 Traditional Fiber-Matrix Composites

The benefits of fiber-matrix composites are certainly attractive. With fiber-matrix composites, a designer can achieve very high specific strength and specific stiffness. Furthermore, the material can be tailored for any specific application. For example, the Vertol CH-47 utilized a boron/epoxy aft rotor blade because the composite materials achieve very long, if not unlimited, fatigue life [28]. Furthermore, a structure can be made very stiff along a single axis if desired. However, the fiber-matrix composites have numerous, highly complicated failure modes and these failure modes are often hard to detect. The failure modes include fiber breakage, fiber/matrix debonding, matrix cracking, microbuckling, and interlaminar debonding or delamination. The failures involve multiple scales of interactions; therefore, they are highly complicated and computationally difficult. In mechanical design, modeling of the full multi-scale failure process is not practical due to the excessive cost of such an analysis. Good techniques have been developed to smear the properties of the fiber and matrix material and to homogenize the material, and failure criteria and progressive failure analysis

techniques have been developed to model, in a macro-scale manner, the material degradation to be able to estimate the useful life of a structure. Some of the different techniques for determination of the progression of damage are reviewed below.

### 1.2.1 Failure Criteria

Numerous empirical failure criteria are available for fiber-reinforced composites [29, 30, 31, 32, 33, 34, 35, 36, 37, 36, 38]. There have been a number of articles surveying the work and comparing failure theories of laminates. Soden *et al.* [39] presented a comprehensive comparison between predictions of many failure theories for fiber-reinforced polymer-composites. They summarized the method and features of 12 failure theories and compared the predictions of the theories against experimental results. These failure criteria attempt to define a failure envelope from a minimum amount of biaxial test data. This work was part of an international level assessment of failure criteria known as the “Worldwide Failure Olympics Exercise” [40]. The work has been bound into a book, which includes the exploration of the leading five theories in greater detail and recommendations, “as to how the theories can be best utilized to provide safe and economic predictions in a wide range of engineering design applications” [41].

Typically, the failure criteria predict damage initiation in the way of microcracking or delamination under transverse tensile/longitudinal shear loading conditions. Properties are selectively degraded as the criteria predict damage. The degradation or “ply discount” results in a redistribution of stresses. The criteria based approaches reduce the elastic moduli and the strength until ultimate failure of the material is predicted. This sort of progressive failure analysis is used because they are convenient and easily implemented; however, they certainly do not capture the complexity of the failure. For this reason research that examines the micromechanics is ongoing.

### 1.2.2 Micromechanical Models

Often in micromechanical models a two parameter Weibull distribution is used to predict the fiber reliability [42, 43]. The most simple micromechanical model for fiber direction tension strength may be developed by assuming fibers only break once. Thus by ignoring the matrix material, an expression can be developed for the strength of a bundle of fibers from the statistical reliability. Cox and Rosen [42, 43] develop an improved model in which multiple fiber breaks are allowed. The model is a “shear-lag” approach to determine the size of the region where load is transferred from the broken fibers into adjacent fibers via the matrix material and resulting in stress concentrations. Hedgepeth and Van Dyke [44] were able to determine the ineffective length and the stress concentration in fibers adjacent to fibers containing breaks for square and hexagonal array of fibers. Batdorf [45] developed a recursion formula to compute the probability of fiber with  $i$  breaks to break again given the stress concentrations and ineffective lengths of the fiber array. As such the load causing catastrophic failure may be predicted.

Several compression strength models have been developed. With compressive stress in the fiber direction, failure results from fiber kinking or microbuckling. Hahn and Williams [46] developed a simple model where fiber imperfection or misalignment was handled through fiber waviness. Budiansky and Feck [47] developed a model for fiber kinking which models initial fiber misalignment as well as matrix plasticity. Budiansky and Feck note that the experimental results show significant scatter and are sensitive to initial fiber misalignment. They note that their method is not capable of predicting the width of the “kink band” or its inclination.

### 1.2.3 Matrix Cracking

Matrix cracking in laminates has been studied extensively. Many investigators have carried out experiments counting the number of cracks during quasi-static loading in different  $[0_n^\circ,$

$90_m^{\circ}$  laminates [48, 49, 50, 51, 52, 53, 54, 55, 56]. In each case, the number of cracks increase with loading until the laminates reach a saturation level. Reifsnider [57] introduced a simple shear-lag analysis in which the plies themselves carry only transverse load while a thin layer between the plies carries the shear load. In Reifsnider's analysis, a single differential equation is solved to yield the stress distribution and effective reduction in stiffness in the presence of matrix cracking. A disadvantage of the shear lag analysis is that the shear transfer parameters are unknown and must be found experimentally. The shear lag method was extended for interlaminar cracking by Dharani and Tang [58]. Hashin [59] developed a more sophisticated approach to determine the stress distribution and reduction in stiffness via a variational approach. Hashin constructs admissible stress fields and obtains the stress distributions on the basis of the principle of minimum complementary strain energy. This method does not have the disadvantage of determining artificial parameters through a curve-fit.

#### 1.2.4 Delamination Analysis

Often composite materials suffer from interlaminar failures at the interface of adhesively bonded layers. Such delaminations most often occur as the result of a matrix crack or in the presence of a free edge [60]. The earliest criterion for delamination, the Quadratic Delamination Criterion was developed by Brewer and Lagace [61]. The criterion is stress-based, in which the sum of the squares of the ratios of interlaminar stresses to interlaminar strengths is one at failure. Often the Quadratic Delamination Criterion is used to determine the onset of delamination and a fracture mechanics based approach is used to determine the propagation of delamination. Several improved delamination criteria have been developed and implemented [62, 63, 64, 65].

An alternative approach for interlaminar damage modeling is the use of interface elements [60]. Cohesive elements use a nonlinear constitutive law to relate the normal and tangent

surface tractions along with the relative normal and the tangential displacements of points on the two sides of the material boundary. Unlike progressive failure criteria, this method allows the lamina to retain their constitutive behavior (the stiffness and the strength are not degraded) while the interlaminar damage propagates. Cohesive finite elements have been used by a number of authors to study delamination [60, 66, 67, 68, 69, 70, 71, 72, 73, 74].

Cohesive interface elements have recently been implemented in commercial finite element (FE) packages. ABAQUS includes cohesive elements that can model behavior of “adhesive joints, interfaces in composites, and other situations where the integrity and the strength of interfaces may be of interest [75].” To implement this approach, the elements are placed between surfaces and given constitutive properties that specify their behavior. The constitutive law can be chosen to specify the traction-separation law of a negligible thin layer, a full continuum-based constitutive behavior, or a gasket-type behavior [75]. The elements may be connected to the substrate material through shared nodes or through the use of a “tie” constraint. For modeling cohesive behavior between plates, ABAQUS’s element library includes continuum-shell elements. These elements have eight nodes and are geometrically 3D, but are formulated as shell elements and therefore are nearly as efficient as the shell elements. Nastran, LS-DYNA, and ANSYS have all included cohesive elements into their commercial FE packages [76, 77, 78].

### **1.3 Other Hybrid materials**

Fiber-metal laminates (FML) were developed at Delft University of Technology as a family of new hybrid material systems consisting of bonded thin metal sheets and pre-impregnated fiber-matrix layers [18, 19]. The FMLs were developed to primarily enhance the fatigue performance of aluminum structures. The FMLs combine the advantages of metallic materials (impact resistance and easy to repair) and fiber-reinforced matrix systems (fatigue characteristics, high specific strengths and stiffness). However, in some respects, the properties of

both are enhanced. By introducing the metal, the composite can behave as a quasi-isotropic material. For polymer matrix composites this is typically achieved by adding many layers of material. Furthermore, metal ductility helps to increase the visibility of damage and acts to transfer load into the fiber reinforced polymer layers [21].

The first candidate, ARALL, “Aramid Reinforced ALuminum Laminates” has been applied as the skin material for the C-17 cargo door. However, widespread application has been limited due to the complicated fabrication techniques [20]. The most successful implementation of FML, has been GLARE and its applications on the Airbus A380.

The high speed civil transport introduces additional material design problems. For such an application high thermal stresses generated by extreme gradients of temperature have brought to the attention of many researchers the functionally graded composites [79]. Functionally graded materials have also been proposed to be used in the rotating blades of turbomachinery [80, 81]. In functionally graded materials (FGM), two or more metals or ceramics or a combination of the two are combined in a micro-structural fashion so that the properties of the resulting material have a continuous variation of properties from each constituent material. Generally, the ceramic in the FGM offers thermal barrier effects and protects the metal from corrosion, while the metal acts to toughen and strengthen the ceramic. Unlike fiber-matrix composites which have abrupt changes in material properties at the layer interface, functionally graded composites have smoothly varying properties and thus are not as prone to damage introduced at the interface between two different materials. Functionally grading of fiber angle in polymer matrix composites has also been considered [82]. By grading the orientation of the fibers, the stress concentrations caused by bonding dissimilar materials is exchanged for subtle changes.

Furthermore, the development of advanced metal processing such as Electron Beam Free Form Fabrication (EBF3) [83], friction stir welding [84], and integral machining allows designers to explore advanced geometric configurations for structural design with metals such

as curvilinear stiffeners. Kapania, Li and Kapoor [85] have shown that curvilinear stiffened panels might give a lighter weight design than straight stiffened panels under certain design loads. Kapania and his colleagues have recently developed a design methodology for optimizing panels with curvilinear stiffeners [86, 87, 88]. With advanced material design such as functionally grading and integral curvilinear stiffening, in the foreseeable future hybrid material systems can be constructed in which structural design is no longer uncoupled into material selection and shape and size optimization but intimately coupled. FML systems, integrally-curvilinear stiffened material systems, and functional gradings could soon be used to design future aerospace vehicle structures. However, a good understanding of the failure mechanisms of combining such material systems is important. Secondly, good analysis techniques and failure criteria should be available so that the failure can be modeled without substantial computational cost.

#### **1.4 Accurate Stress Computation in Composites**

Because of interlaminar bonding imperfections, delamination can be initiated by interlaminar stresses. This effect is amplified in sandwich composites subjected to compressive loads because the facesheets tend to buckle accentuating the risk of delamination growth. The delamination can eventually result in ultimate failure of the composite. Modern composite failure criteria for composite materials incorporate the interlaminar stresses. Therefore, accurate determination of interlaminar stresses is a topic of considerable interest in the research community. We will recapitulate some of the significant developments in this area. The state of interlaminar stress computation has been reviewed extensively by Kapania and Raciti [89] and Kant and Swaminathan [90]. Interlaminar stresses may be computed directly from the constitutive equation when an exact solution is available for the 3D elasticity equations. Vlasov [91], Pagano [92], Pagano and Hatfield [93], Srinivas and Rao [94], and Srinivas, Joga Rao, and Rao [95] developed analytical solutions of 3D elasticity for orthotropic, simply



supported laminates. Srinivas and Rao [96] obtained analytic solutions for other types of boundary conditions. Vel and Batra [97] presented an analytic solution to arbitrary boundary conditions by solving the 3D elasticity equations by a generalization of the Eshelby-Stroh formalism. Vel and Batra [97] compare the analytic solution with the classical laminated plate theory (CLPT), the first-order shear deformable theory (FSDT), and a higher-order shear deformable theory (HSDT) [98] for various layups. However, analytic solutions are generally very specific and often unavailable for a practical engineering application.

The 3D finite element method (FEM) has been used by many authors to determine the interlaminar stresses accurately [99]. However, the 3D FEM is computationally expensive. Two-dimensional theories such as classical laminated plate theory (CLPT) and the first-order shear deformation theory (FSDT) provide much less expensive techniques for determining the displacements and stresses. However, using CLPT assumes that there are no transverse shear strains and therefore using the constitutive stress-strain relations alone yield no shear stresses. Similarly with FSDT assuming constant shear strain results in piecewise constant interlaminar shear strains and require the introduction of a shear correction factor. Higher-order plate theories provide more accurate strain representations, at the cost of additional computational expense.

Reddy [100] provided an alternative to the constitutive relations by integrating the 3D elasticity equations. The technique also provides a method for determining the transverse normal stress distribution through the thickness. However, this technique requires lateral derivatives of lateral strains, a feature not explicitly provided from a CLPT or FSDT finite element implementation. For the transverse shear stresses, the equilibrium integration approach necessitates the first derivatives of strains. A recent review of the use of finite element for composite beams is available in Goyal and Kapania [101]. For the transverse normal stress, the second derivatives of strain are required.

A significant amount of research has been conducted in the area of developing post-

processing schemes to be used with commercial finite element software. Lajczok [102] used a finite differencing scheme to compute the higher-order derivatives of in-plane strain data necessary within the equilibrium equation approach of Reddy. Byun and Kapania [103] used Chebyshev and other orthogonal polynomials to interpolate the displacements and compute the higher derivatives of in-plane strain. Lee and Lee [104] developed a post processing scheme for determining the transverse stresses in geometrically nonlinear composites for cross-ply symmetric composites and sandwich composites with cross-ply Graphite/Epoxy facesheets and isotropic core material. Roos *et al.* [105] developed a post-processing method for determining the interlaminar normal stress in doubly curved laminate shell elements in commercial FE codes. Tessler and Riggs [106] developed a variational smoothing algorithm to accurately obtain the higher order derivatives and achieve the interlaminar stresses. Tessler *et al.* [107] used the “Smoothing Element Analysis” for improving the accuracy of finite element stresses for general application and not just for interlaminar stresses in [107]; however, the approach is essentially a second FEA.

While a lot of work has been done to post-process the results from a FEA, a substantial amount of this thesis deals with the development of an approach that can obtain the necessary derivatives of in-plane strains without post-processing. In general, meshless methods have a higher degree of continuity than the FEMs. Therefore they tend to predict the derivatives of the displacement more accurately. In the next section, the Sinc numerical methods are reviewed and considered as a possible option for determining interlaminar stresses.

## 1.5 Review of Sinc Numerical Methods

In recent years, Sinc approximation has been a highly studied topic in the research literature particularly in conjunction with methods for solving two-point boundary value problems (BVPs). The Sinc approximation has been used as the basis function in both the Sinc-collocation method and the Sinc-Galerkin method because of the ease with which it may

handle the presence of singularities or unbounded domains [108]. Further, the Sinc function is highly effective at capturing oscillating behavior in space, and is thus quite useful for solutions with such characteristics.

Difficulties in the Sinc-collocation method arise in applying it to a BVP with mixed nonhomogeneous boundary conditions because the derivatives of the Sinc functions at the boundaries are undefined [109]. Narasimhan *et al.* [110] use a finite difference method to calculate the derivatives near the boundaries. Wu, Li, and Kong [109] addressed this issue introducing a Sinc-collocation method with boundary treatment (SCMBT) which they showed to provide good convergence properties and easy treatment of all types of boundary conditions.

A lot of attention has been given to the Sinc-Galerkin method and its efficiency has been proved for both linear and nonlinear BVPs [111, 112, 113, 114]. Al-Khaled [115] compared the Sinc-Galerkin method with He's homotopy perturbation method for singular two-point BVPs [116, 117]. El-Gamel [118] applies the Sinc-Galerkin method to a fifth order BVP and compares the results with sixth-degree B-Spline functions and found that the Sinc-Galerkin method obtains reduced absolute error in the unknown function as compared with that obtained using the sixth-degree B-Spline method.

Most numerical methods for solving BVPs approximate the primary variable by some form of interpolation and the derivatives of the basis functions are computed from the primary variable approximation. The FEM, most meshless methods, and even most Sinc methods such as the Sinc-Galerkin and Sinc-collocation methods follow this approach. With such methods, errors in the primary variable are amplified through the process of differentiation. However, the process of integration results in smoothing these inherent errors. This philosophy is employed by the procedure of indirect or integrated radial basis function networks (IRBFN) by Mai-Duy and Tran-Cong [119, 120], by Wu and Ren's Differential quadrature method based on the highest derivative (DQIHD) [121], and by Li and Wu's

Sinc method based on Interpolation of Highest Derivatives (SIHD) [122]. All three of these methods rely on interpolation of the highest-order derivative and integration to obtain the unknown function.

The IRBFN approach has been studied extensively. Mai-Duy and Tran-Cong [119] proposed both the direct or differentiated and indirect or integrated radial basis function networks (DRBFN and IRBFN respectively) for approximation of functions. They used the IRBFN basis function as a collocation method and showed it to provide greater accuracy than the DRBFN used with a collocation method [123]. Mai-Duy and Tran-Cong [124] also used the IRBFN with the weak form of the governing equation in a Galerkin formulation; however, the natural boundary conditions were still satisfied as per the collocation scheme. Their results indicated that the Galerkin procedure exhibited greater accuracy and higher rates of convergence than did the collocation method. Furthermore, they noted that the IRBFN basis function maintained lower matrix condition number than the DRBFN approach.

The Differential Quadrature Method (DQM) was first introduced by Bellman and Casti [125]. Substantial work has been done by Bert and Striz and their colleagues [126, 127, 128, 129, 130] to apply the DQM for structural mechanics problems; however, work implementing the DQIHD has been limited to Wu and his colleagues [121, 131]. The traditional DQM approximates the partial derivative of a function with respect to a variable by a weighted sum of functional values at all discrete points in that direction. The weighting coefficients depend only on the grid space. Thus the DQM can be computationally very efficient, even more than the traditional FEM [132]. The DQIHD tries to use the values of the partial derivative at discrete points to express the functional values [121, 131]. Liu and Wu call the approach Differential Quadrature Trefftz method using the Trefftz basis functions and use the approach to study rectangular and irregular plates [131].

The SIHD by Li and Wu [122] uses numerical indefinite integration based on the double-

exponential (DE) transformation as developed by Mori and Muhammad [133] to efficiently perform the integration. Collocation is used to construct a system of linear or nonlinear equations. The method is still in its infancy. To the author's knowledge, no other work has been done, to advance the SIHD method and implement it for a substantial use. Because the method approximates the highest-order derivative in the governing equation of a BVP and uses integration, not differentiation, the higher-order derivatives of strains needed for accurate interlaminar stress calculation may be found from the method itself and not by post-processing.

## 1.6 Scope of this Dissertation

The scope of this dissertation was to both examine the feasibility of the SIHD method as a practical tool for the analysis of composite and hybrid systems of adhesively bonded materials and enhance its capabilities as an analysis tool.

The remainder of this dissertation is arranged into the following chapters: Chapter 1 is the introduction. Chapter 2 reviews techniques for analysis of composite plates and beams using equivalent single-layer theories. In Chapter 2, the method for obtaining interlaminar stresses from plate analysis is detailed and the necessity of in-plane derivatives of in-plane strains is revealed.

In Chapter 3, the preliminary concepts of the Sinc methods are presented including a detailed presentation of the concept of numerical indefinite integration based on the DE transformation. In Chapter 3, the use of the numerical indefinite integration as a basis function for BVPs in 1D and 2D is presented. Chapter 3 also presents an example of interpolation with the Sinc series and the dilemma of how to appropriately choose the Sinc mesh size.

In Chapter 4, how to implement the SIHD method for solving 1D and 2D BVPs is presented. Li and Wu's approach of satisfying the boundary conditions is revealed to produce

an asymmetric distribution of Sinc points across the domain and is not very well suited for general application in 2D. An alternative symmetric approach is introduced. The results of both approaches are compared for a 1D analysis of a three-layered,  $[0^\circ/90^\circ/0^\circ]$ , graphite-epoxy composite, Timoshenko beam. The results are compared with the analytic solution for the problem. The results indicate that the symmetric approach improves the accuracy of the method and makes the method less dependent on the choice of Sinc mesh size. For 2D, a classical laminated plate is considered using SIHD and compared against the analytic solution for the problem. Some additional difficulties arise for the 2D case. These difficulties are discussed and resolved. The results indicate that the method accurately predicts the higher-order derivatives needed for the interlaminar stress calculation without additional post processing or smoothing.

Chapter 5 addresses how the interlaminar stresses from equivalent single-layer beam theories solved with the SIHD method compare with those from 3D elasticity solution for fiber-matrix laminates and functionally graded composites. Results for interlaminar stresses from the Bickford beam theory [134] and the Timoshenko beam theory are compared with an approximate solution of 3D elasticity equations by the FEM. The results indicate that through the majority of the beam, the stresses are very accurately predicted; however, at the boundary the results are inaccurate. The inaccuracies are likely due to the boundary effects that cannot be captured by the 1D theories. For the functionally graded composite, the numerical indefinite integration by DE transformation is also used to integrate through the core thickness and obtain the interlaminar stresses. This is without substantial computational expense because the SIHD method uses the same integration approach. Thus only matrix multiplication is performed to do the through-the-thickness integration.

In Chapter 6, attempts are made to improve the interlaminar stresses by increasing the order of the assumed displacement field and introducing a piecewise discontinuous displacement field through the higher-order shear and normal deformable theory (HOSNDT) [135]

and the refined zigzag theory [136]. The results indicate that the benefits of adding the discontinuous displacement field are substantial, especially in the case of severe differences in the shear moduli of the constituent materials.

Because of the difficulties with SIHD in 2D and because of apparent benefits in literature of using the weak form rather than the strong form [124, 137], a novel integrated Sinc method is developed. The method utilizes the integrated Sinc basis function of the SIHD method but is based on the Meshless Local Petrov-Galerkin method (MLPG) for domain decomposition. Therefore it was named the Integrated Local Petrov-Galerkin Sinc Method or ILPGSM. The method easily handles 2D problems on non-rectangular domains. The method is developed in Chapter 7, and compared with the SIHD method and the FEM for one and two dimensional problems.

In Chapter 8, the problem of a notched plane-stress panel is considered using the ILPGSM. Both elastic and elastic-plastic panels were analyzed using the ILPGSM. Results for the elastic panel were compared against an analytic solution for the problem and indicated a high level of accuracy was obtained by the ILPGSM. For the elastic-plastic panel, material non-linearity was introduced as a stepping stone toward analysis of hybrid materials involving interlaminar damage evolution. The incremental iterative approach is detailed and the modified Newton's approach is employed to analyze the nonlinear problem. The results compare well with a FE solution for the problem.

In Chapter 9, delamination of composite plane-strain and plane-stress specimens were analyzed using the ILPGSM. A 1D analysis of stacked Timoshenko beams was performed for double cantilever and fixed-ratio mixed mode beams. The top and bottom sublaminates were modeled using the Timoshenko beam theory and the two were coupled using an exponential irreversible traction-separation law representing the adhesive. Analysis of a GLARE 3-3/2-0.4 beam specimen with an initial delamination between the outer-most aluminum and glass-reinforced epoxy layers was conducted. The results were compared with a plane-strain

or plane-stress (where appropriate) FEA using standard interface elements. The results indicated the ILPGSM performs very well and the analysis procedure is able to capture the delamination growth very well as compared with the FEA. For the GLARE specimen, interlaminar stresses through-the-thickness were obtained by integration of the equilibrium equations of 3D elasticity. The interlaminar stresses compare well with the stresses obtained from the FEA.

Finally, a summary and the primary conclusions are given. In addition, future work is proposed which includes modifications to the basis function utilized by the integrated Sinc methods, the use of the integrated basis function as a smoothing algorithm for use with commercial FE software, and the use of the ILPGSM and the SIHD method for dynamic analysis in structural mechanics.



## 2 Equivalent Single-Layer Composite Plate Theories

The term equivalent single-layer (ESL) refers to treating a composite or hybrid material with multiple layers of dissimilar material as a statically equivalent, single layer with a single constitutive law. The ESL plate theories are derived from the 3D elasticity theory making use of assumptions regarding the kinematic behavior of the material system through its thickness. Integration of equilibrium equations through the thickness of the laminate smears the constitutive properties, which results in a much simplified 2D BVP at the cost of some through the thickness details. The next chapter, and the bulk of this dissertation deals with accurately and efficiently re-obtaining the through-the-thickness details with some accuracy. For a good overview of ESL plate and beam theories, refer to Kapania and Raciti [89], Reddy [98], and Goyal and Kapania [101]. The pertinent elements are reviewed in this Chapter.

We begin with the assumed displacement profile of Reddy's consistent third-order shear deformable plate theory (TSDT) [138]:

$$\begin{aligned} U(x, y, z) &= u_0(x, y) + z\phi_x(x, y) - z^3c_1 \left( \phi_x(x, y) + \frac{\partial w_0}{\partial x} \right), \\ V(x, y, z) &= v_0(x, y) + z\phi_y(x, y) - z^3c_1 \left( \phi_y(x, y) + \frac{\partial w_0}{\partial y} \right), \\ W(x, y) &= w_0(x, y), \end{aligned} \tag{2.1}$$

where  $z$  is the rectilinear coordinate in the thickness direction, and the  $xy$ -plane of the Cartesian coordinate system is located in the midplane of the plate. The displacement field is that of the TSDT when  $c_1 = (4/3)h^2$  where  $h$  is the plate thickness; however, the displacement reduces to that of the first-order shear deformable theory (FSDT) by specifying  $c_1 = 0$ . It is in assuming a through the thickness variation of displacement that the primary approximation from the 3D elasticity theory lies. By assuming a continuously differentiable displacement field, the strains are required to be continuous through the thickness including between ma-

terial boundaries. The physics necessitate continuity of tractions between layer boundaries of perfectly (rigidly) bonded materials; however, because of the dissimilar material constitutive relations this cannot be obtained by the continuously differentiable displacement field above. This will be discussed in greater detail in Chapter 6.2 of this dissertation.

The infinitesimal in-plane strains of the assumed displacement field can be expressed as

$$\{\epsilon\} = \{\epsilon^{(0)}\} + z\{\epsilon^{(1)}\} + z^3\{\epsilon^{(3)}\}, \quad (2.2)$$

where  $\{\epsilon\} = \{\epsilon_{xx}, \epsilon_{yy}, \gamma_{xy}\}^T$ . The transverse shear strains are

$$\{\gamma\} = \{\gamma^{(0)}\} + z^2\{\gamma^{(2)}\} \quad (2.3)$$

where  $\{\gamma\} = \{\gamma_{yz}, \gamma_{xz}\}^T$ . The transverse normal strain is taken to be identically zero [ $W(x, y, z) = w_0(x, y)$ ]. The strains can be expressed in terms of the assumed displacement field by defining

$$\begin{aligned} \{\epsilon^{(0)}\} &= \{u_{0,x}, v_{0,y}, u_{0,y} + v_{0,x}\}^T, \\ \{\epsilon^{(1)}\} &= \{\phi_{x,x}, \phi_{y,y}, \phi_{x,y} + \phi_{y,x}\}^T, \\ \{\epsilon^{(3)}\} &= -c_1\{\phi_{x,x} + w_{0,xx}, \phi_{y,y} + w_{0,yy}, \phi_{x,y} + \phi_{y,x} + 2w_{0,xy}\}^T, \\ \{\gamma^{(0)}\} &= \{\phi_y + w_{0,y}, \phi_x + w_{0,x}\}^T, \\ \{\gamma^{(2)}\} &= -2c_1\{\phi_y + w_{0,y}, \phi_x + w_{0,x}\}^T. \end{aligned} \quad (2.4)$$

where subscripts after a comma implies differentiation with respect to the variable indicated [ $(\bullet)_{,xy} = \partial^2(\bullet)/(\partial x \partial y)$ ]. These strains are related to the stresses by the plane-stress reduced

constitutive relation,

$$\begin{Bmatrix} \sigma_{xx}(x, y, z) \\ \sigma_{yy}(x, y, z) \\ \sigma_{xy}(x, y, z) \end{Bmatrix} = \begin{bmatrix} \bar{Q}_{11}(z) & \bar{Q}_{12}(z) & \bar{Q}_{16}(z) \\ \bar{Q}_{12}(z) & \bar{Q}_{22}(z) & \bar{Q}_{26}(z) \\ \bar{Q}_{16}(z) & \bar{Q}_{26}(z) & \bar{Q}_{66}(z) \end{bmatrix} \begin{Bmatrix} \epsilon_{xx}(x, y, z) \\ \epsilon_{yy}(x, y, z) \\ \gamma_{xy}(x, y, z) \end{Bmatrix}, \quad (2.5)$$

and

$$\begin{Bmatrix} \sigma_{yz}(x, y, z) \\ \sigma_{xz}(x, y, z) \end{Bmatrix} = K \begin{bmatrix} \bar{Q}_{44}(x, y, z) & \bar{Q}_{45}(x, y, z) \\ \bar{Q}_{45}(x, y, z) & \bar{Q}_{55}(x, y, z) \end{bmatrix} \begin{Bmatrix} \gamma_{yz}(x, y, z) \\ \gamma_{xz}(x, y, z) \end{Bmatrix},$$

where  $K$  is the shear correction factor, only applicable for the FSDT and its 1D analog, the Timoshenko beam theory. For the TSDT, take  $K = 1$ .

The stress resultants defined by

$$\{N_{\alpha\beta}, M_{\alpha\beta}, P_{\alpha\beta}\} = \int_{-h/2}^{h/2} \sigma_{\alpha\beta} \{1, z, z^3\} dz, \quad \{Q_\alpha, R_\alpha\} = K \int_{-h/2}^{h/2} \sigma_{\alpha z} \{1, z^2\} dz, \quad (2.6)$$

( $\alpha$  and  $\beta$  can each take the value of  $x$  and  $y$ ), may be written in terms of strains by

$$\begin{Bmatrix} \{N\} \\ \{M\} \\ \{P\} \end{Bmatrix} = \begin{bmatrix} [A] & [B] & [E] \\ [B] & [D] & [F] \\ [E] & [F] & [H] \end{bmatrix} \begin{Bmatrix} \{\epsilon^{(0)}\} \\ \{\epsilon^{(1)}\} \\ \{\epsilon^{(3)}\} \end{Bmatrix}, \quad (2.7)$$

$$\begin{Bmatrix} \{Q\} \\ \{R\} \end{Bmatrix} = \begin{bmatrix} [AS] & [DS] \\ [DS] & [FS] \end{bmatrix} \begin{Bmatrix} \{\gamma^{(0)}\} \\ \{\gamma^{(2)}\} \end{Bmatrix}, \quad (2.8)$$

where

$$\{A_{ij}, B_{ij}, D_{ij}, E_{ij}, F_{ij}, H_{ij}\} = \int_{-h/2}^{h/2} \bar{Q}_{ij}(z) \{1, z, z^2, z^3, z^4, z^6\} dz, \quad (2.9)$$

$$\{AS_{lm}, DS_{lm}, FS_{lm}\} = \int_{-h/2}^{h/2} \bar{Q}_{lm}(z) \{1, z^2, z^4\} dz. \quad (2.10)$$

Here  $i$  and  $j$  may take values of 1, 2, and 6 and  $l$  and  $m$  may take values of 4 and 5.

Static equilibrium equations and the variationally consistent boundary conditions may be derived from the principle of virtual work:

$$\delta W_{int} = \delta W_{ext} \quad (2.11)$$

with the internal work given by

$$\delta W_{int} = \int_{\Omega} \int_{z_0}^{z_k} \sigma_{ij} \delta \epsilon_{ij} dz d\Omega \quad (2.12)$$

where the composite or hybrid structure has thickness  $z_k - z_0$  and assuming the tractions are continuous across the the laminate interface boundary. By substituting the displacement definition and constitutive relations for each material into Eq. (2.12) and evaluating, the integration along the  $z$  direction, the importance of the stress resultants are realized.

The governing equations for the CLPT, the FSDT, and the TSDT are given in Ref. [98]. The Timoshenko beam theory and the Bickford beam theory [134], akin to the FSDT and TSDT respectively, are given in Appendix B. A solution to the BVP provides a less expensive approximation to the 3D elasticity solution.

Modern commercial FE codes typically implement shell elements which are first-order shear deformable. ABAQUS has a library of shell elements which include thin, thick, and general purpose shell elements. The elements, when operating under the small strain, small displacement assumption, use the Koiter-Sanders shell theory [75]. Through-the-thickness transverse shear and normal stresses are not accurately computed and post-processing techniques have been sought to better estimate these stress components.

## 2.1 Interlaminar Stresses

The transverse shear stresses ( $\sigma_{xz}$  and  $\sigma_{yz}$ ) and the transverse normal stress ( $\sigma_{zz}$ ) are critical for delamination of composite laminates or any adhesively bonded material system. These stresses collectively are referred to as interlaminar stresses. In general, these stress components are not accurately provided by an ESL plate theories.

After solving for the in-plane deformation field from static equilibrium, the in-plane stresses are obtained on a layer-by-layer basis from the constitutive relation [Eq. (2.5)]. However, using the definition of shear strains would result in a quadratic variation of stresses through the thickness using the TSDT. This would be excellent were the material homogeneous. However, for a multi-layered structure, the traction continuity between layers is not obtained using the constitutive law. Furthermore, if tangential tractions are imposed on the top layer, the TSDT does not satisfy them. The strains are continuous through the thickness and thus the transverse shear stresses cannot be continuous through the thickness due to the discontinuities in the constitutive relation [98]. Furthermore, using the FSDT theory, the shear strains are constant through the thickness and thus will never accurately reflect variation of transverse shears through the individual layer. For these reasons, a more accurate approach to obtain the through-the-thickness distribution of transverse shears was developed by Reddy [100]. The approach is reviewed for the TSDT.

The interlaminar stresses may be computed from the equilibrium equation of the 3D elasticity theory. The equilibrium equations with no body forces are given by

$$0 = \sigma_{ij,j}, \quad (2.13)$$

where repeated index implies summation on all components in that index and  $\sigma_{11} = \sigma_{xx}$ ,  $\sigma_{22} = \sigma_{yy}$ ,  $\sigma_{33} = \sigma_{zz}$ ,  $\sigma_{12} = \sigma_{xy}$ , and so forth.

Consider laminated composite or hybrid beams or plates whose geometry may be seen in

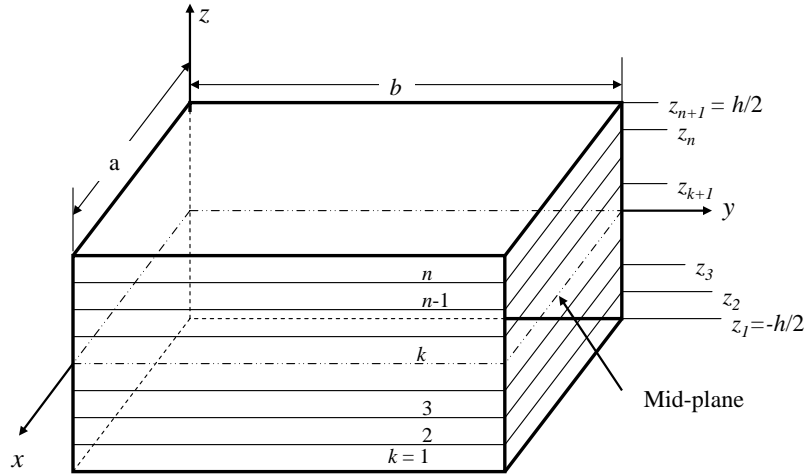


**Figure 2.1.** Geometry of a laminated composite plate. The thickness dimension has been exaggerated to illustrate the layers and mid-plane. In general  $a \gg h$  and  $b \gg h$ .

Fig. 2.1. While plates have  $h \ll a$  and  $h \ll b$ , the thickness dimension was exaggerated for clarity. The equilibrium equations of the 3D elasticity theory are integrated through the thickness of each orthotropic layer to obtain the interlaminar stresses for each layer ( $z_k \leq z \leq z_{k+1}$ ).

$$\sigma_{xz}^{(k)} = - \int_{z_k}^z \left( \frac{\partial \sigma_{xx}}{\partial x} + \frac{\partial \sigma_{xy}}{\partial y} \right) dz + G^{(k)} \quad (2.14)$$

$$\sigma_{yz}^{(k)} = - \int_{z_k}^z \left( \frac{\partial \sigma_{xy}}{\partial x} + \frac{\partial \sigma_{yy}}{\partial y} \right) dz + F^{(k)} \quad (2.15)$$

$$\sigma_{zz}^{(k)} = - \int_{z_k}^z \left( \frac{\partial \sigma_{xz}}{\partial x} + \frac{\partial \sigma_{yz}}{\partial y} \right) dz + H^{(k)} \quad (2.16)$$

Note that  $G^{(k)}$ ,  $F^{(k)}$ , and  $H^{(k)}$  are functions of  $x$  and  $y$  that may be determined from traction equilibrium between the layer boundaries. The third-order displacement field is adopted so that the in-plane strains are given by Eqs. (2.2) and Eq. (2.3). For the FSDT formulation, the higher-order strains are neglected ( $\epsilon_{\alpha\beta}^{(3)} = \gamma_{\alpha 3}^{(2)} = 0$ ). For the CLPT take  $\epsilon_{\alpha\beta}^{(3)} = \gamma_{\alpha 3}^{(0)} = \gamma_{\alpha 3}^{(2)} = 0$ .

Typically composite plates are thin in the thickness direction. Thus the plate theories

are derived assuming that  $\epsilon_{zz} = \sigma_{zz} = 0$ . The former is done by assuming the out of plane deformation  $W(x, y, z) = w_0(x, y)$ . Thus the normal strain component is identically zero. The plane-stress assumption,  $\sigma_{zz} = 0$ , is imposed by reducing the stiffness matrix to solve for  $\epsilon_{zz}$  in terms of the other strain components. Thus there is some inconsistency between the two assumptions. A nonzero  $\sigma_{zz}$  is computed from Eq. (2.16), even though the plane-stress assumption was used.

Assume  $\bar{Q}_{ij}^{(k)}$  is the plane stress-reduced stiffness matrix for the  $k$ th laminate layer. Substitute the stress-strain relations and the assumed strain into Eqs. (2.14-2.16) and perform the integration. Accordingly, the interlaminar stresses within the  $k$ th orthotropic material layer are given by:

$$\begin{aligned} \sigma_{13}^{(k)} = & \sigma_{13}(x, y, z_k) - \bar{Q}_{1j}\epsilon_{j,1}^{(0)}(z - z_k) - \frac{1}{2}\bar{Q}_{1j}\epsilon_{j,1}^{(1)}(z^2 - z_k^2) - \frac{1}{4}\bar{Q}_{1j}\epsilon_{j,1}^{(3)}(z^4 - z_k^4) \\ & - \bar{Q}_{6j}\epsilon_{j,2}^{(0)}(z - z_k) - \frac{1}{2}\bar{Q}_{6j}\epsilon_{j,2}^{(1)}(z^2 - z_k^2) - \frac{1}{4}\bar{Q}_{6j}\epsilon_{j,2}^{(3)}(z^4 - z_k^4), \quad (2.17) \end{aligned}$$

$$\begin{aligned} \sigma_{23}^{(k)} = & \sigma_{23}(x, y, z_k) - \bar{Q}_{2j}\epsilon_{j,2}^{(0)}(z - z_k) - \frac{1}{2}\bar{Q}_{2j}\epsilon_{j,2}^{(1)}(z^2 - z_k^2) - \frac{1}{4}\bar{Q}_{2j}\epsilon_{j,2}^{(3)}(z^4 - z_k^4) \\ & - \bar{Q}_{6j}\epsilon_{j,1}^{(0)}(z - z_k) - \frac{1}{2}\bar{Q}_{6j}\epsilon_{j,1}^{(1)}(z^2 - z_k^2) - \frac{1}{4}\bar{Q}_{6j}\epsilon_{j,1}^{(3)}(z^4 - z_k^4), \quad (2.18) \end{aligned}$$

$$\begin{aligned}
\sigma_{33}^{(k)} = & \sigma_{33}(x, y, z_k) - \sigma_{23,2}(x, y, z_k)(z - z_k) - \sigma_{13,1}(x, y, z_k)(z - z_k) + \frac{1}{2}\bar{Q}_{2j}\epsilon_{j,22}^{(0)}z^2 \\
& - \bar{Q}_{2j}\epsilon_{j,22}^{(0)}zz_k + \frac{1}{2}\bar{Q}_{2j}\epsilon_{j,22}^{(0)}z_k^2 + \frac{1}{6}\bar{Q}_{2j}\epsilon_{j,22}^{(1)}z^3 - \frac{1}{2}\bar{Q}_{2j}\epsilon_{j,22}^{(1)}zz_k^2 + \frac{1}{3}\bar{Q}_{2j}\epsilon_{j,22}^{(1)}z_k^3 \\
& + \frac{1}{20}\bar{Q}_{2j}\epsilon_{j,22}^{(3)}z^5 - \frac{1}{4}\bar{Q}_{2j}\epsilon_{j,22}^{(3)}zz_k^4 + \frac{1}{5}\bar{Q}_{2j}\epsilon_{j,22}^{(3)}z_k^5 + \bar{Q}_{6j}\epsilon_{j,12}^{(0)}z^2 - 2\bar{Q}_{6j}\epsilon_{j,12}^{(0)}zz_k \\
& + \bar{Q}_{6j}\epsilon_{j,12}^{(0)}z_k^2 + \frac{1}{3}\bar{Q}_{6j}\epsilon_{j,12}^{(1)}z^3 - \bar{Q}_{6j}\epsilon_{j,12}^{(1)}zz_k^2 + \frac{2}{3}\bar{Q}_{6j}\epsilon_{j,12}^{(1)}z_k^3 + \frac{1}{10}\bar{Q}_{6j}\epsilon_{j,12}^{(3)}z^5 \\
& - \frac{1}{2}\bar{Q}_{6j}\epsilon_{j,12}^{(3)}zz_k^4 + \frac{2}{5}\bar{Q}_{6j}\epsilon_{j,12}^{(3)}z_k^5 + \frac{1}{2}\bar{Q}_{1j}\epsilon_{j,11}^{(0)}z^2 - \bar{Q}_{1j}\epsilon_{j,11}^{(0)}zz_k \\
& + \frac{1}{2}\bar{Q}_{1j}\epsilon_{j,11}^{(0)}z_k^2 + \frac{1}{6}\bar{Q}_{1j}\epsilon_{j,11}^{(1)}z^3 - \frac{1}{2}\bar{Q}_{1j}\epsilon_{j,11}^{(1)}z_k^2z + \frac{1}{3}\bar{Q}_{1j}\epsilon_{j,11}^{(1)}z_k^3 \\
& + \frac{1}{20}\bar{Q}_{1j}\epsilon_{j,11}^{(3)}z^5 - \frac{1}{4}\bar{Q}_{1j}\epsilon_{j,11}^{(3)}zz_k^4 + \frac{1}{5}\bar{Q}_{1j}\epsilon_{j,11}^{(3)}z_k^5, \quad (2.19)
\end{aligned}$$

where  $j$  may take a value of 1, 2, or 6,  $\epsilon_{xx} = \epsilon_1$ ,  $\epsilon_{yy} = \epsilon_2$ ,  $\gamma_{xy} = \epsilon_6$ , the partial derivatives are indicated by  $\epsilon_{j,1} = \partial\epsilon_j/\partial x$  and  $\epsilon_{j,2} = \partial\epsilon_j/\partial y$ ,  $z$  is the global transverse coordinate, and  $z_k$  is the global coordinate of the bottom plane of the  $k$ th laminate layer (See Fig. 2.1).

The terms  $\sigma_{\alpha 3}(x, y, z_k)$ ,  $\sigma_{\alpha 3,\alpha}(x, y, z_k)$ , and  $\sigma_{33}(x, y, z_k)$  ( $\alpha = \{1, 2\}$ ) are known for  $k = 1$  from the boundary condition. If the bottom surface is traction free then  $\sigma_{\alpha 3}(x, y, z_1) = \sigma_{\alpha 3,\alpha}(x, y, z_1) = \sigma_{33}(x, y, z_1) = 0$ . If a traction is applied, then the appropriate conditions can be applied. For  $k > 1$ , continuity of tractions between layers is analytically enforced ( $\sigma_{\alpha 3}(x, y, z_k) = \sigma_{\alpha 3}(x, y, z_{k-1})$ ,  $\sigma_{33}(x, y, z_k) = \sigma_{33}(x, y, z_{k-1})$ ). This condition implies the continuity of the in-plane derivatives of the interlaminar shear stresses  $\sigma_{\alpha 3,\alpha}(x, y, z_k) = \sigma_{\alpha 3,\alpha}(x, y, z_{k-1})$  should also be enforced. Equations (2.17 - 2.19) necessitate second derivatives of in-plane strain which are not easily obtained from the solution of the 2D problem by a  $C^0$  FEM.

## 2.2 Beam Theory Reduction

Beams are also important structural members in design. Moreover, analysis of a beam theory serves as 1D analog to the use of ESL theories for plates. In this dissertation, the analysis of beams by the integrated Sinc methods serves as an important contribution to the literature.



The primary assumptions and reductions from the ESL plate theories to their beam analogs are presented in this section.

### 2.2.1 Plane-Stress Beams

A beam having small cross-sectional dimensions relative to the length ( $a \gg h$  and  $a \gg b$ ) would behave according to the plane-stress assumption in the  $y$  direction as well as the  $z$  direction. To implement this reduction, the stress resultants  $N_{yy}$ ,  $N_{xy}$ ,  $M_{yy}$ ,  $M_{xy}$ ,  $P_{xy}$ ,  $P_{yy}$ ,  $Q_y$ , and  $R_y$  are assumed to vanish. The strains  $\epsilon_{yy}$  and  $\gamma_{xy}$ , however, are nonzero but should be removed so that only derivatives with respect to  $x$  remain and the problem is effectively 1D.

To reduce the stress resultant-strain relations, Eq. (2.7) is inverted and the constraints  $N_{yy} = N_{xy} = M_{yy} = M_{xy} = P_{xy} = P_{yy} = Q_y = R_y = 0$  are imposed.

$$\begin{bmatrix}
 A_{11} & A_{12} & A_{16} & B_{11} & B_{12} & B_{16} & E_{11} & E_{12} & E_{16} \\
 A_{21} & A_{22} & A_{26} & B_{21} & B_{22} & B_{26} & E_{21} & E_{22} & E_{26} \\
 A_{61} & A_{62} & A_{66} & B_{61} & B_{62} & B_{66} & E_{61} & E_{62} & E_{66} \\
 B_{11} & B_{12} & B_{16} & D_{11} & D_{12} & D_{16} & F_{11} & F_{12} & F_{16} \\
 B_{21} & B_{22} & B_{26} & D_{21} & D_{22} & D_{26} & F_{21} & F_{22} & F_{26} \\
 B_{61} & B_{62} & B_{66} & D_{61} & D_{62} & D_{66} & F_{61} & F_{62} & F_{66} \\
 E_{11} & E_{12} & E_{16} & F_{11} & F_{12} & F_{16} & H_{11} & H_{12} & H_{16} \\
 E_{21} & E_{22} & E_{26} & F_{21} & F_{22} & F_{26} & H_{21} & H_{22} & H_{26} \\
 E_{61} & E_{62} & E_{66} & F_{61} & F_{62} & F_{66} & H_{61} & H_{62} & H_{66}
 \end{bmatrix}^{-1}
 \begin{pmatrix}
 N_{xx} \\
 0 \\
 0 \\
 M_{xx} \\
 0 \\
 0 \\
 P_{xx} \\
 0 \\
 0
 \end{pmatrix}
 =
 \begin{pmatrix}
 \epsilon_{xx}^{(0)} \\
 \epsilon_{yy}^{(0)} \\
 \gamma_{xy}^{(0)} \\
 \epsilon_{xx}^{(1)} \\
 \epsilon_{yy}^{(1)} \\
 \gamma_{xy}^{(1)} \\
 \epsilon_{xx}^{(3)} \\
 \epsilon_{yy}^{(3)} \\
 \gamma_{xy}^{(3)}
 \end{pmatrix}
 \quad (2.20)$$

$$\begin{bmatrix} AS_{44} & AS_{45} & DS_{44} & DS_{45} \\ AS_{54} & AS_{55} & DS_{54} & DS_{55} \\ DS_{44} & DS_{45} & FS_{44} & FS_{45} \\ DS_{54} & DS_{55} & FS_{54} & FS_{55} \end{bmatrix}^{-1} \begin{pmatrix} Q_x \\ 0 \\ R_x \\ 0 \end{pmatrix} = \begin{pmatrix} \gamma_{yz}^{(0)} \\ \gamma_{xz}^{(0)} \\ \gamma_{yz}^{(2)} \\ \gamma_{xz}^{(2)} \end{pmatrix} \quad (2.21)$$

By doing so, the strain components  $\epsilon_{yy}^{(i)}$ ,  $\gamma_{xy}^{(i)}$ , and  $\gamma_{yz}^{(j)}$  ( $i = 0, 1, 3$  and  $j = 0, 2$ ) are expressed in terms of  $\epsilon_{xx}^{(i)}$  and  $\gamma_{xz}^{(j)}$ . Then solving for the nonzero stress-resultants, the following relations are obtained

$$\begin{pmatrix} N_{xx} \\ M_{xx} \\ P_{xx} \end{pmatrix} = \begin{bmatrix} A_{11}^* & B_{11}^* & E_{11}^* \\ B_{11}^* & D_{11}^* & F_{11}^* \\ E_{11}^* & F_{11}^* & H_{11}^* \end{bmatrix} \begin{pmatrix} \epsilon_{xx}^{(0)} \\ \epsilon_{xx}^{(1)} \\ \epsilon_{xx}^{(3)} \end{pmatrix}, \quad (2.22)$$

$$\begin{pmatrix} Q_x \\ R_x \end{pmatrix} = \begin{bmatrix} AS_{55}^* & DS_{55}^* \\ DS_{55}^* & FS_{55}^* \end{bmatrix} \begin{pmatrix} \gamma_{xz}^{(0)} \\ \gamma_{xz}^{(2)} \end{pmatrix},$$

where the stars are introduced to indicate the reduction from the stress resultant-strain relations given in Eqs. (2.6) and (2.8). For a single orthotropic layer, the resulting stiffnesses are:

$$\begin{aligned} A_{11}^* &= E_1 h, & D_{11}^* &= \frac{E_1 h^3}{12}, \\ F_{11}^* &= \frac{E_1 h^5}{80}, & H_{11}^* &= \frac{E_1 h^7}{448} \\ B_{11}^* &= 0 & E_{11}^* &= 0 \end{aligned} \quad (2.23)$$

$$\begin{aligned} AS_{55}^* &= G_{13} h, & DS_{55}^* &= \frac{G_{13} h^3}{12} \\ FS_{55}^* &= \frac{G_{13} h^5}{80}. \end{aligned}$$

### 2.2.2 Plane-Strain Beams

Often a structure will have  $a \gg h$ ,  $b \gg h$ , and boundary conditions and loading that do not change along the  $y$  direction. This case is typically referred to as a plate under cylindrical bending [98]. For this case, the stresses and displacements are not functions of  $y$ . Thus the strain components  $\epsilon_{yy}$ ,  $\epsilon_{xy}$ , and  $\gamma_{yz}$  are assumed to vanish. For this case, the stress resultant-strain relations utilize the form given in Eqs. (2.7) and (2.8). For a single orthotropic layer, the resulting stiffnesses are:

$$\begin{aligned}
 A_{11} &= \frac{E_1 h}{1 - \nu_{12}\nu_{21}}, & D_{11} &= \frac{E_1 h^3}{12(1 - \nu_{12}\nu_{21})} \\
 F_{11} &= \frac{E_1 h^5}{80(1 - \nu_{12}\nu_{21})}, & H_{11} &= \frac{E_1 h^7}{448(1 - \nu_{12}\nu_{21})} \\
 B_{11} &= 0, & E_{11} &= 0 \\
 AS_{55} &= G_{13} h, & DS_{55} &= \frac{G_{13} h^3}{12} \\
 FS_{55} &= \frac{G_{13} h^5}{80}.
 \end{aligned} \tag{2.24}$$

For both the plane-stress case and the plane-strain case, a 1D displacement field that is independent of  $y$  can be taken as

$$U(x, z) = u_0(x) + z\phi_x - c_1 z^3 \left( \phi_x + \frac{dw_0}{dx} \right) \quad \text{and} \quad W(x, z) = w_0(x). \tag{2.25}$$

The displacement field is that of the Bickford beam theory [134] which is completely analogous to the TSDT in 2D taking  $c_1 = (4/3)h^2$ . If  $c_1 = 0$  is taken and the shear correction factor is used, the displacement reduces to the Timoshenko beam theory, the 1D analog to the FSDT.

The development of the equilibrium equation for the Bickford beam theory is presented in Appendix B. The equilibrium equations for the Timoshenko beam theory are also given in Appendix B.

For obtaining the interlaminar stresses, the full in-plane strain field ( $\epsilon_{xx}$ ,  $\gamma_{xy}$  and  $\epsilon_{yy}$ ) is needed. For the plane-stress assumption, this is done by first obtaining  $N_{xx}$ ,  $M_{xx}$ , and  $P_{xx}$  by Eq. (2.22) and then plugging these into Eq. (2.20). For the plane-strain, the full strain field is known by solving the BVP. The interlaminar stresses for each case are found by evaluating Eqs. (2.17 - 2.19) assuming derivatives with respect to  $y$  are zero. For the plane-stress this results from assuming  $\sigma_{xy} = \sigma_{yy} = \sigma_{yz} = 0$ . For the plane-strain this results from the appropriate zero valued strain components.

### 3 Sinc Numerical Methods

In this chapter, the preliminary concepts of Sinc numerical methods are reviewed.

A function  $f(t)$  may be approximated on the real line  $t \in (-\infty, \infty)$  by the Sinc series:

$$f(t) \approx \sum_{j=-N}^N f(jh) \operatorname{sinc}[(\pi/h)(t - jh)] \quad (3.1)$$

where the Sinc function is defined by

$$\operatorname{sinc}(x) = \begin{cases} 1 & \text{for } x = 0 \\ \sin(x)/x & \text{for } x \neq 0 \end{cases}, \quad (3.2)$$

and where  $h$  is the Sinc mesh size or spacing of particles on the domain  $(-\infty, \infty)$ . The Sinc

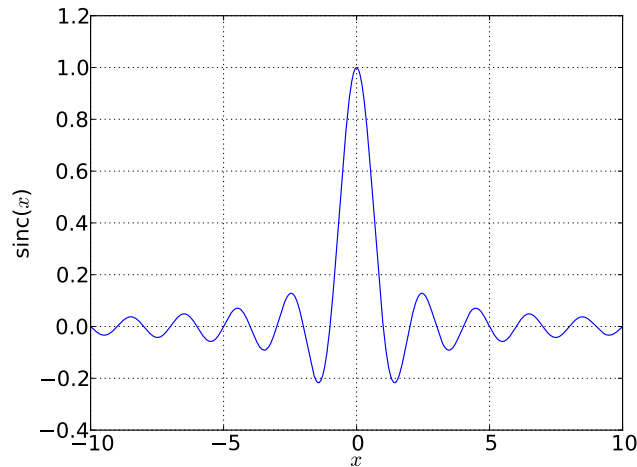


**Figure 3.1.** Plot of the Sinc function for  $-10 \leq x \leq 10$

function is shown plotted in Fig. 3.1.

Assuming that  $f(t)$  is analytic and decays exponentially on the real line, Sugihara and Matsuo [139, 140] showed that the error of the approximation given in Eq. (3.1) decays

exponentially with increasing  $N$  when the Sinc point mesh size is given by

$$h = \left(\frac{c_1}{N}\right)^{1/2} \tag{3.3}$$

for some positive constant  $c_1$ .

The Sinc interpolation may be extended to approximate  $f(t)$  on the finite interval  $(0, 1)$  by selection of an appropriate transfer function to transform the finite interval onto the entire real line and impose the necessary exponential decay. While there is nothing special about the interval  $(0, 1)$  it represents an interval onto which any domain may be transformed without additional complication. Such a variable transformation is denoted by  $\tau = \phi(t)$  and the inverse transformation by  $t = \psi(\tau)$  such that the boundary is transformed by  $\phi(0) = -\infty$  and  $\phi(1) = \infty$ . The Sinc approximation, employing the transformation, may be written for the function  $f(t)$  by

$$f(t) \approx \sum_{j=-N}^N f(\psi(jh)) \text{sinc}[(\pi/h)(\phi(t) - jh)], \tag{3.4}$$

where the Sinc mesh size,  $h$ , represents the separation between Sinc points on the  $(-\infty, \infty)$  domain. Figure 3.2 indicates such a possible transformation with mesh size indicated.

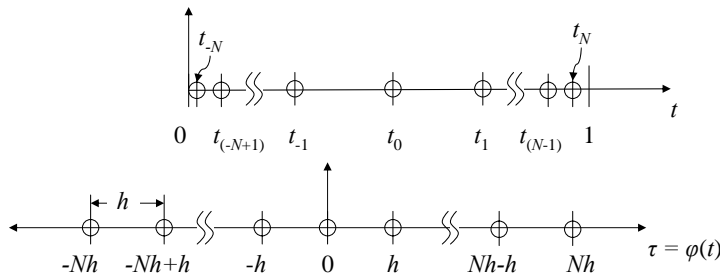


**Figure 3.2.** Transformation from  $t \in (0, 1)$  onto the real line  $\tau \in (-\infty, \infty)$ .

The double-exponential (DE) transformation was proposed by Takahasi and Mori [141] in 1974 for the evaluation of integrals of analytic functions with end-point singularities; the

name referring to the double-exponential decay rate that such a transformation imposes. For this study and the work of Li and Wu [122], the DE transformation suggested by Sugihara and Matsuo [140] was used:

$$t = \psi(\tau) = \frac{1}{2} \tanh\left(\frac{\pi}{2} \sinh(\tau)\right) + \frac{1}{2} \quad (3.5)$$

The proof of convergence of Eq. (3.4) using the DE transformation was provided by Sugihara and Matsuo [140] and is reviewed below. Consider a function  $f(\psi(\tau))$ , analytic on the infinite strip domain  $\mathcal{D}_d$  of width  $2d$  ( $d > 0$ ) in the complex plane,  $\mathcal{D}_d \equiv \{\tau \in \mathbb{C} : |\text{Im } \tau| < d\}$ , with

$$\lim_{\epsilon \rightarrow 0} \int_{\partial \mathcal{D}_d(\epsilon)} |f(\tau)| |d\tau| < \infty$$

$$\mathcal{D}_d(\epsilon) = \{\tau \in \mathbb{C} : |\text{Re } \tau| < 1/\epsilon, |\text{Im } \tau| < d(1 - \epsilon)\}$$

and with double-exponential decay rate:

$$|f(\psi(\tau))\psi'(\tau)| \leq \alpha \exp(-\beta \exp(\gamma|\tau|)) \quad (3.6)$$

for  $\tau \in \mathbb{R}$  and with  $\alpha$ ,  $\beta$ , and  $\gamma > 0$ . Sugihara and Matsuo [140] showed that for such a function, the error of the Sinc approximation is bounded by:

$$\sup_{0 \leq t \leq 1} \left| f(t) - \sum_{j=-N}^N f(\psi(jh)) \text{sinc}[(\pi/h)(\phi(t) - jh)] \right| \leq C \exp\left[\frac{-\pi d \gamma N}{\log(\pi d \gamma N / \beta)}\right] \quad (3.7)$$

for some  $C > 0$ , with the mesh size  $h$  taken as:

$$h = \frac{\log(\pi d \gamma N / \beta)}{\gamma N} \quad (3.8)$$

Sugihara and Matsuo [140] also assert that the DE decay rate is the optimal convergence

rate for the Sinc approximation.

### 3.1 Numerical Indefinite Integration

Muhammad and Mori [133] developed a method of “numerical indefinite” integration based on the DE transformation. The method is called “numerical indefinite” integration because the value of the anti-derivative of a function is found at a series of points, given the value of the function at those discrete points. The approach was used by Muhammad *et al.* [142] for solving integral equations by the Sinc collocation method and is essential to the Sinc method based on Interpolation of Highest Derivative (SIHD) as presented by Li and Wu [122]. The reader should also refer to the work of Mori and Sugihara [143, 144] for a good background on numerical integration using the DE transformation.

Consider evaluation of an integral over the domain  $(0, s)$ ,

$$\int_0^s f(t)dt, \quad 0 < s < 1. \quad (3.9)$$

The integrand is transformed to the  $\tau \in (-\infty, \infty)$  domain, obtaining:

$$\int_0^s f(t)dt = \int_{-\infty}^{\phi(s)} f(\psi(\tau))\psi'(\tau)d\tau. \quad (3.10)$$

Note that  $s = 1$  corresponds to  $\tau = \infty$ . The integrand,  $f(\psi(\tau))\psi'(\tau)$ , may be expanded employing the Sinc series approximation,

$$f(\psi(\tau))\psi'(\tau) = \sum_{j=-N}^N f(\psi(jh))\psi'(jh)\text{sinc}[(\pi)(\tau/h - j)]. \quad (3.11)$$

Substituting Eq. (3.11) into the integrand of Eq. (3.10), the following expression is obtained.

$$\int_0^s f(t)dt = h \sum_{j=-N}^N f(\psi(jh))\psi'(jh) \left( \frac{1}{2} + \frac{1}{\pi} \text{Si}(\pi\phi(s)/h - \pi j) \right) \quad (3.12)$$



Eq. (3.12) holds for all  $s \in (0, 1)$ , where  $\text{Si}(x)$  is the sine-integral function [145] defined by

$$\text{Si}(x) = \int_0^x \frac{\sin(s)}{s} ds. \quad (3.13)$$

Muhammad *et al.* [142] note that the convergence rate is of the order

$$(\log(N)/N) \exp(-c_1 N / \log(c_2 N)),$$

for some positive  $c_1$  and  $c_2$  when the mesh size is chosen according to Eq. (3.8).

It should be noted that evaluating the sine-integral is not trivial. MATLAB offers a function “SININT” as part of its special functions. However, inspecting the m-file reveals symbolic math is used to perform the operation. Numerical experiments have revealed the SININT function to take 42 sec to perform the operation just 5,000 times on a 1.61 GHz dual-processor, Windows XP, PC with 2 GB of RAM. There are both trig and polynomial series expansions for the sine-integral; however, the trig series is divergent for  $x \gg 1$  and the polynomial series is slowly convergent and not precise for  $x \gg 1$  [145]. Recently, an algorithm for the rational approximation of the sine- and the cosine-integrals was developed by MacLeod [146]. While MacLeod provides the algorithm via the NUMERALGO section of NETLIB [146], for this dissertation, the algorithm was implemented by the author in both MATLAB and Fortran 90. The same operations using the rational approximation of MacLeod run in only 0.015 sec on the same PC, 2,800 times faster than MATLAB’s SININT function.

## 3.2 Basic Features of Sinc Approximation and Numerical Indefinite Integration

Consider interpolation of the function  $f(x) = x^{1/2}(1-x)^{3/4}$  on the domain  $x \in [0, 1]$  using Eq. (3.4) with Eq. (3.5) to impose the double exponential decay. Knowing the decay rate of  $f(\psi(\tau))\psi'(\tau)$ , i.e. solving for  $\beta$  and  $\gamma$  in Eq. (3.7) the mesh size is chosen by Eq. (3.8). For the present example function, Sugihara and Matsuo [140] indicated that taking  $d = \pi/4$ ,  $\beta = \pi/4$ , and  $\gamma = 1$  satisfy the mesh size requirements for a convergence rate given by Eq. (3.7). Note that selection of the mesh size depends on the function itself. If the interpolation is desired as the basis function of an approximate method for solving boundary value problems, the function being approximated is the unknown and thus satisfying the mesh size requirement given by Eq. (3.8) is not practical. The problem has been noted by Sugihara and Matsuo [140]. Sugihara and Matsuo note that this feature makes the Sinc collocation method less tractable in practice.

In this dissertation, the choice of the mesh size was taken using a different approach. Consider Fig. 3.2. If the span of Sinc points in the  $\tau$  domain is  $\alpha$ , then increasing  $N$  should serve to increase the number of Sinc points within this span. Let  $\alpha$  be constant for increasing Sinc points. Then the mesh size would be defined by  $h = \alpha/N$ . This approach was considered for the present example interpolation in Figs. 3.3 and 3.4. In Fig. 3.4, the error is defined by:

$$\frac{\int_0^1 (f_{exact} - f_{approx})^2 dx}{\int_0^1 f_{exact}^2 dx} \quad (3.14)$$

The theoretical choice of mesh size by Sugihara and Matsuo results in an excellent interpolation for the present example. The point-wise error in the approximation converges very rapidly. However, there are a very large number of Sinc points concentrated near  $x = 0$  and  $x = 1$ . In a BVP, such a large concentration of Sinc points near the edges could result in

poor numerical conditioning of the solution approach.

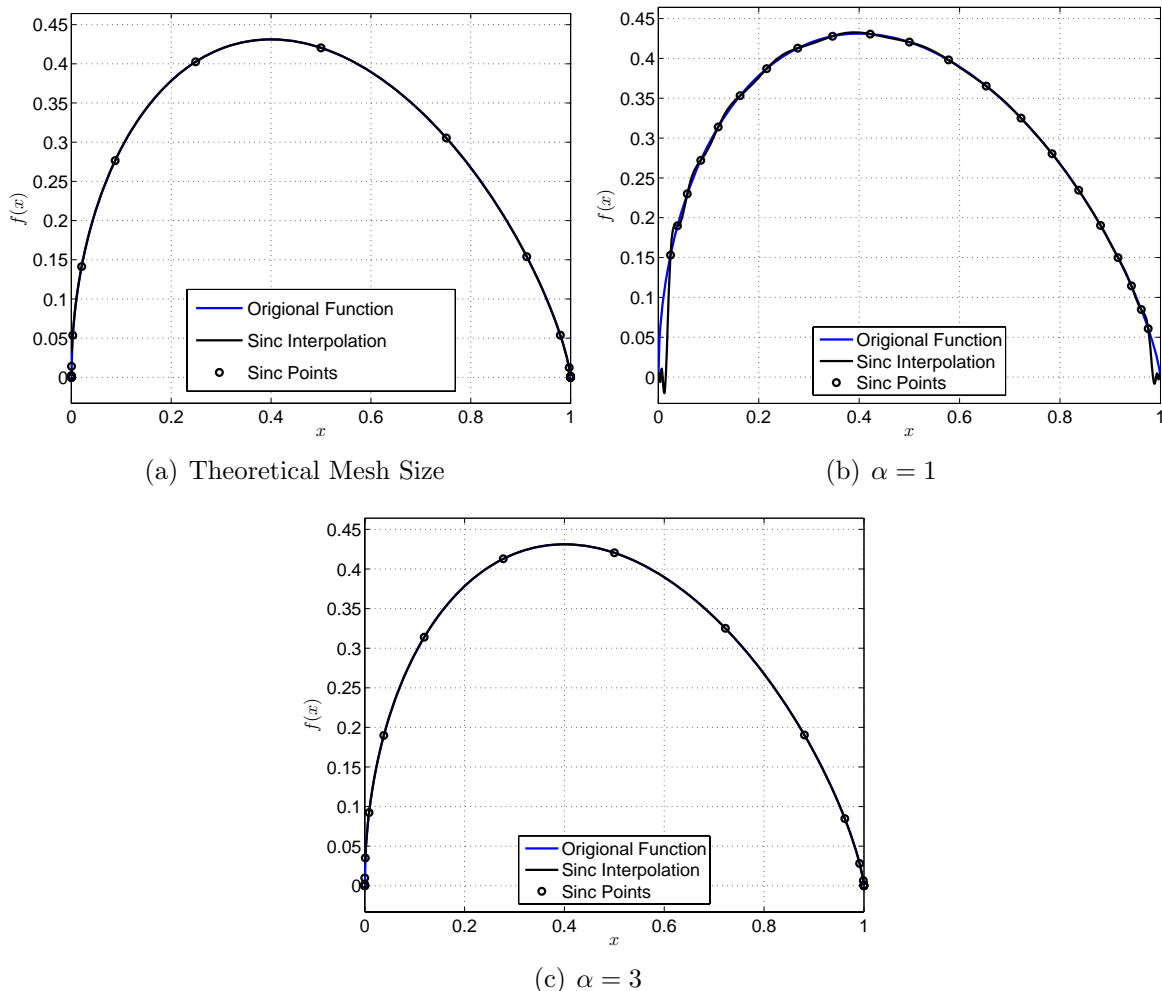


**Figure 3.3.** Approximation of the example function with various choices of mesh size using  $N = 10$  or 21 Sinc points.

The selection of span gives some control over the distribution of Sinc points. Notice in Fig. 3.3 ( $\alpha = 1$ ), the Sinc points are more uniformly distributed across the domain than by the theoretical mesh size selection. However, the interpolation results in large error with large oscillations between Sinc points. Furthermore, it should be noted that between  $x = 0$  and the first Sinc point, the Sinc series becomes zero and does not approximate the value of the function very well. A similar feature is seen at  $x = 1$ . With the span  $\alpha = 3$ , the accuracy is similar to that obtained using the theoretical mesh size; however, the points are highly

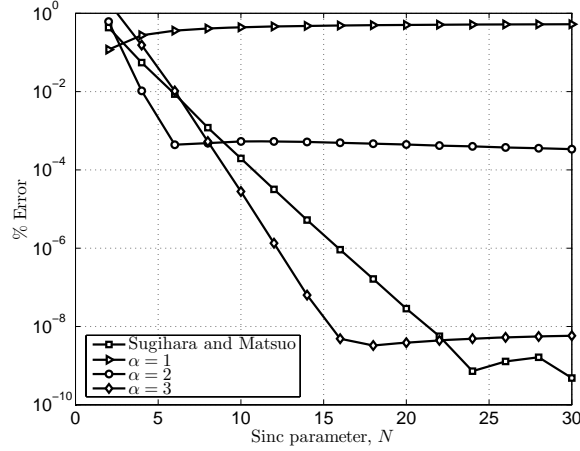


Figure 3.4. Error of Sinc approximation for various mesh size choices.

concentrated near the edges which could in turn increase the matrix condition number when implemented as a basis function of a numerical method to solve BVPs. This will be revisited in Chapter 4 when using the SIHD method to solve both a 1D, Timoshenko beam problem and a 2D classical laminated plate problem.

### 3.3 Integrated Sinc Basis Function

In this section the principle of numerical indefinite integration are used to develop a basis function in both 1D and 2D for solving BVPs.

#### 3.3.1 Problems Involving only First-Order Derivatives

For a 1D BVP of the unknown function  $f(\xi)$  where only the first-order derivative is of interest, assume that  $f'(\xi_i)$  is known for all  $\xi_i$  such that  $0 < \xi_i < 1$  and corresponding to  $\xi_i = \psi(ih)$  with  $i = \{-N, -N + 1, \dots, -1, 0, 1, \dots, N - 1, N\}$ . The derivative,  $f'(\xi_i)$ , may be interpolated using a Sinc series:

$$f'(\xi) = \sum_{j=-N}^N f'(\xi_j) \text{sinc}[(\pi/h)(\phi(\xi) - jh)]$$

Employing the method of indefinite integration, the value of the function at a point  $\xi$  is given by:

$$f(\xi) = \sum_{j=-N}^N f'(\xi_j) h \psi'(jh) \left[ \frac{1}{2} + \frac{1}{\pi} \text{Si} \left( \frac{\pi \phi(\xi)}{h} - \pi j \right) \right] + C$$

Both the approximations for  $f(\xi)$  and  $f'(\xi)$  can be expressed in matrix form by:

$$\begin{aligned} f'(\xi) &= \mathbf{E}(\xi) \mathbf{u}, \\ f(\xi) &= \mathbf{A}(\xi) \mathbf{u} \end{aligned} \tag{3.15}$$

where  $\mathbf{u} = \{f'(x_{-N}), f'(x_{-N+1}), \dots, f'(x_N), C\}^T$ ,

$$\begin{aligned} \mathbf{E}(\xi) &= \begin{bmatrix} T_1(\xi, -N), & T_1(\xi, -N+1), & \dots, & T_1(\xi, N), & 0 \end{bmatrix} \\ \mathbf{A}(\xi) &= \begin{bmatrix} T_2(\xi, -N), & T_2(\xi, -N+1), & \dots, & T_2(\xi, N), & 1 \end{bmatrix} \end{aligned}$$

$$T_1(\xi, j) = \text{sinc} \left( \frac{\pi \phi(\xi)}{h} - \pi j \right) \tag{3.16}$$

$$T_2(\xi, j) = h \psi'(jh) \left[ \frac{1}{2} + \frac{1}{\pi} \text{Si} \left( \frac{\pi \phi(\xi)}{h} - \pi j \right) \right]. \tag{3.17}$$

The process can also be extended to 2D. Now assume  $f_{,\xi\eta}(\xi_i, \eta_j)$  is known and is interpolated using a Sinc series along each coordinate:

$$f_{,\xi\eta}(\xi, \eta) = \sum_{i=-N}^N \sum_{j=-N}^N f_{,\xi\eta}(\xi_i, \eta_j) \left[ \text{sinc} \left( \frac{\pi \phi(\xi)}{h} - \pi i \right) \right] \left[ \text{sinc} \left( \frac{\pi \phi(\eta)}{h} - \pi j \right) \right] \tag{3.18}$$

Employing the indefinite integration on  $\xi$  and applying Eq. (3.12), the derivative with respect

to  $\eta$  may be written by:

$$f_{,\eta}(\xi, \eta) = \sum_{i=-N}^N \sum_{j=-N}^N f_{,\xi\eta}(\xi_i, \eta_j) \left\{ h\psi'(ih) \left[ \frac{1}{2} + \frac{1}{\pi} \text{Si} \left( \frac{\pi\phi(\xi)}{h} - \pi i \right) \right] \right\} \\ \times \left[ \text{sinc} \left( \frac{\pi\phi(\eta)}{h} - \pi j \right) \right] + C_1(\eta) \quad (3.19)$$

Note that in Eq. (3.19),  $C_1(\eta)$  is a function of  $\eta$  only. The function  $C_1(\eta)$  is approximated by the Sinc series of the form

$$C_1(\eta) = \sum_{j=-N}^N C_1(\eta_j) \text{sinc} \left( \frac{\phi(\pi\eta)}{h} - \pi j \right)$$

Thus Eq. (3.19) becomes

$$f_{,\eta}(\xi, \eta) = \sum_{i=-N}^N \sum_{j=-N}^N f_{,\xi\eta}(\xi_i, \eta_j) T_2(\xi, i) T_1(\eta, j) + \sum_{j=-N}^N C_1(\eta_j) T_1(\eta, j) \quad (3.20)$$

Similarly, the derivative with respect to  $\xi$  can be written by integrating Eq. (3.18),

$$f_{,\xi}(\xi, \eta) = \sum_{j=-N}^N \sum_{i=-N}^N f_{,\xi\eta}(\xi_i, \eta_j) T_1(\xi, i) T_2(\eta, j) + \sum_{i=-N}^N C_2(\xi_i) T_1(\xi, i) \quad (3.21)$$

The indefinite integration is performed on Eqs. (3.20) and (3.21) yielding:

$$f(\xi, \eta) = \int f_{,\eta}(\xi, \eta) d\eta = \int \left( \sum_{i=-N}^N \sum_{j=-N}^N f_{,\xi\eta}(\xi_i, \eta_j) T_2(\xi, i) T_1(\eta, j) \right. \\ \left. + \sum_{j=-N}^N C_1(\eta_j) T_1(\eta, j) \right) d\eta + \tilde{C}_3(\xi) + \tilde{C}_4 \quad (3.22)$$

$$f(\xi, \eta) = \int f_{,\xi}(\xi, \eta) d\xi = \int \left( \sum_{i=-N}^N \sum_{j=-N}^N f_{,\xi\eta}(\xi_i, \eta_j) T_1(\xi, i) T_2(\eta, j) + \sum_{i=-N}^N C_2(\xi_i) T_1(\xi, i) \right) d\xi + \tilde{C}_5(\eta) + \tilde{C}_6 \quad (3.23)$$

Simplifying Eqs. (3.22) and (3.23) the following relations were obtained.

$$f(\xi, \eta) = \int f_{,\eta}(\xi, \eta) d\eta = \sum_{i=-N}^N \sum_{j=-N}^N f_{,\xi\eta}(\xi_i, \eta_j) T_2(\xi, i) T_2(\eta, j) + \sum_{j=-N}^N C_1(\eta_j) T_2(\eta, j) + \tilde{C}_3(\xi) + \tilde{C}_4 \quad (3.24)$$

$$f(\xi, \eta) = \int f_{,\xi}(\xi, \eta) d\xi = \sum_{i=-N}^N \sum_{j=-N}^N f_{,\xi\eta}(\xi_i, \eta_j) T_2(\xi, i) T_2(\eta, j) + \sum_{i=-N}^N C_2(\xi_i) T_2(\xi, i) + \tilde{C}_5(\eta) + \tilde{C}_6 \quad (3.25)$$

Now whether it was chosen to integrate first with respect to  $\xi$  and then  $\eta$  or vice versa,  $f(\xi, \eta)$  should be the same. By inspection, the two expressions are equivalent only when:

$$\begin{aligned} \tilde{C}_3(\xi) &= \sum_{i=-N}^N C_2(\xi_i) T_2(\xi, i), \\ \tilde{C}_5(\eta) &= \sum_{j=-N}^N C_1(\eta_j) T_2(\eta, j), \\ \tilde{C}_4 &= \tilde{C}_6 = C_3, \end{aligned}$$

where  $C_3$  is a constant of integration. Therefore,  $f(\xi, \eta)$  may be expressed by:

$$f(\xi, \eta) = \sum_{i=-N}^N \sum_{j=-N}^N f_{,\xi\eta}(\xi_i, \eta_j) T_2(\xi, i) T_2(\eta, j) + \sum_{j=-N}^N C_1(\eta_j) T_2(\eta, j) + \sum_{i=-N}^N C_2(\xi_i) T_2(\xi, i) + C_3$$

The global unknown vector,  $\mathbf{u} = \{\mathbf{f}_{,\xi\eta}, \mathbf{C}_1, \mathbf{C}_2, C_3\}^T$ , is introduced with the definitions:

$$\mathbf{C}_1 = \{C_1(\xi_{-N}), C_1(\xi_{-N+1}), \dots, C_1(\xi_N)\},$$

$$\mathbf{C}_2 = \{C_2(\eta_{-N}), C_2(\eta_{-N+1}), \dots, C_2(\eta_N)\},$$

$$\mathbf{f}_{,\xi\eta} = \{f_{,\xi\eta}(\xi_{-N}, \eta_{-N}), f_{,\xi\eta}(\xi_{-N+1}, \eta_{-N}), \dots, f_{,\xi\eta}(\xi_N, \eta_{-N}), f_{,\xi\eta}(\xi_{-N}, \eta_{-N+1}), \dots, f_{,\xi\eta}(\xi_N, \eta_N)\}.$$

The basis functions may be written in matrix form:

$$\begin{aligned} f_{,\xi}(\xi, \eta) &= \mathbf{A}_1(\xi, \eta)\mathbf{u}, \\ f_{,\eta}(\xi, \eta) &= \mathbf{A}_2(\xi, \eta)\mathbf{u}, \\ f(\xi, \eta) &= \mathbf{B}(\xi, \eta)\mathbf{u}, \end{aligned} \tag{3.26}$$

where

$$\begin{aligned} \mathbf{A}_1 &= \begin{bmatrix} \mathbf{a}_1 & \mathbf{0}_{1 \times n} & \mathbf{a}_{12} & 0 \end{bmatrix}, \\ \mathbf{A}_2 &= \begin{bmatrix} \mathbf{a}_2 & \mathbf{a}_{21} & \mathbf{0}_{1 \times n} & 0 \end{bmatrix}, \\ \mathbf{B} &= \begin{bmatrix} \mathbf{b} & \mathbf{b}_1 & \mathbf{b}_2 & 1 \end{bmatrix}, \end{aligned} \tag{3.27}$$

$$\begin{aligned} \mathbf{a}_{12} &= \{T_1(\xi, -N), T_1(\xi, -N+1), \dots, T_1(\xi, N)\}, \\ \mathbf{a}_{21} &= \{T_1(\eta, -N), T_1(\eta, -N+1), \dots, T_1(\eta, N)\}, \\ \mathbf{b}_1 &= \{T_2(\eta, -N), T_2(\eta, -N+1), \dots, T_2(\eta, N)\}, \\ \mathbf{b}_2 &= \{T_2(\xi, -N), T_2(\xi, -N+1), \dots, T_2(\xi, N)\}, \end{aligned}$$

$$\mathbf{a}_1 = \{T_1(\xi, -N)T_2(\eta, -N), T_1(\xi, -N+1)T_2(\eta, -N), \dots, T_1(\xi, N)T_2(\eta, -N),$$

$$T_1(\xi, -N)T_2(\eta, -N+1), T_1(\xi, -N+1)T_2(\eta, -N+1), \dots, T_1(\xi, N)T_2(\eta, -N+1),$$

$$T_1(\xi, -N)T_2(\eta, N), T_1(\xi, -N+1)T_2(\eta, N), \dots, T_1(\xi, N)T_2(\eta, N)\},$$



$$\begin{aligned} \mathbf{a}_2 = \{ & T_2(\xi, -N)T_1(\eta, -N), T_2(\xi, -N + 1)T_1(\eta, -N), \dots, T_2(\xi, N)T_1(\eta, -N), \\ & T_2(\xi, -N)T_1(\eta, -N + 1), T_2(\xi, -N + 1)T_1(\eta, -N + 1), \dots, T_2(\xi, N)T_1(\eta, -N + 1), \\ & T_2(\xi, -N)T_1(\eta, N), T_2(\xi, -N + 1)T_1(\eta, N), \dots, T_2(\xi, N)T_1(\eta, N)\}, \end{aligned}$$

and

$$\begin{aligned} \mathbf{b} = \{ & T_2(\xi, -N)T_2(\eta, -N), T_2(\xi, -N + 1)T_2(\eta, -N), \dots, T_2(\xi, N)T_2(\eta, -N), \\ & T_2(\xi, -N)T_2(\eta, -N + 1), T_2(\xi, -N + 1)T_2(\eta, -N + 1), \dots, T_2(\xi, N)T_2(\eta, -N + 1), \\ & T_2(\xi, -N)T_2(\eta, N), T_2(\xi, -N + 1)T_2(\eta, N), \dots, T_2(\xi, N)T_2(\eta, N)\}. \end{aligned}$$

Therefore, the value of the function and all pertinent derivatives are given anywhere in the domain by Eq. (3.26).

### 3.3.2 Problems Involving only First- and Second-Order Derivatives

If a problem involves first- and second-order derivatives of the unknown function, the following approximation may be used. In 1D, the second-order derivative is approximated using a Sinc series where  $f''(\xi_j)$  is assumed to be known for all  $\xi_j$  such that  $0 < \xi_j < 1$  and corresponding to  $\xi_j = \psi(jh)$  with  $j = \{-N, -N + 1, \dots, -1, 0, 1, \dots, N - 1, N\}$ .

Employing the indefinite integration scheme, the first-order derivative may be expressed by:

$$f'(\xi) = \sum_{j=-N}^N f''(\xi_j)h\psi'(jh) \left[ \frac{1}{2} + \frac{1}{\pi} \text{Si} \left( \frac{\pi\phi(\xi)}{h} - \pi j \right) \right] + C_1 \quad (3.28)$$

The value of the first derivative may be evaluated at the Sinc points and the integration

process may be repeated to obtain the function itself.

$$f(\xi) = \sum_{i=-N}^N \sum_{j=-N}^N h^2 \psi'(ih) \psi'(jh) \left[ \frac{1}{2} + \frac{1}{\pi} \text{Si} \left( \frac{\pi \phi(\xi)}{h} - \pi i \right) \right] \\ \times \left[ \frac{1}{2} + \frac{1}{\pi} \text{Si}(\pi(i-j)) \right] f''(\xi_j) + C_1 \xi + C_2 \quad (3.29)$$

The first- and the second-order derivatives are expressed in the matrix form by:

$$\begin{aligned} f''(\xi) &= \mathbf{E}(\xi) \mathbf{u} \\ f'(\xi) &= \mathbf{A}(\xi) \mathbf{u} \\ f(\xi) &= \mathbf{B}(\xi) \mathbf{u} \end{aligned} \quad (3.30)$$

where  $\mathbf{u} = \{f''(\xi_{-N}), f''(\xi_{-N+1}), \dots, f''(\xi_N), C_1, C_2\}^T$ ,

$$\begin{aligned} \mathbf{E}(\xi) &= \begin{bmatrix} T_1(\xi, -N) & T_1(\xi, -N+1) & \dots & T_1(\xi, N) & 0 & 0 \end{bmatrix}, \\ \mathbf{A}(\xi) &= \begin{bmatrix} T_2(\xi, -N) & T_2(\xi, -N+1) & \dots & T_2(\xi, N) & 1 & 0 \end{bmatrix}, \\ \mathbf{B}(\xi) &= \begin{bmatrix} T_3(\xi, -N) & T_3(\xi, -N+1) & \dots & T_3(\xi, N) & \xi & 1 \end{bmatrix}. \end{aligned}$$

$T_1(\xi, j)$  and  $T_2(\xi, j)$  were given by Eqs. (3.16) and (3.17), and

$$T_3(\xi, j) = \sum_{i=-N}^N h^2 \psi'(ih) \psi'(jh) \left[ \frac{1}{2} + \frac{1}{\pi} \text{Si} \left( \frac{\pi \phi(\xi)}{h} - \pi i \right) \right] \left[ \frac{1}{2} + \frac{1}{\pi} \text{Si}(\pi(i-j)) \right]. \quad (3.31)$$

The same procedure is used for 2D. The derivative  $f_{,\xi\xi\eta\eta}(\xi, \eta)$  is approximated by the scalar product of Sinc series. Applying the indefinite integration rule as before, the necessary derivatives are given by:

$$f_{,\xi\xi\eta\eta}(\xi, \eta) = \sum_{i=-N}^N \sum_{j=-N}^N T_1(\xi, i) T_1(\eta, j) f_{,\xi\xi\eta\eta}(\xi_i, \eta_j)$$

$$f_{,\xi\xi\eta}(\xi, \eta) = \sum_{i=-N}^N \sum_{j=-N}^N T_1(\xi, i)T_2(\eta, j)f_{,\xi\xi\eta\eta}(\xi_i, \eta_j) + \sum_{i=-N}^N C_2(\xi_i)T_1(\xi, i)$$

$$f_{,\xi\eta\eta}(\xi, \eta) = \sum_{i=-N}^N \sum_{j=-N}^N T_2(\xi, i)T_1(\eta, j)f_{,\xi\xi\eta\eta}(\xi_i, \eta_j) + \sum_{j=-N}^N C_1(\eta_j)T_1(\eta, j)$$

$$f_{,\xi\eta}(\xi, \eta) = \sum_{i=-N}^N \sum_{j=-N}^N T_2(\xi, i)T_2(\eta, j)f_{,\xi\xi\eta\eta}(\xi_i, \eta_j) + \sum_{j=-N}^N C_1(\eta_j)T_2(\eta, j) \\ + \sum_{i=-N}^N C_2(\xi_i)T_2(\xi, i) + C_5$$

$$f_{,\xi}(\xi, \eta) = \sum_{i=-N}^N \sum_{j=-N}^N T_2(\xi, i)T_3(\eta, j)f_{,\xi\xi\eta\eta}(\xi_i, \eta_j) + \sum_{j=-N}^N C_1(\eta_j)T_3(\eta, j) \\ + \sum_{i=-N}^N [C_2(\xi_i)T_2(\xi, i)\eta + C_4(\xi_i)T_2(\xi, i)] + C_5\eta + C_6$$

$$f_{,\eta}(\xi, \eta) = \sum_{i=-N}^N \sum_{j=-N}^N T_3(\xi, i)T_2(\eta, j)f_{,\xi\xi\eta\eta}(\xi_i, \eta_j) + \sum_{i=-N}^N C_2(\xi_i)T_3(\xi, i) \\ + \sum_{j=-N}^N [C_1(\eta_j)T_2(\eta, j)\xi + C_3(\eta_j)T_2(\eta, j)] + C_5\xi + C_7$$

$$f(\xi, \eta) = \sum_{i=-N}^N \sum_{j=-N}^N T_3(\xi, i)T_3(\eta, j)f_{,\xi\xi\eta\eta}(\xi_i, \eta_j) + \sum_{i=-N}^N [C_1(\eta_j)T_3(\eta, j)\xi + C_3(\eta_j)T_3(\eta, j)] \\ + \sum_{i=-N}^N [C_2(\xi_i)T_3(\xi, i)\eta + C_4(\xi_i)T_3(\xi, i)] + C_5\xi\eta + C_6\xi + C_7\eta + C_8$$

To write the basis function in the matrix form, the global unknown vector  $\mathbf{u} = \{\mathbf{f}_{,\xi\xi\eta\eta},$

$\mathbf{C}_1, \mathbf{C}_2, \mathbf{C}_3, \mathbf{C}_4, C_5, C_6, C_7, C_8\}^T$  is introduced where  $\mathbf{C}_1 = \{C_1(\xi_{-N}), C_1(\xi_{-N+1}), \dots, C_1(\xi_N)\}$  and with similar definitions for  $\mathbf{C}_2, \mathbf{C}_3$ , and  $\mathbf{C}_4$ , and

$$\mathbf{f}_{,\xi\xi\eta\eta} = \{f_{,\xi\xi\eta\eta}(\xi_{-N}, \eta_{-N}), f_{,\xi\xi\eta\eta}(\xi_{-N+1}, \eta_{-N}), \dots, \\ f_{,\xi\xi\eta\eta}(\xi_N, \eta_{-N}), f_{,\xi\xi\eta\eta}(\xi_{-N}, \eta_{-N+1}), \dots, f_{,\xi\xi\eta\eta}(\xi_N, \eta_N)\}.$$

Accordingly, the basis function can easily be expressed in matrix form by defining matrix functions of  $\xi$  and  $\eta$  that multiply the global unknown vector for each of the required derivatives; however, for the sake of brevity this is not done here.

Higher-order basis functions could easily be developed by selecting the appropriate highest order derivative based on what is required by the BVP. A fourth-order basis function was necessary for this dissertation. This will be developed in Chapter 4 and the details are given in Appendix A.

## 4 The Sinc Method Based on Interpolation of Highest Derivative (SIHD)

The SIHD method was developed by Li and Wu [122] as a collocation method based on numerical indefinite integration for solving BVPs. The method approximates the highest-order derivative in a BVP and implements numerical indefinite integration to determine the unknown function. Li and Wu's SIHD approach is reviewed below, first for a 1D problem and then for 2D problems.

In SIHD as presented by Li and Wu, the way in which boundary conditions are applied differently to the two edges causes a natural asymmetry to the distribution of Sinc points. For this reason, an alternative method to applying the boundary conditions was developed and is also discussed in this chapter. The two approaches are compared for a 1D, composite, Timoshenko beam in this chapter.

### 4.1 One-Dimensional BVPs

Consider the 1D BVP on the domain  $[a, b]$ ,

$$\begin{aligned} L^{(m)}u(x) &= s(x), \quad x \in [a, b], \\ Bu(x) &= f(x), \quad x = a, b, \end{aligned}$$

where  $L^{(m)}$  is a linear differential operator with highest-order derivative of order  $m$ , and  $B$  is a linear differential operator of order less than or equal to  $m - 1$ .

A total of  $n = 2N + 1$  Sinc points on the domain  $\xi \in (0, 1)$  are selected by the DE transformation, Eq. (3.5). For a mesh size  $h$ , the Sinc points are chosen by

$$\xi_j = \psi(jh) = \frac{1}{2} \tanh \left[ \frac{\pi}{2} \sinh(jh) \right] + \frac{1}{2}, \quad j = \{-N, -N + 1, \dots, N - 1, N\}. \quad (4.1)$$

The domain of the BVP is transformed from  $x \in [a, b]$  to  $\xi \in [0, \xi_N]$  by the linear transformation,  $\xi = (x - a)/(b - a)(\xi_N)$ . Accordingly, the BVP is re-written in the  $\xi$  domain by:

$$\tilde{L}^{(m)}\tilde{u}(\xi) = \tilde{s}(\xi), \quad \xi \in [0, \xi_N], \quad (4.2)$$

$$\tilde{B}\tilde{u}(\xi) = \tilde{f}(\xi), \quad \xi = 0, \xi_N. \quad (4.3)$$

The basis function is developed by assuming that  $d^m\tilde{u}(\xi_j)/d\xi^m$ , the highest-order derivative within the governing equation, is known at the Sinc points. An approximation for the lower-order derivatives and the unknown function is obtained at each Sinc point by evaluating Eq. (3.12). Accordingly, the lower-order derivatives and unknown functions are expressed by:

$$\begin{aligned} \frac{d^{m-1}\tilde{u}(\xi_i)}{d\xi^{m-1}} &= k_{ij} \frac{d^m\tilde{u}(\xi_j)}{d\xi^m} + C_1, \\ \frac{d^{m-2}\tilde{u}(\xi_i)}{d\xi^{m-2}} &= k_{il}k_{lj} \frac{d^m\tilde{u}(\xi_j)}{d\xi^m} + C_1\xi_i + C_2, \\ \frac{d\tilde{u}(\xi_i)}{d\xi} &= k_{ij}^{m-1} \frac{d^m\tilde{u}(\xi_j)}{d\xi^m} + \sum_{l=1}^{m-1} \frac{C_{m-l}\xi_i^{l-1}}{(l-1)!}, \\ \tilde{u}(\xi_i) &= k_{ij}^m \frac{d^m\tilde{u}(\xi_j)}{d\xi^m} + \sum_{l=0}^{m-1} \frac{C_{m-l}\xi_i^l}{(l!)}, \end{aligned}$$

where  $\{C_1, C_2, \dots, C_m\}$  are constants of integration, and where

$$k_{ij} = h\psi'(jh) \left( \frac{1}{2} + \frac{1}{\pi} \text{Si}(\pi i - \pi j) \right). \quad (4.4)$$

Now consider a system of equations in terms of the unknowns

$$\mathbf{u} = \{C_1, C_2, \dots, C_m, d^m\tilde{u}(\xi_j)/d\xi^m\}^T. \quad (4.5)$$

The system is partially composed by imposing the governing equation, Eq. (4.2), at each of the  $2N + 1$  Sinc points. The boundary conditions complete the system.

By Li and Wu's approach, the boundary conditions, Eq. (4.3), are imposed differently at each end. At  $x = b$  or  $\xi = \xi_N$  the boundary conditions are imposed at the Sinc point in a collocation fashion,

$$\tilde{B}\tilde{u}(\xi_N) = \tilde{f}(\xi_N).$$

However, at the end  $x = a$  or  $\xi = 0$ , there is no Sinc point. Li and Wu suggest that the integration constants,  $\{C_1, C_2, \dots, C_m\}$ , correspond to the value of derivatives at  $\xi = 0$ , i.e.

$$\{C_1, C_2, \dots, C_m\} = \left\{ \frac{d^{m-1}\tilde{u}(0)}{d\xi^{m-1}}, \frac{d^{m-2}\tilde{u}(0)}{d\xi^{m-2}}, \dots, \tilde{u}(0) \right\}.$$

Accordingly, the boundary condition are imposed by writing the expression  $\tilde{B}\tilde{u}(\xi_N) = \tilde{f}(\xi_N)$  in terms of the appropriate integration constants.

Applying the boundary conditions differently at the two edges results in asymmetry of the Sinc points. The author's experience has lead to proposing an alternative approach for applying the boundary conditions to the one proposed by Li and Wu [122]. A alternative domain transformation from the  $x \in [a, b]$  domain to the  $\xi \in [\xi_{-N}, \xi_N]$  domain is performed by:

$$x = a + \frac{(b-a)(\xi - \xi_{-N})}{\xi_N - \xi_{-N}}. \quad (4.6)$$

It should be noted that with this approach, the integration constants do not correspond to derivatives at  $x = 0$  but only to the derivatives at the fictitious point  $\xi = 0$ . Moreover, the boundary conditions are imposed uniformly by collocation at the ends in this approach. The following relations are imposed:

$$\begin{aligned} \tilde{B}\tilde{u}(\xi_{-N}) &= \tilde{f}(\xi_{-N}), \\ \tilde{B}\tilde{u}(\xi_N) &= \tilde{f}(\xi_N). \end{aligned}$$

This approach will be referred to as the symmetric approach.

A complete flowchart of the SIHD method with Li and Wu's boundary condition treatment and the symmetric approach is given in Fig. 4.1 for the Timoshenko beam problem.

#### 4.1.1 Composite Timoshenko Beam

To assess the accuracy and convergence of SIHD with the two presented boundary condition approaches and develop some preliminary measure of the accuracy of the higher-order derivatives necessary for the interlaminar stresses, a composite Timoshenko beam was considered. The SIHD method with boundary conditions applied by Li and Wu's approach and by the symmetric approach were used to solve the Timoshenko beam problem for a three-layer  $[0^\circ/90^\circ/0^\circ]$  composite beam. The discretization approach using both Li and Wu's boundary condition approach and the symmetric approach are detailed in Appendix C.

The material properties of an AS4-3502 graphite-epoxy composite lamina were used (Table 4.1) (see [98]). A shear correction factor of  $5/6$  was used<sup>1</sup>. A uniformly distributed load was applied,  $q(x) = p_0$ . The deflection, rotation and stress results were normalized in the following manner:

$$\begin{aligned}\bar{\sigma}_{11} &= \sigma_{11}h^2b/L^2p_0, & \bar{\sigma}_{13} &= \sigma_{13}hb/Lp_0, \\ \bar{w} &= wE_1bh^3/p_0L^4 & \bar{\phi}_x &= \phi_xE_1bh^3/p_0L^3\end{aligned}$$

The bending stress,  $\sigma_{11}$ , was determined from the constitutive law while the transverse shear stress,  $\sigma_{13}$ , was determined from integration of the equilibrium equations of the 3D elasticity theory as described in Chapter 2.

To compare the accuracy of the methods, the numerical results were compared against the exact solution for this BVP. The mesh size was chosen by selecting the span,  $\alpha$  as defined in Section 3.2. The effects of span within the  $\tau$  domain,  $\alpha$ , and number of Sinc points,  $N$ , on

<sup>1</sup>A shear correction factor of  $5/6$  corresponds to analytic shear correction factor of a homogeneous material. For a general laminate, the correct shear correction factor should be chosen so that the transverse shear stresses, integrated through the thickness match with those given by the theory of elasticity. However,  $5/6$  is often assumed when a better approximation is not computed [98].



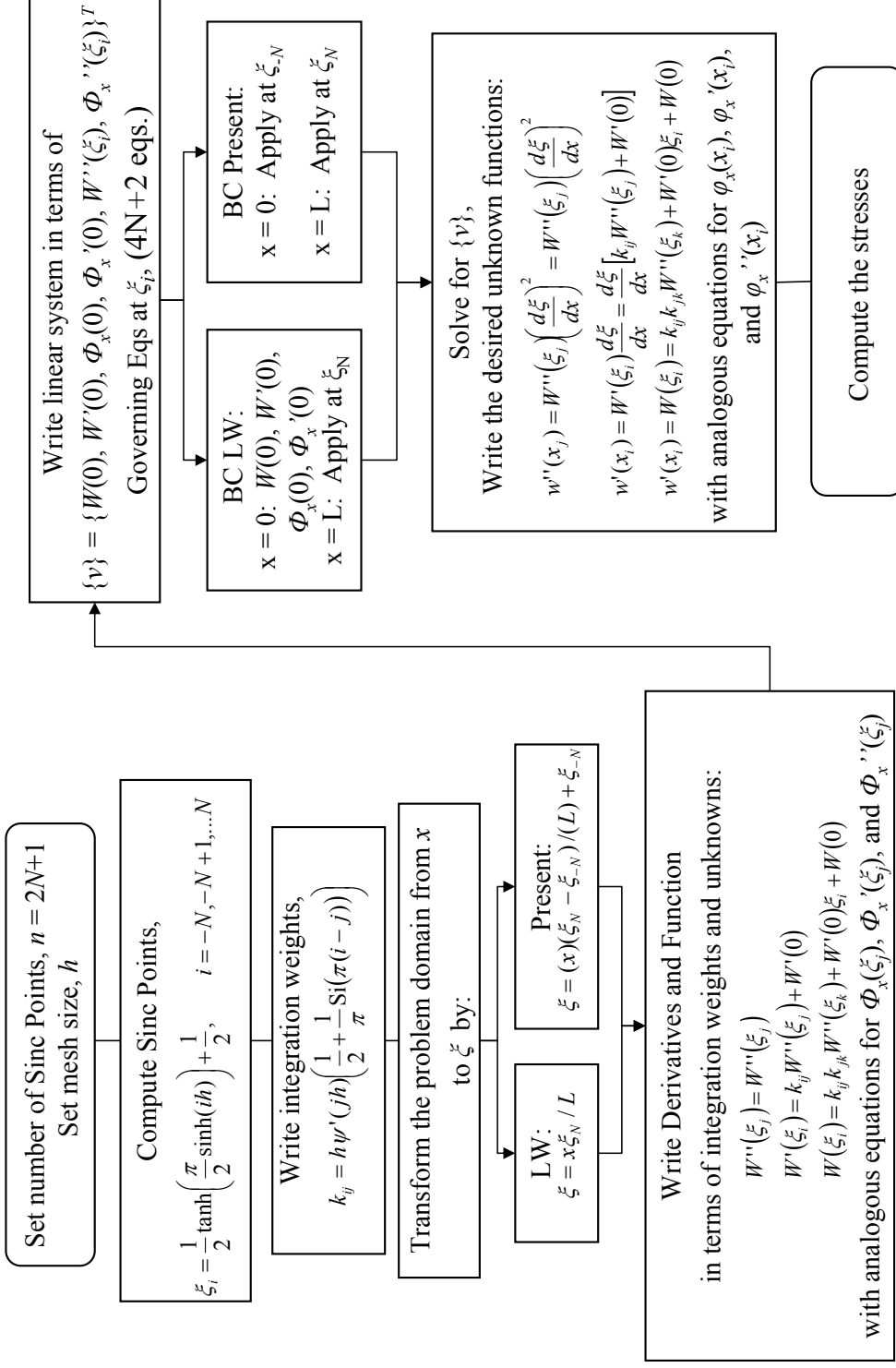


Figure 4.1. Flowchart of the SIHD method. (LW: Li and Wu's approach, Present: The alternative approach.)

**Table 4.1. Material properties for the AS4-3502 composite material.**

$E_1$ [Msi/GPa]	18.5 / 127.6
$E_2$ [Msi/GPa]	1.67 / 11.5
$G_{12}, G_{13}$ [Msi / GPa]	0.87 / 6.00
$G_{23}$ [Msi / GPa]	0.258 / 1.78
$\nu_{12}$	0.25

accuracy of the methods was examined. The span  $\alpha$  was varied between 1 and 3 to illustrate its effects.

The deflection and rotation results are compared for Li and Wu’s approach, indicated “LW”, and the present suggested symmetric approach, indicated “P” in Fig. 4.2 with  $N = 100$  and  $\alpha = 1$ . This results in 201 Sinc points along the length of the beam, 406 equations and 406 unknowns. The figure indicates significant error when using Li and Wu’s method, as evident by a maximum of about 8% error in the deflection and about 13% error in rotation. The present suggested method experiences only about 0.2% error in deflection and only 0.08% error in rotation; a significant improvement over Li and Wu’s original method.

With Li and Wu’s approach, there is no Sinc point placed at  $x = 0$ . In this approach, the Sinc points are naturally biased toward  $x = L$ . This is illustrated in the histogram of Sinc points in Fig. 4.3. The present method benefits from placing a Sinc point at  $x = 0$ .

Increasing the span is expected to improve the accuracy of Li and Wu’s method and removes the bias toward  $x = L$  because the Sinc point  $\xi_{-N}$  will approach 0 as  $\alpha$  approaches  $\infty$ . A histogram showing the distribution of Sinc points for  $\alpha = 2$  and 3 may be seen in Fig. 4.4. With the larger span, the distribution of Sinc points using Li and Wu’s method is indistinguishable from the present method.

Figure 4.5 compares the deflection and rotation results obtained using Li and Wu’s approach and the present suggested approach with  $N = 100$  and  $\alpha = 3$ . Comparing Figs. 4.2 and 4.5 indicates both methods significantly improve in accuracy with the increased span. The present method still compares well to Li and Wu’s approach as evident by about

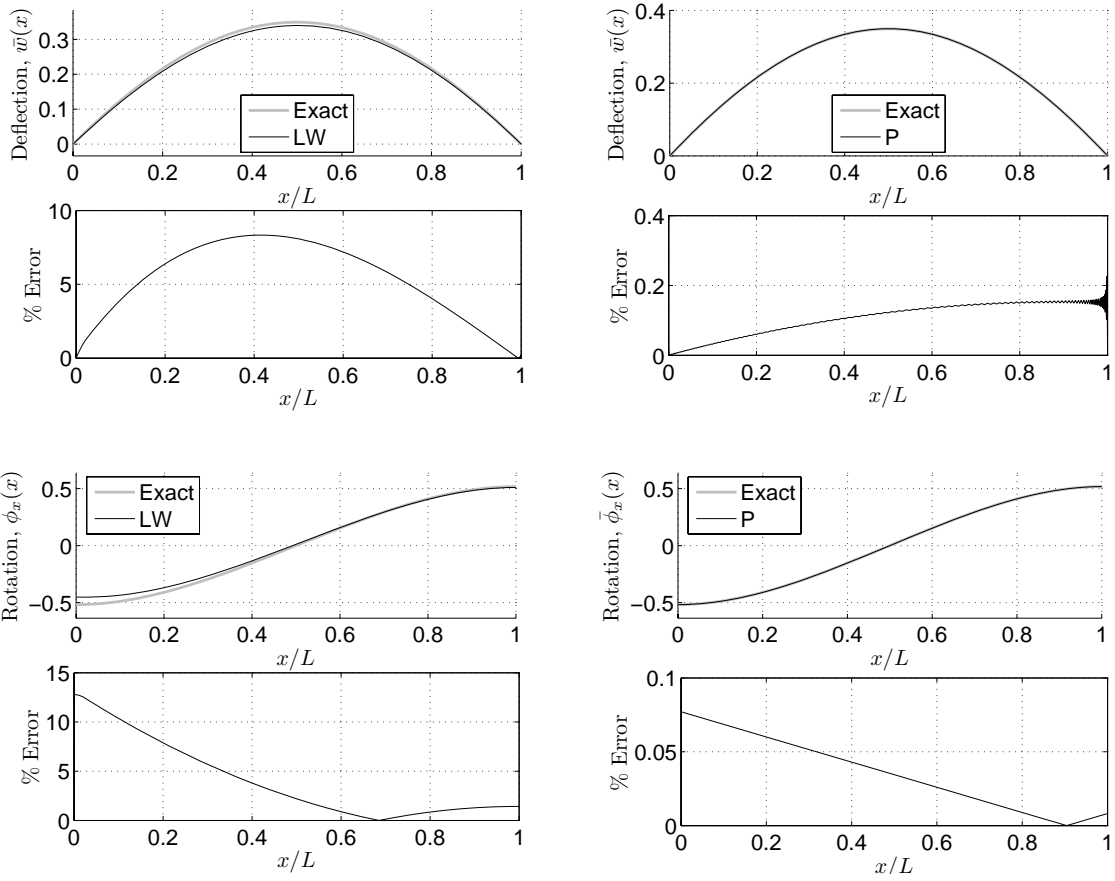


Figure 4.2. Deflection and rotation results for  $h = \alpha/N$ ,  $\alpha = 1$ , and  $N = 100$ . (LW - Li and Wu, P - Present)

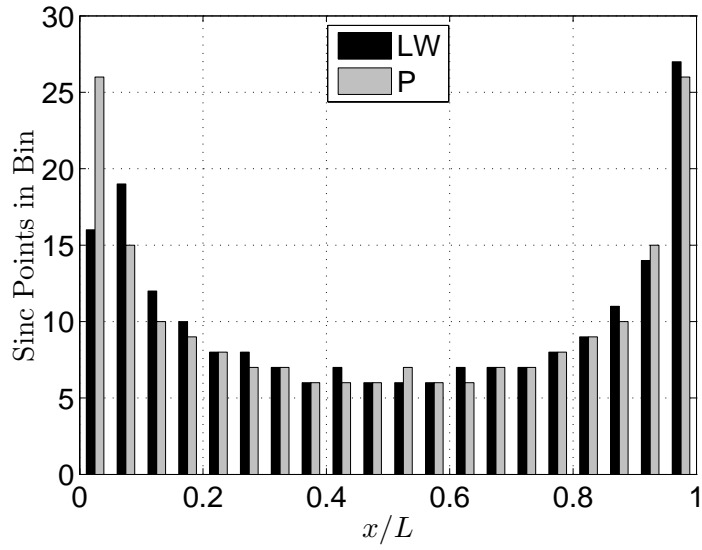


Figure 4.3. Histogram of Sinc point distribution within the domain using  $N = 100$  and  $h = 1/N$ . (LW - Li and Wu, P - Present)

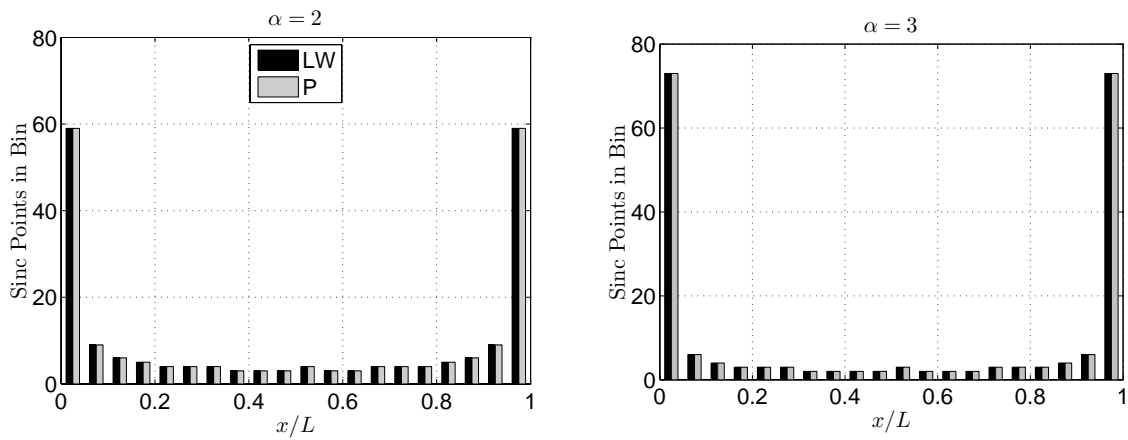
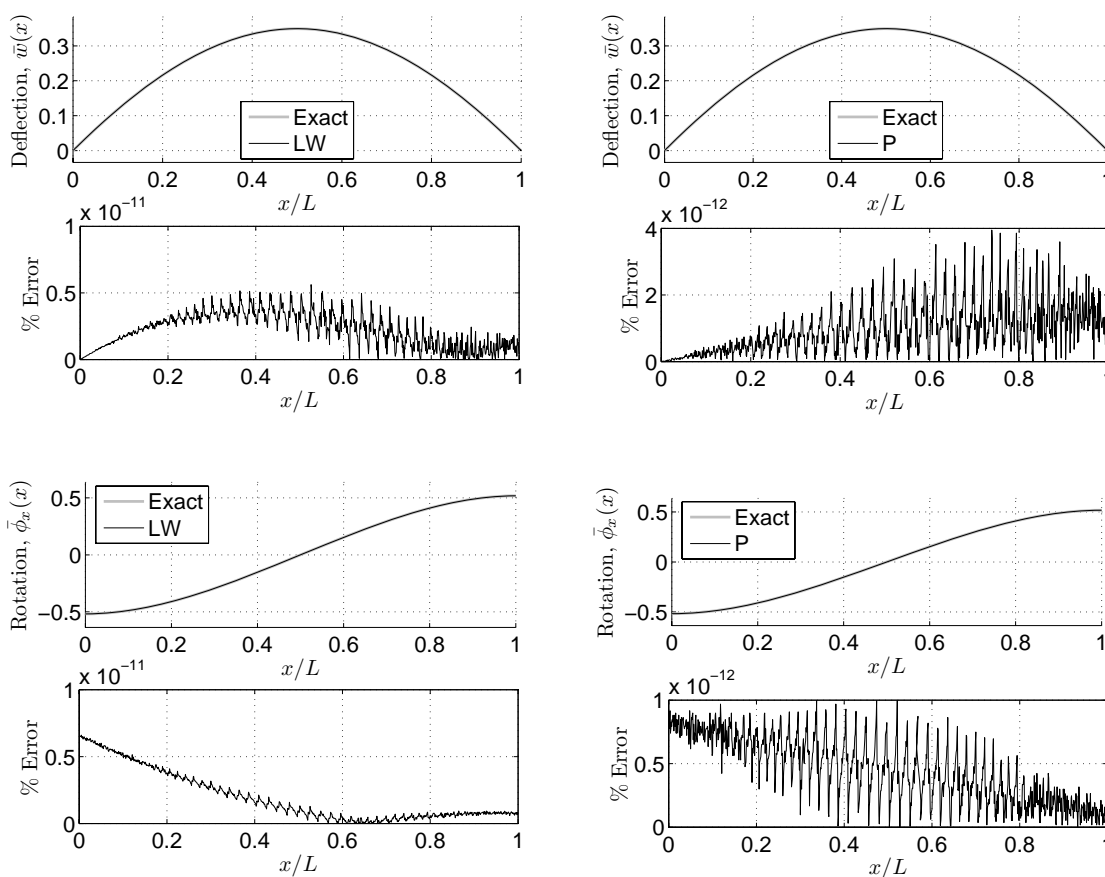


Figure 4.4. Histogram of Sinc point distribution within the domain using  $N = 100$  and  $h = \alpha/N$ . (LW - Li and Wu, P - Present)

$4 \times 10^{-12}\%$  error in the present method compared to  $5 \times 10^{-12}\%$  error in Li and Wu's method; however, this is an insignificant decrease in error which may be attributed to numerical noise. The rotation results, however, show the suggested approach to be superior to those by Li and Wu's method by almost an order of magnitude. Placing a Sinc point at zero, experiences  $1 \times 10^{-12}\%$  error compared to Li and Wu's  $7 \times 10^{-12}\%$  error.



**Figure 4.5.** Deflection and rotation results for  $h = \alpha/N$ ,  $\alpha = 3$ , and  $N = 100$ . (LW - Li and Wu, P - Present)

The effect of the number of Sinc points was studied by modifying the parameter  $N$  between  $N = 3$  (7 Sinc points) and  $N = 100$  (201 Sinc points) while holding the span

constant by setting the mesh size to be  $h = \alpha/N$ . The following error norm is defined:

$$\|e\|_0 = \frac{\int_{\Omega} (w_{approx} - w_{exact})^2 d\Omega}{\int_{\Omega} (w_{exact})^2 d\Omega} \quad (4.7)$$

where  $w_{approx}$  is the approximate quantity obtained by SIHD and  $w_{exact}$  is the exact quantity. For the beam  $\Omega = \{x : x \in [0, L]\}$ . Gauss quadrature was used to evaluate Eq. (4.7). The domain was divided between the Sinc points and five integration points were used between each Sinc point to approximate the domain integrals. The error of the deflection, rotation, and stresses (lateral and transverse shear) from Li and Wu's method and the present method are plotted against the parameter  $N$  in Fig. 4.6 for  $\alpha = 1$ . The results indicate that increasing the number of Sinc points does not provide improved accuracy for Li and Wu's approach with the current mesh size. In fact, the accuracy of the deflection and the rotation initially deteriorates with increasing number of Sinc points while the stress results show neither improvement nor deterioration. For the present suggested approach, the accuracy of the deflection, rotation, and stresses generally improves for increasing number of Sinc points. Note that with the present approach, acceptable accuracy may be obtained with the present selection of span. The users' selection of span does not guarantee that the mesh size meets the theoretical requirement for mesh size given in Eq. (3.8); however, an acceptable level of accuracy is obtained.

The effect of the number of Sinc points was also examined using a span of  $\alpha = 3$ . The error in the deflection, rotation, and stresses from Li and Wu's method and the present method are plotted against the parameter  $N$  in Fig. 4.7. The figure shows linear convergence for all results until  $N = 30$  at which point both methods do not improve. The benefit of the present approach seen for  $\alpha = 1$  is nearly entirely diminished for  $\alpha = 3$ . However, the deflection, rotation, and stresses are computed very accurately by both methods.

The error in the deflection, rotation, and stresses from Li and Wu's method and the

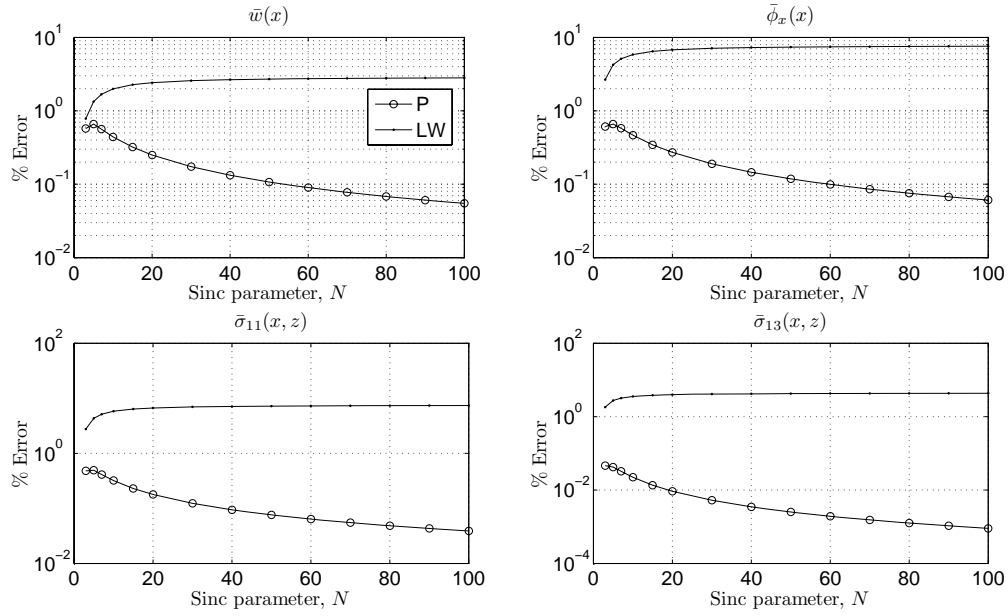


Figure 4.6. Convergence of SIHD for increasing number of Sinc points with  $h = 1/N$ . (LW - Li and Wu, P - Present)

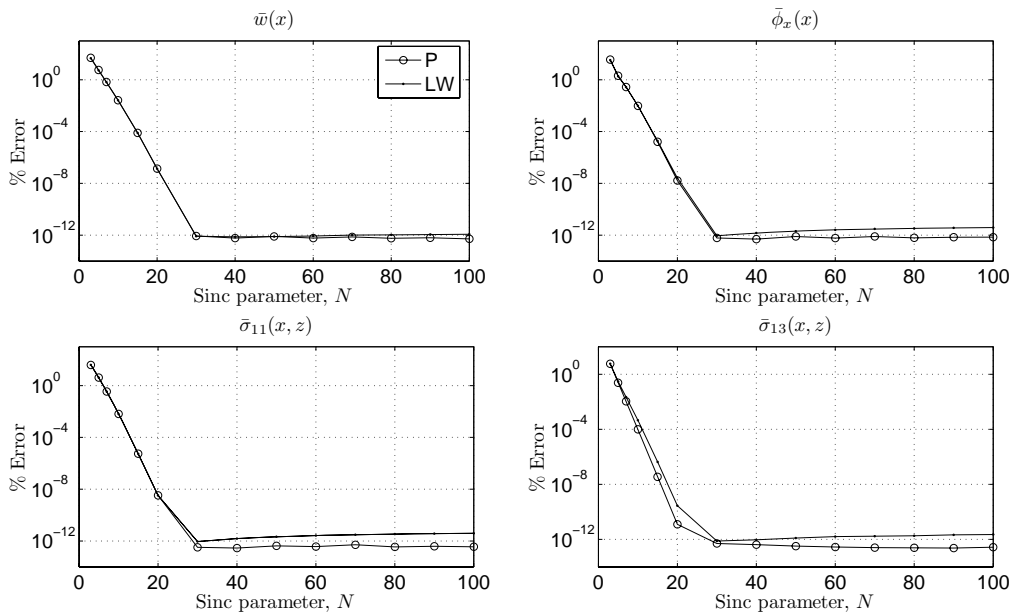
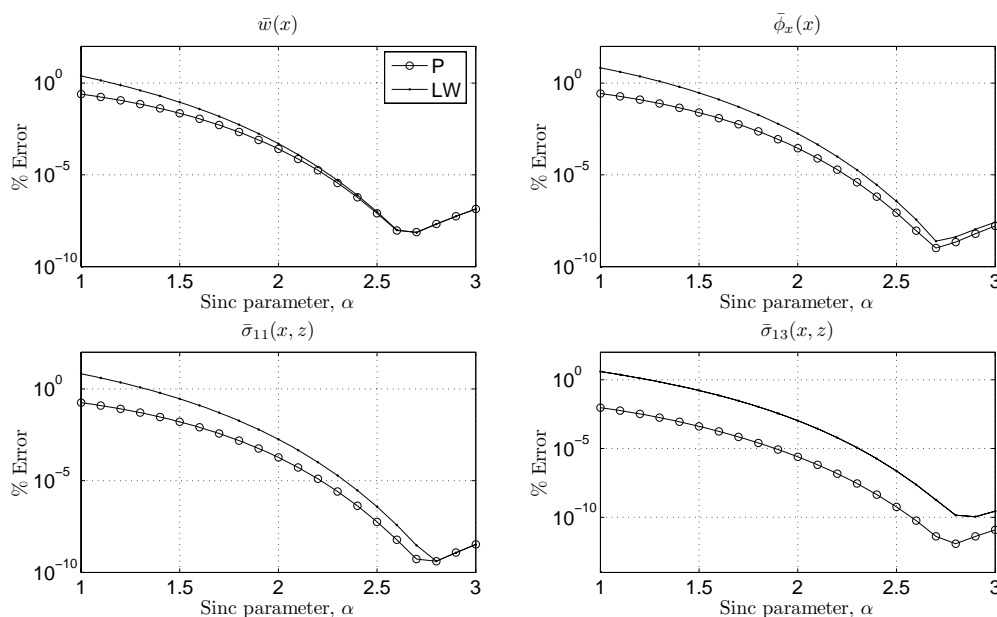


Figure 4.7. Convergence of SIHD for increasing number of Sinc points with  $h = 3/N$ . (LW - Li and Wu, P - Present)

symmetric approach are plotted for increasing mesh size in Fig. 4.8 while maintaining the number of Sinc points constant using  $N = 20$  (41 Sinc points). The figure demonstrates the significant improvement of the present symmetric boundary condition application over Li and Wu's approach for small span. The present method is as good as Li and Wu's approach for large span. For both cases, the accuracy improves for increasing  $\alpha$  until  $\alpha = 2.7$ . The results start to deteriorate after  $\alpha = 2.7$ ; indicating  $\alpha = 2.7$  to be optimal for  $N = 20$ .



**Figure 4.8. Error versus Sinc span,  $\alpha$ , with  $N = 20$  for a  $[0^\circ/90^\circ/0^\circ]$  graphite/epoxy Timoshenko beam.**

The optimal span from Fig. 4.8 may not always be desirable. The histograms in Fig. 4.4 indicate increasing the mesh size results in a higher concentration of Sinc points near the ends. Smaller spans such as  $\alpha = 1$  result in a more uniform distribution of Sinc points. Thus if a large number of Sinc points are desired near  $x = L/2$ , reducing the span may be preferred over increasing the number of Sinc points and thus the computational requirements of the problem. For such a problem, the additional freedom provided by the present approach is certainly preferred over Li and Wu's boundary condition approach.



## 4.2 2D BVPs

For a 2D analysis, additional difficulties arise in applying the SIHD method. To illustrate these difficulties, a simply-supported classical composite plate is considered. Equilibrium is governed by:

$$D_{11} \frac{\partial^4 w(x, y)}{\partial x^4} + 2(D_{12} + 2D_{66}) \frac{\partial^4 w(x, y)}{\partial x^2 \partial y^2} + D_{22} \frac{\partial^4 w(x, y)}{\partial y^4} = p(x, y) \quad (4.8)$$

on the domain  $x \in [0, a]$  and  $y \in [0, b]$ ,  $a$  and  $b$  being the length and width of the plate respectively. A symmetric composite scheme was chosen so that the in-plane and bending equations are uncoupled.  $D_{ij}$  are the bending stiffnesses given in Eq. (2.10), and  $w(x, y)$  is the transverse plate deflection. The boundary conditions for a simple support on all four edges of the rectangular plate can be expressed as:

$$\begin{aligned} w(0, y) &= 0 & w(a, y) &= 0 \\ w(x, 0) &= 0 & w(x, b) &= 0 \\ M_{xx}(0, y) &= 0 & M_{xx}(a, y) &= 0 \\ M_{yy}(x, 0) &= 0 & M_{yy}(x, b) &= 0 \end{aligned}$$

where the bending moments are related to the transverse deflection by:

$$\begin{aligned} M_{xx} &= - \left( D_{11} \frac{\partial^2 w}{\partial x^2} + D_{12} \frac{\partial^2 w}{\partial y^2} \right) \\ M_{yy} &= - \left( D_{12} \frac{\partial^2 w}{\partial x^2} + D_{22} \frac{\partial^2 w}{\partial y^2} \right) \end{aligned}$$

As for the 1D problem with the SIHD method, the problem is transformed from the  $(x, y)$  domain to  $(\xi, \eta)$  domain by the transformation  $\xi = x \xi_N/a$  and  $\eta = y \eta_N/b$  for Li and Wu's boundary condition approach or to  $\xi = x(\xi_N - \xi_{-N})/a + \xi_{-N}$  and  $\eta = y(\eta_N - \eta_{-N})/b + \eta_{-N}$  for the suggested symmetric approach. Both  $\xi$  and  $\eta$  are discretized by the DE transformation.

Accordingly, the deflection and its partial derivatives in the  $(\xi, \eta)$  domain are given by:

$$\begin{aligned}
 w(x, y) &= W(\xi, \eta) \\
 \frac{\partial w(x, y)}{\partial x} &= \frac{\partial \xi}{\partial x} \frac{\partial W(\xi, \eta)}{\partial \xi} \\
 \frac{\partial^2 w(x, y)}{\partial x^2} &= \left( \frac{\partial \xi}{\partial x} \right)^2 \frac{\partial^2 W(\xi, \eta)}{\partial \xi^2} \\
 &\vdots \\
 \frac{\partial^{n+m} w(x, y)}{\partial x^n \partial y^m} &= \left( \frac{\partial \xi}{\partial x} \right)^n \left( \frac{\partial \eta}{\partial y} \right)^m \frac{\partial^{n+m} W(\xi, \eta)}{\partial \xi^n \partial \eta^m}
 \end{aligned}$$

The scalar product of Sinc series with DE transformation was used to approximate  $\partial^8 W(\xi, \eta) / \partial \xi^4 \partial \eta^4$ :

$$\frac{\partial^8 W(\xi, \eta)}{\partial \xi^4 \partial \eta^4} = \sum_{i=-N}^N \sum_{j=-N}^N T_1(\xi, i) T_1(\eta, j) \frac{\partial^8 W(\xi_i, \eta_j)}{\partial \xi^4 \partial \eta^4} \quad (4.9)$$

where  $T_1(\xi, i)$  is given by Eq. (3.16). The lower-order derivative and the unknown function are found by integration of  $\partial^8 W(\xi, \eta) / \partial \xi^4 \partial \eta^4$ . The process is quite tedious; however the result is critical. For the present problem, the full list of lower derivatives are given in Appendix A. Note that the basis function contains  $n^2 + 8n + 16$  unknowns which are summarized in Table 4.2.

**Table 4.2. Summary table of unknowns in the SIHD method for analysis of a classical laminated composite plate.**

Unknown term*	Number
$W_{,11112222}(\xi_k, \eta_l)$	$n^2$
$W_{,1112222}(0, \eta_l), W_{,1111222}(\xi_k, 0), W_{,112222}(0, \eta_l), W_{,111122}(\xi_k, 0),$ $W_{,12222}(0, \eta_l), W_{,11112}(\xi_k, 0), W_{,2222}(0, \eta_l), W_{,1111}(\xi_k, 0)$	$n$ each, $8n$ total
$W_{,111222}(0, 0), W_{,11222}(0, 0), W_{,111122}(0, 0), W_{,1122}(0, 0),$ $W(0, 0)_{,1222}, W_{,1112}(0, 0), W_{,112}(0, 0), W_{,122}(0, 0),$ $W_{,222}(0, 0), W_{,111}(0, 0), W_{,11}(0, 0), W_{,22}(0, 0),$ $W_{,12}(0, 0), W_{,1}(0, 0), W_{,2}(0, 0), W(0, 0)$	1 each, 16 total

\*  $W_{,112}$  implies  $\partial W^3 / \partial \xi^2 \partial \eta$

For 1D problems with the SIHD method, the Sinc points were used as the collocation points with boundary Sinc point being used to apply both the governing equation and the boundary conditions. Thus governing equations plus the boundary conditions provided a complete system of equations that completely determined the system. However, it is not as easy for the 2D case. Following the 1D SIHD method, the governing equation is imposed at each Sinc point, yielding  $n^2$  linear equations in terms of the unknowns.

For the edges with  $x = a$  and  $y = b$ , both Li and Wu and the present method apply the boundary conditions at all Sinc points along these edges.

$$\begin{aligned}
 W(\xi_N, \eta_j) &= 0 & W(\xi_i, \eta_N) &= 0 \\
 M_{xx}(\xi_N, \eta_j) &= 0 & M_{yy}(\xi_i, \eta_N) &= 0
 \end{aligned}$$

for  $i = -N + 1, \dots, N$ ,  $j = -N, \dots, N - 1$ . The points  $\xi_i = -N$  and  $\eta_i = N$  are omitted because these points are attributed to the edges  $y = 0$  and  $x = a$  respectively. These conditions provide  $4n - 4$  additional linear equations in terms of the unknowns. The  $-4$  arrives because each corner point lies on two edges. Therefore, no information is gained by applying the zero deflection condition at this point twice.

At the edges  $x = 0$  and  $y = 0$ , Li and Wu [122] suggest the boundary conditions be applied through the constants of integration. For example, to apply  $W(0, \eta) = 0$  the following conditions are imposed:

$$W(0, \eta_j) = e_{jl} \frac{\partial^4 W(0, \eta_i)}{\partial \xi^4} + \frac{\partial^3 W(0, 0) \eta_j^3}{\partial \eta^3} + \frac{\partial^2 W(0, 0) \eta_j^2}{\partial \eta^2} + \frac{\partial W(0, 0)}{\partial \eta} \eta_j + W(0, 0) = 0$$

for  $j = -N, \dots, N$  with similar expressions for the moments. In this way, Li and Wu's method obtains  $4n - 4$  additional equations. Because in the symmetric approach,  $x = 0$  corresponds to  $\xi_{-N}$ , the boundary conditions may be applied to all Sinc points along the edges  $x = 0$  and  $y = 0$ . These conditions provide  $4n - 4$  additional equations as well.

Both Li and Wu's boundary condition approach and the suggested approach yield a total of  $n^2 + 8n - 8$  equations with all boundary conditions exhausted, 24 equations deficient. Li and Wu suggest applying additional constraints based on intuition regarding the boundary conditions. Because in their simple example, Li and Wu apply the Dirichlet boundary conditions everywhere, it is possible to set a few of the unknown integration constants to be zero. However, for more general boundary conditions it may be very difficult to obtain enough additional relations to constrain all integration constants. Even for the simply-supported plate problem, obtaining enough relations is not a trivial task. One may easily say  $W(0, 0) = \partial W / \partial x(0, 0) = \partial^2 W / \partial x^2(0, 0) = \partial^3 W / \partial x^3(0, 0) = \partial^4 W / \partial x^4(0, 0) = 0$  and  $\partial W / \partial y(0, 0) = \partial^2 W / \partial y^2(0, 0) = \partial^3 W / \partial y^3(0, 0) = \partial^4 W / \partial y^4(0, 0) = 0$ ; however, one cannot say  $\partial^2 W / \partial x \partial y(0, 0) = 0$ . Perhaps with much effort relations could be obtained; however, a more standard procedure is certainly desired.

The additional necessary information is implied by the boundary conditions. For example, the boundary condition  $w(0, y) = 0$  suggests  $\partial w(0, y)/\partial y = 0$ ,  $\partial^2 w(0, y)/\partial y^2 = 0, \dots$ ,  $\partial^n w(0, y)/\partial y^n = 0$ . Naturally, these relations are true at every point along the edge  $x = 0$ ; however, because only 24 additional equations are needed, each higher-order derivative of the boundary condition that are given by the basis function was applied at only a single point along the 4 edges. That is at the midpoint along each edge the derivatives of boundary conditions - up to the highest-order derivative that can be written by the basis function - should be imposed. For the simply-supported plate problem the following constraints were imposed in addition to the boundary conditions.

$$\begin{aligned}
\frac{\partial W(\xi_0, \eta_{-N})}{\partial \xi} &= \frac{\partial^2 W(\xi_0, \eta_{-N})}{\partial \xi^2} = \frac{\partial^3 W(\xi_0, \eta_{-N})}{\partial \xi^3} = \frac{\partial^4 W(\xi_0, \eta_{-N})}{\partial \xi^4} = 0 \\
\frac{\partial W(\xi_0, \eta_N)}{\partial \xi} &= \frac{\partial^2 W(\xi_0, \eta_N)}{\partial \xi^2} = \frac{\partial^3 W(\xi_0, \eta_N)}{\partial \xi^3} = \frac{\partial^4 W(\xi_0, \eta_N)}{\partial \xi^4} = 0 \\
\frac{\partial W(\xi_N, \eta_0)}{\partial \eta} &= \frac{\partial^2 W(\xi_N, \eta_0)}{\partial \eta^2} = \frac{\partial^3 W(\xi_N, \eta_0)}{\partial \eta^3} = \frac{\partial^4 W(\xi_N, \eta_0)}{\partial \eta^4} = 0 \\
\frac{\partial W(\xi_{-N}, \eta_0)}{\partial \eta} &= \frac{\partial^2 W(\xi_{-N}, \eta_0)}{\partial \eta^2} = \frac{\partial^3 W(\xi_{-N}, \eta_0)}{\partial \eta^3} = \frac{\partial^4 W(\xi_{-N}, \eta_0)}{\partial \eta^4} = 0 \\
\frac{\partial M_{yy}(\xi_0, \eta_{-N})}{\partial \xi} &= \frac{\partial^2 M_{yy}(\xi_0, \eta_{-N})}{\partial \xi^2} = \frac{\partial M_{yy}(\xi_0, \eta_N)}{\partial \xi} = \frac{\partial^2 M_{yy}(\xi_0, \eta_N)}{\partial \xi^2} = 0 \\
\frac{\partial M_{xx}(\xi_N, \eta_0)}{\partial \eta} &= \frac{\partial^2 M_{xx}(\xi_N, \eta_0)}{\partial \eta^2} = \frac{\partial M_{xx}(\xi_{-N}, \eta_0)}{\partial \eta} = \frac{\partial^2 M_{xx}(\xi_{-N}, \eta_0)}{\partial \eta^2} = 0
\end{aligned}$$

These additional 24 conditions completely constrain the problem ( $n^2 + 8n + 16$  equations and  $n^2 + 8n + 16$  unknowns). It is not possible to apply similar equations for Li and Wu's boundary condition approach because there are no Sinc points along the edges  $x = 0$  and  $y = 0$ .

Alternatively, a pure collocation approach was used. That is to say a number of collocation points were chosen which do not necessarily coincide with the Sinc points. The basis function was used to approximate the function and its derivatives at the collocation points

which were chosen by:

$$\begin{aligned}\hat{\xi}_j = \hat{\eta}_j &= \frac{1}{2} \tanh\left(\frac{\pi}{2} \sinh(jh)\right) + \frac{1}{2} \\ j &= \{-N, -N + 2N/N_u, -N + 4N/N_u, \dots, N\}\end{aligned}\tag{4.10}$$

where the hats indicate the collocation points and  $N_u$  is the number of collocation points chosen. A system of linear equations is formed by imposing the governing equation at collocation points in the interior domain and imposing both natural and essential boundary conditions at collocation points on the boundary.

#### 4.2.1 Classical Laminated Composite Plate

The SIHD method was used to obtain a numerical solution for bending of a classical laminated composite plate. Numerical results were compared imposing boundary conditions by the midpoint approach and by the pure collocation approach. A square ( $a/b = 1$ ), three-layer,  $[0^\circ/90^\circ/0^\circ]$  composite plate was considered. The material properties of an AS4-3502 graphite-epoxy composite lamina were used (Table 4.1). A sinusoidally distributed load was applied,  $q(x) = p_0 \sin(\pi x/a) \sin(\pi y/b)$ . The deflection and stress results were normalized in the following manner:

$$\begin{aligned}\bar{\sigma}_{ij} &= \sigma_{ij} h^2 / a^2 p_0, & \bar{\sigma}_{i3} &= \sigma_{i3} h / a p_0, \\ \bar{\sigma}_{33} &= \sigma_{33} / p_0, & \bar{w} &= w E_2 h^3 / p_0 a^4\end{aligned}$$

with  $i, j = 1, 2$ . The in-plane stresses are determined from the constitutive law while the interlaminar stresses are determined from integration of the equilibrium equations of the 3D elasticity theory.

To examine the accuracy of the SIHD method, the numerical results were compared against the exact solution for this problem obtained by the Navier method [98]. The normalized plate deflection is plotted for  $N = 20$  with mesh size  $h = a/N$  and span selected

by  $\alpha = 1$  and 3 in Figs. 4.9 and 4.10 respectively. The boundary conditions were applied by the midpoint approach. The error as a percentage of the exact maximum deflection is also plotted in Figs. 4.9 and 4.10. The figures indicate a maximum deflection error of 0.4% for  $\alpha = 1$  and  $6 \times 10^{-6} \%$  for  $\alpha = 3$ .

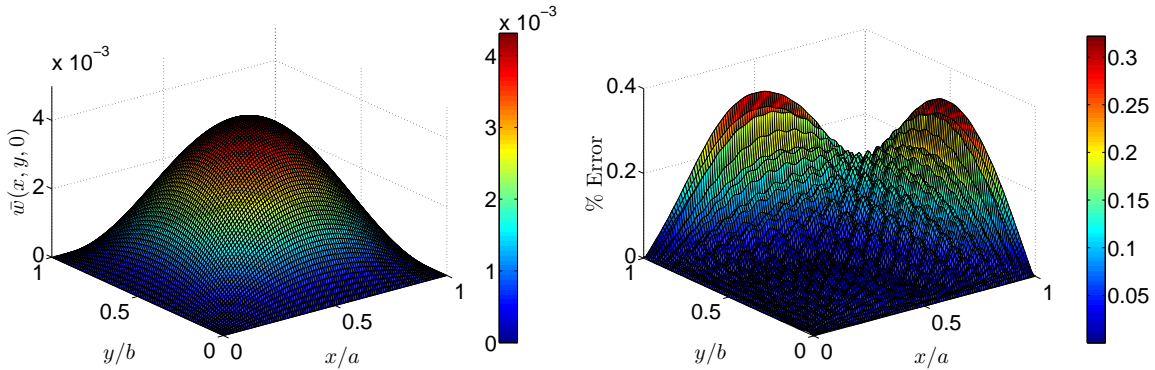


**Figure 4.9.** Normalized plate deflection and error in the deflection for a classical laminated composite plate using  $\alpha = 1$  and  $N = 20$ .

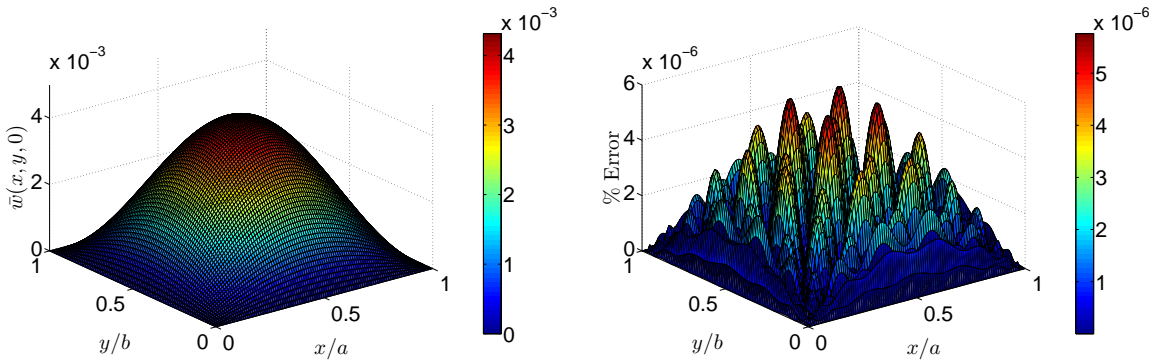


**Figure 4.10.** Normalized plate deflection and error in the deflection for a classical laminated composite plate using  $\alpha = 3$  and  $N = 20$ .

The error, as computed by Eq. (4.7), is plotted against the parameter  $N$  in Fig. 4.11 while taking the span to be  $\alpha = 1, 2,$  and 3. The deflection and stress results indicate that with  $\alpha = 1$  there was a very slow rate of convergence for all deflection and stresses. The error generally remains  $\sim 1\%$ . However,  $\alpha = 1$  is superior to larger span when the number of Sinc points is limited ( $N < 5$ ). This result is probably due to the uniformity of the distribution

of Sinc points. For  $\alpha = 2$ , the method converges very quickly; however, beyond  $N = 11$ , adding Sinc points does not improve the error magnitude of the deflections and stresses. For  $\alpha = 3$ , our method converges at a slower rate than for  $\alpha = 2$ , but less error is achieved using a large number of Sinc points.

Figure 4.11 further indicates the success of the SIHD method as a tool for efficiently determining the interlaminar stresses. The transverse shear stresses ( $\sigma_{13}$  and  $\sigma_{23}$ ) are computed with excellent accuracy  $< 1\%$  error using as few as 9 Sinc points with  $\alpha = 2$  or 3. The transverse normal stress is also very accurately computed. The accuracy of these stresses results from a high level of accuracy in both the primary variable  $w(x, y)$  as well as its derivatives. It should be emphasized that because the method is an integrated method, the derivatives are accurately computed along with the primary variable. This is a distinct advantage over methods used in [102] and [103].

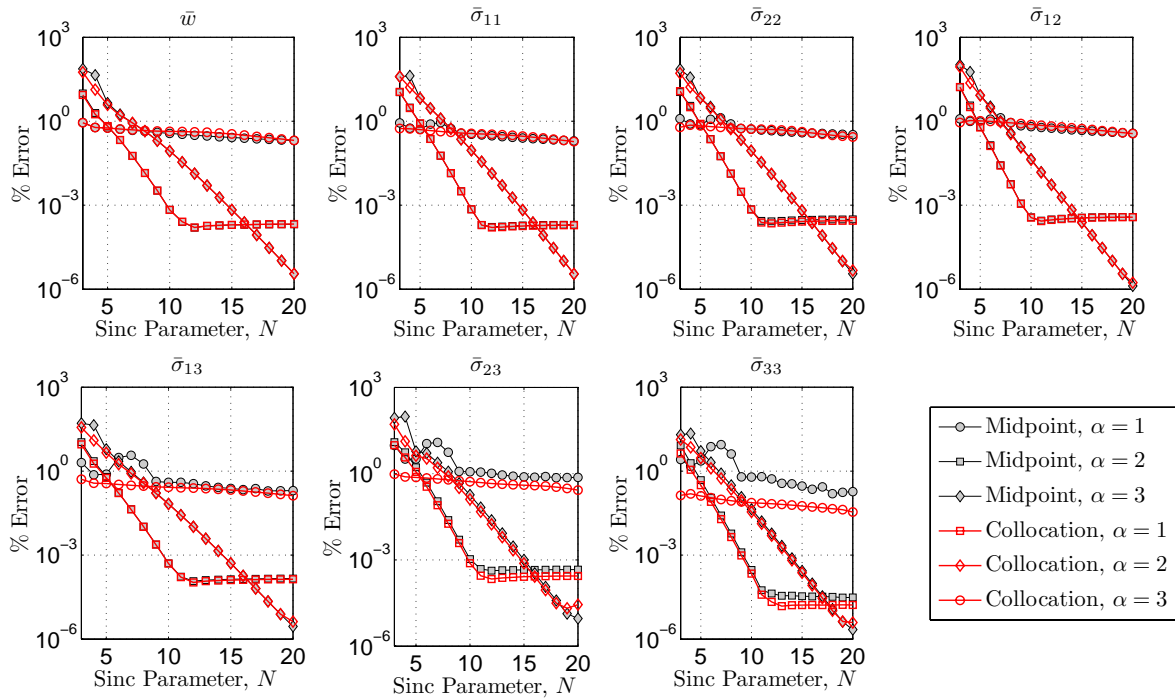


**Figure 4.11.** Convergence of displacement and stresses for increasing number of Sinc points with  $\alpha = 1, 2$ , and 3 for a classical laminated composite plate.

In Fig. 4.12, the error is plotted for increasing the span,  $\alpha$ , while the number of Sinc



points was maintained constant using  $N = 20$  (41 Sinc points). As with the 1D beam problem, the results improve while increasing  $\alpha$  until about  $\alpha = 2.6$ . The results do not improve significantly beyond  $\alpha = 2.6$ . In fact, the accuracy deteriorates beyond  $\alpha = 2.6$ .

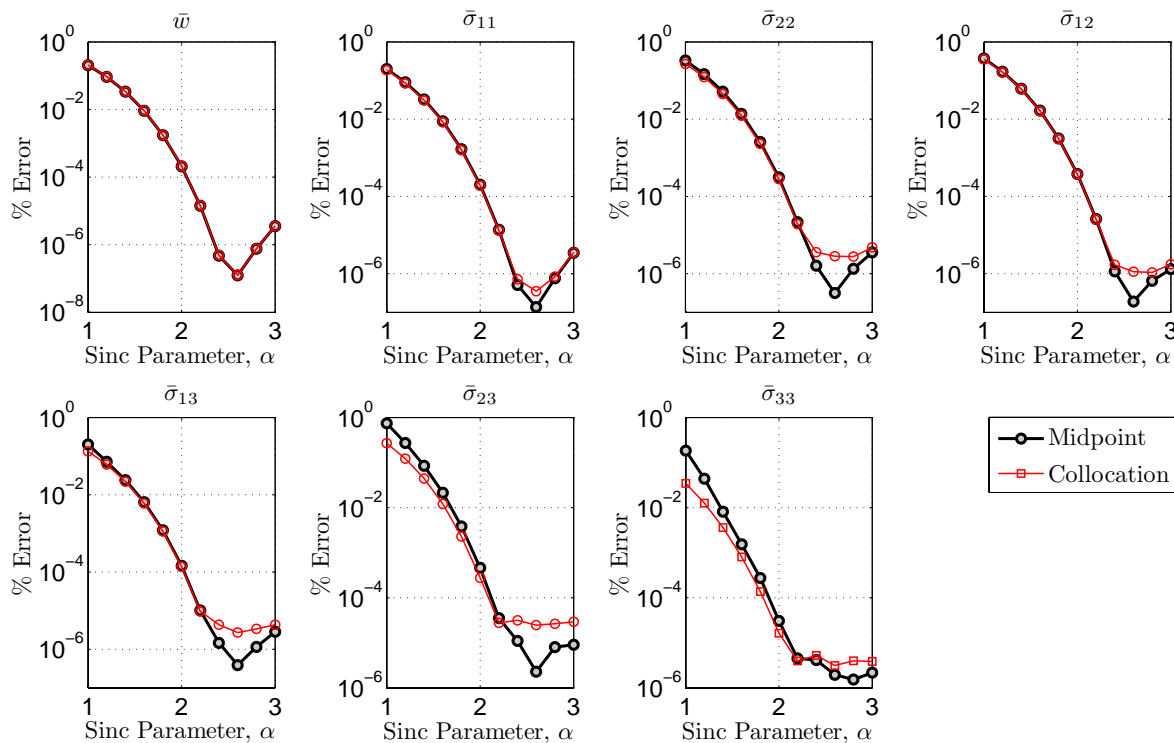


Figure 4.12. Error versus Sinc span,  $\alpha$ , with  $N = 20$  for a classical laminated composite plate.

### 4.3 Summary and Conclusions

In this chapter, the SIHD method was examined for analysis of composite beams and plates in which the interlaminar stresses are desired. The SIHD method was presented as developed by Li and Wu [122]. However, the boundary conditions are applied in a fashion that results in asymmetry of the Sinc points. Thus an alternative method for applying the boundary conditions was presented in which the Sinc points are symmetrically distributed and the boundary conditions are applied to the Sinc points along the boundary.

The numerical results for a composite Timoshenko beam showed that the SIHD method

with the symmetric boundary condition approach provides good accuracy, relatively independent of the selection of the Sinc mesh size. By specifying the span rather than the mesh size, the user has some freedom to control the Sinc point distribution. The numerical results indicate very accurate deflection, rotation, and stresses, including transverse shear stress obtained by integration of the equilibrium equations of 3D elasticity. The symmetric approach obtains significantly less error at small Sinc span than Li and Wu's approach and also compares well when the span is larger. The results indicate that the accuracy of both methods increases with increasing span. However, with increasing span the Sinc points are increasingly biased toward the ends. Such a bias could be a disadvantage when more Sinc points are desired in the middle of the domain.

The SIHD method was also implemented to analyze bending of a simply-supported, classical, laminated composite plate. This 2D example shows that obtaining equal equations as unknowns is not trivial using Li and Wu's approach. The governing equation and boundary conditions applied at the Sinc points results in an equation deficiency. A standard procedure for applying additional necessary equations from derivatives of the boundary conditions was discussed and compared with a traditional collocation implementation. The numerical results for the SIHD method with the midpoint and collocation approaches indicate that the deflection and stresses may be computed very accurately, relatively independent of the selection of the Sinc mesh size. The results indicate the SIHD method is easily implemented, provides good accuracy, and has good convergence behavior.

Both the Timoshenko beam and the classical laminated plate illustrate the success of the SIHD method as a tool for computation of interlaminar stresses by integration of the equilibrium equations of 3D elasticity theory. Moreover, the SIHD method is successful at accurately obtaining the higher-order derivatives necessary for computation of the interlaminar stresses.

To this point, the interlaminar stress accuracy was measured against the stresses obtained

from the exact solution of the BVP; however, the accuracy of those stresses as compared with 3D elasticity theory has not yet been verified. That is the topic of Chapter 5.

## 5 Composite Beam Analysis with SIHD

The bending of composite beams was examined using the 3D FEM and the ESL beam theories solved by the SIHD method. Both cross-ply laminated composite beams and beams with isotropic facesheets and functionally graded core material were considered in this Chapter. The beams were subjected to static uniform loading. The displacements and stresses, including transverse normal and transverse shear stress components computed by integration of the equilibrium equations of 3D elasticity, were compared with an approximate 3D elasticity solution using the conventional FEM. All stress and displacement results were normalized in the following manner.

$$\begin{aligned}\bar{\sigma}_{xx} &= \sigma_{xx}h^2/a^2p_0, & \bar{\sigma}_{xz} &= \sigma_{xz}h/ap_0, & \bar{\sigma}_{yy} &= \sigma_{yy}h^2/a^2p_0, \\ \bar{\sigma}_{yz} &= \sigma_{yz}h/ap_0, & \bar{\sigma}_{zz} &= \sigma_{zz}/p_0, & \bar{w} &= wE_1h^3/p_0a^4\end{aligned}$$

where  $h$  is the beam thickness,  $a$  is the beam length and  $p_0$  is the magnitude of applied load.

### 5.1 Laminated Beams

Three-layered  $[0^\circ/90^\circ/0^\circ]$ , graphite/epoxy laminates were considered. Beams with length-to-thickness ( $a/h$ ) ratios of 5, 10, and 20 and slenderness ratio equal to length-to-thickness ratio ( $a/b = a/h$ ) were examined. For each case, numerical results were obtained using the SIHD method with both the Timoshenko beam theory and Bickford's consistent higher-order beam theory. The material properties used were that of a typical orthotropic graphite/epoxy lamina [103] as given in Table 5.3.

Eight-node, linear, reduced-integration, brick elements (C3D8R) in ABAQUS/Standard were used to obtain an approximate 3D elasticity solution for each length-to-thickness ratio. The beam's thickness was maintained while the length of the beam was increased to vary  $a/h$  ( $a/b$  maintained). The simply-supported boundary condition imposed for the FEA is

**Table 5.3. Material properties for a typical graphite/epoxy lamina.**

$E_1$ [Msi/GPa]	24.9 / 172
$E_2$ [Msi/GPa]	1.00 / 6.89
$G_{12}, G_{13}$ [Msi / GPa]	0.50 / 3.45
$G_{23}$ [Msi / GPa]	0.20 / 1.38
$\nu_{12}$	0.25

expressed as follows:

$$\begin{aligned}
 \Omega &= \{(x_1, x_2, x_3) \mid 0 \leq x_1 \leq a, -b/2 \leq x_2 \leq b/2, -h/2 \leq x_3 \leq h/2\} \\
 u_3 &= 0, \quad \{(x_1, x_2, x_3) \in \Omega \mid x_1 = 0 \cup x_1 = a\} \\
 u_1 &= 0, \quad \{(x_1, x_2, x_3) \in \Omega \mid x_1 = 0 \cap x_3 = 0\} \\
 u_2 &= 0, \quad \{(x_1, x_2, x_3) \in \Omega \mid x_1 = 0 \cap x_2 = 0 \cap x_3 = 0\}
 \end{aligned} \tag{5.1}$$

A converged FE solution was verified by computing the L2 norm of the difference in the displacement variables resulting from two successively fine meshes. The L2 norm of the difference in  $u_1$ ,  $u_2$  and  $u_3$  displacements was computed by Eq. (4.7) where the  $w_{exact}$  was the displacement variable in the fine mesh and  $w_{approx}$  was the displacement variable in the coarse mesh. The L2 norm of the converged mesh are summarized in Table 5.4. The distribution of elements in the converged mesh is given in Table 5.5. To better capture the stresses in the vicinity of the boundary, the elements were biased to the edges. A “bias ratio” or the ratio of element size at the coarse end to the element size at the fine end, of 5 was selected along each end of the beam length and through the thickness of the top material layers. The FE mesh for laminates with  $a/h = 10$  and with boundary conditions and loading indicated may be seen in Fig. 5.1.

The results were also obtained using the SIHD method implemented in MATLAB R14 Service Pack 2<sup>2</sup>. For the SIHD method’s results,  $N = 100$  (201 Sinc Points) was used in the Sinc approximation in Eq. (3.4), an excessively large number of points, guaranteeing

<sup>2</sup>MATLAB is the registered trademark of Math Works, Inc.

**Table 5.4. L2 norm of displacements between fine and coarse mesh solution of graphite-epoxy, laminated beams.**

$a/h$	# Elements Coarse	# Elements Fine	$e_{u_1}$	$e_{u_2}$	$e_{u_3}$
5	20,160	174,720	0.33 %	0.76 %	0.12 %
10	20,306	152,880	0.21 %	0.68 %	0.11 %
120	43,680	237,120	0.078 %	0.52 %	0.079 %

**Table 5.5. FE mesh sizes for  $[0^\circ/90^\circ/0^\circ]$ , graphite/epoxy, laminated composite beams.**

$a/h$	Length	Height	Width
5	140 <sup>*</sup>	48 <sup>†</sup>	26
10	140 <sup>*</sup>	42 <sup>‡</sup>	26
20	240 <sup>*</sup>	38 <sup>‡</sup>	26

<sup>\*</sup> Elements spacing biased toward beam ends with a bias ratio of 5.

<sup>†</sup> Element spacing biased in both 0 deg laminate layer with a bias ratio of 5.

<sup>‡</sup> Element spacing biased in top 0 deg laminate layer with a bias ratio of 5.

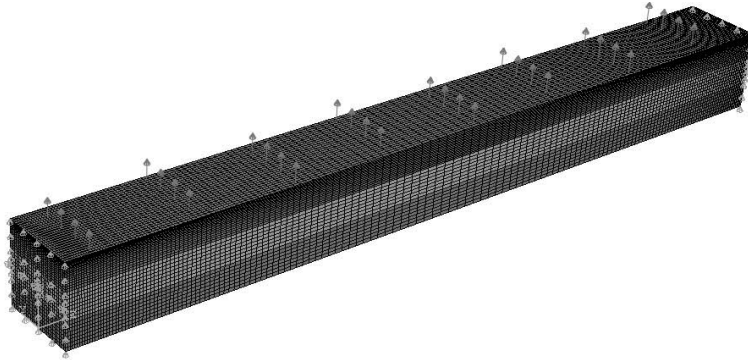


**Figure 5.1. FE mesh for  $[0/90/0]$  graphite/epoxy laminated composite beam.**

convergence at the cost of a nearly undetectable computation time, on the order of 0.5 seconds on a typical dual processor PC. The Sinc mesh size,  $h$  [see Eq. (3.4)] was selected by specifying the span to remain constant at 2.5 with increasing number of Sinc points. The simply-supported boundary condition for the Timoshenko and Bickford theories are given in Appendix B.

In Fig. 5.2, the displacement of the mid-plane and fringe plots of through-the-thickness stresses were plotted for  $a/h = 5$ . The figure indicates the displacements are very accurately computed using the Bickford theory. Figure 5.2(b) indicates the trend of  $\sigma_{xx}$  is captured very well by the Timoshenko (FSDT) and Bickford theories (TSDT). Figure 5.2(c) indicates for most of the beam the trend of  $\sigma_{xz}$  is captured by both theories; however, in the vicinity of the boundary, the Bickford theory appears to differ significantly from the FEM results. Figure 5.2(d) also indicates the trend of  $\sigma_{zz}$  is not well captured in the vicinity of the boundaries. Neither, the Timoshenko theory nor the Bickford theory fully capture the transverse normal stress component in these areas.

Through-the-thickness stress distributions are plotted in Figs. 5.3 and 5.4. The longitudinal normal stress component  $\sigma_{xx}$  is plotted at the midpoint of the beam in Fig. 5.3. The figure indicates the stress distribution is very accurately predicted by the Bickford theory. However, the Timoshenko theory fails to capture the trend precisely. This result is due to the higher-order of the Bickford theory, a beam theory akin to TSDT [98], beneficial for studying thick beams such as  $a/h = 5$ . The transverse normal stress component is also plotted in Fig. 5.3. At the midpoint, the transverse normal stress component is very accurately predicted by both theories for this beam.

In Fig. 5.4, through-the-thickness distributions of transverse shear ( $\sigma_{xz}$ ) and transverse normal ( $\sigma_{zz}$ ) stresses are plotted at the end ( $x/a = 0$ ) and near the end of the beam ( $x/a = 0.1$ ). The figures indicate erroneous stresses computed by the ESL theories in the vicinity of the edge. The Bickford theory captures the trend of transverse shear stress at

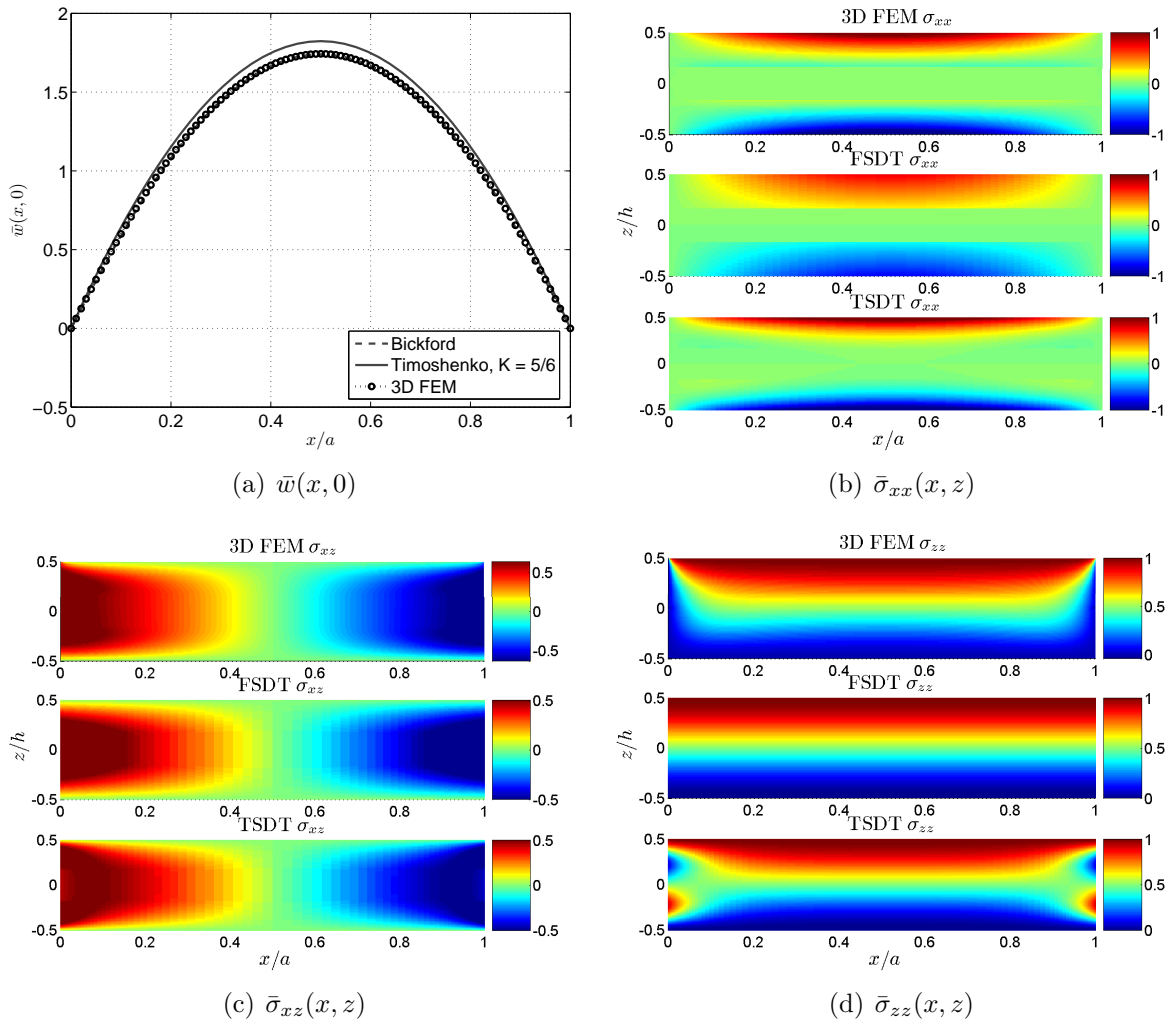


Figure 5.2. Fringe plots of stress components in simply-supported laminated beam with length-to-thickness ratio of  $a/h = 5$ .



$x = 0$ ; however, the peak stress in the  $0^\circ$  layers is reported higher than the FEM.

The transverse normal stress component  $\sigma_{zz}$  is also very poorly approximated by the ESL theories at  $x/a = 0$ . However, the inaccuracies of the FE solution in this vicinity should be noted. The FEM results for transverse normal stress only approximately achieve the applied load on the top surface. Significant further refinement is necessary to obtain exactly the boundary condition at additional cost to an already expensive analysis. It is safe to assume that the results obtained by the ESL theories are, nonetheless, inaccurate. In this area, the relative dimensions of thickness and width are both on the same scale as the distance from the end. Therefore, the error seen at  $x/a = 0$  is likely due to 3D effects that cannot be predicted by the 1D analysis. Nonetheless, the present results compare well with FEM at  $x/a = 0.1$ . The transverse shear stress component is very accurately computed by the Bickford theory. Both ESL theories compare well with FEM for transverse normal stress.

The mid-plane displacement ( $z = 0, y = 0$ ) and fringe plots of through-the-thickness mid-plane ( $y = 0$ ) stresses were plotted in Fig. 5.5 for  $a/h = 10$ . The figure indicates the displacements are very accurately computed using both the ESL theories. Figures 5.5(b) and 5.5(c) indicate the trends of  $\sigma_{xx}$  and  $\sigma_{xz}$  are captured very well by the Timoshenko (FSDT) and Bickford theories (TSDT). Figure 5.5(d) indicates the trend of  $\sigma_{zz}$  is not captured by either ESL theory in the vicinity of the boundary.

For  $a/h = 10$ , through-the-thickness stress distributions were plotted in Figs. 5.6 - 5.7. The longitudinal normal stress component  $\sigma_{xx}$  is plotted at the midpoint of the beam in Fig. 5.6. The figure indicates the stress distribution is very accurately predicted by both ESL theories. However, the Bickford theory more accurately predicts the longitudinal stress. The transverse normal stress component is also plotted in Fig. 5.6; both ESL theories accurately predict this distribution.

In Fig. 5.7 through-the-thickness stress distributions of transverse shear ( $\sigma_{xz}$ ) and transverse normal ( $\sigma_{zz}$ ) stresses are plotted at the end ( $x/a = 0$ ) and near the end of the beam

( $x/a = 0.1$ ). The results are similar to the thick beam ( $a/h = 5$ ). The ESL theories fail to predict the stresses in the vicinity of the boundary; however, the error is contained only within a small region around the boundary and improve significantly outside this region. At  $x/a = 0.1$  both stress components are very accurately computed.

The mid-plane displacement and fringe plots of through-the-thickness mid-plane ( $y = 0$ ) stresses were plotted in Fig. 5.8 for  $a/h = 20$ . The figure indicates the displacements are very accurately computed using both of the ESL theories. The fringe plots indicate that these stress components compare very well with the FEM in the bulk of the domain; however, the transverse normal stress component appears to be poorly predicted at the boundary.

In Figs. 5.9 - 5.10 through-the-thickness stress distributions of longitudinal ( $\sigma_{xx}$ ), transverse shear ( $\sigma_{xz}$ ), and transverse normal ( $\sigma_{zz}$ ) stress components were plotted at the midpoint and near the end of the beam ( $x/a = 0.5, 0, 0.1$ ). Other than at  $x/a = 0$ , the results from Timoshenko theory and Bickford theory are indistinguishable, indicating there to be no benefit of using the higher-order Bickford theory for thin beams. Furthermore Fig. 5.10 echoes the previous comments regarding the erroneous stress at the boundary. While neither  $\sigma_{xz}$  nor  $\sigma_{zz}$  are accurately computed at the boundary, both ESL theories compare well with the FEM at  $x/a = 0.1$ .

The fringe plots in Figs. 5.2, 5.5, and 5.8 implicitly indicate the relative magnitude of the stresses. The stresses  $\sigma_{xx}$ ,  $\sigma_{xz}$ , and  $\sigma_{zz}$  were normalized by  $(a/h)^2 p_0$ ,  $(a/h)p_0$ , and  $p_0$  respectively. Note that the maximum  $\bar{\sigma}_{xx}$ ,  $\bar{\sigma}_{xz}$ , and  $\bar{\sigma}_{zz}$  from the fringe plots are approximately 1, 0.5, and 1 for each  $a/h$ . Thus the relative magnitude of  $\sigma_{xx}/\sigma_{xz} \approx 2a/h$  and  $\sigma_{xx}/\sigma_{zz} \approx (a/h)^2$ . It is reasonable to conclude for thin beams,  $\sigma_{xx}$  is large relative to the other stress components and the inaccuracies of the transverse shear and normal stresses may be negligible compared to the magnitude of the longitudinal bending stress.

## 5.2 Functionally Graded Sandwich Composites

A sandwich plate with isotropic facesheets and a functionally graded core as seen in Fig. 5.11 was considered. The core had varying volume fractions of two constituent materials. There are several methods for homogenization of a multi-constituent material. Both the rule of mixtures approach and Mori-Tanaka [147] methods have been used in conjunction with functionally graded materials [148, 149, 150]. For this dissertation, the Mori-Tanaka approach was employed. Accordingly, the material properties may be determined by

$$\begin{aligned}\frac{K - K_1}{K_2 - K_1} &= \frac{V_2}{1 + (1 - V_2)\frac{K_2 - K_1}{K_1 + 4/3G_1}}, \\ \frac{G - G_1}{G_2 - G_1} &= \frac{V_2}{1 + (1 - V_2)\frac{G_2 - G_1}{G_1 + f_1}}, \\ f_1 &= \frac{G_1(9K_1 + 8G_1)}{6(K_1 + 2G_1)},\end{aligned}\tag{5.2}$$

where  $K$ ,  $K_1$ , and  $K_2$  are the bulk moduli of the homogenized material, constituent 1, and constituent 2 respectively,  $G$ ,  $G_1$ , and  $G_2$  are the shear moduli of the homogenized material, constituent 1, and constituent 2 respectively. The effective values of Young's modulus and Possion's ratio are found from the bulk and shear moduli. With the homogenized engineering constants, the plane-stress reduced stiffness matrix  $\bar{Q}_{ij}(z)$  is known.

### 5.2.1 Numerical Integration of Interlaminar Stresses in FGM

The variations of Young's modulus are found from Eq. (5.2). For even simple material volume fraction variations, the resulting variation of plane-stress stiffnesses are not easy to integrate. Therefore analytic integration similar to that used for the laminated beams is not practical through the functionally graded core material. Through the facesheets,  $-h/2 \leq z \leq -h/2 + t_f$  and  $h/2 - t_f \leq z \leq h/2$ , the integration may be performed in an identical fashion to laminated composites, i.e. in an analytic fashion through each layer. However, in the present study, the core was integrated numerically using the numerical

indefinite integration as detailed in Chapter 3. To that end, the interlaminar stresses are written by simplifying the general expressions given in Eq. (2.16). The transverse shear and normal stresses are given by:

$$\sigma_{xz}(x, s) - \sigma_{xz}(x, z_0) = - \int_{z_0}^s \left( \{\bar{Q}_{1j}(z)\} \frac{d\{\epsilon^{(0)}\}}{dx} + z\{\bar{Q}_{1j}(z)\} \frac{d\{\epsilon^{(1)}\}}{dx} + z^3\{\bar{Q}_{1j}(z)\} \frac{d\{\epsilon^{(3)}\}}{dx} \right) dz, \quad (5.3)$$

$$\sigma_{yz}(x, s) - \sigma_{yz}(x, z_0) = - \int_{z_0}^s \left( \{\bar{Q}_{6j}(z)\} \frac{d\{\epsilon^{(0)}\}}{dx} + z\{\bar{Q}_{6j}(z)\} \frac{d\{\epsilon^{(1)}\}}{dx} + z^3\{\bar{Q}_{6j}(z)\} \frac{d\{\epsilon^{(3)}\}}{dx} \right) dz, \quad (5.4)$$

with  $z_0 = -h/2 + t_f$  for  $(-h/2 + t_f) \leq s \leq (h/2 - t_f)$ . To compute the transverse shear stress components evaluation of

$$\int_{z_0}^s \{\bar{Q}(z)\} dz, \quad \int_{z_0}^s z\{\bar{Q}(z)\} dz, \quad \text{and} \quad \int_{z_0}^s z^3\{\bar{Q}(z)\} dz$$

is necessary. This is done by implementing a change of domain from  $z \in (-h/2 + t_f, h/2 - t_f)$  to  $\xi \in (0, \xi_N)$  by the transformation  $z = (\xi)(h - 2t_f)/\xi_N - h/2 + t_f$ . Accordingly, the integrals become:

$$\int_0^{\xi_j} \{\bar{Q}(z(\xi))\} \frac{dz}{d\xi} d\xi, \quad \int_0^{\xi_j} z(\xi)\{\bar{Q}(z(\xi))\} \frac{dz}{d\xi} d\xi, \quad \text{and} \quad \int_0^{\xi_j} z(\xi)^3\{\bar{Q}(z(\xi))\} \frac{dz}{d\xi} d\xi.$$

These integrals may be evaluated at each Sinc point through the thickness of the core according to Eq. (3.12). Because it is only necessary to evaluate these integrals at the Sinc points, Eq. (4.4) may be recalled and employed. Thus the integration is performed approximately

in the the following manner.

$$\begin{aligned}\int_0^{\xi_j} \{\bar{Q}(z(\xi))\} \frac{dz}{d\xi} d\xi &\approx \sum_{i=-N}^N \frac{dz}{d\xi} k_{ij} \{\bar{Q}(z(\xi_i))\} \\ \int_0^{\xi_j} z(\xi) \{\bar{Q}(z(\xi))\} \frac{dz}{d\xi} d\xi &\approx \sum_{i=-N}^N \frac{dz}{d\xi} k_{ij} z(\xi_i) \{\bar{Q}(z(\xi_i))\} \\ \int_0^{\xi_j} z(\xi)^3 \{\bar{Q}(z(\xi))\} \frac{dz}{d\xi} d\xi &\approx \sum_{i=-N}^N \frac{dz}{d\xi} k_{ij} z(\xi_i)^3 \{\bar{Q}(z(\xi_i))\}\end{aligned}$$

Note that  $k_{ij}$  was already computed in order to obtain an approximate solution to the BVP by the SIHD method. Thus *the transverse shear stress components may be obtained numerically without significant additional computational expense.*

The through-the-thickness interlaminar stresses are computed by:

$$\begin{aligned}\sigma_{xz}(x, z(\xi_i)) - \sigma_{xz}(x, z_0) &= - \sum_{i=-N}^N k_{li} \frac{dz}{d\xi} \left( \{\bar{Q}_{1j}(z(\xi_i))\} \frac{d\{\epsilon^{(0)}\}}{dx} \right. \\ &\quad \left. + z(\xi_i) \{\bar{Q}_{1j}(z(\xi_i))\} \frac{d\{\epsilon^{(1)}\}}{dx} + z(\xi_i)^3 \{\bar{Q}_{1j}(z(\xi_i))\} \frac{d\{\epsilon^{(3)}\}}{dx} \right), \quad (5.5)\end{aligned}$$

$$\begin{aligned}\sigma_{yz}(x, z(\xi_i)) - \sigma_{yz}(x, z_0) &= - \sum_{i=-N}^N k_{li} \frac{dz}{d\xi} \left( \{\bar{Q}_{6j}(z(\xi_i))\} \frac{d\{\epsilon^{(0)}\}}{dx} \right. \\ &\quad \left. + z(\xi_i) \{\bar{Q}_{6j}(z(\xi_i))\} \frac{d\{\epsilon^{(1)}\}}{dx} + z(\xi_i)^3 \{\bar{Q}_{6j}(z(\xi_i))\} \frac{d\{\epsilon^{(3)}\}}{dx} \right), \quad (5.6)\end{aligned}$$

with  $z_0 = -h/2 + t_f$  for all Sinc points  $z(\xi_i) \in (-h/2 + t_f, h/2 - t_f)$ .

The transverse normal stress distribution is given as

$$\begin{aligned}\sigma_{zz}(x, s) - \sigma_{zz}(x, z_0) &= - \int_{z_0}^s \left( - \int_{z_0}^{s_1} \left( \{\bar{Q}_{1j}(z)\} \frac{d^2\{\epsilon^{(0)}\}}{dx^2} + z \{\bar{Q}_{1j}(z)\} \frac{d^2\{\epsilon^{(1)}\}}{dx^2} \right. \right. \\ &\quad \left. \left. + z^3 \{\bar{Q}_{1j}(z)\} \frac{d^2\{\epsilon^{(3)}\}}{dx^2} \right) dz + \frac{\partial \sigma_{xz}(x, z_0)}{\partial x} \right) ds_1. \quad (5.7)\end{aligned}$$

Note that Eq. (5.7) necessitates evaluating

$$\int_{z_0}^s \int_{z_0}^{s_1} \{\bar{Q}(z)\} dz ds_1, \quad \int_{z_0}^s \int_{z_0}^{s_1} z \{\bar{Q}(z)\} dz ds_1, \quad \int_{z_0}^s \int_{z_0}^{s_1} z^3 \{\bar{Q}(z)\} dz ds_1.$$

Both the  $z$  domain and the dummy  $s_1$  domains are transformed. The  $z$  domain is transformed from  $z \in (-h/2 + t_f, h/2 - f_f)$  to  $\xi \in (0, \xi_N)$  by  $z = (\xi)[(h - 2t_f)/\xi_N] - h/2 + t_f$ . Similarly, the  $s_1$  domain is transformed such that the integrals become:

$$\int_0^{\xi_j} \int_0^{s_1} \{\bar{Q}(z(\xi))\} \left(\frac{dz}{d\xi}\right)^2 d\xi ds_1, \quad \int_0^{\xi_j} \int_0^{s_1} z(\xi) \{\bar{Q}(z(\xi))\} \left(\frac{dz}{d\xi}\right)^2 d\xi ds_1, \\ \text{and} \quad \int_0^{\xi_j} \int_0^{s_1} z(\xi)^3 \{\bar{Q}(z(\xi))\} \left(\frac{dz}{d\xi}\right)^2 d\xi ds_1.$$

These integrals are evaluated approximately by Eq. (3.12) and utilizing Eq. (4.4):

$$\int_0^{\xi_j} \int_0^{s_1} \{\bar{Q}(z(\xi))\} \left(\frac{dz}{d\xi}\right)^2 d\xi ds_1 \approx \sum_{l=-N}^N \sum_{i=-N}^N \left(\frac{dz}{d\xi}\right)^2 k_{jl} k_{li} \{\bar{Q}(z(\xi_i))\}, \\ \int_0^{\xi_j} \int_0^{s_1} z(\xi) \{\bar{Q}(z(\xi))\} \left(\frac{dz}{d\xi}\right)^2 d\xi ds_1 \approx \sum_{l=-N}^N \sum_{i=-N}^N \left(\frac{dz}{d\xi}\right)^2 k_{jl} k_{li} z(\xi_i) \{\bar{Q}(z(\xi_i))\}, \\ \int_0^{\xi_j} \int_0^{s_1} z^3(\xi) \{\bar{Q}(z(\xi))\} \left(\frac{dz}{d\xi}\right)^2 d\xi ds_1 \approx \sum_{l=-N}^N \sum_{i=-N}^N \left(\frac{dz}{d\xi}\right)^2 k_{jl} k_{li} z(\xi_i)^3 \{\bar{Q}(z(\xi_i))\}.$$

Evaluation of Eq. (5.7) is now trivial. The transverse normal stress is computed in an approximate manner by:

$$\sigma_{zz}(x, z(\xi_i)) - \sigma_{zz}(x, z_0) = - \sum_{m=-N}^N \sum_{i=-N}^N k_{lm} k_{mi} \left(\frac{dz}{d\xi}\right)^2 \left\{ - \left( \{\bar{Q}_{1j}(z(\xi_i))\} \frac{d^2\{\epsilon^{(0)}\}}{dx^2} \right. \right. \\ \left. \left. + z(\xi_i) \{\bar{Q}_{1j}(z(\xi_i))\} \frac{d^2\{\epsilon^{(1)}\}}{dx^2} + z(\xi_i)^3 \{\bar{Q}_{1j}(z(\xi_i))\} \frac{d^2\{\epsilon^{(3)}\}}{dx^2} \right) \right\} \\ - \frac{\partial \sigma_{xz}(x, z_0)}{\partial x} (z(\xi_i) - z_0). \quad (5.8)$$

It should be emphasized that because the SIHD method is employed to solve the BVP,  $k_{ij}$  was previously evaluated. Thus obtaining the transverse normal and transverse shear stress components from the equilibrium equations of the 3D elasticity theory is simply reduced to matrix multiplication.

### 5.2.2 Numerical Results for Functionally Graded Sandwich Composite

Numerical results were obtained for sandwich composites with functionally graded core material. The core was composed of two constituent materials: a lightweight material with relatively low stiffness and the high stiffness facesheet material. The volume fraction varies through the core, providing smooth material property variation from point to point. The following form was taken for the volume fraction grading through the core:

$$V_1 = |2z/t_c|^p, \quad -t_c/2 \leq z \leq t_c/2 \quad (5.9)$$

where  $t_c$  is the core thickness (see Fig. 5.11),  $V_1$  is the volume fraction of facesheet material, and  $p$  is the order of the polynomial variation. The core was considered to have  $p = 1, 2$ , and  $\infty$ . In Fig. 5.12, the volume fraction grading for each case examined was plotted.

Isotropic constituent materials were considered. The facesheet material had the following properties:  $E = 7.0 \times 10^{10}$  N/m<sup>2</sup> and  $\nu = 0.3$ . The core material had the following properties:  $E = 7.0 \times 10^8$  N/m<sup>2</sup> and  $\nu = 0.3$ . The Mori-Tanaka homogenization technique was used to determine the equivalent modulus at a point in the core from the two constituent materials. A single beam geometric configuration was considered ( $a/h = 10$ ,  $a/b = 10$ , and  $t_f/h = 0.1$ ).

Eight-node linear reduced-integration brick elements (C3D8R) in ABAQUS/Standard were used to obtain an approximate 3D elasticity solution for each material variation. For the FE solution, the C3D8R use the reduced integration scheme, therefore, a single integration point is used within the elements. Through the core material, the material distribution was assigned at each of the integration points. A converged FE solution was verified by

**Table 5.6. L2 norm of displacements between fine and coarse mesh solution for sandwich beam with functionally graded core.**

$p$	# Elements Coarse	# Elements Fine	$e_u$	$e_v$	$e_w$
1	26,600	133,280	0.94 %	0.21 %	0.47 %
2	26,600	133,280	1.16 %	0.26 %	0.82 %
$\infty$	26,600	133,280	0.92 %	0.37 %	0.96 %

computing the L2 norm of the difference in the displacement variables resulting from two successively fine meshes. The L2 norm of the difference in  $u$ ,  $v$  and  $w$  displacements was computed by Eq. (4.7). The L2 norm between coarse and fine meshes are summarized in Table 5.6. The distribution of elements in the converged mesh is summarized in Table 5.7. The simply-supported boundary condition was enforced at both edges in the same manner as for the laminated beams.

**Table 5.7. FE mesh size for sandwich beam with functionally graded core.**

$p$	Length	Height	Width
1	280*	34 <sup>†</sup>	14
2	280*	34 <sup>†</sup>	14
$\infty$	280*	34 <sup>†</sup>	14

\* Elements spacing biased toward beam ends with a bias ratio of 5.

<sup>†</sup> Elements spacing in the facesheets biased toward top and bottom surfaces with a bias ratio of 5.

The present results were obtained using the SIHD method implemented in MATLAB. As for the the results for the laminated beams, 201 Sinc Points were used in the original Sinc approximation in Eq. (3.4). The Sinc mesh size,  $h$ , was determined by specifying the span,  $\alpha$ , to be 2.5.

For  $p = 1, 2$ , and  $\infty$  through-the-thickness stress distributions were plotted in Figs. 5.13 - 5.14. The longitudinal normal stress  $\sigma_{xx}$  was plotted at the midpoint of the beam in Fig. 5.13. The figure indicates the stress distribution is very accurately predicted by both ESL theories for all material variations. The stress is very accurately predicted through the



functionally graded core. The transverse normal stress  $\sigma_{zz}$  is also plotted at the midpoint of the beam. The figure indicates that while neither ESL theory captures exactly the stress distribution, both approximate the trend quite well.

In Fig. 5.14, through-the-thickness stress distributions of transverse shear ( $\sigma_{xz}$ ) and transverse normal ( $\sigma_{zz}$ ) stresses were plotted at the end ( $x/a = 0$ ) and near the end of the beam ( $x/a = 0.1$ ). The results are very similar to the laminated beams in that both stress components are inaccurate at  $x/a = 0$ ; however, by  $x/a = 0.1$ , the stresses very accurately approximate the stress distribution of the 3D FEM. Note that the transverse shear stress component  $\sigma_{xz}$  is very closely approximated for all  $p$  at  $x/a = 0.1$ . This indicates the success with which the integration is performed using the numerical indefinite integration technique at little additional computation expense because the integration weights were retained from the SIHD method.

### 5.3 Summary and Conclusions

Computation of transverse shear and transverse normal stresses or interlaminar stresses from ESL beam theories using the SIHD method was performed in this chapter. Stresses in simply-supported, symmetric, cross-ply, laminated beams and simply-supported, sandwich composite beams with functionally graded cores were obtained using the SIHD method to approximately solve the BVP of the Timoshenko beam theory and Bickford's consistent higher-order beam theory. Integration of the equilibrium equations of the 3D elasticity theory was performed to obtain the transverse normal and transverse shear stress components. For the sandwich composites, numerical indefinite integration by the DE transformation was used to approximately integrate the equilibrium equations of the 3D elasticity theory through the thickness to obtain the transverse shear and transverse normal stresses.

The numerical results obtained by the SIHD method were compared with an approximate elasticity solution using the 3D FEM. The results indicate the stress may be accurately found

from the ESL theories throughout the majority of the domain. However, near the ends of the beam, the present results differ significantly from the FEM results because of edge effects not captured by the 1D analysis.

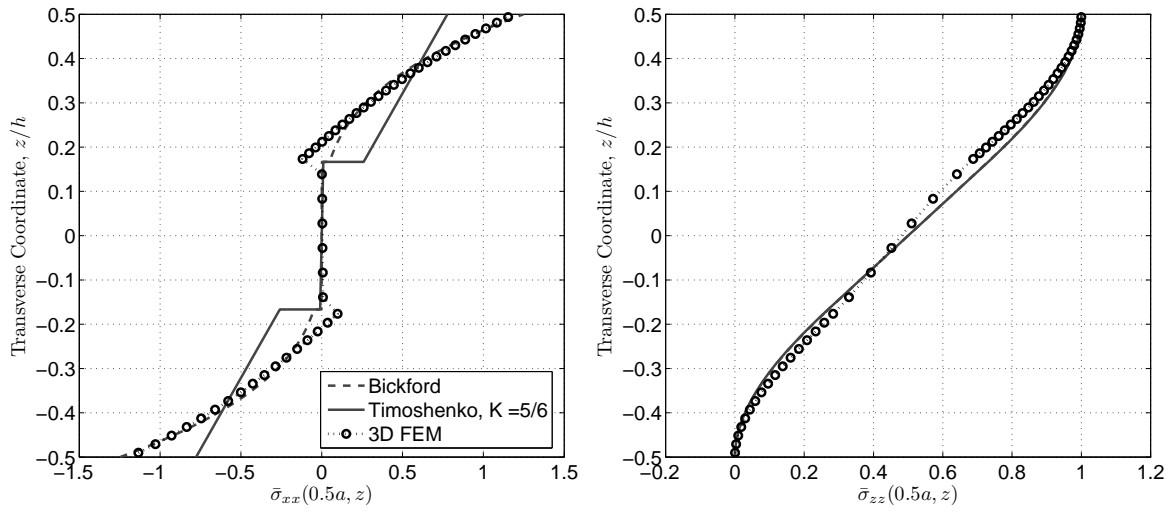


Figure 5.3. Longitudinal and transverse normal stress components at beam center for simply-supported laminated beam with  $a/h = 5$ .

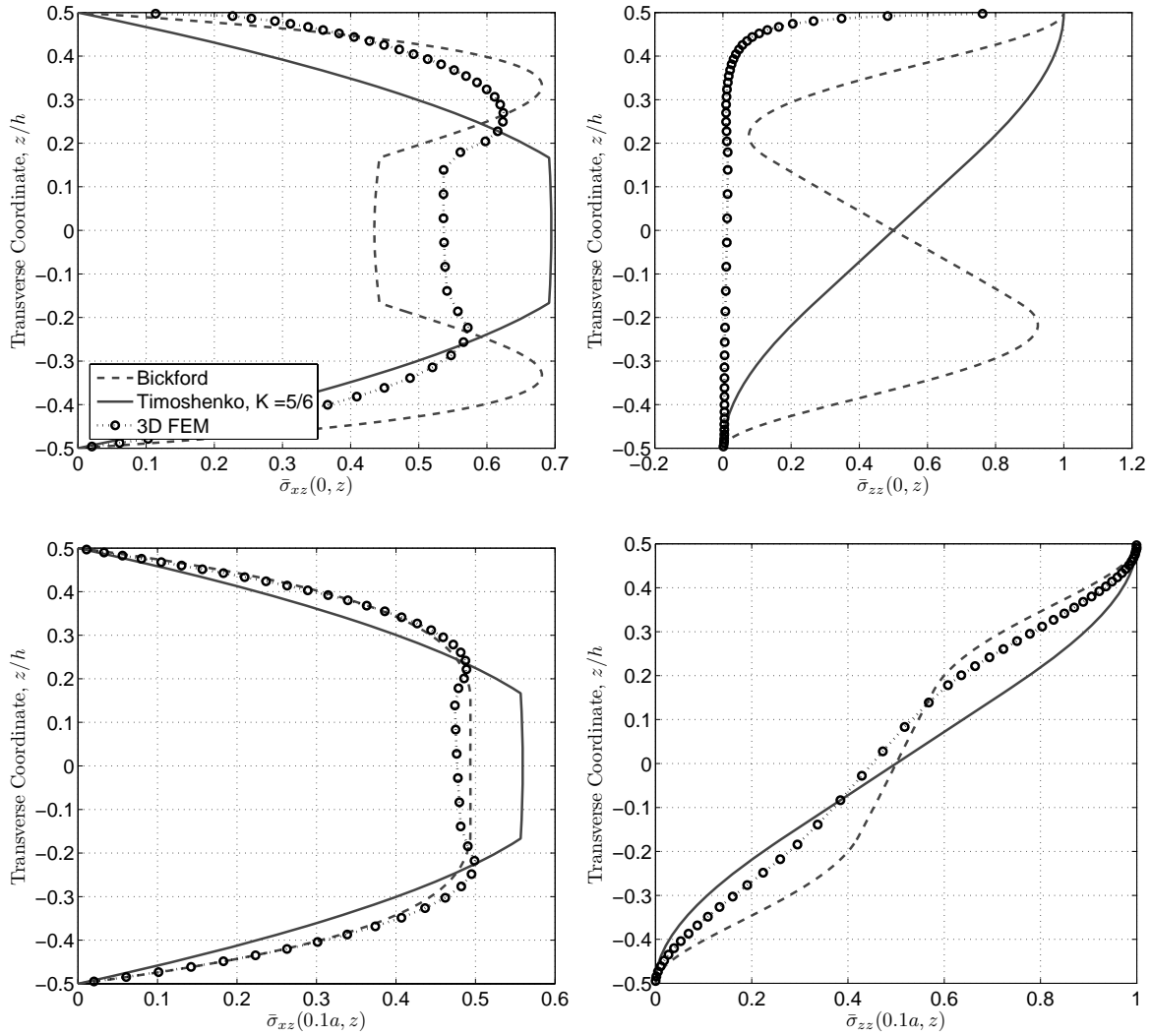


Figure 5.4. Transverse shear and normal stress components at  $x = 0, 0.1a$  for simply-supported laminated beam with  $a/h = 5$ .

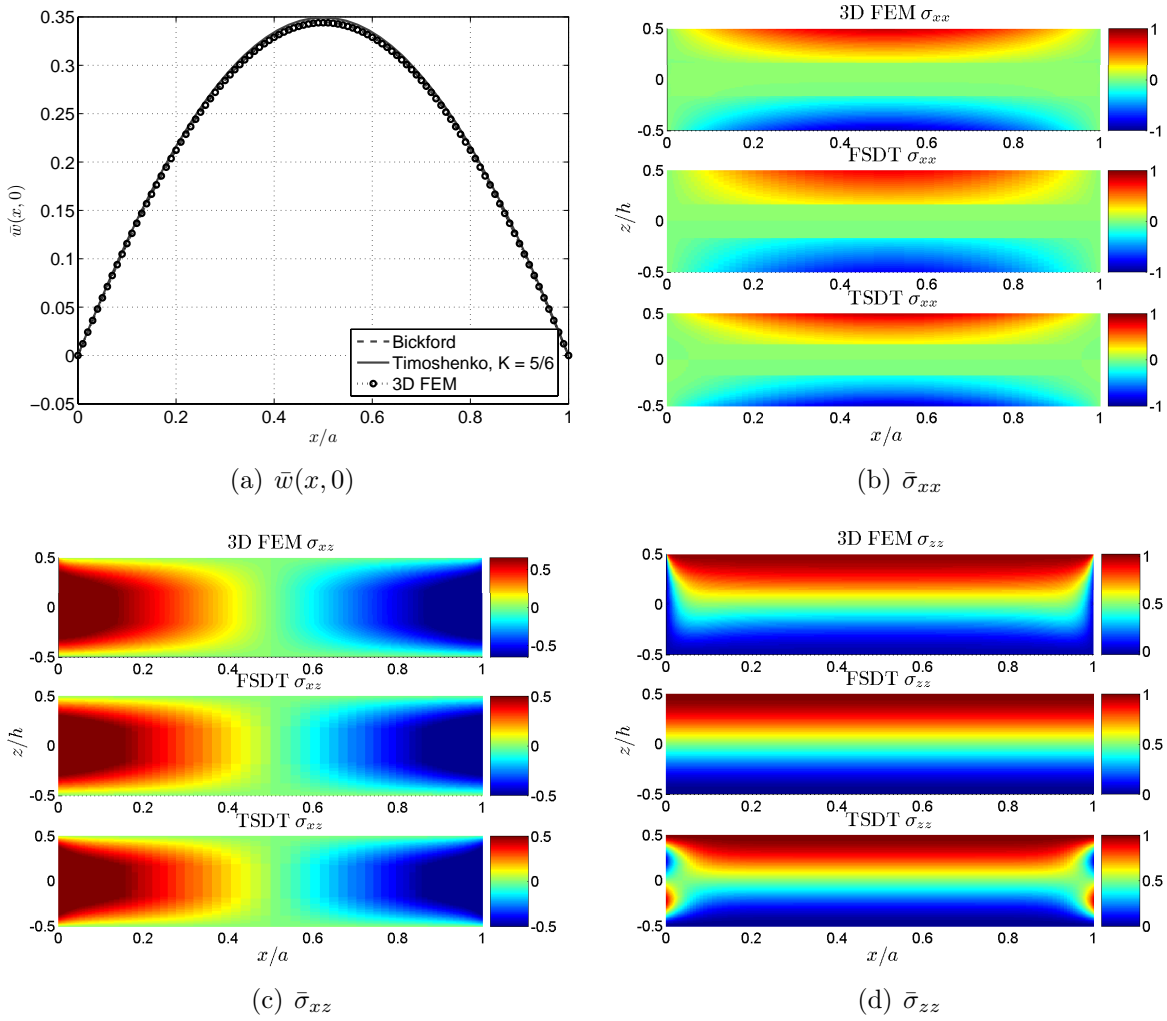


Figure 5.5. Fringe plots of stress components in simply-supported laminated beam with length-to-thickness ratio of  $a/h = 10$ .

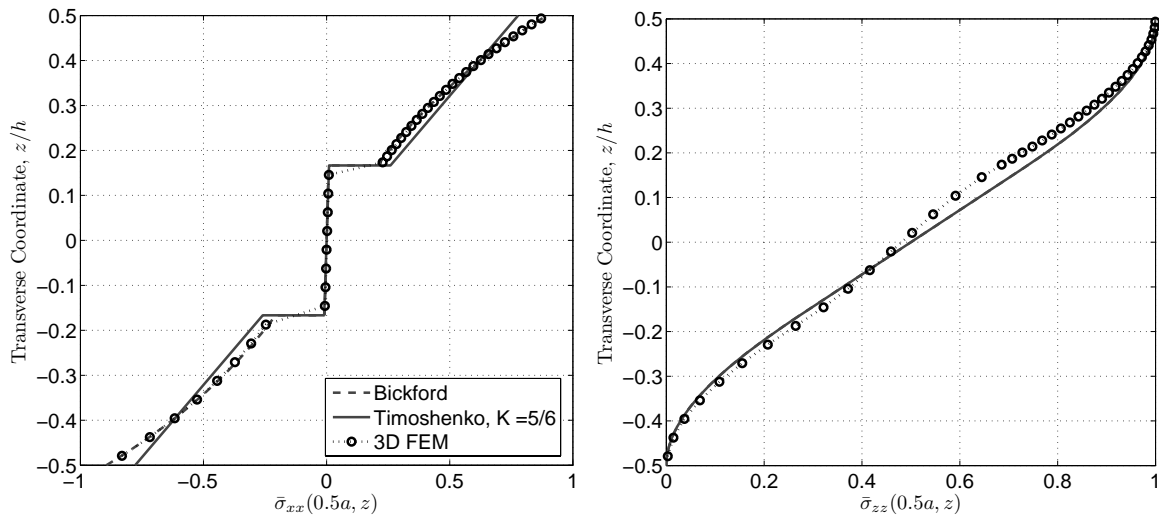


Figure 5.6. Longitudinal and transverse normal stress components at beam center for simply-supported laminated beam with  $a/h = 10$ .

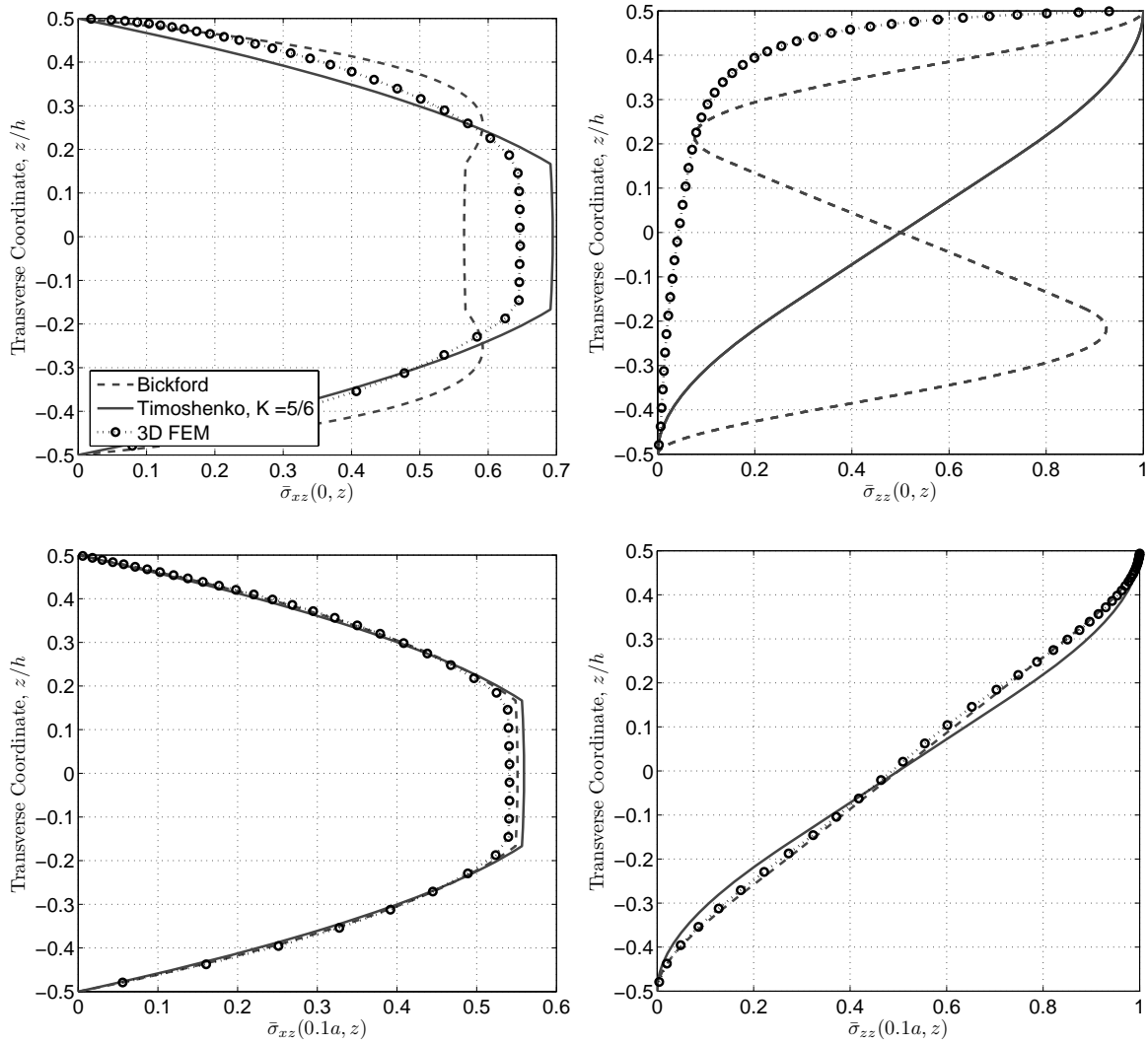


Figure 5.7. Transverse shear and normal stress components at  $x = 0, 0.1a$  for simply-supported laminated beam with  $a/h = 10$ .

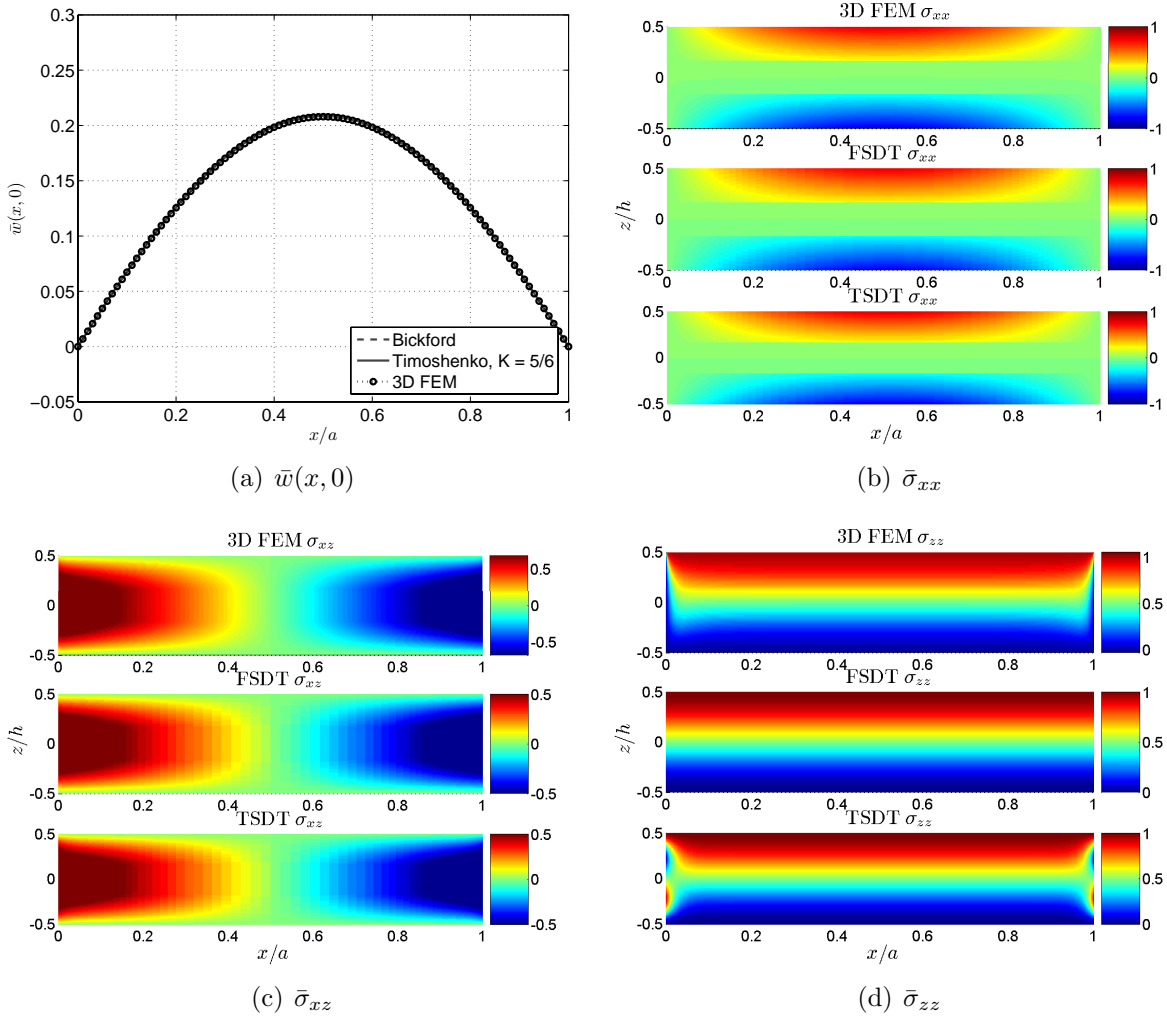


Figure 5.8. Fringe plots of stress components in simply-supported laminated beam with length-to-thickness ratio of  $a/h = 20$ .



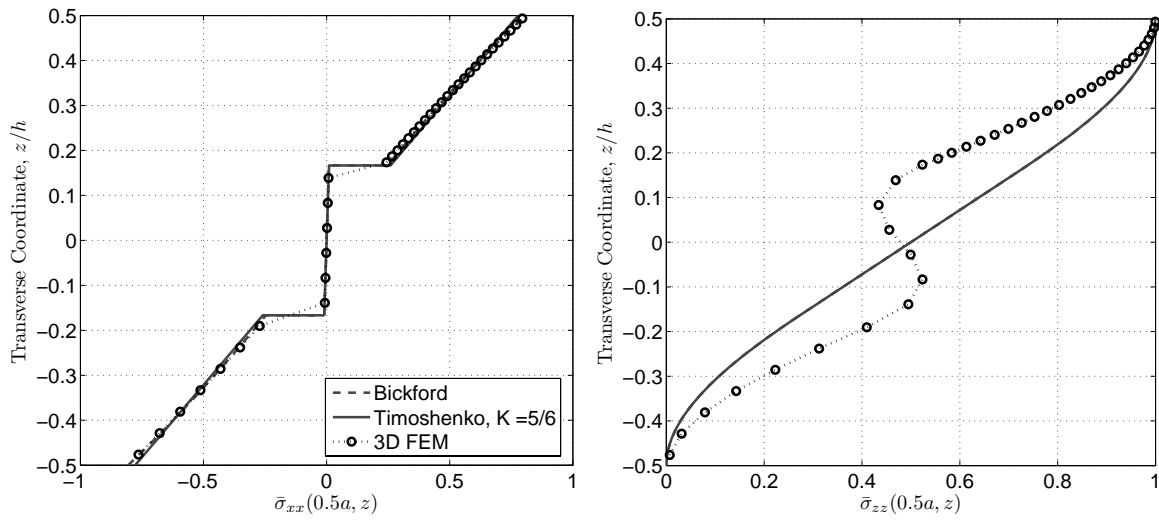


Figure 5.9. Longitudinal and transverse normal stress components at beam center for simply-supported laminated beam with  $a/h = 20$ .

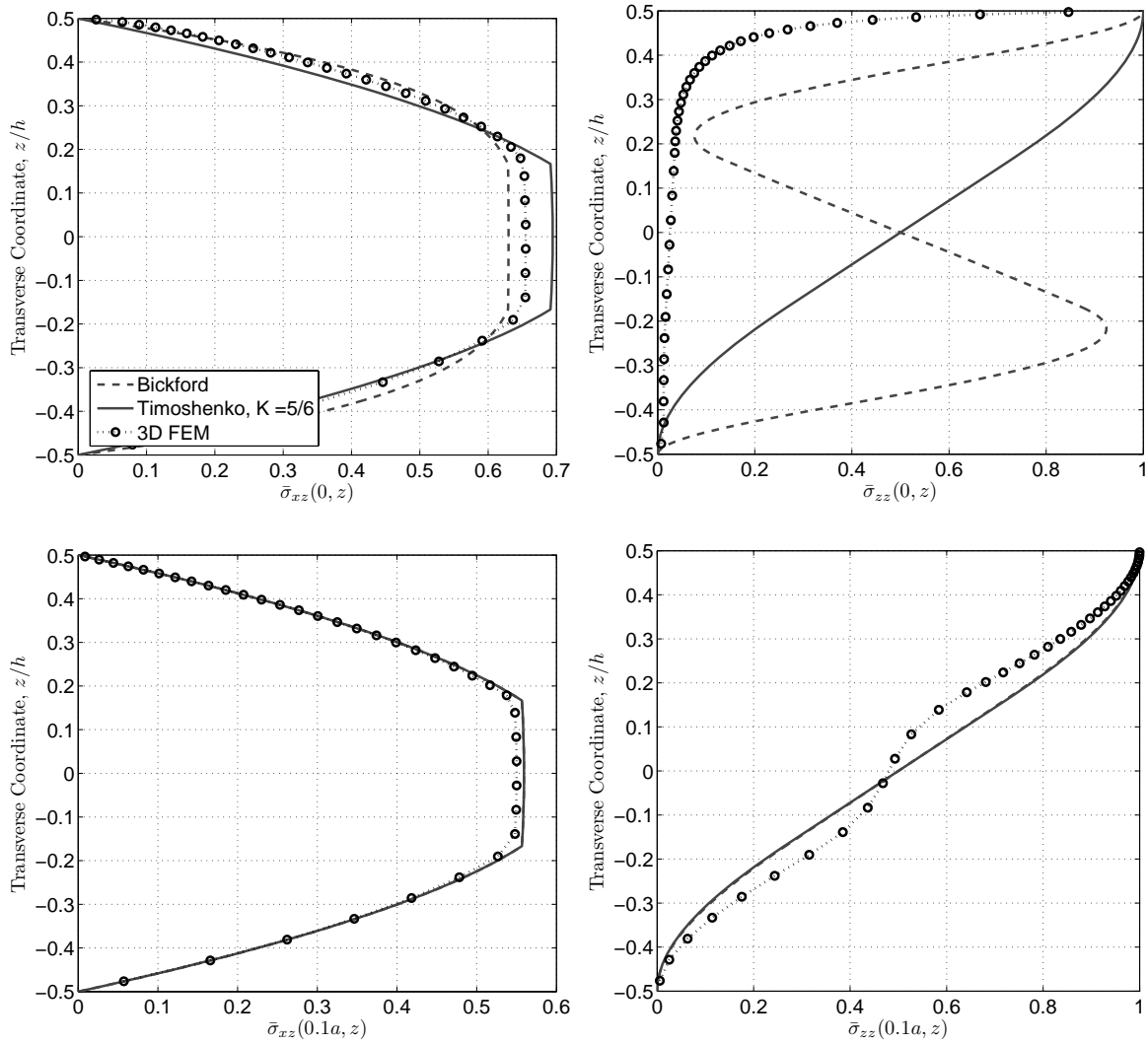


Figure 5.10. Transverse shear and normal stress components at  $x = 0, 0.1a$  for simply-supported laminated beam with  $a/h = 20$ .

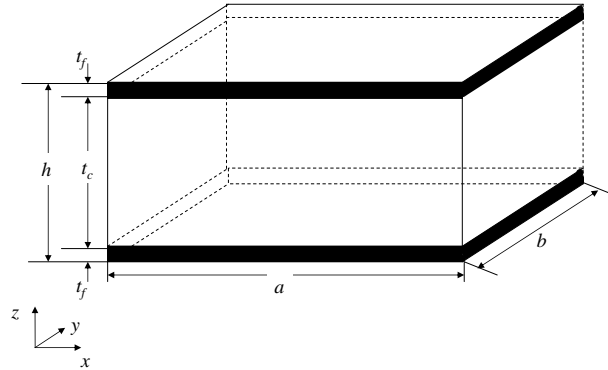


Figure 5.11. Geometry of a plate with functionally graded core that was considered in the present analysis.

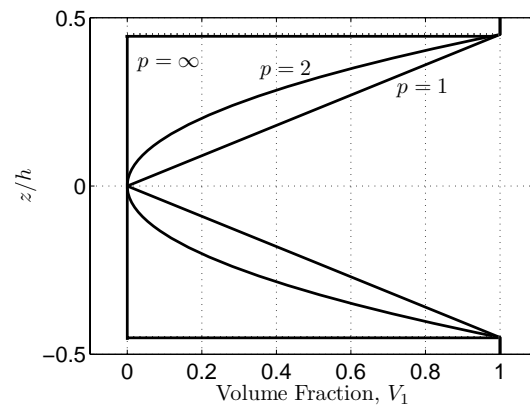


Figure 5.12. Through-the-thickness material volume fraction variation for functionally graded sandwich composite beam.

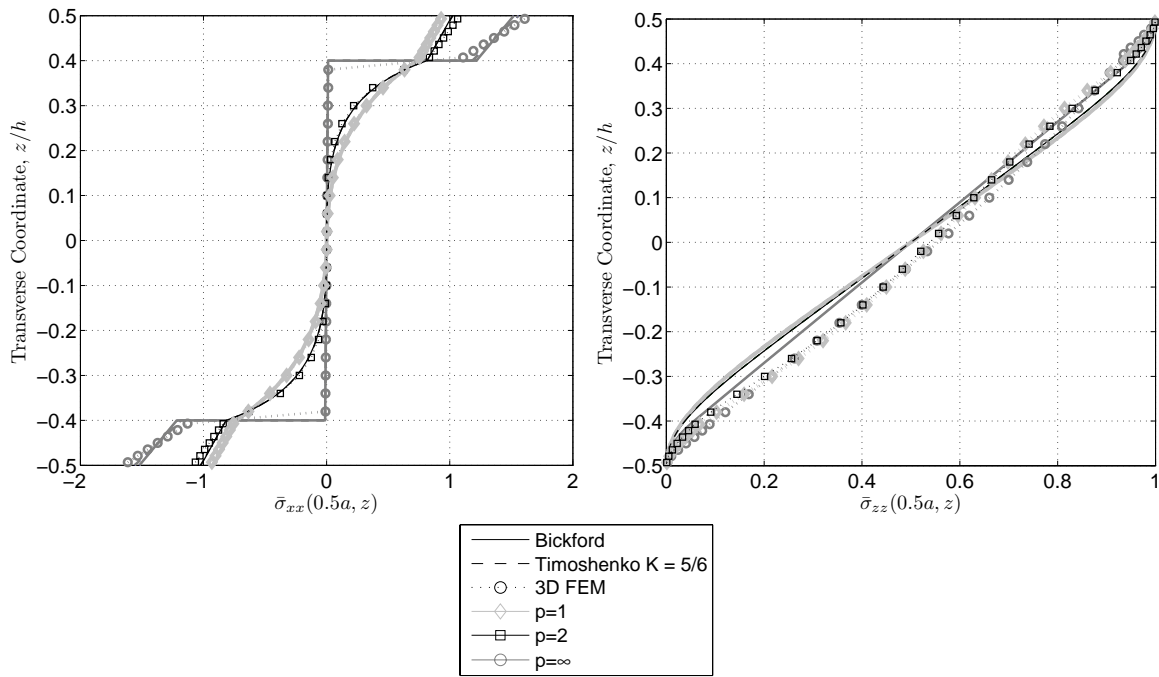


Figure 5.13. Longitudinal and transverse normal stress components at beam center for functionally graded sandwich beam with  $p = 1, 2, 4, \infty$ .

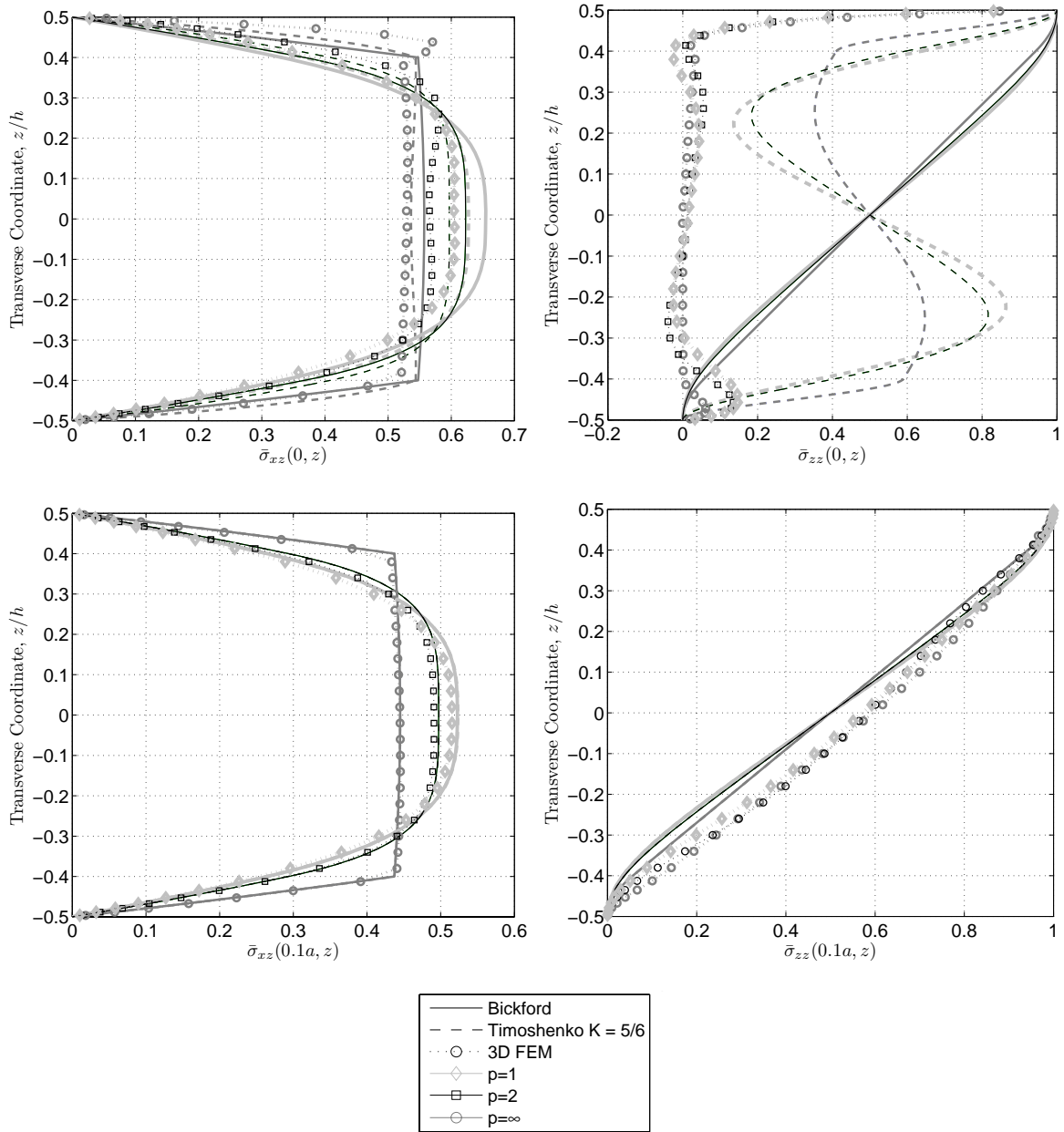


Figure 5.14. Transverse shear and transverse normal stress components at  $x = 0, 0.1a$  for functionally graded sandwich beam with length-to-thickness ratio of  $a/h = 20$ .

## 6 Refined Beam Theories

There are two philosophies for improving results from ESL beam theories. First, the order of approximation for the displacement fields may be increased. Both the in-plane displacement and the transverse deflection fields could take a higher-order polynomial approximation. Such an approach is typically referred to as a higher-order shear and normal deformable plate theory (HOSNDT). HOSNDTs have been used by many authors to analyze composite laminates and functionally graded materials. The higher-order shear and normal deformable theories as derived by Batra and Vidoli [151, 135] allows users the ability to specify the order of the assumed displacement field. Xiao *et al.* [152, 153] used the MLPG with radial basis functions to analyze both thick isotropic and thick composite plates. Their results showed that the HOSNDT produces excellent through-the-thickness longitudinal stress variations for thick laminates. Transverse normal and transverse shear stresses in some cross-ply laminates computed by the constitutive equations were accurate using as low as a fifth-order theory. These theories have also been used to study functionally graded materials. Qian, Batra, and Chen [154] used HOSNDT to study functionally graded plates comprised of aluminum and zirconia or aluminum and another ceramic such as SiC.

A central drawback of the HOSNDT is the inability of continuous functions to approximate discontinuities. It is this philosophy that spurred the development of the so called layer-wise theories [98]. In layer-wise theories, the displacement is piecewise linear through the thickness. A new displacement degree of freedom is introduced for each layer and continuity of tractions between each layer is imposed. While the methods are very accurate, even comparable to 3D elasticity theory [98, 155], the increased number of kinematic degrees-of-freedom (DOF) becomes a significant drawback when a laminate has many layers. The “zigzag” theories attempt to introduce the piecewise linear displacement while keeping the number of degrees-of-freedom constant with increasing number of layers. Because the slope of the displacements are discontinuous, the strains need not be continuous through the thick-

ness allowing the stresses, if desired, to satisfy the traction continuity between adhesively bonded layers. Early work by Di Sciuva [156] and Murakami [157] suggested displacements that satisfied the interlaminar traction continuity. However, the Di Sciuva theory suffers from the inability to find physical significance in the computed shear stress. The area integral of shear stress does not equal the shear force applied.

Averill [158] modified Di Sciuva's theory by introducing a penalty term in the variational principle to enforce interlaminar shear continuity. However, the theory suffers in much the same way as Di Sciuva. Averill resolves the issue at the cost of variational consistency of the boundary conditions. Recently, Tessler, Di Sciuva, and Gherlone [136, 155] presented a variationally consistent refined zigzag theory in which interlaminar shear continuity was not enforced. However, the theory serves as a substantial improvement over the Timoshenko beam theory or the FSDT plate theory. Tessler, Di Sciuva, and Gherlone [155] compare transverse shear stresses from the constitutive relation with Pagano's elasticity solution [92]. Tessler, Di Sciuva, and Gherlone also obtained interlaminar stresses by integration of the equations of three dimensional elasticity and showed that they very accurately approximated the 3D elasticity solution [159].

In this chapter, cross-ply, laminated beams are analyzed by the SIHD method using the HOSNDT and Tessler's refined zigzag theory [155]. The interlaminar stresses are computed using the equilibrium integration technique and compared with a FE solution. The remainder of this Chapter is arranged as follows: The higher-order shear and normal deformable theory for laminated beams and the refined zigzag theory are presented in Sections 6.1 and 6.2 respectively with details provided for computing interlaminar stresses from the two theories. Two numerical examples are presented in Section 6.3. Finally, a brief conclusion is given.

## 6.1 Higher-Order Shear and Normal Deformable Theory for Beams

The development of the higher-order shear and normal deformable beam theory (HOSNDT) following the general approach of Batra and Vidoli [151] is reviewed. First, consider a beam with rectangular cross-section as shown in Fig. 6.1. Because the beam has small width ( $b \ll a$ ), the problem can be reduced to consider only the displacement field  $U$  and  $W$ . Begin by assuming a displacement field of the form,

$$\begin{aligned} U(x, z) &= \sum_{i=0}^{n_u} z^i u_i(x), \\ W(x, z) &= \sum_{i=0}^{n_w} z^i w_i(x), \end{aligned} \tag{6.1}$$

where  $U$  and  $W$  are the longitudinal displacement and the transverse deflection respectively, and where the domain is  $x \in [0, a]$  and  $z \in [-h/2, h/2]$ . Accordingly, the strains are

$$\begin{aligned} \epsilon_{xx} &= \frac{\partial U}{\partial x} = \sum_{i=0}^{n_u} z^i u_{i,x}, \\ \epsilon_{zz} &= \frac{\partial W}{\partial z} = \sum_{i=0}^{n_w} (i) z^{i-1} w_i, \\ \gamma_{xz} &= \frac{\partial U}{\partial z} + \frac{\partial W}{\partial x} = \sum_{i=0}^{n_u} (i) z^{i-1} u_i + \sum_{i=0}^{n_w} z^i w_{i,x}. \end{aligned} \tag{6.2}$$

Note that  $(i)z^{i-1}$  should be zero for all  $z$  when  $i = 0$ ; however, to avoid further complication by defining these in a piecewise fashion, the inconsistency is noted textually.

The constitutive law is reduced assuming plane stress in the  $y$  direction. For this HOSNDT each lamina is assumed to experience plane stress ( $b \ll a$ ) with stress components



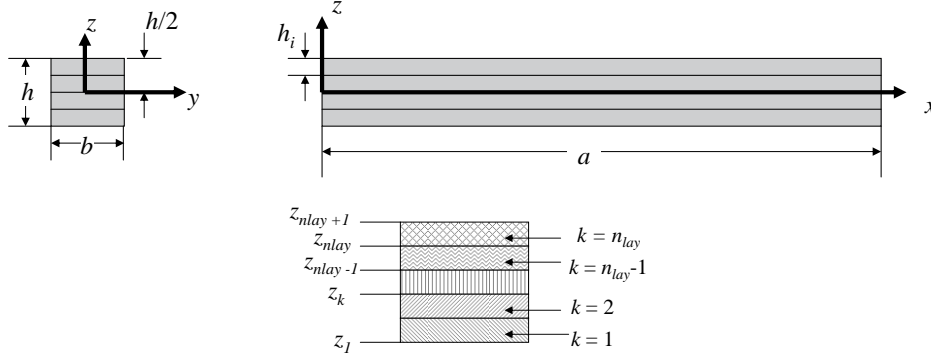


Figure 6.1. Definition of beam geometry and coordinate system.

$\sigma_{yy} = \sigma_{xy} = \sigma_{yz} = 0$ . Accordingly, the reduced constitutive relation is given by:

$$\begin{aligned}\sigma_{xx} &= \bar{Q}_{11}^{(k)} \epsilon_{xx} + \bar{Q}_{13}^{(k)} \epsilon_{zz}, \\ \sigma_{zz} &= \bar{Q}_{13}^{(k)} \epsilon_{xx} + \bar{Q}_{33}^{(k)} \epsilon_{zz} \\ \sigma_{xz} &= \bar{Q}_{55}^{(k)} \gamma_{xz}\end{aligned}\tag{6.3}$$

where  $\bar{Q}_{ij}^{(k)}$  is the plane stress reduced stiffness matrix for the  $k$ th lamina (See Fig. 6.1). To obtain  $\bar{Q}_{ij}^{(k)}$ , in terms of the lamina engineering constants, see Reddy [98]. Note, the stiffnesses were reduced for plane stress about the  $y$  axis and not the  $z$  axis in this sense.

The governing equations are derived using the principle of virtual work. The internal virtual work is written as:

$$\delta \mathcal{W}_{int} = \int_{\Omega} \sigma_{ij}^{(k)} \delta \epsilon_{ij}^{(k)} d\Omega\tag{6.4}$$

where a repeated index implies summation (where appropriate) and  $\Omega$  is the beam volume. Substituting Eqs. (6.2) and (6.3) into the internal virtual work and integrating by parts

where appropriate yields

$$\begin{aligned} \delta \mathcal{W}_{int} = b \int_0^a & \left[ - (T_{11ij} u_{j,xx} + T_{13ij} w_{j,x}) \delta u_i + (T_{31ij} u_{j,x} + T_{33ij} w_j) \delta w_i \right. \\ & \left. + (T_{51ij} u_j + T_{53ij} w_{j,x}) \delta u_i - (T_{61ij} u_{j,x} + T_{63ij} w_{j,xx}) \delta w_i \right] dx \\ & + b (T_{11ij} u_{j,x} + T_{13ij} w_j) \delta u_j \Big|_0^a + b (T_{61ij} u_j + T_{63ij} w_{j,x}) \delta w_i \Big|_0^a, \end{aligned} \quad (6.5)$$

where

$$\begin{aligned} T_{11ij} &= \sum_{k=1}^{n_{lay}} \bar{Q}_{11}^{(k)} \left[ \frac{z_{k+1}^{i+j+1} - z_k^{i+j+1}}{i+j+1} \right], & T_{13ij} &= \sum_{k=1}^{n_{lay}} \bar{Q}_{13}^{(k)}(j) \left[ \frac{z_{k+1}^{i+j-1} - z_k^{i+j-1}}{i+j} \right], \\ T_{31ij} &= \sum_{k=1}^{n_{lay}} \bar{Q}_{13}^{(k)}(i) \left[ \frac{z_{k+1}^{i+j} - z_k^{i+j}}{i+j} \right], & T_{33ij} &= \sum_{k=1}^{n_{lay}} \bar{Q}_{33}^{(k)}(ij) \left[ \frac{z_{k+1}^{i+j-1} - z_k^{i+j-1}}{i+j-1} \right], \\ T_{51ij} &= \sum_{k=1}^{n_{lay}} \bar{Q}_{55}^{(k)}(ij) \left[ \frac{z_{k+1}^{i+j-1} - z_k^{i+j-1}}{i+j-1} \right], & T_{53ij} &= \sum_{k=1}^{n_{lay}} \bar{Q}_{55}^{(k)}(i) \left[ \frac{z_{k+1}^{i+j} - z_k^{i+j}}{i+j} \right], \\ T_{61ij} &= \sum_{k=1}^{n_{lay}} \bar{Q}_{55}^{(k)}(j) \left[ \frac{z_{k+1}^{i+j} - z_k^{i+j}}{i+j} \right], & T_{63ij} &= \sum_{k=1}^{n_{lay}} \bar{Q}_{55}^{(k)} \left[ \frac{z_{k+1}^{i+j+1} - z_k^{i+j+1}}{i+j+1} \right], \end{aligned}$$

$n_{lay}$  is the total number of composite layers, and repeated index of  $i$  and  $j$  implies summation over the terms in that index. For  $T_{11ij}$ ,  $T_{13ij}$ ,  $T_{51ij}$ , and  $T_{53ij}$ ,  $i = 0, 1, 2, \dots, n_u$ ; for  $T_{31ij}$ ,  $T_{33ij}$ ,  $T_{61ij}$ ,  $T_{63ij}$ ,  $i = 0, 1, 2, \dots, n_w$ ; for  $T_{11ij}$ ,  $T_{31ij}$ ,  $T_{51ij}$ , and  $T_{61ij}$ ,  $j = 0, 1, 2, \dots, n_u$ ; for  $T_{13ij}$ ,  $T_{33ij}$ ,  $T_{53ij}$ , and  $T_{63ij}$ ,  $j = 0, 1, 2, \dots, n_w$ . Also, note that if a zero-denominator is encountered in any  $T_{ijkl}$ , these terms are set to zero. The zero-denominator only results from differentiation of a  $z^i$  when  $i = 0$ . Therefore, these terms are zero and no denominator is computed.

The external virtual work for a beam under the simply-supported condition with trans-

verse pressure loading  $q(x)$  applied on the top surface of the beam ( $z = h/2$ ) has the form:

$$\delta W_{ext} = \int_0^a q(x) \delta W(x, h/2) dx = \int_0^a -q(x) \sum_{i=0}^{n_w} (h/2)^i \delta w_i dx$$

The variational statement,

$$\begin{aligned} b \int_0^a \left[ -(-T_{11ij} u_{j,xx} - T_{13ij} w_{j,x} + T_{51ij} u_j + T_{53ij} w_{j,x}) \delta u_i \right. \\ \left. - (+T_{31ij} u_j + T_{33ij} w_j - T_{61ij} u_{j,x} - T_{63ij} w_{j,xx} + q(x)(h/2)^i) \delta w_i \right] dx \\ - b (T_{11ij} u_{j,x} + T_{13ij} w_j) \delta u_i \Big|_0^a - b (T_{61ij} u_j + T_{63ij} w_{j,x}) \delta w_i \Big|_0^a = 0, \quad (6.6) \end{aligned}$$

governs equilibrium and boundary conditions. Because the variations,  $\delta u_i$  and  $\delta w_i$ , are arbitrary the BVP may be written by the following Euler equations of equilibrium:

$$\delta u_i : \quad T_{11ij} u_{j,xx} + T_{13ij} w_{j,x} - T_{51ij} u_j - T_{53ij} w_{j,x} = 0 \quad (6.7)$$

$$\delta w_i : \quad -T_{31ij} u_{j,x} - T_{33ij} w_j + T_{61ij} u_{j,x} + T_{63ij} w_{j,xx} = q(x)(h/2)^i \quad (6.8)$$

For the simply support condition, the kinematics require  $W(0, z) = 0$  and  $W(a, z) = 0$ . This is imposed by constraining all  $w_i$  at the edges. At the edge  $x = 0$ , a point constraint is applied to the  $U$  degree of freedom ( $U(0, 0) = 0$ ). This is satisfied by setting  $u_i(0) = 0$  for  $i = 0, 2, 4, \dots$ . No constraints on the  $u_i$  for  $i = 1, 3, 5, \dots$  were imposed. Thus the complete

set of essential and natural boundary conditions used for the analysis are:

$$\begin{aligned}
w_i(0) &= 0 \quad (i = 0, 1, 2, \dots, n_w) \\
u_i(0) &= 0 \quad (i = 0, 2, 4, \dots) \\
(T_{11ij}u_{j,x} + T_{13ij}w_j) \Big|_{x=0} &= 0 \quad (i = 1, 3, 5, \dots) \\
w_i(a) &= 0 \quad (i = 0, 1, 2, \dots, n_w) \\
(T_{11ij}u_{j,x} + T_{13ij}w_j) \Big|_{x=a} &= 0 \quad (i = 0, 1, 2, \dots, n_u)
\end{aligned} \tag{6.9}$$

where repeated index implies summation over all elements in that index.

Note that by selecting the order of polynomial expressions for  $U$  and  $W$ ,  $n_u$  and  $n_w$  respectively, the governing equations and boundary conditions are given by Eqs. (6.8) and (6.9). The BVP may be solved using the SIHD method.

The interlaminar stresses can be found by integrating the equilibrium equations of 3D elasticity through the thickness of the  $k$ th lamina layer ( $z_k \leq z \leq z_{k+1}$ ). First, the transverse shear stresses are considered. Substituting the Hooke's law and strain-displacement relations into Eq. (2.14), the transverse shear stress,  $\sigma_{xz}^{(k)}$ , is expressed by:

$$\sigma_{xz}^{(k)} = - \int_{z_k}^z \left[ \bar{Q}_{11}^{(k)} \sum_{i=0}^{n_u} (z^i u_{i,xx}) + \bar{Q}_{13}^{(k)} \sum_{i=1}^{n_w} (i z^{i-1} w_{i,x}) \right] dz + G^{(k)} \tag{6.10}$$

Performing the integration through the layer thickness, this is expressed by:

$$\sigma_{xz}^{(k)} = - \left[ \bar{Q}_{11}^{(k)} \sum_{i=0}^{n_u} \left( \frac{z^{i+1} - z_k^{i+1}}{i+1} u_{i,xx} \right) + \bar{Q}_{13}^{(k)} \sum_{i=1}^{n_w} ((z^i - z_k^i) w_{i,x}) \right] + \sigma_{xz}^{(k)}(x, z_k) \tag{6.11}$$

Differentiating with respect to  $x$  and substituting into Eq. (2.16) yields:

$$\sigma_{zz}^{(k)} = - \int_{z_k}^z \left[ -\bar{Q}_{11} \sum_{i=0}^{n_u} \left( \frac{z^{i+1} - z_k^{i+1}}{i+1} u_{i,xxx} \right) - \bar{Q}_{13} \sum_{i=1}^{n_w} \left( (z^i - z_k^i) w_{i,xx} \right) + \sigma_{xz,x}^{(k)}(x, z_k) \right] dz + H^{(k)} \quad (6.12)$$

Evaluating the integration on a layer-by-layer basis through the lamina thickness yields:

$$\begin{aligned} \sigma_{zz}^{(k)} = & \bar{Q}_{11} \sum_{i=0}^{n_u} \left[ \left( \frac{z^{i+2} - z_k^{i+2}}{(i+1)(i+2)} - \frac{z_k^{i+1}(z - z_k)}{i+1} \right) u_{i,xxx} \right] \\ & + \bar{Q}_{13} \sum_{i=1}^{n_w} \left[ \left( \frac{z^{i+1} - z_k^{i+1}}{i+1} - z_k^i(z - z_k) \right) w_{i,xx} \right] - \sigma_{xz}^{(k)}(x, z_k)(z - z_k) + \sigma_{zz}^{(k)}(x, z_k) \end{aligned} \quad (6.13)$$

Thus the transverse shear and transverse normal stresses can be found from the displacement variables. The terms  $\sigma_{xz}(x, z_k)$ ,  $\sigma_{xz,x}(x, z_k)$ , and  $\sigma_{zz}(x, z_k)$  are determined by imposing continuity of the tractions in a layer-by-layer fashion, starting from the bottom free surface.

## 6.2 Refined Zigzag Theory for Beam Analysis

The development of the refined zigzag theory for beam analysis, following the approach of Tessler, Di Sciuva, and Gherlone [155], is reviewed below. Consider the same beam geometry shown in Fig. 6.1. Begin by assuming a displacement field of the form,

$$\begin{aligned} U(x, z) &= u_0(x) + z\theta(x) + \phi^{(k)}(z)\psi(x), \\ W(x, z) &= w_0(x), \end{aligned} \quad (6.14)$$

where  $U$  and  $W$  are the longitudinal displacement and the transverse deflections respectively,  $\phi^{(k)}(z)$  is a piecewise linear function of the thickness coordinate, and the domain is  $x \in [0, a]$

and  $z \in [-h/2, h/2]$ . Accordingly, the strains are

$$\begin{aligned}\epsilon_{xx}(x, z) &= u_{0,x}(x) + z\theta_{,x}(x) + \phi^{(k)}(z)\psi_{,x}(x), \\ \gamma_{xz}(x, z) &= \theta(x) + \beta^{(k)}(z)\psi(x) + w_{0,x}(x),\end{aligned}\tag{6.15}$$

where  $\beta^{(k)} = \phi_{,z}^{(k)}$ . Note that  $\beta^{(k)}$  is a constant within a given layer.

The function,  $\phi^{(k)}$  is set to zero on the bottom and top surfaces of the beam and is  $C^0$  continuous at the interfaces. Therefore, the distribution over the  $k$ th lamina may be written as:

$$\phi^{(k)}(z) = \beta^{(k)}(z - z_k) + \phi^{(k-1)}(z_k)\tag{6.16}$$

Note that  $\phi^{(k-1)}(z_k)$  implies evaluation at  $z_k$  and not multiplication. Thus determining  $\beta^{(k)}$ , fully prescribes the displacement field. Rather than prescribing traction continuity between layers, Tessler, Di Sciuva, and Gherlone [155] requires that the following equation holds:

$$\bar{Q}_{55}^{(k)}(1 + \beta^{(k)}) = \left[ \frac{1}{h} \int_{-h/2}^{h/2} \frac{dz}{\bar{Q}_{55}^{(k)}} \right]^{-1}\tag{6.17}$$

The assumption is made that each beam layer is in a state of plane stress in the  $z$  and  $y$  directions. Thus the bending stiffness,  $\bar{Q}_{11}^{(k)}$ , and shear stiffnesses,  $\bar{Q}_{55}^{(k)}$ , reduce to the elastic moduli,  $E_{xx}^{(k)}$  and  $G_{xz}^{(k)}$ , respectively. The governing equation and boundary conditions are derived from the variational principle (see Tessler, Di Sciuva, and Gherlone [155]). The governing equations are:

$$\begin{aligned}N_{xx,x} &= 0 \\ M_{xx,x} - V_x &= 0 \\ V_{x,x} + q &= 0 \\ M_{\phi,x} - V_\phi &= 0\end{aligned}\tag{6.18}$$

The kinematic variables are  $u_0$ ,  $\theta$ ,  $w$ , and  $\psi$ . The stress resultants are defined by:

$$\{N_{xx}, M_{xx}, M_\phi, V_x, V_\phi\} = \int_{-h/2}^{h/2} \{\sigma_{xx}^{(k)}, \sigma_{xx}^{(k)} z, \sigma_{xx}^{(k)} \phi^{(k)}(z), \sigma_{xz}^{(k)}, \sigma_{xz}^{(k)} \beta^{(k)}\} dz. \quad (6.19)$$

To impose the simply support condition in a similar manner to the HOSNDT formulation, the kinematic conditions require  $w_0(0) = 0$ ,  $w_0(a) = 0$ , and  $u_0(0) = 0$  with no constraints on  $u_0(a)$ ,  $\psi(0)$ ,  $\psi(a)$ ,  $\theta(0)$ , and  $\theta(a)$ . Thus the complete set of essential and natural boundary conditions are:

$$\begin{aligned} w_0(0) &= 0, & w_0(a) &= 0, \\ u_0(0) &= 0, & N_{xx}(a) &= 0, \\ M_{xx}(0) &= 0, & M_{xx}(a) &= 0, \\ V_x(0) &= 0, & V_x(a) &= 0, \\ M_\phi(0) &= 0, & M_\phi(a) &= 0. \end{aligned} \quad (6.20)$$

The SIHD method was used to approximately solve the BVP. It should be noted that by doing so provides all derivatives up to  $u_{0,xxx}$ ,  $\theta_{,xxx}$ , and  $\psi_{,xxx}$  so that  $\epsilon_{xx,xx}$  and its lower derivatives are known across the beam without post-processing.

The interlaminar stresses can be derived from integration of 3D elasticity equations in a similar fashion to the HOSNDT. The following relations for transverse shear and transverse normal stresses were obtained.

$$\begin{aligned} \sigma_{xz}^{(k)} &= -(z - z_k) [u_{0,xx} - \psi_{,xx} (\beta^{(k)} z_k + \phi^{(k-1)}(z_k))] + \frac{z^2 - z_k^2}{2} (\theta_{,xx} + \psi_{,xx} \beta^{(k)}) \\ &\quad + \sigma_{xz}^{(k)}(x, z_k) \end{aligned} \quad (6.21)$$

$$\begin{aligned} \sigma_{zz}^{(k)} = & \left( \frac{z^2 - z_k^2}{2} - z_k(z - z_k) \right) [u_{0,xxx} - \psi_{,xxx} (\beta^{(k)} z_k - \phi^{(k-1)}(z_k))] \\ & + \left( \frac{z^3 - z_k^3}{6} - \frac{z_k^2(z - z_k)}{2} \right) (\theta_{,xxx} + \psi_{,xxx}\beta^{(k)}) - \sigma_{xz,x}^{(k)}(x, z_k)(z - z_k) + \sigma_{zz}^{(k)}(x, z_k) \end{aligned} \quad (6.22)$$

The transverse shear and transverse normal stresses can be found from the displacement variables. The terms  $\sigma_{xz}(x, z_k)$ ,  $\sigma_{xz,x}(x, z_k)$ , and  $\sigma_{zz}(x, z_k)$  are determined from traction equilibrium between the layer boundaries.

### 6.3 Numerical solution of HOSNDT and Refined Zigzag Theory with the SIHD method

The three-layered,  $[0^\circ/90^\circ/0^\circ]$ , graphite/epoxy, laminated beam of Chapter 5 was revisited using the HOSNDT and the refined zigzag. This material configuration was referred to as Material A. The properties for this beam are given in Table 6.8. A second beam was taken with Material B, a fictitious lamina with extremely different shear moduli for  $G_{13}$  and  $G_{23}$ . The properties are given in Table 6.8. For each case the length-to-thickness ratio was  $a/h = 5$  where  $a$  and  $h$  are the length and thickness of the beam respectively.

**Table 6.8.** Material properties for a graphite/epoxy lamina (A) and a fictitious orthotropic lamina with extremely different shear moduli (B).

	A	B
$E_1$ [Msi/GPa]	24.9 / 172	24.9 / 172
$E_2$ [Msi/GPa]	1.00 / 6.89	1.00 / 6.89
$G_{12}, G_{13}$ [Msi / GPa]	0.50 / 3.45	14.5 / 100
$G_{23}$ [Msi / GPa]	0.20 / 1.38	0.145 / 1
$\nu_{12}$	0.25	0.25

#### 6.3.1 Material A

The converged mesh of eight-node, linear, reduced-integration, brick elements (C3D8R) used in Chapter 5 was used to approximate 3D elasticity for the beam.



An approximate solution to the HOSNDT and the refined zigzag beam theories was obtained using the SIHD method. The HOSNDT was solved using the SIHD method implemented in Fortran 90. The Sinc mesh size was set by specifying the Sinc span to be  $\alpha = 2.0$ . A total of 81 ( $N = 40$ ) Sinc points were used to obtain a converged solution. The zigzag theory was implemented in MATLAB using 201 ( $N = 100$ ) Sinc points. In this case the Sinc mesh size was also set by specifying the Sinc span to be  $\alpha = 2.0$ . In Fig. 6.2, the longitudinal and transverse normal stress components using the Bickford and Timoshenko beam theories, the HOSNDT with  $n_u = 5$  and 10 and  $n_w = 3$ , and the refined zigzag theory of Tessler, Di Sciuva, and Gherlone [155] were compared with the 3D FEM solution.

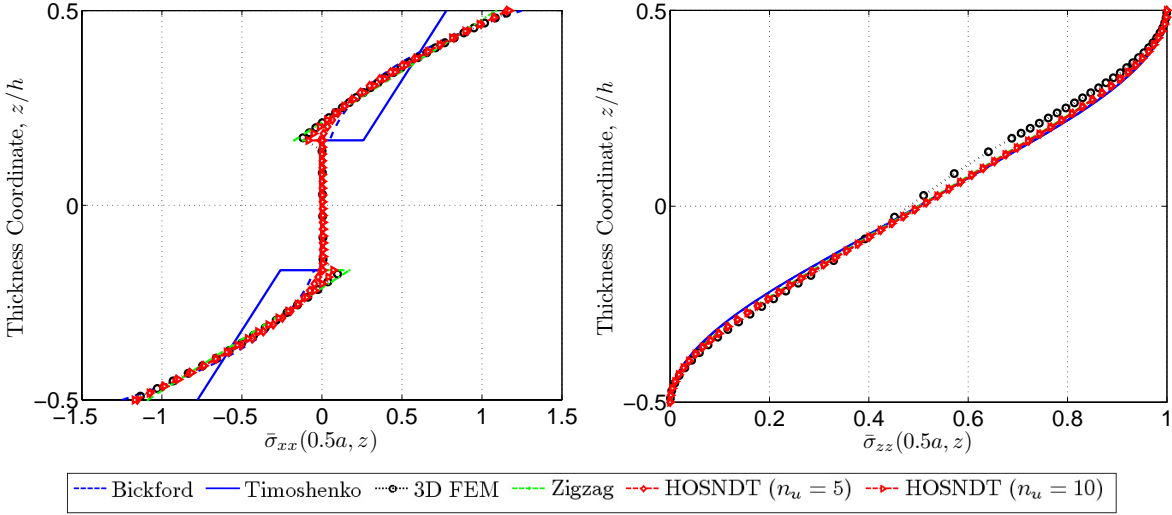


**Figure 6.2. Longitudinal and transverse normal stress components at  $x = 0.5$  for simply supported laminated beam with Material A.**

The transverse normal stress was very accurately approximated by each of the approaches and there is little benefit to the additional complexity of the HOSNDT or the zigzag theory. However, the benefit is apparent with the in-plane longitudinal stress. The Bickford theory performs very well at capturing the trend of the curve; however, at the material interface it is erroneous. The zigzag theory, while it predicts only linear through lamina distributions of in-plane stress, it matches very well with the FEA for the lamina interfacial stresses. The zigzag

theory is superior to the Timoshenko beam theory and performs better than the Bickford theory even though it lacks the ability to produce the curved through-the-lamina-thickness stress distribution present in this thick laminate.

For the HOSNDT, the increasing order of  $u$  displacement appears to push the interfacial longitudinal normal stress toward the FEA results; however, it is only with significant additional unknowns that similar accuracy as the zigzag theory is achieved.

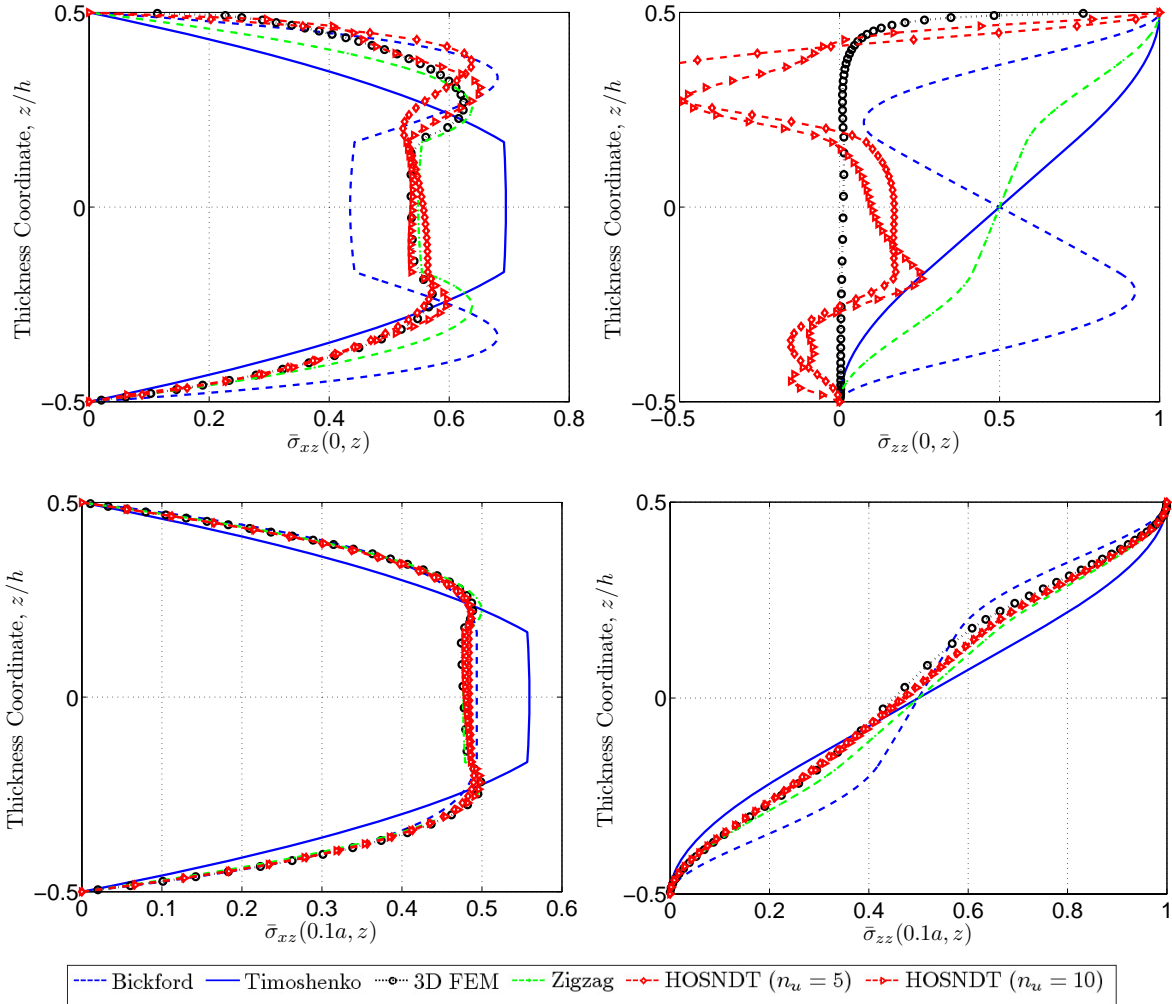


**Figure 6.3.** Transverse shear and normal stress components at  $x = 0, 0.1a$  for simply supported laminated beam with Material A.

If Fig. 6.3, the transverse shear and normal stresses are plotted at the end and near the end of the beam. The refined theories appear to improve substantially the transverse

shear stress at the edge of the beam. The interfacial stress is approximated very well by the HOSNDTs and the zigzag theory; however, the zigzag theory is unable to capture the stress asymmetry about the mid-plane (higher transverse normal stress in the top lamina). The HOSNDTs appear to account for the stress asymmetry quite well; though neither  $n_u = 5$  nor  $n_u = 10$  ( $n_w = 3$  for both) is sufficient to exactly capture the stress distribution.

While the refined theories do a better job particularly for the transverse shear stress at the edge, none of the present theories capture the transverse normal stress at the boundary very well. The HOSNDTs improve upon this stress component significantly; however, they appear to oscillate about the FEA solution. Further increasing the order of the in-plane and transverse deflection profiles do not significantly improve the results. The HOSNDT suffers from the so called Gibbs phenomenon. Continuous functions are never able to approximate discontinuities very well.

At  $0.1a$ , the refined theories each perform well at capturing both the transverse normal and transverse shear stresses. The refined theories are a substantial improvement over the ESL theories for these stresses.

If the normal deformability is neglected (i.e. taking  $n_w = 0$ ), HOSNDT produces results very similar to the zigzag theory. It should be noted that the present problem is quite a difficult one in that the loading is uniform. The edge experiences a sudden drop in applied load. Even the 3D FEM solution is not plausible because the boundary conditions are not exactly satisfied. The stress should equal the applied load on the top surface and the derivative of the transverse normal stress with respect to  $z$  should be zero (by 3D equilibrium); however, neither of these are exactly satisfied by the FEA solution.

### 6.3.2 Material B

The fictitious lamina (Material B) was chosen to demonstrate a key shortcoming of using ESL theories to calculate interlaminar stresses. Namely, computation of interlaminar stresses

**Table 6.9. L2 norm of displacements between fine and coarse mesh solution for laminated beam with material configuration B.**

# Elements Coarse	# Elements Fine	$e_{u_1}$	$e_{u_3}$
8,400	33,600	0.16 %	0.14 %

from the 3D equilibrium equations of elasticity relies on the accuracy of the in-plane derivatives of in-plane stresses. However, there are some lamina for which the material properties are so discontinuous that obtaining accurate derivatives of in-plane stresses is not possible. The present example clearly demonstrates the refined zigzag theories superiority to the Timoshenko beam theory and the HOSNDT.

Analysis was performed using SIHD with the Timoshenko beam theory, the refined zigzag theory, and the HOSNDT with  $n_u = 5, 10, \text{ and } 15$  and with  $n_w = 3$ . The Timoshenko beam theory and the zigzag theory were implemented in MATLAB while the HOSNDT was implemented in Fortran 90. The results were compared with a 2D plane-stress FEA. The simply support boundary condition imposed for the FEA was similar to that in the 3D FEA. The simply-supported boundary condition imposed for the FEA is expressed as follows:

$$\begin{aligned} \Omega &= \{(x_1, x_3) | 0 \leq x_1 \leq a, -h/2 \leq x_3 \leq h/2\} \\ u_3 &= 0, \quad \{(x_1, x_3) \in \Omega | x_1 = 0 \cup x_1 = a\} \\ u_1 &= 0, \quad \{(x_1, x_3) \in \Omega | x_1 = 0 \cap x_3 = 0\} \end{aligned} \quad (6.23)$$

The L2 norm of the difference in  $u_1$  and  $u_3$  was computed by Eq. (4.7) where the  $w_{exact}$  was the displacement variable in the fine mesh and  $w_{approx}$  was the displacement variable in the coarse mesh. The L2 norm of the converged mesh are summarized in Table 6.9. The converged mesh size had a total of 200 elements along the length. The elements were biased toward the ends with a bias ratio of 50. Through the thickness of the top and bottom layer 36 elements were used which were biased toward the top and bottom respectively. Though the thickness of the middle lamina, 12 elements were used in a uniformly distributed manner.

The longitudinal and transverse normal stress components for material configuration B were plotted in Fig. 6.4. The bending stresses are very accurately predicted by the zigzag theory, nearly indistinguishable from the FEM results. Note that the Timoshenko beam theory fails to estimate the bending stresses. The Timoshenko beam theory prediction for bending stress at the interface is wrong by about 175 % and about 40 % at the top and bottom surface. The HOSNDT with using ten monomials approximating the in-plane displacement performs somewhat better; however, at a substantial computational cost. With fifteen monomials, the HOSNDT results approach the accuracy of the zigzag theory.

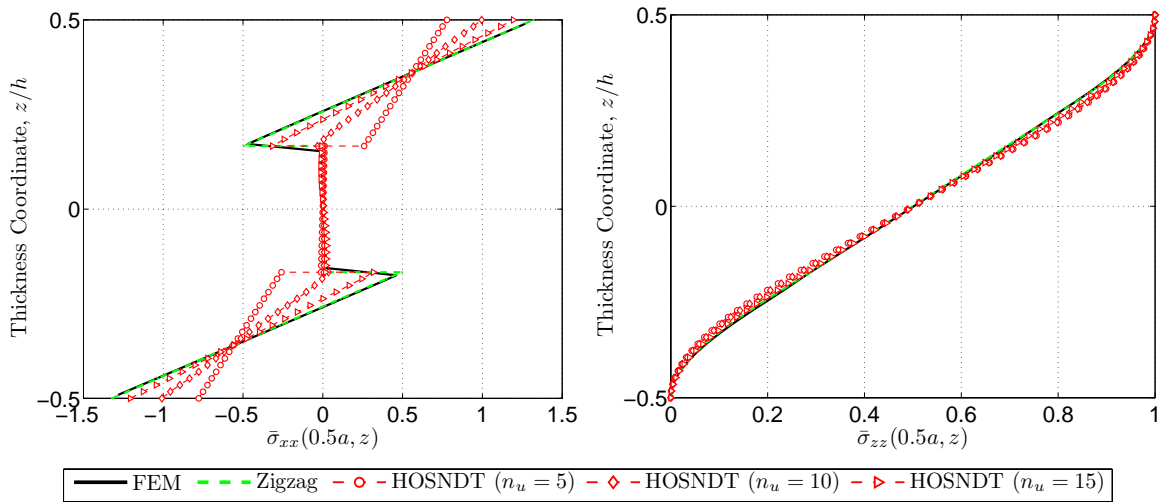


**Figure 6.4. Longitudinal and transverse normal stress components at  $x = 0.5$  for simply supported laminated beam with Material B.**

The transverse shear and normal stresses were plotted in Fig. 6.5 at the edge of the beam and one-tenth of the length of the beam. The transverse shear stress is also very well approximated using the refined theories; however, the zigzag theories advantage is somewhat less convincing. While the interfacial shear stress is accurately approximated with the zigzag theory, the asymmetry of shear through the thickness cannot be captured without normal deformability. However, including normal deformability alone does not grant accuracy for these stress components. Note that with fifteen monomials approximating the  $U$  displace-

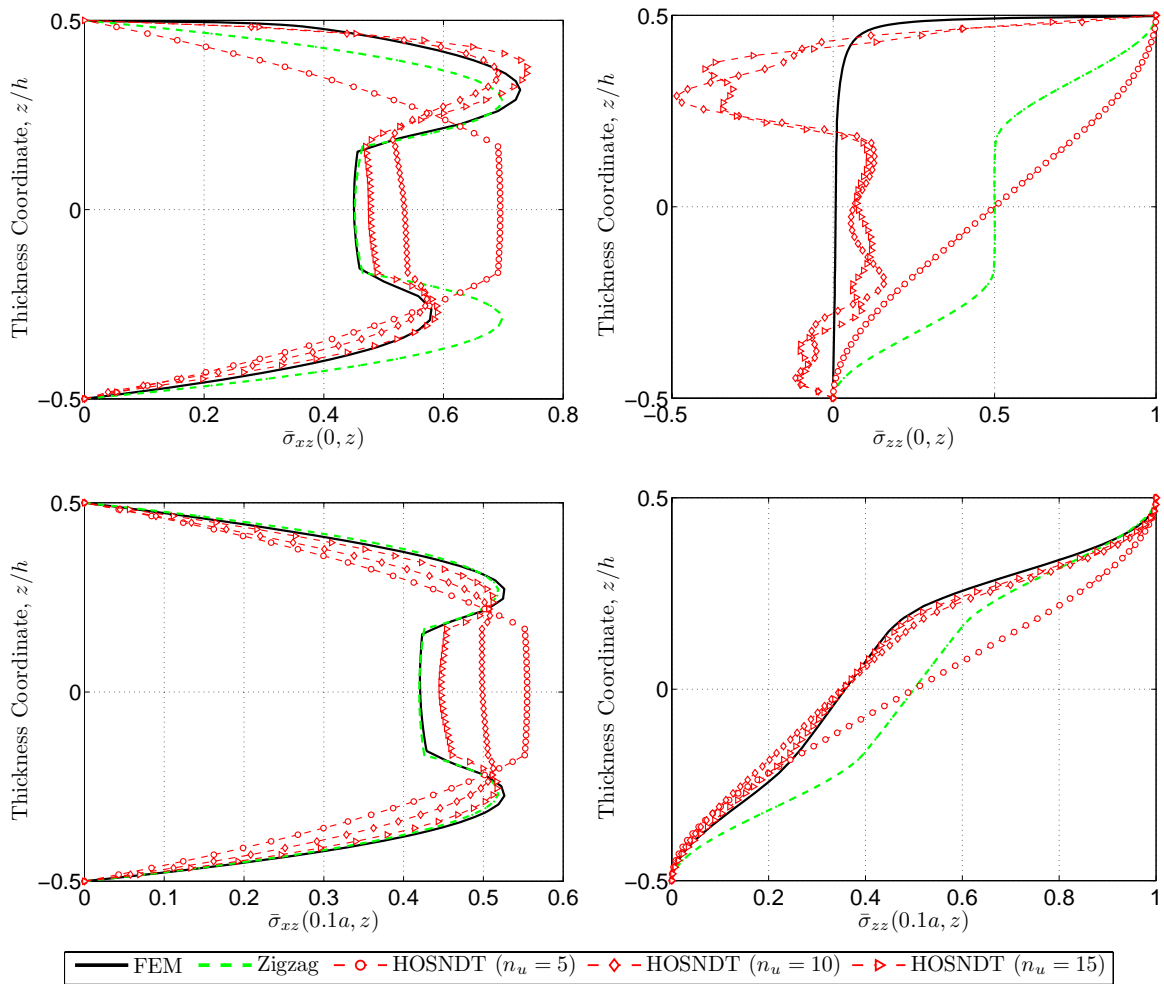


Figure 6.5. Transverse shear and normal stress components at  $x = 0, 0.1a$  for simply supported laminated beam with Material B.

ment, the transverse shear component at the lamina interfaces is still not as accurately computed using the HOSNDT than with the zigzag theory - a piecewise discontinuous linear theory.

The transverse normal stress component is again inaccurate at the boundary. While introducing normal deformability is necessary to very accurately capture the stress at one-tenth of the length of the beam, the transverse normal stress at the edge is not captured very well at all by the theories studied.

## 6.4 Summary and Conclusions

In this Chapter, computation of transverse shear and transverse normal stresses or interlaminar stresses from refined beam theories was performed using the SIHD method. The HOSNDT and the refined zigzag theory were introduced. Integration of the equilibrium equations of 3D elasticity was performed to obtain the transverse normal and transverse shear stress components for each theory.

The aims of this Chapter were to determine if the erroneous nature of interlaminar stresses computed by the Timoshenko and Bickford beam theories could be improved by refining the assumed displacement field. The results illustrate that the SIHD method can be beneficial for this type of problem because the higher-order derivatives of the strain needed to perform through the thickness integration are accurately obtained without post processing. Two material configurations were considered. First, comparison was made between the refined theories using SIHD with the results with the Timoshenko and Bickford beam theories. A second material configuration was examined which demonstrated the serious limitations of the traditional ESL theories when the shear moduli of lamina vary substantially.

The HOSNDTs were used to illustrate the effects of increasing the order of the assumed displacement field and including the transverse normal strain. However, the present implementation of the HOSNDT does not allow for discontinuities of the shear strains through the

thickness. The numerical results provide very compelling evidence that the refined zigzag theory provides an excellent way to introduce a discontinuous displacement field without significant computational costs, and its accuracy benefits substantially. The present results have shown that the refined zigzag theory provides excellent accuracy of the interfacial bending and transverse shear stresses. While the transverse normal stress was not improved substantially and cannot be accurately predicted without allowing a nonzero transverse normal strain component, the refined zigzag theory should be used over simple increasing the order of the in-plane displacement field.



## 7 Integrated Local Petrov-Galerkin Sinc Method

There are some difficulties in applying the SIHD method to 2D problems. These problems were discussed in Chapter 4. For the midpoint method of applying the boundary conditions, there is some arbitrariness in the selection of where to apply the additional conditions. The midpoint was arbitrarily chosen and derivatives of the boundary conditions were applied. The pure collocation approach does not have this arbitrary selection; however, explicitly imposing both natural and essential boundary conditions can become difficult, especially when the approach is mapped onto a non-rectangular domain.

Several authors have shown that weak form based approaches are more accurate than using the strong form of the governing equation through collocation [160, 119, 123, 124, 161]. A recent review of meshless methods was provided by Nguyen *et al.* [162]. They note that meshless methods are typically implemented either by the collocation method or by Petrov- or Bubnov-Galerkin methods. The MLPG method serves as the basis for domain decomposition in many meshless methods [163]. Atluri and Shen [161] compared the accuracy of the MLPG method implemented with various weight functions. One of those weight functions was the Kronecker Delta making the approach the collocation scheme. However, the results indicated that the local weak formulation performed better than the strong formulation. Batra and Zhang [160] compare collocation and the MLPG method implemented with the symmetric smoothed particle hydrodynamics (SSPH) basis function for 2D static structural mechanics problems. Their results indicate that the MLPG method provides greater accuracy than the collocation method with the SSPH basis function. The work of Mai-Duy and Tran-Cong related to the Direct or Differentiated and Indirect or Integrated Radial Basis Function Networks (DRBFN and IRBFN respectively) was implemented in the collocation method and also with the weak form of the governing equation in a Galerkin formulation [119, 123, 124]. Their results indicated that the Galerkin procedure exhibited greater accuracy and higher rates of convergence than the collocation scheme.

It is for these reasons that a novel weak-form based approach was developed which may easily handle 2D problems on a non-rectangular domain. In this Chapter the Integrated Local Petrov-Galerkin Sinc method (ILPGSM) is developed and compared with the SIHD method for analysis of both 1D and 2D static structural mechanics problems.

## 7.1 Basis Functions

The ILPGSM implements the integrated Sinc basis function as presented in Chapter 3. However, because the weak form of a second-order BVP involves only first-order derivatives, one may implement the basis function by approximating the first derivative by a Sinc series and integrating to find the function itself. In this case, the basis function would be implemented in an identical fashion to that given in Section 3.3.1. Implementation of the basis function in this manner is referred to as the “Sinc-1” basis function for this dissertation.

As it was shown in the preliminary study of Sinc interpolation (Section 3.2), the Sinc series may be compromised by large oscillations between Sinc points if the theoretical mesh size is not taken. There were two approaches considered to improving upon using the Sinc interpolation in the first derivative. First, it was noted that the integrated expression [Eq. (3.12)] varies smoothly between points even when the theoretical mesh size is not taken. Thus by approximating the second-order derivative by a Sinc series, the oscillations are not introduced into the weak form. This approach would implement a basis function in an identical fashion to that given in Section 3.3.2. Implementation of the basis function in this manner is referred to as the “Sinc-2” basis function in this dissertation.

Finally, it was noted that the oscillations occur between the Sinc points. Therefore it was proposed that between these points, both the first derivative and the function are linearly interpolated. This method is suggested because evaluating the sine-integral function could be a very expensive computation. However, the sine-integral evaluation cost was substantially reduced by implementing the algorithm of MacLeod [146]. Furthermore, because the Sinc in-

terpolation is not used, but rather linear interpolation is used, the first-order derivatives may be approximated without introducing oscillations. Secondly, using this approach allows the Sinc integration weights  $k_{ij}$  as defined in Eq. (4.4) to be used as opposed to the  $T_2$  functions defined in Eq. (3.17), thus potentially saving computational time. For a 1D problem, the linear interpolation may be accomplished by evaluating Eq. (3.15) only at each Sinc point. For 2D, Eq. (3.26) is evaluated only at each Sinc point. Between the Sinc points, both the first derivatives and the function are linearly interpolated from that at the surrounding Sinc points. This may be performed by:

$$f(\mathbf{X}) = \sum_{i=1}^{n_e} N_i(\mathbf{X})f(\mathbf{X}_i) \quad (7.1)$$

where  $\mathbf{X}$  is the coordinates of the point of interest,  $n_e$  is the number of surrounding Sinc points to be interpolated between ( $n_e = 2$  for 1D,  $n_e = 4$  for 2D),  $N_i(\mathbf{X})$  are the Lagrange interpolation polynomials evaluated at the point of interest, and  $f(\mathbf{X}_i)$  are the function values evaluated at the surrounding Sinc points. This basis function was referred to as the “linear” basis function.

## 7.2 Formulation of 2D Elasto-Static Problems

To develop the ILPGSM, consider an elastic panel in a state of plane-stress on the domain  $\Omega$  whose boundary is  $\Gamma$  (see Fig. 7.1). To develop the governing equations, the principle of virtual work is employed. The internal and external virtual work are given by:

$$\delta W_{int} = \int_{\Omega} (\sigma_{11}\delta\epsilon_{11} + \sigma_{12}\delta\gamma_{12} + \sigma_{22}\delta\epsilon_{12}) d\Omega, \quad (7.2)$$

$$\delta W_{ext} = \int_{\Gamma} (t_1\delta u_1 + t_2\delta u_2) d\Gamma, \quad (7.3)$$

where  $u_i$  is the displacement vector,  $\sigma_{ij}$  is the stress tensor,  $t_i$  is a vector representing the traction applied to the edge  $\Gamma$  ( $i, j = 1, 2$ ). Note that  $\Gamma = \{\mathbf{X} : \mathbf{X} \in \Gamma_u \cup \Gamma_t\}$  where  $\Gamma_u$  and  $\Gamma_t$  are portions of the boundary on which an applied displacement and traction are imposed respectively.

The constitutive relation for linearly-elastic isotropic material in the plane-stress condition is given by:

$$\begin{Bmatrix} \sigma_{11} \\ \sigma_{22} \\ \sigma_{12} \end{Bmatrix} = \begin{bmatrix} \bar{Q}_{11} & \bar{Q}_{12} & 0 \\ \bar{Q}_{12} & \bar{Q}_{22} & 0 \\ 0 & 0 & \bar{Q}_{66} \end{bmatrix} \begin{Bmatrix} \epsilon_{11} \\ \epsilon_{22} \\ \gamma_{12} \end{Bmatrix} \quad (7.4)$$

Where the plane-stress reduced stiffnesses are defined such that  $\bar{Q}_{11} = \bar{Q}_{22} = E/(1 - \nu^2)$ ,  $\bar{Q}_{12} = \nu\bar{Q}_{11}$ , and  $\bar{Q}_{66} = G$ . The infinitesimal strains are defined by:

$$\{\epsilon_{11}, \epsilon_{22}, \gamma_{12}\}^T = \{u_{1,1}, u_{2,2}, u_{1,2} + u_{2,1}\}^T \quad (7.5)$$

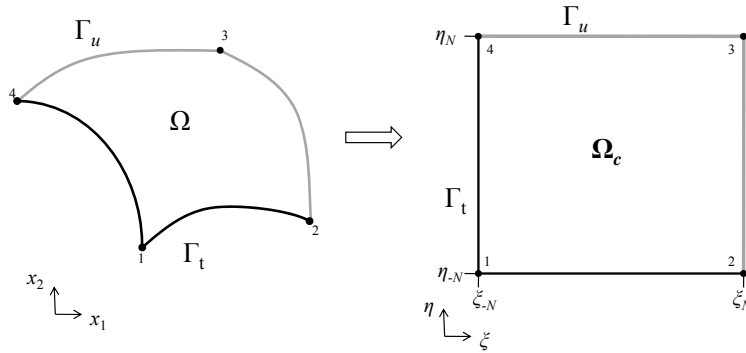


**Figure 7.1.** Diagram of physical and computational domain for the ILPGSM.

The balance of internal and external virtual work, expressed in terms of displacements

and their variations, is written as:

$$\begin{aligned} \int_{\Omega} (\bar{Q}_{11}u_{1,1} + \bar{Q}_{12}u_{2,2})\delta u_{1,1} + \bar{Q}_{66}(u_{1,2} + u_{2,1})\delta u_{1,2} \\ + (\bar{Q}_{22}u_{2,2} + \bar{Q}_{12}u_{1,1})\delta u_{2,2} + \bar{Q}_{66}(u_{1,2} + u_{2,1})\delta u_{2,1}d\Omega = \int_{\Gamma} t_1\delta u_1 + t_2\delta u_2d\Gamma \end{aligned} \quad (7.6)$$

In the fashion of the MLPG method, the variations of displacements are independently selected to be a weight function with a compact support,  $W^I(\mathbf{X})$ , where  $I$  identifies the  $I$ th support domain. Therefore, the equilibrium equation [Eq. (7.6)] becomes a system of equations, each with the following form:

$$\begin{aligned} \int_{\Omega_I} (\bar{Q}_{11}u_{1,1} + \bar{Q}_{12}u_{2,2})W_{,1}^I(\mathbf{X}) + \bar{Q}_{66}(u_{1,2} + u_{2,1})W_{,2}^I(\mathbf{X})d\Omega_I = \int_{\Gamma_I} t_1W^I(\mathbf{X})d\Gamma_I \\ \int_{\Omega_I} (\bar{Q}_{22}u_{2,2} + \bar{Q}_{12}u_{1,1})W_{,2}^I(\mathbf{X}) + \bar{Q}_{66}(u_{1,2} + u_{2,1})W_{,1}^I(\mathbf{X})d\Omega_I = \int_{\Gamma_I} t_2W^I(\mathbf{X})d\Gamma_I \end{aligned} \quad (7.7)$$

where  $\Omega_I$  is the support of weight function  $W^I$ ,  $\Gamma_I = \{\mathbf{X} : \mathbf{X} \in \Omega_I \cap \Gamma\}$ , and  $u_i(\mathbf{X})$  and their derivatives are approximated by the previously introduced basis functions. The weight functions are selected such that  $W^I \in H^1$  and  $W^I(\mathbf{X}) > 0$  for  $\mathbf{X} \in \Omega_I$ , and such that  $W^I(\mathbf{X}) = 0$  for  $\mathbf{X} \notin \Omega_I$ .

### 7.2.1 Domain transformation

The physical domain is transformed to a rectangular computational domain defined by  $\Omega_c = \{\mathbf{X}_c = (\xi, \eta) : (\xi_{-N} \leq \xi \leq \xi_N) \cap (\eta_{-N} \leq \eta \leq \eta_N)\}$  where  $(\xi_i, \eta_j)$  are Sinc points, distributed by the DE transformation. For a mesh size  $h$ , the Sinc points correspond to  $i, j = \{-N, -N + 1, \dots, -1, 0, 1, \dots, N - 1, N\}$  defined by,  $\xi_i = \psi(ih)$  and  $\eta_j = \psi(jh)$  [See Eq. (3.5)]. There are a total of  $n = 2N + 1$  Sinc points along each axis. The domain transformation between the physical and computational domain is performed using a mapping of the form  $x_1 = f_1(\xi, \eta)$ ,  $x_2 = f_2(\xi, \eta)$ . Lagrange interpolation polynomials were used to

perform the geometric transformation in a similar manner to the isoparametric elements in the FEM [164, 165]; in general, however, any generic angle preserving mapping is applicable. The primary displacement variables and their pertinent derivatives in the physical and computational domain are related by:

$$\begin{aligned} u_i(x_1, x_2) &= \bar{u}_i(\xi, \eta), \\ \frac{\partial u_i}{\partial x_j}(x_1, x_2) &= \frac{\partial \bar{u}_i}{\partial \xi} \frac{\partial \xi}{\partial x_j} + \frac{\partial \bar{u}_i}{\partial \eta} \frac{\partial \eta}{\partial x_j}, \end{aligned} \quad (7.8)$$

where  $i$  and  $j$  may take the values of 1 and 2, and the variables with an overbar are expressed in the computational domain. The weight functions,  $W^I(\mathbf{X})$ , may be related to those expressed in the computational domain,  $\bar{W}^I(\mathbf{X}_c)$ , by Eq. (7.8) as well.

The area,  $d\Omega_I$ , is mapped into the computational domain by:

$$\begin{aligned} d\Omega_I &= \left( \frac{\partial f_1}{\partial \xi} \frac{\partial f_2}{\partial \eta} - \frac{\partial f_1}{\partial \eta} \frac{\partial f_2}{\partial \xi} \right) d\xi d\eta, \\ d\Omega_I &= |J| d\xi d\eta. \end{aligned} \quad (7.9)$$

Note that each edge of the boundary in the computational domain,  $\Gamma_c$ , corresponds to either constant  $\xi$  or constant  $\eta$ . Therefore, the boundary integrals can be transformed to the computational domain by relating the differential line elements to differential changes in  $\xi$  or  $\eta$ :

$$\begin{aligned} d\Gamma_{\xi=c} &= \sqrt{\left( \frac{\partial f_1}{\partial \eta} \right)^2 + \left( \frac{\partial f_2}{\partial \eta} \right)^2} d\eta, \\ d\Gamma_{\eta=c} &= \sqrt{\left( \frac{\partial f_1}{\partial \xi} \right)^2 + \left( \frac{\partial f_2}{\partial \xi} \right)^2} d\xi, \end{aligned} \quad (7.10)$$

where  $\Gamma_{\xi=c}$  and  $\Gamma_{\eta=c}$  are portions of boundary in the physical domain on which  $\xi$  and  $\eta$  are

respectively constant in the computational domain. By defining the following matrices

$$\mathbf{K}_{ij}^I = \int_{\Omega_I} W_{,i}^I \left( \frac{\partial \xi}{\partial x_j} \mathbf{A}_1(\xi, \eta) + \frac{\partial \eta}{\partial x_j} \mathbf{A}_2(\xi, \eta) \right) |J| d\xi d\eta, \quad (7.11)$$

the local Petrov-Galerkin approximation can be written as:

$$\begin{bmatrix} \bar{Q}_{11} \mathbf{K}_{11}^I + \bar{Q}_{66} \mathbf{K}_{22}^I & \bar{Q}_{12} \mathbf{K}_{12}^I + \bar{Q}_{66} \mathbf{K}_{21}^I \\ \bar{Q}_{12} \mathbf{K}_{21}^I + \bar{Q}_{66} \mathbf{K}_{12}^I & \bar{Q}_{12} \mathbf{K}_{22}^I + \bar{Q}_{66} \mathbf{K}_{11}^I \end{bmatrix} \begin{pmatrix} \bar{\mathbf{u}}_1 \\ \bar{\mathbf{u}}_2 \end{pmatrix} = \begin{pmatrix} \int_{\Gamma_I} t_1 W^I(\mathbf{X}) d\Gamma_I \\ \int_{\Gamma_I} t_2 W^I(\mathbf{X}) d\Gamma_I \end{pmatrix} \quad (7.12)$$

where  $\bar{\mathbf{u}}_1$  and  $\bar{\mathbf{u}}_2$  are the unknowns of the basis functions. By selecting  $n_u$  weight functions of compact support where  $n_u$  is the number of unknowns per primary variable, equal number of equations as unknowns are obtained. Because the Sinc points are distributed such that they lie on a rectangular domain, weight functions with rectangular support were selected as indicated in Fig. 7.2. The support of the  $I$ th weight function in the computational domain is defined by  $\Omega_{cI} = \{ \mathbf{X}_c : (\xi_{min} \leq \xi \leq \xi_{max}) \cap (\eta_{min} \leq \eta \leq \eta_{max}) \cap \Omega_c \}$ .

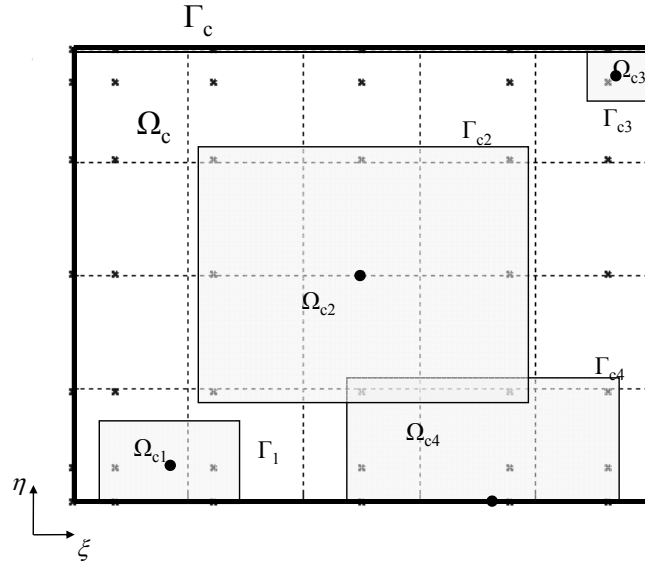


Figure 7.2. Local Petrov-Galerkin subdomains in the computational domain. The dots indicate centers of the given subdomain. The “x’s” indicate Sinc points within the computational domain.

Traditionally, the MLPG method would select Gauss functions or other radial basis functions [160, 166, 167] as weights; however, weight functions having quadratic variations of the form,

$$\bar{W}^I(\xi, \eta) = \begin{cases} (a_1^I \xi^2 + b_1^I \xi + c_1^I) (a_2^I \eta^2 + b_2^I \eta + c_2^I), & (\xi, \eta) \in \Omega_{cI} \\ 0, & (\xi, \eta) \notin \Omega_{cI} \end{cases} \quad (7.13)$$

$$a_1^I = \frac{-4}{(\xi_{max} - \xi_{min})^2}, \quad b_1^I = \frac{4(\xi_{max} + \xi_{min})}{(\xi_{max} - \xi_{min})^2}, \quad c_1^I = \frac{-4\xi_{max}\xi_{min}}{(\xi_{max} - \xi_{min})^2},$$

$$a_2^I = \frac{-4}{(\eta_{max} - \eta_{min})^2}, \quad b_2^I = \frac{4(\eta_{max} + \eta_{min})}{(\eta_{max} - \eta_{min})^2}, \quad c_2^I = \frac{-4\eta_{max}\eta_{min}}{(\eta_{max} - \eta_{min})^2},$$

were used in the present implementation.

### 7.2.2 Essential Boundary Conditions

Because the basis functions do not possess the Kronecker delta property, applying the essential boundary conditions is not trivial. To do so, two approaches were implemented: the traditional penalty method and the Lagrange multiplier method.

For the traditional penalty method, the work done by the local reaction given by  $\int_{\Gamma_I} t_i \delta u_i$  are replaced by a penalty term for a subdomain intersecting the boundary on which the essential boundary conditions are imposed. That is the local reaction forces are replaced by the following term:

$$\beta \int_{\Gamma_I} (u_i - \tilde{u}_i) \delta u_i d\Gamma_I, \quad (7.14)$$

where  $\beta$  is a penalty parameter. Zhu and Atluri [168] suggest a range of  $(10^3 - 10^7)E$  for the penalty parameter where  $E$  is the relative magnitude of the governing equations. For structures problems,  $E$  is taken to be the Young's modulus of the material. Because of the large penalty parameter  $\beta$ , the essential boundary conditions are imposed in an approximate sense.

The present analysis also utilizes the Lagrange multiplier approach. For a boundary on



which an essential boundary condition is imposed, the work done by the local reaction force given by  $\int_{\Gamma_I} t_i \delta u_i$  is replaced by:

$$\lambda_i^I \int_{\Gamma_I} (\delta u_i) d\Gamma_I + \int_{\Gamma_I} \delta \lambda_i^I (u - \tilde{u}) d\Gamma_I, \quad (7.15)$$

where  $\lambda_i^I$ , is introduced as an additional unknown. Because  $\delta \lambda_i^I$  are arbitrary, they are independently set to  $\beta W^I(\mathbf{X})$  resulting in an additional equation where  $\beta$  is included to provide a similar magnitude between equations resulting from  $\delta \lambda_i^I$  and equations resulting from  $\delta u_i$ . In practice,  $\lambda_i^I \int_{\Gamma_I} (\delta u_i) d\Gamma_I$  need not be evaluated. This term can simply be lumped into the unknown  $\lambda_i^I$ . Furthermore, in order to maintain a similar magnitude of the unknowns and prevent ill conditioning,  $\lambda_i^I$  was normalized by  $\beta$ .

### 7.2.3 Integration Scheme

The integration in the weak form merits some discussion. Gauss quadrature was used to integrate over each of the subdomains. Because the integrals involve expressions with Sinc and sine-integral functions, an exact quadrature rule cannot be used. To compensate, five integration points were used to integrate over each subdomain.

## 7.3 Analysis of a 1D, Tapered, Axial Bar

To assess the accuracy of the ILPGSM, 1D, static analysis of a fixed-fixed, homogeneous, axial bar that is subjected to a uniform distributed force was performed. The boundary value problem is expressed by,

$$\begin{aligned} [EA(x)u_{,1}(x)]_{,1} + p_0 &= 0, \text{ in } \Omega = \{x : 0 < x < L\} \\ u(0) &= 0, \text{ and } u(L) = 0. \end{aligned}$$

where  $E$  is Young's Modulus,  $A(x)$  is the cross-sectional area at a given  $x$ , and  $p_0$  is the distributed force per unit length. Let  $A_0$  represent the area at the root ( $x = 0$ ). Accordingly, the problem is normalized by introducing  $\bar{u} = EA_0u(x)/(p_0L^2)$ ,  $\bar{x} = x/L$ , and  $a(\bar{x}) = A(x)/A_0$ . The overbar is dropped throughout the remaining discussion. Note that the normalized stress is given by  $\sigma = u_{,1}(x)$ .

The local weak form may be obtained by multiplying by a weight function of compact support, integrating over that support, and carry out the integration by parts:

$$W^I(x)a(x)u_{,1}(x)\Big|_{x_{min}^I}^{x_{max}^I} - \int_{\Omega_I} (W_{,1}^I(x)a(x)u_{,1}(x) - W^I(x))d\Omega_I = 0, \quad (7.16)$$

with  $\Omega_I = \{x : x_{min}^I \leq x \leq x_{max}^I\}$ .

The physical and computational domains are related by  $x = (\xi - \xi_{-N})/(\xi_N - \xi_{-N})$ . The displacement and its pertinent derivatives in the physical and computational domain are related in an analogous manner to the 2D case presented in Section 7.2. The primary variable and its derivative,  $u(\xi)$  and  $u_{,1}(\xi)$ , are approximated by the basis functions. Note that by selecting  $n_u$  weight functions, Eq. (7.16) becomes a system of  $n_u$  equations of the form  $\mathbf{K}\mathbf{u} = \mathbf{f}$ . For the first-order basis functions,  $n_u = n + 1$ . For the second-order basis function,  $n_u = n + 2$ .

Weight functions of compact support were constructed by the following scheme. A total of  $n_u$  weight functions whose subdomains were centered at  $\xi_{I-mid}$  according to the DE transformation. For mesh size  $h$ ,  $\xi_{I-mid}$  was defined by:

$$\xi_{I-mid} = \phi \left( Nh \frac{2I - n_u - 1}{n_u - 1} \right), \quad I = 1, 2, 3, \dots, n_u$$

The subdomain widths are selected such that there are at least two Sinc points within the subdomain. Let  $\mathbf{x}$  be the vector of Sinc points,  $\mathbf{x}_{mid}$  be the vector of subdomain centers, and the function  $\text{min2}(\mathbf{a})$  returns the second-smallest entry in a vector  $\mathbf{a}$ . Then the width of each

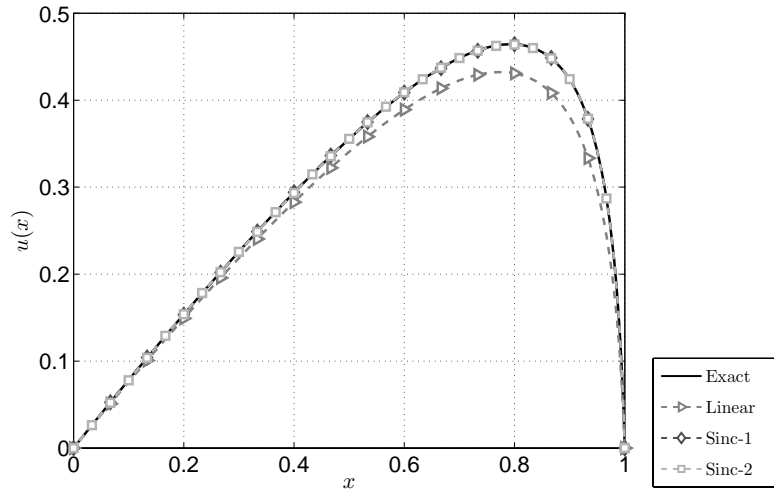
subdomain is given by  $d_I = 2 \min_2(|\mathbf{x} - \mathbf{x}_{sup}|)$ , the  $I$ th subdomain maximum is given by  $\xi_{max} = \xi_{I-mid} + d_I/2$ , and the  $I$ th subdomain minimum is given by  $\xi_{min} = \xi_{I-mid} - d_I/2$ . Note that there are some subdomains whose maximum or minimum lies outside of the domain  $\Omega$ . The  $\xi_{min}$  and  $\xi_{max}$  are used in the 1D equivalent to Eq. (7.13) to construct the weighting functions. However, the integration is performed over  $\Omega_{cI} = \{\xi : (\xi_{min} \leq \xi \leq \xi_{max}) \cap (\xi \in \Omega_c)\}$ .

The ILPGSM was implemented for the axial bar in MATLAB using all three basis functions. The Sinc mesh size,  $h$  (see Eq. (3.8) and Fig. 3.2), was taken to be  $2.5/N$ .

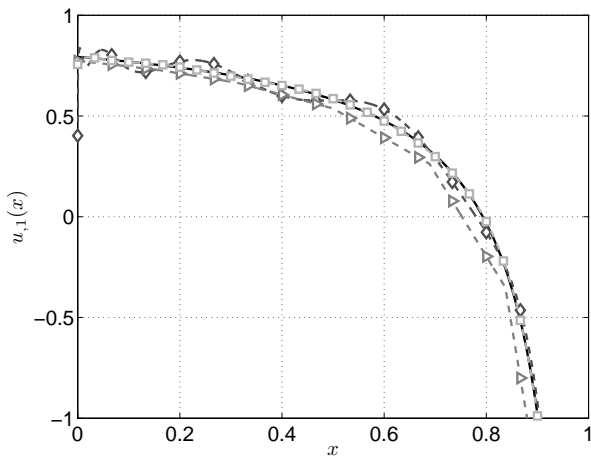
A tapered bar with vanishing tip area was analyzed. The area is selected having the form  $a(x) = (1 - x + \delta)/(1 + \delta)$  with  $\delta = 0.01$  and  $0.0001$ , a linear area variation with root-to-tip area ratios of 101:1 and 10,001:1 respectively. Our results were compared with the analytic solution defined in Appendix D.

In Fig. 7.3, the normalized displacement and stress obtained by the ILPGSM and the three basis functions using  $N = 10$  for  $\delta = 0.01$  were plotted. For the ILPGSM results, the essential boundary conditions were imposed by the Lagrange multiplier method; however, similar results were obtained using the penalty method with a penalty parameter of  $10^5$ . The figure indicates that the displacement and stress were predicted accurately using both the Sinc-1 and Sinc-2 basis functions. However, the displacement results obtained using the linear basis function are erroneous by 7% at its maximum and the stress results are erroneous by 29% at  $x = L$ . The Sinc-1 basis function exhibits some oscillations in the stress, a characteristic of the Sinc interpolation.

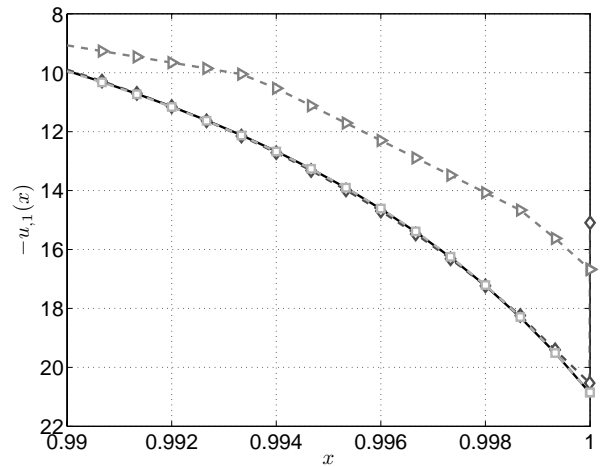
In Fig. 7.4, similar results were plotted for  $\delta = 0.0001$  or a root-to-tip area ratio of 10,001:1. For this case, both the Sinc-1 and Sinc-2 basis functions provide a very accurate approximation for displacement; however, the stress is only accurately approximated using the Sinc-2 basis function. The linear basis function provides 13% error in maximum displacement and 41% error in the tip stress. The Sinc-1 basis function exhibits substantial



(a) Displacement

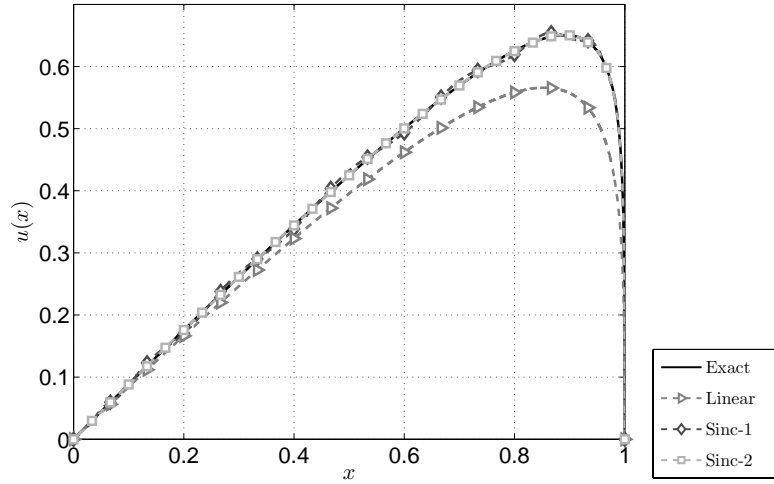


(b) Stress

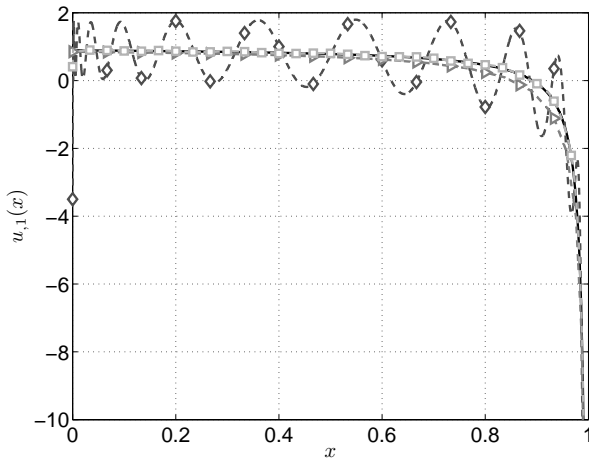


(c) Stress near the tip

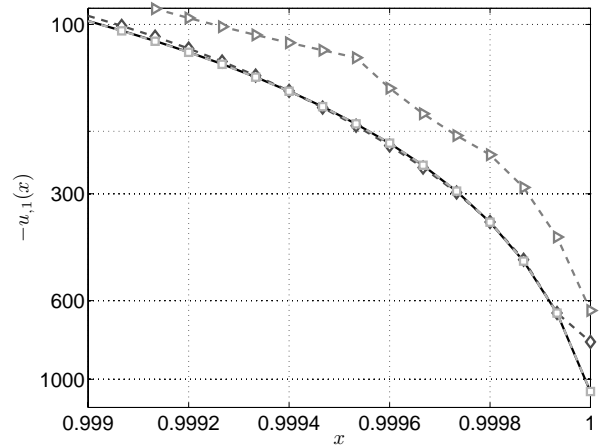
Figure 7.3. Displacement and stress obtained with  $N = 10$  (21 Sinc points) and the ILPGSM using the Lagrange multiplier method to impose essential boundary conditions for  $\delta = 0.01$ . Results are compared with the analytic solution.



(a) Displacement



(b) Stress



(c) Stress near the tip

**Figure 7.4.** Displacement and stress obtained with  $N = 20$  (41 Sinc points) and the ILPGSM method using the Lagrange multiplier method to impose essential boundary conditions for  $\delta = 0.0001$ . Results are compared with the analytic solution.

oscillations in the stress. The results obtained using the Sinc-2 basis function are indistinguishable from the analytic solution, despite the substantial stress concentration. Similar results were obtained using the penalty method to apply the essential boundary conditions with a similar level of accuracy.

To further numerically quantify the error, the following error metrics were defined: one for the displacement,  $\|\epsilon\|_0$ , and one for the stress,  $\|\epsilon\|_1$ .

$$\|\epsilon\|_0 = \sqrt{\frac{\int_{\Omega} (u - u_a)^2 d\Omega}{\int_{\Omega} u_a^2 d\Omega}} \quad \text{and} \quad \|\epsilon\|_1 = \sqrt{\frac{\int_{\Omega} (u_{,1} - u_{a,1})^2 d\Omega}{\int_{\Omega} u_{a,1}^2 d\Omega}} \quad (7.17)$$

The error in displacement and stress were compared for each of the basis function in Figs. 7.5 - 7.8. The convergence properties are compared with the SIHD method, a  $C^0$  continuous displacement based FE solution, and a mixed FEA where both the displacements and stresses are independently approximated using  $C^0$  continuous basis functions [169, 170]. A 2D mixed FE for plane-stress analysis was developed in the Appendix. The FE meshes were chosen such that the nodes were coincident to the Sinc points of the SIHD and ILPGSM solutions. Each analysis approach was implemented in MATLAB for the sake of comparison of computational time.

The error in displacement and stress was plotted in Fig. 7.5 for an axial bar having root-to-tip area ratio of 101:1 and using each of the analysis approaches. The following observations were made. The Sinc-2 basis function provides a very accurate solution, with greater accuracy and a higher rate of convergence than both the  $C^0$  FEA and the mixed FEA when the Lagrange multiplier method was used to apply the essential boundary conditions. Furthermore, the Sinc-2 basis function provides greater accuracy of the stress than the SIHD method; however, the SIHD method provides comparable accuracy for the displacements. The Sinc-1 basis function using the Lagrange multiplier method to apply the

essential boundary conditions resulted in accurate displacements; however, the stress was erroneously approximated. This is likely to be the result of the oscillations seen in Fig. 7.4. The linear basis function with the ILPGSM provides the least accurate solution. The Lagrange multiplier method for applying the essential boundary conditions results in greater or equal accuracy to the penalty method for all basis functions.

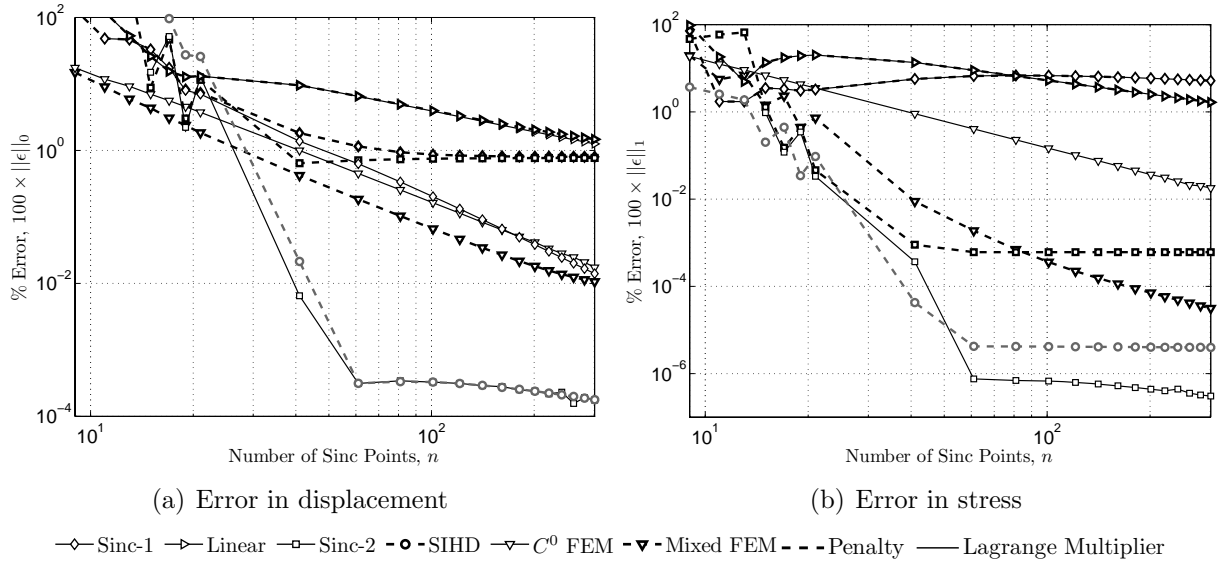


**Figure 7.5.** Numerical error of the displacement and stress for tapered axial bar with taper ratio of 101:1 and increasing number of Sinc points.

To examine the efficiency of the ILPGSM method and compare it with the traditional and mixed FEAs, the stress accuracy was plotted against the total number of DOF and the total computational time in Fig. 7.6. Only the ILPGSM results obtained using the Sinc-2 basis function were compared with the FEAs and the SIHD method. The ILPGSM solution provides substantially improved accuracy over the SIHD method and traditional and mixed FEAs for equal number of degrees of freedom; however, this does not translate directly into greater efficiency. In general, the ILPGSM is less efficient than the strong form based SIHD and the FEA analyses. However, the figure indicates that the present method obtained greater accuracy of the stress for equal computational cost to the FEAs and the SIHD method if a higher accuracy is desired. The additional computational cost of the ILPGSM

is the result of a large number of integration points and therefore a large number of basis function evaluations needed, and a more fully populated stiffness matrix. For  $N = 150$  or a total of 305 degrees of freedom, the stiffness matrix contains 92,114 nonzero components. Whereas for the  $C^0$  continuous FE with  $N = 150$  or 301 degrees of freedom, the stiffness matrix contains only 901 nonzero components. The mixed FE with  $N = 75$  or 302 DOF, the stiffness matrix contains only 1,206 nonzero components. Thus while the present method is somewhat inefficient, the high rate of convergence may achieve improved accuracy of the stress compared with both  $C^0$  and mixed FEA for equal computational cost.

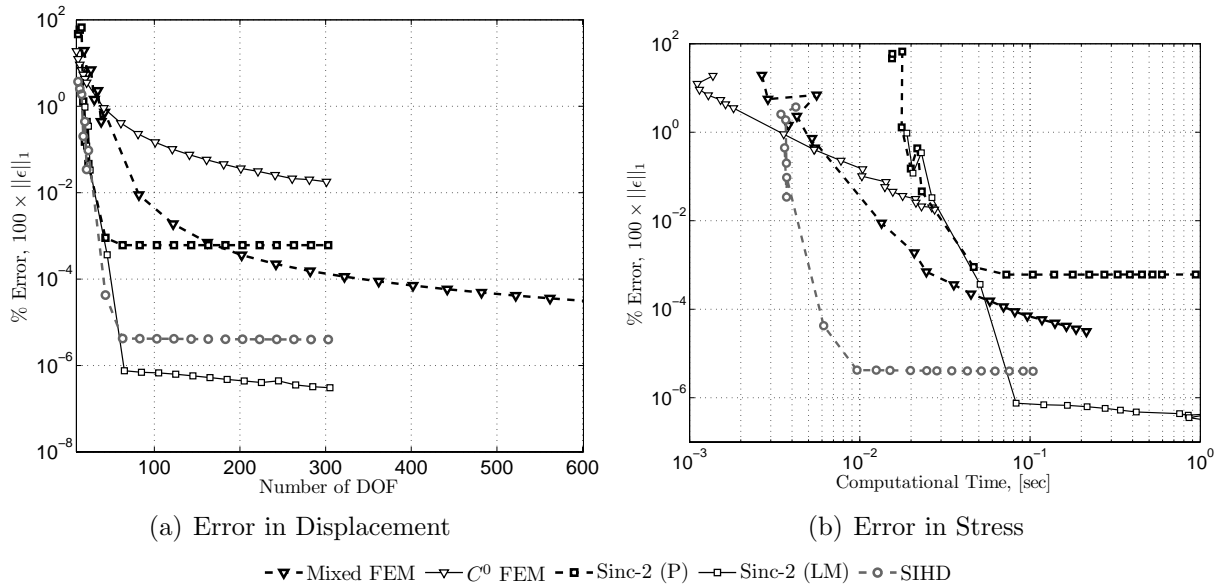


**Figure 7.6.** Numerical error of the stress versus number of degrees of freedom and computational time for axial bar with taper ratio of 101:1.

Similar results were obtained for an axial bar with taper ratio of 10,001:1 in Figs. 7.7 and 7.8. While most of the previous discussion regarding the results in Figs. 7.5 and 7.6 may also be seen in the present example, it should be noted that the ILPGSM provides far superior results to the SIHD method for the 10,001:1 taper ratio. Furthermore, it should be noted that Fig. 7.8 indicates that the Sinc-2 basis function and ILPGSM may be able to provide improved accuracy of stress in the presence of a stress concentration for the same



computational cost as the FEM.

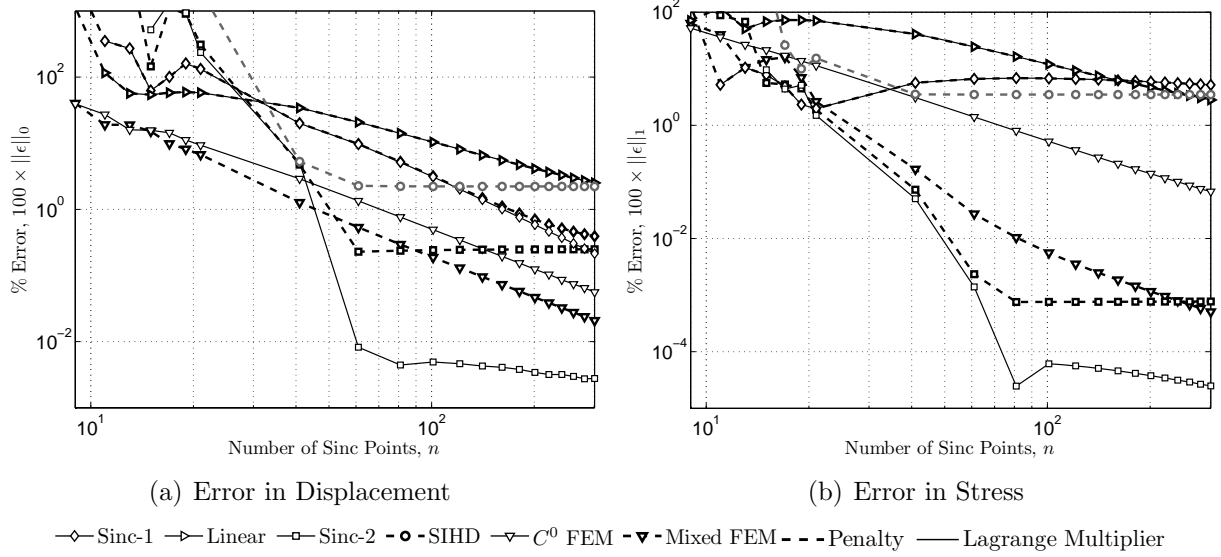


**Figure 7.7.** Numerical error of the displacement and stress for tapered axial bar with taper ratio of 10,001:1 and increasing number of Sinc points.

## 7.4 Analysis of a 2D, Timoshenko Cantilever Beam

Results were also obtained by implementing the ILPGSM for a Timoshenko cantilever [171]. The formulation developed in Section 7.2 was used for a plane-stress analysis of a rectangular panel (see Fig. 7.9). The dimensions of the panel are  $a = 1.0$  m long and  $b = 0.2$  m wide. A parabolic shear traction is applied to the right edge ( $x_1 = a$ ). The traction defined by:

$$\begin{aligned} \sigma_{11}(a, x_2) &= 0, \\ \sigma_{12}(a, x_2) &= t(x_2) = \frac{6P(bx_2 - x_2^2)}{b^3}, \end{aligned} \quad (7.18)$$

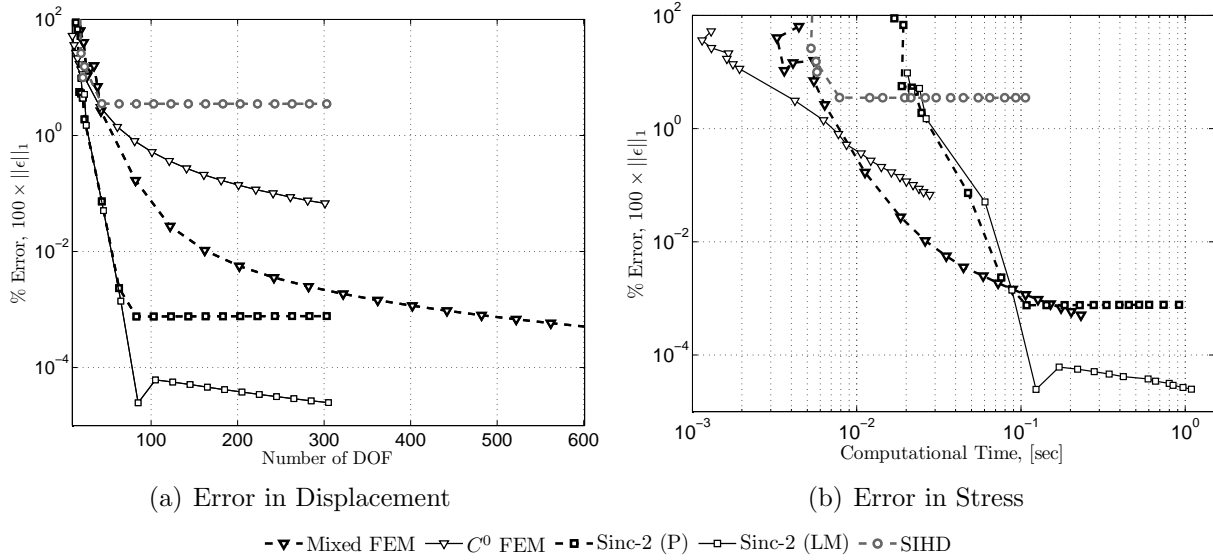


Figure 7.8. Numerical error of the stress versus number of degrees of freedom and computational time for axial bar with taper ratio of 10,001:1.

where  $P = 10^6$  N/m. The top ( $x_2 = b$ ) and bottom ( $x_2 = 0$ ) surfaces are traction free. On the left edge, ( $x_1 = 0$ ), the displacement is constrained such that:

$$\begin{aligned}
 u_1(0, x_2) = \tilde{u}_1(x_2) &= -\frac{2Px_2(2 + \nu)}{Eb} \left( \frac{x_2}{b} - \frac{1}{2} \right) \left( \frac{x_2}{b} - 1 \right) \\
 u_2(0, x_2) = \tilde{u}_2(x_2) &= \frac{6P\nu a}{Eb} \left( \frac{x_2}{b} - \frac{1}{2} \right)^2
 \end{aligned}
 \tag{7.19}$$

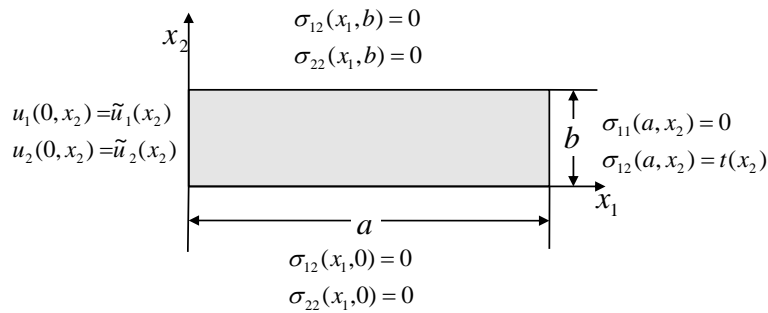


Figure 7.9. Boundary conditions and dimensions of the Timoshenko cantilever problem.

An analytical solution to this problem was given by Timoshenko and Goodier [171] and

has been used by Batra and Zhang [160] to verify the accuracy of the SSPH meshless method.

The analytical solution for displacement is:

$$\begin{aligned} u_1(x_1, x_2) &= -\frac{2P}{E} \left( \frac{x_2}{b} - \frac{1}{2} \right) \left[ \frac{3x_1(2a - x_1)}{b^2} + \frac{x_2(2 + \nu)}{b} \left( \frac{x_2}{b} - 1 \right) \right], \\ u_2(x_1, x_2) &= \frac{2P}{E} \left[ \left( \frac{x_1}{b} \right)^2 \left( \frac{3a}{b} - \frac{x_1}{b} \right) + 3\nu \left( \frac{a}{b} - \frac{x_1}{b} \right) \left( \frac{x_2}{b} - \frac{1}{2} \right)^2 + \frac{x_1(4 + 5\nu)}{4b} \right]. \end{aligned} \quad (7.20)$$

The ILPGSM was implemented in MATLAB R14 Service Pack 2 using all three basis functions and with the boundary conditions imposed by the penalty method and the Lagrange multiplier method. The Sinc mesh size,  $h$  [see Eq. (3.8) and Fig. 3.2], was taken to be  $2.0/N$ . The physical domain was transformed to the computational domain by the mapping

$$x_1 = \frac{a(\xi - \xi_{-N})}{(\xi_N - \xi_{-N})}, \quad x_2 = \frac{b(\eta - \eta_{-N})}{(\eta_N - \eta_{-N})}. \quad (7.21)$$

Weight functions were chosen having the form of Eq. (7.13) with  $\xi_{max}$ ,  $\xi_{min}$ ,  $\eta_{max}$ , and  $\eta_{min}$  chosen for each subdomain in an identical fashion to the tapered bar problem.

Displacements and stresses were obtained, using the ILPGSM with essential boundary conditions imposed using the Lagrange multiplier method and penalty method. For the sake of brevity, the contours of displacements and stresses were only presented using the Sinc-2 basis function with essential boundary conditions imposed by the Lagrange multiplier method, though similar results were obtained using the other basis functions and with the penalty method for imposing essential boundary conditions. In Fig. 7.10, the contours of displacement and stresses were plotted from the results obtained using the Sinc-2 basis function with  $N = 10$  or 21 Sinc points along each axis. Note the contours are indistinguishable from the analytic solution implying a very accurate numerical solution. Additionally, the displacement and stress contours indicated that the linear basis function performs quite well for the present problem; however, no feasible solution could be obtained using the Sinc-1

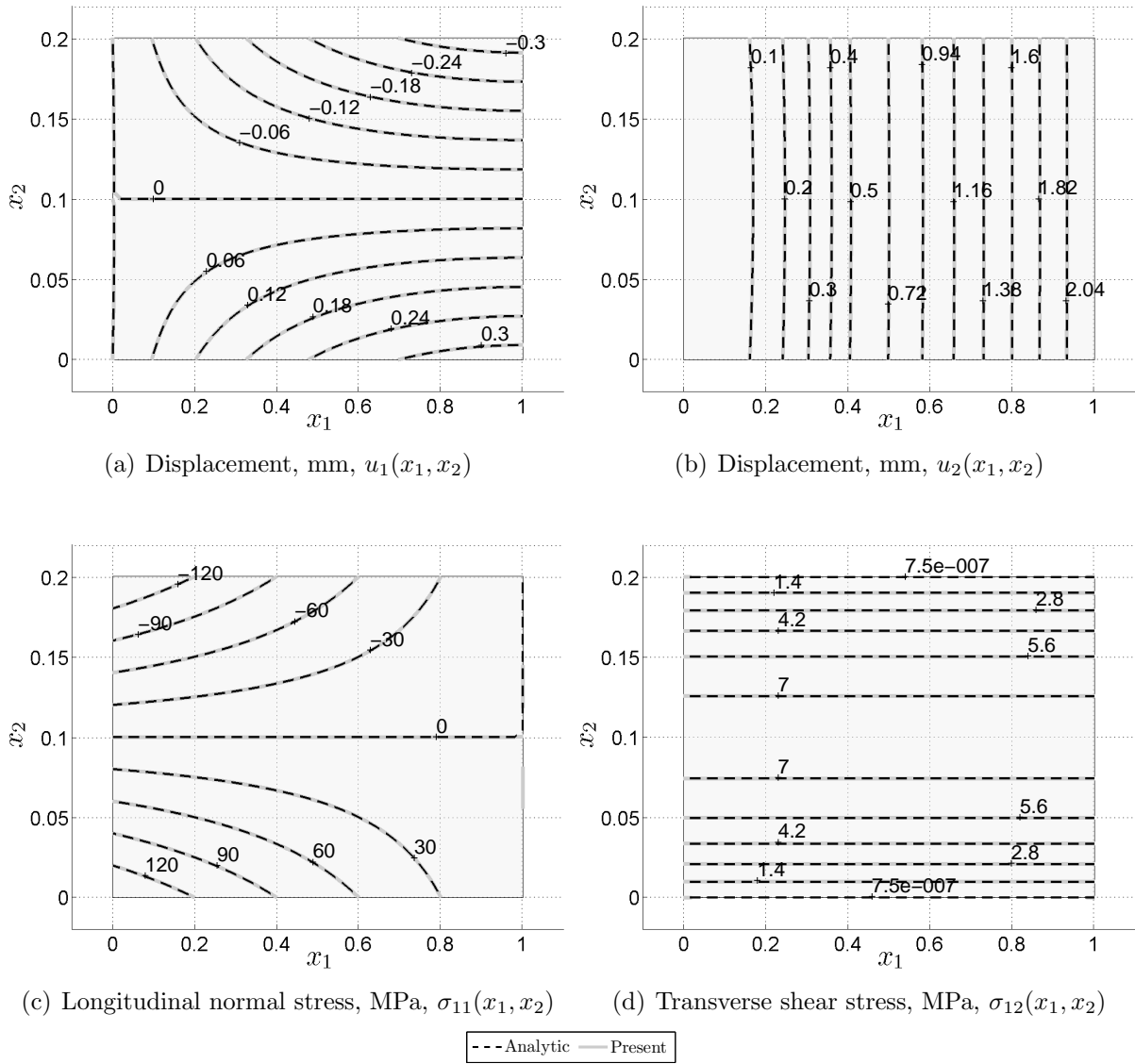


**Figure 7.10.** Contours of displacement and stress in the Timoshenko cantilever obtained by the ILPGSM with the Sinc-2 basis function ( $N = 10$ ). The essential boundary conditions are imposed by the Lagrange multiplier method.

basis function. It was also noted that for this case the stresses exhibit significant oscillations similar to those seen in the tapered bar example.

In Fig. 7.11, the convergence properties are compared for the ILPGSM with each basis function and both boundary conditions approaches. For the sake of comparison the SIHD method, a  $C^0$  continuous FE with  $u_1$  and  $u_2$  degrees of freedom, and a mixed FE in which  $u_1$ ,  $u_2$ ,  $\sigma_{11}$ ,  $\sigma_{12}$ , and  $\sigma_{22}$  were each independently approximated using  $C^0$  basis functions were used to analyze the present problem. Each approach was implemented in MATLAB for the present problem. The details for the mixed FEM solutions are provided in the Appendix E. For the FE meshes, the nodes were placed coincidental to the location of Sinc points. It should be noted that while the current meshing approach may not be the most efficient approach for the present problem, it provides a reasonable mechanism for comparison. Naturally, as the number of Sinc points increases, the element size decreases resulting in convergence of the FEA.

Figure 7.11 indicates that the Sinc-2 basis function provides very accurate displacement and stress results with very few Sinc points when the Lagrange multiplier method is employed; however, the solution exhibits diminishing returns beyond 21 Sinc points along both axes. Nonetheless, of all the methods implemented, the Sinc-2 basis function with the Lagrange multiplier approach for essential boundary conditions provides the best accuracy for displacements and stresses. The method's accuracy is a significant improvement from the SIHD method and both the  $C^0$  and mixed FEA for equal number of Sinc points. If the boundary conditions are imposed by the penalty method, the Sinc-2 basis function is generally less accurate than with the Lagrange multiplier method.

The linear basis function provided acceptable accuracy; however, a slow, strictly monotonic rate of convergence was achieved using the Lagrange multiplier method for imposing the essential boundary conditions. As indicated by Fig. 7.11, the ILPGSM with this basis function was less accurate than the SIHD method. Note that using the linear basis function

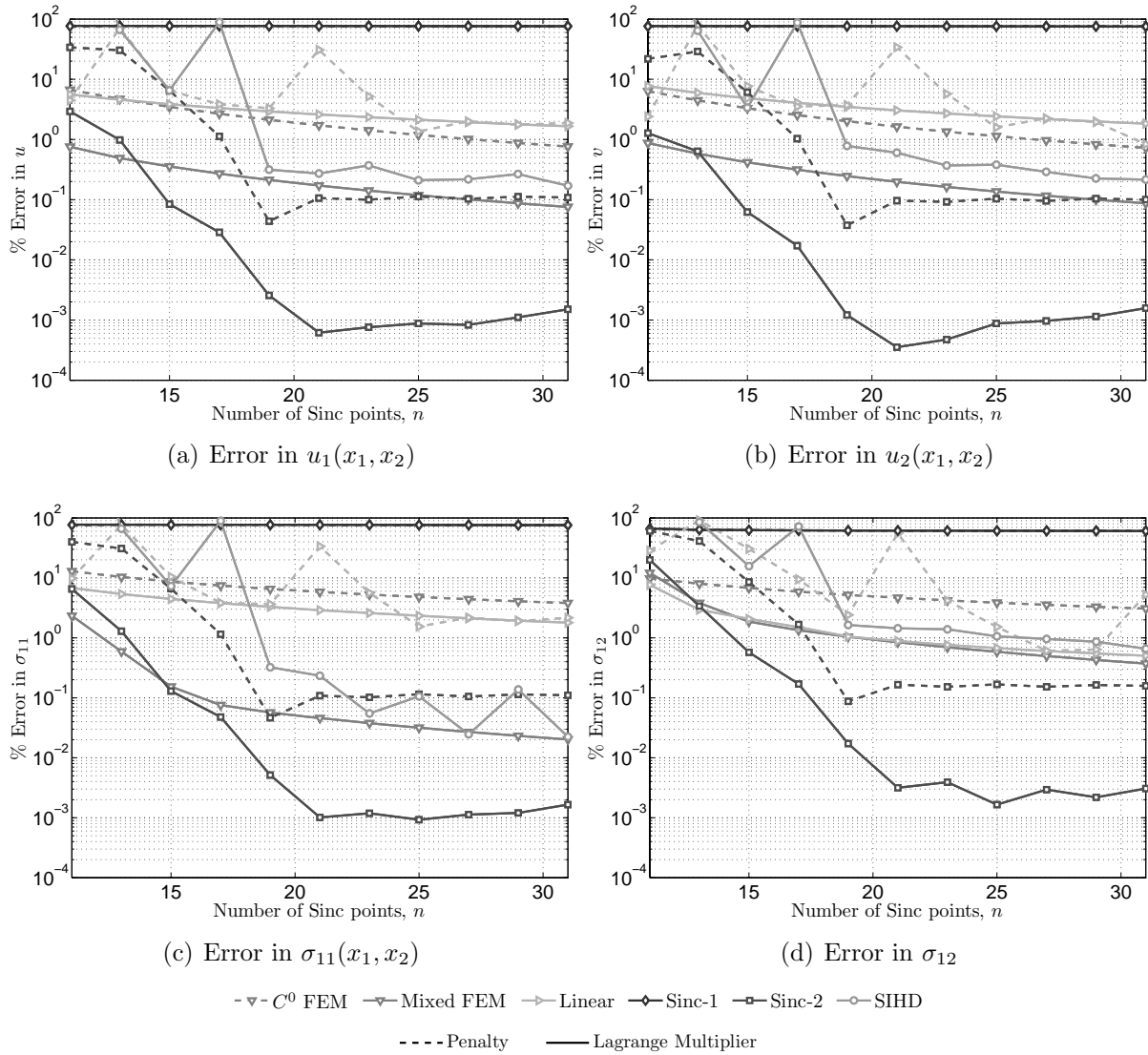


Figure 7.11. Numerical error of the displacements and stresses with increasing number of Sinc points. Numerical result are compared with the SIHD method, a displacement-based  $C^0$  FEA, and a mixed FEA.

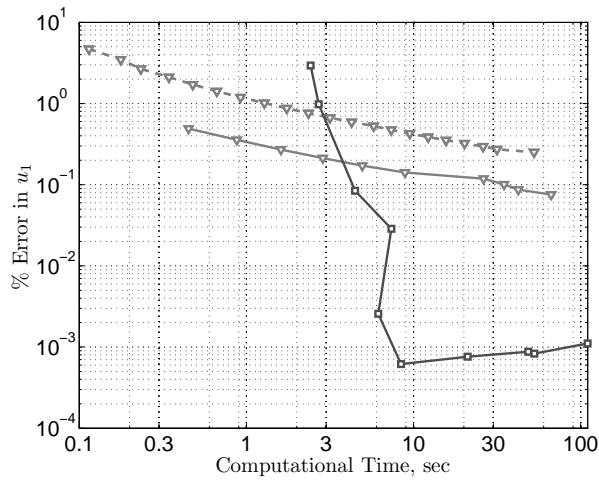
resulted in comparable displacement accuracy to the standard  $C^0$  FEM; however, the linear basis function achieved greater stress accuracy than the  $C^0$  FEM. The mixed FEA provides greater accuracy than the linear basis function in both stresses and displacements. Figure 7.11 also confirms that the Sinc-1 basis function was not a feasible option for the analysis.

The efficiency of the Sinc-2 basis function with ILPGSM and the Lagrange multiplier method was compared with the displacement and mixed FEAs in Fig. 7.12. While both the mixed and displacement based FEAs provided acceptable accuracy (less than one percent error in the displacements) at a reduced computational cost compared with that of the ILPGSM, the ILPGSM can achieve greater overall accuracy. There is an initial cost penalty relative to the FEAs; however, if the analysis goal is very accurate stresses, the ILPGSM may be advantageous over the traditional displacement FEA. Also, it should be noted that for the same number of DOF, the ILPGSM provides greater stress accuracy.

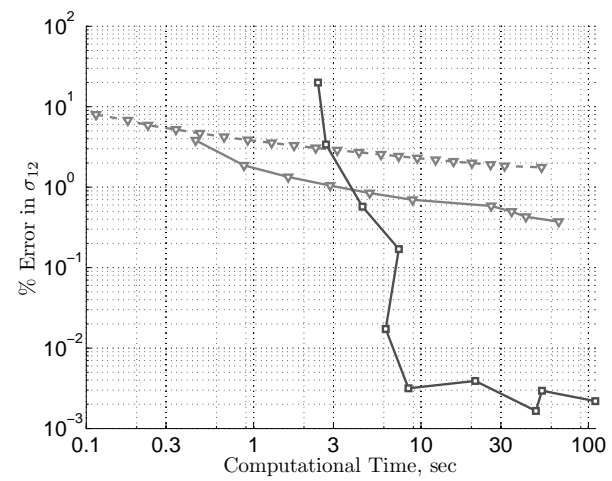
## 7.5 Conclusions

In the present chapter, a new integrated Sinc method was proposed and assessed for 1D and 2D analysis of static structural mechanics problems. The method, named the Integrated Local Petrov-Galerkin Sinc Method (ILPGSM) is very similar to the SIHD method [122]; however, the present method utilizes the methodology of the MLPG approximation. Because the basis functions do not possess the Kronecker delta property, results were compared imposing essential boundary conditions using the traditional penalty method and the Lagrange multiplier method.

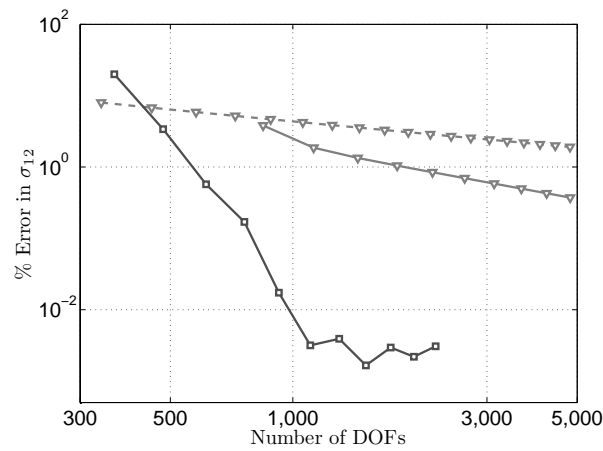
Results were compared utilizing three different basis functions. Each of these basis functions use numerical indefinite integration based on the DE transformation. The primary differences of the basis function are the order of the derivative initially approximated and the method of interpolating between Sinc points. First-order (Sinc-1) and second-order (Sinc-2) basis function using Sinc interpolation and a first-order basis function using linear



(a) Time v. Error in  $u_1$



(b) Time v. Error in  $\sigma_{12}$



(c) Number of DOFs v. Error in  $\sigma_{12}$

- - -  $C^0$  FEM    - - - Mixed FEM    - - - Sinc - 2

**Figure 7.12.** Numerical error of displacement and stress verse computational time and number of degrees of freedom for solution from ILPGSM with the Sinc-2 basis function and Lagrange multiplier method, a displacement-based  $C^0$  FEA, and a mixed FEA.



interpolation (Linear) were introduced and assessed.

Analysis of a 1D, fixed-fixed, tapered bar whose tip area approaches zero was performed using the present method. The results indicated that the Sinc-2 basis function with ILPGSM provides a highly convergent solution and performs very well in the presence of the stress concentration. The method was shown to provide greater accuracy than the SIHD method, although, the cost of integration over a local subdomain is substantial. The method also suffers from a fully populated stiffness matrix which adds additional computational time in matrix factorization when compared with the FEM. The results indicated that despite these inefficiencies, the present method can provide additional accuracy for stresses in the presence of a stress concentration than traditional FEM. Due to its high rate of convergence, the ILPGSM can provide greater accuracy for equal computational cost than a displacement-based,  $C^0$  continuous and mixed FEA.

The ILPGSM was also implemented for a 2D, plane-stress elasticity problem. The results were compared with the analytic solution and the accuracy and convergence properties were compared with the SIHD method and both a displacement-based,  $C^0$  continuous and mixed FEA. For the 2D problem, the Sinc-2 basis function with ILPGSM once again provided greater accuracy and higher rates of convergence than the FEAs. Furthermore, the 2D example also demonstrated that the ILPGSM could obtain greater accuracy of displacements and stresses for the same computational time as both a displacement based and mixed FEA.

Finally, it should be noted that the potential benefits of the present method are assessed based on observations seen for the sample problems analyzed with the present implementation. A formal proof of improved accuracy and convergence rate is beyond the scope of this thesis. The comparisons made with the FEM do not reflect an optimized implementation that may be achieved with the very mature FEM and are provided only to illustrate the potential benefits that could be achieved with additional development of the proposed method.

## 8 Plane-Stress Analysis of Notched Panels

Stress analysis of notched and cracked aircraft components is an important part of understanding the fatigue-crack growth process. Stable crack growth in metallic materials under Mode I loading has been extensively studied using elastic–plastic FEA [172]. Efficient techniques have been developed to predict unstable crack growth. Fracture criteria include crack-tip stress or strain intensity factors, crack-tip-opening displacement or angle, crack-tip force, energy-release rates, J-integral, and the tearing modulus. The present study focuses on the evaluation of J-integral for panels with elastic-plastic materials.

The J-integral, was proposed by Rice in 1968 as a way to calculate the strain energy release rate in a material [173]. The J-integral is often useful for predicting brittle fracture when there is a large amount of plasticity [174]. Testing procedures for determining the fracture toughness of metallic materials using the J-integral method are prescribed according to ASTM Standard No. E1820. The use of J-integral allows testing of small specimen (outside the limits of linearly elastic fracture mechanics) to obtain the critical, Mode I fracture energy,  $J_{Ic}$ . While the J-integral is typically applied to line cracks, its application to rounded and V-shaped notches was proposed by Livieri [175, 176] and Berto and Lazzarin [177].

Kuang and Chen [178] studied the evaluation of the J-integral on contours which do not fully enclose the plastic zone. Kuang and Chen concluded that the the path independence of the J-integral is maintained only when the crack fully encloses the plastic zone. Batra and Love [179] studied the use of the J-integral for cracking of a functionally graded plate under dynamic loading. Their results indicate that the J-integral exhibits substantial oscillations after crack initiation for high strain rates. For nonlinear-elastic materials or for elastic-plastic material with proportional loading, the path-independence of the J-integral still holds [180]. Furthermore, the comparison of the J-integral with the known critical value predicts an unstable brittle crack growth quite well [181]. However, for non-proportional loading the J-

integral is path dependent [182]. The J-integral is based on deformation theory of plasticity and holds for nonlinear elastic materials. The path independence vanishes when crack growth occurs as most engineering materials unload drastically. Recently, the near-tip J-integral was shown to be the “scalar driving force at the crack tip even in incrementally elastic-plastic materials, based on the second law of thermodynamics” by Simha *et al.* [182].

Meshless methods are often advantageous over FEMs in that they possess a higher degree of continuity in the solution field. For elastic-plastic materials, this continuity of higher-order derivatives is advantageous in areas apart from the elastic–plastic boundary. Discontinuities in the derivative of the strain field across elastic-plastic boundaries; however, are physical. Therefore the application of highly continuous methods for elastic–plastic problems should be considered carefully.

Gu *et al.* [183] studied material nonlinearity using the local radial point interpolation method, a meshless local Petrov-Galerkin method (MLPG) with the radial basis function. The paper examined a constant tension specimen, a pressurized thick walled cylinder, and a V-notched plate. In each example, the method performs quite well compared with FEM. Ma, Xin, and Krishnaswami [184] studied the use of the meshless integral method for simple elastic-plastic plane stress and plane strain problems. A square constant tension stress patch, a square constant shear stress patch, a finite panel with a circular hole subjected to uniform applied displacement, and a pressurized thick walled cylinder were analyzed to verify the accuracy of the meshless integral method.

In impact analysis, meshless methods have been suggested and implemented by many authors because there is no need to re-mesh when failures and shear bands occur. Zhang and Chen [185] used the Moving Least Squares approximation in the Element Free Galerkin formulation to study high velocity impact of an elastic-plastic plate. Zhang and Chen noted that one drawback of the method is that it needs a large number of particles for accurate results for the dynamic fracture study.

The remainder of this chapter is arranged as follows. The ILPGSM is extended to analysis of nonlinear boundary value problems using the modified Newton's method. The numerical results for infinite elastic plane-stress panels with elliptical center notches are presented, with results including the J-integral. Comparison is made with the analytic solution for the infinite elastic panel with elliptical center notch. The accuracy of both displacements and stresses is compared by utilizing two and four subdomains or elements. Numerical results for an elastic-plastic panel with bilinear material behavior and kinematic hardening are presented and compared with similar results from the finite element method. The chapter concludes with a summary and conclusions.

## 8.1 Analysis Method

The ILPGSM approach was used to solve the problem of plane-stress deformation of elastic and elastic-plastic notched panels to demonstrate its effectiveness for non-rectangular domains and material nonlinearity. First, the transformation to finite number of rectangular domains is achieved by the same methodology as "isoparametric" finite elements. Next the incremental weak form is developed and the solution approach is described.

### 8.1.1 Domain Decomposition by "Isoparametric" Mapping

The present analysis considers domains with elliptic and circular holes. Thus the rectangular computational domain  $(\xi, \eta)$  must be transformed to the physical domain. The simplest method for domain transformation is to follow the methodology of isoparametric elements in a quadrilateral finite element. While using the displacement shape functions to describe the shape of element boundaries is not the intent, using the Lagrange interpolation polynomials with a discrete number of "nodes," provides a good means to approximately represent the geometry. Consider Fig. 8.1. The figure indicates a "nine-node" subdomain in the computational domain  $(\xi, \eta)$  and physical domain. Note that the term "nodes" is used to describe

points of exact geometric match between the physical domain and the computational domain. These points are not related to the Sinc points of the ILPGSM method. The mapping

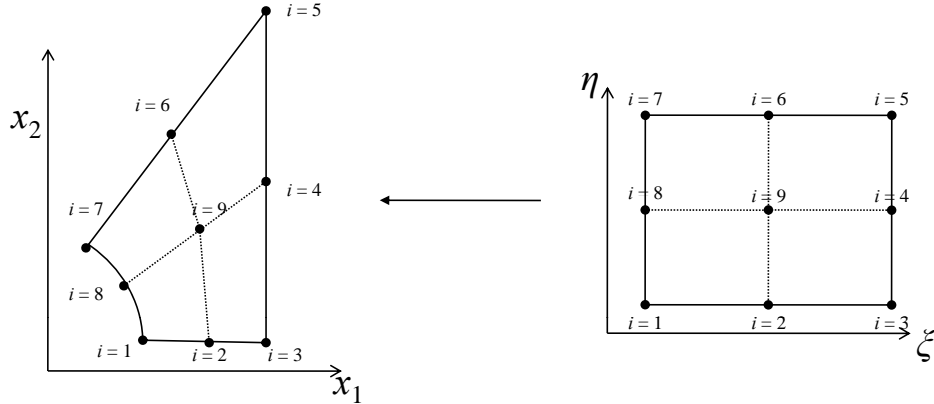


**Figure 8.1. Domain transformation using Lagrange interpolation polynomials.**

between the two domains is given by:

$$\begin{aligned} x_1 &= N_i(\xi, \eta)x_{1i} \\ x_2 &= N_i(\xi, \eta)x_{2i} \end{aligned} \tag{8.1}$$

where  $N_i(\xi, \eta)$  are the Lagrange shape functions [186].

Consider a quarter of a symmetric panel with a center elliptic notch as shown in Fig. 8.2 with dimensions, loads, and boundary conditions indicated. Because the domain has five distinct edges, a single mapping between computational and physical domains would not provide a good geometric match using the mapping technique. However, by dividing the domain, each subdomains has four distinct edges and the mapping can be done with very little error. For the present study, results were compared utilizing two subdomains, by dividing the quarter panel along the line  $(x_1 = x_2)$  [see Fig. 8.3], and four subdomains as indicated in Fig. 8.4.

To express derivatives with respect to the physical domain coordinates  $x_1$  and  $x_2$ , the

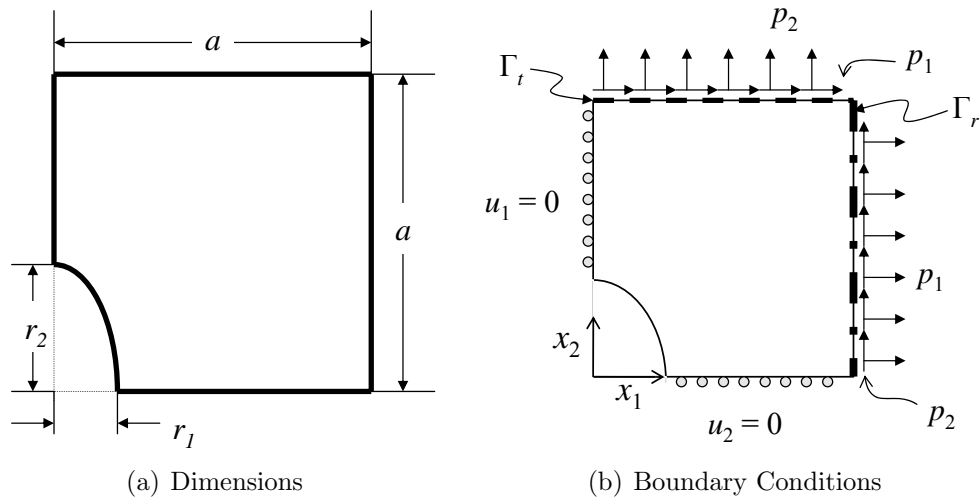


Figure 8.2. Dimensions and loading for a notched plane-stress panel.

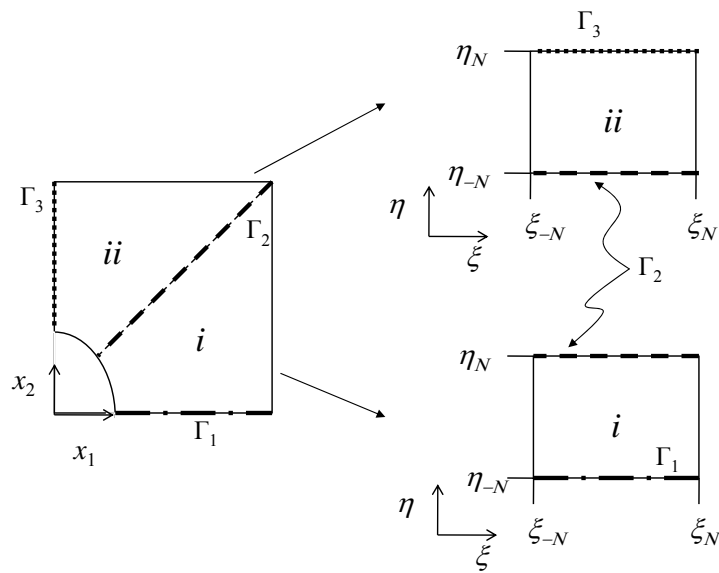


Figure 8.3. Domain decomposition and transformation onto two rectangular domains with boundary contours  $\Gamma_1$ ,  $\Gamma_2$  and  $\Gamma_3$  indicated.

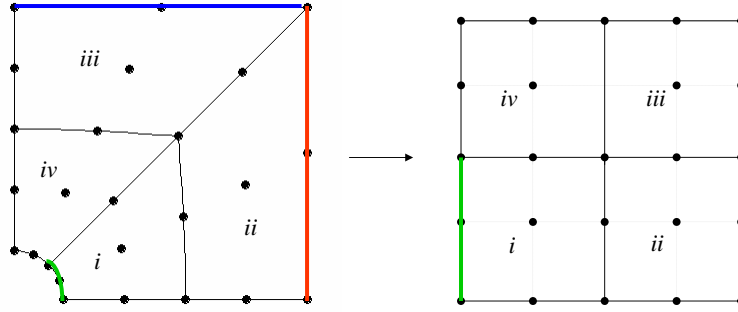


Figure 8.4. Four subdomain decomposition and transformation onto four rectangular domains.

domain mapping is differentiated resulting in the following relations:

$$\begin{aligned}
 \frac{\partial \xi}{\partial x_1} &= \frac{1}{|J|} \frac{\partial N_i}{\partial \eta} x_{2i}, & \frac{\partial \xi}{\partial x_2} &= -\frac{1}{|J|} \frac{\partial N_i}{\partial \eta} x_{1i}, \\
 \frac{\partial \eta}{\partial x_1} &= -\frac{1}{|J|} \frac{\partial N_i}{\partial \xi} x_{2i}, & \frac{\partial \eta}{\partial x_2} &= \frac{1}{|J|} \frac{\partial N_i}{\partial \xi} x_{1i}, \\
 |J| &= \left( \frac{\partial N_i}{\partial \xi} x_{1i} \frac{\partial N_j}{\partial \eta} x_{2j} - \frac{\partial N_i}{\partial \eta} x_{1i} \frac{\partial N_j}{\partial \xi} x_{2j} \right)
 \end{aligned} \tag{8.2}$$

with repeated index implying summation. Thus derivatives in the physical domain can be expressed through the basis function by:

$$\begin{aligned}
 \frac{\partial f}{\partial x_1} &= \frac{\partial \xi}{\partial x_1} \mathbf{A}_1 \mathbf{u} + \frac{\partial \eta}{\partial x_1} \mathbf{A}_2 \mathbf{u} = \mathbf{A}_{x_1}(\xi, \eta) \mathbf{u}, \\
 \frac{\partial f}{\partial x_2} &= \frac{\partial \xi}{\partial x_2} \mathbf{A}_1 \mathbf{u} + \frac{\partial \eta}{\partial x_2} \mathbf{A}_2 \mathbf{u} = \mathbf{A}_{x_2}(\xi, \eta) \mathbf{u}, \\
 f(\xi, \eta) &= \mathbf{B}(\xi, \eta) \mathbf{u}.
 \end{aligned} \tag{8.3}$$

where  $\mathbf{A}_1$ ,  $\mathbf{A}_2$ , and  $\mathbf{B}$  were defined in Eq. (3.27).

### 8.1.2 Incremental-Iterative Approach

For an inelastic plane-stress problem, the BVP is derived from the principle of virtual work for the geometry shown in Fig. 8.2 with loading on the top and right edges. The balance of

internal and external virtual work can be written as:

$$\int_{\Omega} {}^{t+\Delta t}\sigma_{ij}\delta{}^{t+\Delta t}\epsilon_{ij}d\Omega = \int_{\Gamma_r} {}^{t+\Delta t}p_i\delta{}^{t+\Delta t}u_id\Gamma_r + \int_{\Gamma_t} {}^{t+\Delta t}p_j\delta{}^{t+\Delta t}u_jd\Gamma_t \quad (8.4)$$

where  $p_i$  are the components of traction applied to the top edge,  $\Gamma_t$ , and the right edge,  $\Gamma_r$ , as indicated in Fig. 8.2. Note that  $p_1$  is an applied normal stress  $\sigma_{11}$  and  $p_2$  is an applied shear  $\sigma_{12}$  on the edge  $\Gamma_r$ ; and  $p_1$  is an applied shear  $\sigma_{12}$  and  $p_2$  is an applied normal  $\sigma_{22}$  on the edge  $\Gamma_t$ . To linearize the principle of virtual work equation, the stress, strain, and displacement increments are expressed by an increment from the stresses, strains, and displacements that satisfy equilibrium in the previous load step “ $t$ ”.

$$\int_{\Omega} ({}^t\sigma_{ij} + \Delta\sigma_{ij})\delta\Delta\epsilon_{ij}d\Omega = \int_{\Gamma_r} {}^{t+\Delta t}p_i\delta\Delta u_id\Gamma_r + \int_{\Gamma_t} {}^{t+\Delta t}p_j\delta\Delta u_jd\Gamma_t \quad (8.5)$$

Note that variations of stresses, strains, and displacements at load step “ $t$ ” are zero because equilibrium is satisfied at that load step. By expressing the strain increments in terms of the displacements, the variational statement is written as:

$$\int_{\Omega} [({}^t\sigma_{11} + \Delta\sigma_{11})\delta\Delta u_{1,1} + ({}^t\sigma_{22} + \Delta\sigma_{22})\delta\Delta u_{2,2} + ({}^t\sigma_{12} + \Delta\sigma_{12})(\delta\Delta u_{1,2} + \delta\Delta u_{2,1})] d\Omega = \int_{\Gamma_r} {}^{t+\Delta t}p_i\delta\Delta u_id\Gamma_r + \int_{\Gamma_t} {}^{t+\Delta t}p_j\delta\Delta u_jd\Gamma_t. \quad (8.6)$$

Because the variations are arbitrary, equilibrium is satisfied by letting  $\delta u_1 = 0$  with  $\delta u_2 = w_2$  and  $\delta u_2 = 0$  with  $\delta u_1 = w_1$  where  $w_1$  and  $w_2$  are arbitrary. For the present study, we choose  $w_1 = w_2 = W^I$  where  $W^I$  is a weight function of compact support for the  $I$ th



subdomain. Therefore, the equilibrium equations may be uncoupled to yield:

$$\begin{aligned} \int_{\Omega} [({}^t\sigma_{11} + \Delta\sigma_{11})W_{,1}^I + ({}^t\sigma_{12} + \Delta\sigma_{12})W_{,2}^I] d\Omega &= \int_{\Gamma_r} {}^{t+\Delta t}p_1 W^I d\Gamma_r + \int_{\Gamma_t} {}^{t+\Delta t}p_1 W^I d\Gamma_t \\ \int_{\Omega} [({}^t\sigma_{22} + \Delta\sigma_{22})W_{,2}^I + ({}^t\sigma_{12} + \Delta\sigma_{12})W_{,1}^I] d\Omega &= \int_{\Gamma_r} {}^{t+\Delta t}p_2 W^I d\Gamma_r + \int_{\Gamma_t} {}^{t+\Delta t}p_2 W^I d\Gamma_t. \end{aligned} \quad (8.7)$$

The increment on stress is expressed in terms of the increment of strain and the plane-stress reduced, tangential stiffness matrix  ${}^t\bar{C}_{ijkl}$ . Next, the increment of strains is expressed in terms of derivatives of increment of displacements. The Voigt notation was adopted to reduce the fourth rank stiffness tensor into a second rank tensor and the isotopicity was explicitly implemented ( $\bar{C}_{1111} = \bar{C}_{11}$ ,  $\bar{C}_{2222} = \bar{C}_{22}$ ,  $\bar{C}_{1122} = \bar{C}_{2211} = \bar{C}_{12} = \bar{C}_{21}$ ,  $\bar{C}_{1112} = \bar{C}_{1121} = \bar{C}_{1211} = \bar{C}_{2111} = 0$ ,  $\bar{C}_{2212} = \bar{C}_{2221} = \bar{C}_{1222} = \bar{C}_{2122} = 0$ ,  $\bar{C}_{1212} = \bar{C}_{2121} = \bar{C}_{1221} = \bar{C}_{2112} = \bar{C}_{66}$ ). Accordingly, the equilibrium equation is expressed in terms of the previous load step, stiffnesses, weight functions, and increments on the derivatives of displacements:

$$\begin{aligned} \int_{\Omega} (W_{,1}^I \bar{C}_{11} \Delta u_{1,1} + W_{,2}^I \bar{C}_{66} \Delta u_{1,2}) d\Omega + \int_{\Omega} (W_{,1}^I \bar{C}_{12} \Delta u_{2,2} + W_{,2}^I \bar{C}_{66} \Delta u_{2,1}) d\Omega \\ = \int_{\Gamma_r} {}^{t+\Delta t}p_1 W^I d\Gamma_r + \int_{\Gamma_t} {}^{t+\Delta t}p_1 W^I d\Gamma_t - \int_{\Omega} (W_{,1}^I {}^t\sigma_{11} + W_{,2}^I {}^t\sigma_{12}) d\Omega \end{aligned} \quad (8.8)$$

$$\begin{aligned} \int_{\Omega} (W_{,1}^I \bar{C}_{66} \Delta u_{1,2} + W_{,2}^I \bar{C}_{12} \Delta u_{1,1}) d\Omega + \int_{\Omega} (W_{,1}^I \bar{C}_{66} \Delta u_{2,1} + W_{,2}^I \bar{C}_{22} \Delta u_{2,2}) d\Omega \\ = \int_{\Gamma_r} {}^{t+\Delta t}p_2 W^I d\Gamma_r + \int_{\Gamma_t} {}^{t+\Delta t}p_2 W^I d\Gamma_t - \int_{\Omega} (W_{,1}^I {}^t\sigma_{12} + W_{,2}^I {}^t\sigma_{22}) d\Omega \end{aligned} \quad (8.9)$$

The basis function, Eq. (8.3), was used to approximate the incremental displacements and

their derivatives. Equilibrium can be expressed in matrix form by the following equations.

$$\begin{aligned}\mathbf{K}_{11}^I \Delta \mathbf{U}_1 + \mathbf{K}_{12}^I \Delta \mathbf{U}_2 &= \mathbf{F}_1^I \\ \mathbf{K}_{21}^I \Delta \mathbf{U}_1 + \mathbf{K}_{22}^I \Delta \mathbf{U}_2 &= \mathbf{F}_2^I\end{aligned}\tag{8.10}$$

where

$$\begin{aligned}\mathbf{K}_{11}^I &= \int_{\Omega} (W_{,1}^I \bar{C}_{11} \mathbf{A}_{x_1} + W_{,2}^I \bar{C}_{66} \mathbf{A}_{x_2}) d\Omega \\ \mathbf{K}_{12}^I &= \int_{\Omega} (W_{,1}^I \bar{C}_{12} \mathbf{A}_{x_2} + W_{,2}^I \bar{C}_{66} \mathbf{A}_{x_1}) d\Omega \\ \mathbf{K}_{21}^I &= \int_{\Omega} (W_{,1}^I \bar{C}_{66} \mathbf{A}_{x_2} + W_{,2}^I \bar{C}_{12} \mathbf{A}_{x_1}) d\Omega \\ \mathbf{K}_{22}^I &= \int_{\Omega} (W_{,1}^I \bar{C}_{66} \mathbf{A}_{x_1} + W_{,2}^I \bar{C}_{22} \mathbf{A}_{x_2}) d\Omega \\ \mathbf{F}_1^I &= \int_{\Gamma_r} {}^{t+\Delta t} p_1 W^I d\Gamma_r + \int_{\Gamma_t} {}^{t+\Delta t} p_1 W^I \Gamma_t - \int_{\Omega} (W_{,1}^I {}^t \sigma_{11} + W_{,2}^I {}^t \sigma_{12}) d\Omega \\ \mathbf{F}_2^I &= \int_{\Gamma_r} {}^{t+\Delta t} p_2 W^I d\Gamma_r + \int_{\Gamma_t} {}^{t+\Delta t} p_2 W^I \Gamma_t - \int_{\Omega} (W_{,1}^I {}^t \sigma_{12} + W_{,2}^I {}^t \sigma_{22}) d\Omega\end{aligned}\tag{8.11}$$

By selecting  $N_{int}$  weight functions of compact support, Eq. (8.10) becomes  $2N_{int}$  equations.

In the present study, the weight functions were chosen to have a quadratic variation over a rectangular support in the  $(\xi, \eta)$  domain. The weight functions are zero outside of this support. By Eq. (8.2), the derivatives of the weights with respect to the physical coordinates may be evaluated at a given  $(\xi, \eta)$ . Therefore, the integration in Eq. (8.11) is well suited to be done by Gauss quadrature in the  $(\xi, \eta)$  domain over the support of weight function  $I$ . Assuming a Gauss integration rule is chose with  $N_{ipt}$  integration points along the  $\xi$  and  $\eta$  directions indicated by  $\xi_i$  and  $\xi_j$  ( $i, j = \{1, 2, \dots, N_{it}\}$ ) and the Gauss weights are  $w(\xi_i)$  and

$w(\eta_j)$ , the approximation to  $\mathbf{K}_{11}^I$  in Eq. (8.11) can be written as

$$\begin{aligned} \mathbf{K}_{11}^I = & \sum_{i=1}^{N_{ipt}} \sum_{j=1}^{N_{ipt}} w(\xi_i) w(\eta_j) \left( W_{,1}^I(\xi_i, \eta_j) \bar{C}_{11}(\xi_i, \eta_j) \mathbf{A}_{x_1}(\xi_i, \eta_j) \right. \\ & \left. + W_{,2}^I(\xi_i, \eta_j) \bar{C}_{66}(\xi_i, \eta_j) \mathbf{A}_{x_2}(\xi_i, \eta_j) \right) |J|(\xi_i, \eta_j) \frac{(\xi_{max} - \xi_{min})(\eta_{max} - \eta_{min})}{4} \end{aligned} \quad (8.12)$$

where  $J$  is the Jacobian of the domain transformation given in Eq. (8.2) and  $\xi_{min}$ ,  $\xi_{max}$ ,  $\eta_{min}$ , and  $\eta_{max}$  are the boundaries in the support of weight function  $I$ . Similarly, the contour integrals in  $\mathbf{F}_1^I$  may be approximated by:

$$\begin{aligned} \int_{\Gamma_r} p_1 W^I d\Gamma_r &= \sum_{j=1}^{N_{ipt}} w(\eta_j) p_1(\xi_N, \eta_j) W^I(\xi_N, \eta_j) \sum_{i=1}^9 \sqrt{\left(\frac{\partial N_i}{\partial \eta} x_{1i}\right)^2 + \left(\frac{\partial N_i}{\partial \eta} x_{2i}\right)^2} \frac{\eta_{max} - \eta_{min}}{2}, \\ \int_{\Gamma_t} p_1 W^I d\Gamma_t &= \sum_{i=1}^{N_{ipt}} w(\xi_i) p_1(\xi_i, \eta_N) W^I(\xi_i, \eta_N) \sum_{i=1}^9 \sqrt{\left(\frac{\partial N_i}{\partial \xi} x_{1i}\right)^2 + \left(\frac{\partial N_i}{\partial \xi} x_{2i}\right)^2} \frac{\xi_{max} - \xi_{min}}{2}. \end{aligned} \quad (8.13)$$

For the case of two subdomains, there are two sets of  $2N_{int}$  equations. Let  $^{(i)}\mathbf{K}_{kl}$  indicate the collection of row matrices,  $\mathbf{K}_{kl}^I$ , for all integration weights ( $I = 1, 2, \dots, N_{int}$ ) and for the  $i$  subdomain as indicated in Fig. 8.3, and let  $^{(ii)}\mathbf{K}_{kl}$  indicate the collection of row matrices,  $\mathbf{K}_{kl}^I$ , for all integration weights ( $I = 1, 2, \dots, N_{int}$ ) and for the  $ii$  subdomain. Then the complete system of equations is given by:

$$\begin{bmatrix} ^{(i)}\mathbf{K}_{11} & ^{(i)}\mathbf{K}_{12} & 0 & 0 \\ ^{(i)}\mathbf{K}_{21} & ^{(i)}\mathbf{K}_{22} & 0 & 0 \\ 0 & 0 & ^{(ii)}\mathbf{K}_{11} & ^{(ii)}\mathbf{K}_{12} \\ 0 & 0 & ^{(ii)}\mathbf{K}_{21} & ^{(ii)}\mathbf{K}_{22} \end{bmatrix} \begin{Bmatrix} ^{(i)}\Delta\mathbf{U}_1 \\ ^{(i)}\Delta\mathbf{U}_2 \\ ^{(ii)}\Delta\mathbf{U}_1 \\ ^{(ii)}\Delta\mathbf{U}_2 \end{Bmatrix} = \begin{Bmatrix} ^{(i)}\mathbf{F}_1 \\ ^{(i)}\mathbf{F}_2 \\ ^{(ii)}\mathbf{F}_1 \\ ^{(ii)}\mathbf{F}_2 \end{Bmatrix} \quad (8.14)$$

It should be noted that in Eq. (8.14) the subdomains are uncoupled. The stiffness matrix is singular because the essential boundary conditions have yet to be enforced. To enforce the

essential boundary conditions and continuity between the two subdomains the traditional penalty method was used. The following additional contour integrals were evaluated:

$$\begin{aligned}
\mathbf{P}_1 &= \beta \int_{\Gamma_1} {}^{(i)}W^I {}^{(i)}\mathbf{B}(\xi, \eta) d\Gamma_1 \\
\mathbf{P}_2 &= \beta \int_{\Gamma_2} {}^{(i)}W^I {}^{(i)}\mathbf{B}(\xi, \eta) d\Gamma_2 \\
\mathbf{P}_3 &= \beta \int_{\Gamma_2} {}^{(i)}W^I {}^{(ii)}\mathbf{B}(\xi, \eta) d\Gamma_2 \\
\mathbf{P}_4 &= \beta \int_{\Gamma_2} {}^{(ii)}W^I {}^{(i)}\mathbf{B}(\xi, \eta) d\Gamma_2 \\
\mathbf{P}_5 &= \beta \int_{\Gamma_2} {}^{(ii)}W^I {}^{(ii)}\mathbf{B}(\xi, \eta) d\Gamma_2 \\
\mathbf{P}_6 &= \beta \int_{\Gamma_3} {}^{(i)}W^I {}^{(ii)}\mathbf{B}(\xi, \eta) d\Gamma_3
\end{aligned} \tag{8.15}$$

where the contours  $\Gamma_1$ ,  $\Gamma_2$ , and  $\Gamma_3$  are defined in Fig. 8.3 and  $\beta$  is a penalty parameter. For the present implementation,  $\beta$  was chosen to be  $10^6 E$ . These matrices can be approximated by Gauss quadrature in a similar fashion to that given in Eq. (8.13).

The two subdomain problem is fully constrained by augmenting the system of equations in the appropriate fashion:

$$\begin{aligned}
& \begin{bmatrix} {}^{(i)}\mathbf{K}_{11} + \mathbf{P}_2 & {}^{(i)}\mathbf{K}_{12} & -\mathbf{P}_3 & 0 \\ {}^{(i)}\mathbf{K}_{21} & {}^{(i)}\mathbf{K}_{22} + \mathbf{P}_1 + \mathbf{P}_2 & 0 & -\mathbf{P}_3 \\ -\mathbf{P}_5 & 0 & {}^{(ii)}\mathbf{K}_{11} + \mathbf{P}_4 + \mathbf{P}_6 & {}^{(ii)}\mathbf{K}_{12} \\ 0 & -\mathbf{P}_5 & {}^{(ii)}\mathbf{K}_{21} & {}^{(ii)}\mathbf{K}_{22} + \mathbf{P}_4 \end{bmatrix} \begin{Bmatrix} {}^{(i)}\Delta\mathbf{U}_1 \\ {}^{(i)}\Delta\mathbf{U}_2 \\ {}^{(ii)}\Delta\mathbf{U}_1 \\ {}^{(ii)}\Delta\mathbf{U}_2 \end{Bmatrix} \\
& = \begin{Bmatrix} {}^{(i)}\mathbf{F}_1 - \mathbf{P}_2 {}^{(i)}\mathbf{U}_1 + \mathbf{P}_3 {}^{(ii)}\mathbf{U}_1 \\ {}^{(i)}\mathbf{F}_2 - (\mathbf{P}_1 + \mathbf{P}_2) {}^{(i)}\mathbf{U}_2 + \mathbf{P}_3 {}^{(ii)}\mathbf{U}_2 \\ {}^{(ii)}\mathbf{F}_1 - (\mathbf{P}_4 + \mathbf{P}_6) {}^{(ii)}\mathbf{U}_1 + \mathbf{P}_5 {}^{(i)}\mathbf{U}_1 \\ {}^{(ii)}\mathbf{F}_2 - \mathbf{P}_4 {}^{(ii)}\mathbf{U}_2 + \mathbf{P}_5 {}^{(i)}\mathbf{U}_2 \end{Bmatrix} \tag{8.16}
\end{aligned}$$

or in a simplified form:

$${}^t\mathbf{K}^{(i)}\Delta\mathbf{u} = {}^t\mathbf{f}^{(i)} \quad (8.17)$$

where right superscript “(i)” implies the  $i$ th iteration of load step  $t$ . The global unknown vector  ${}^t\mathbf{u}^{(i)}$  may be iterated by the Newton-Raphson method:

$${}^t\mathbf{u}^{(i)} = \Delta\mathbf{u} + {}^t\mathbf{u}^{(i-1)} \quad (8.18)$$

Eq. (8.17) and (8.18) can be repeatedly used to increment  ${}^t\mathbf{u}$  until a convergence criterion is satisfied.

It should be noted that the development of the governing equations is for any nonlinear elastic material. The present analysis considers proportional loading of elastic-plastic materials. The von Mises yield criteria is used in a fashion that is applicable for both proportional loading and non-proportional loading. The complete procedure for determining the direction of loading, the stress, and plastic strain within a load step follows that given by Kojić and Bathe [187] and is detailed in Appendix G. This approach is applicable for both proportional loading or a general loading and unloading loop. In each iteration, the stress integration procedure identifies

$${}^{t+\Delta t}\sigma_{ij}, \quad {}^{t+\Delta t}\epsilon_{ij}^p, \quad {}^{t+\Delta t}\alpha_{ij}, \quad {}^{t+\Delta t}\bar{C}_{ij},$$

that is the total stress, the plastic strain, the back stress, and the tangential stiffness matrix at load step  $t+\Delta t$  knowing the total strain of load step  $t+\Delta t$  (derived from the displacements) and the values of plastic strain and stress from the previous load step

$${}^{t+\Delta t}\epsilon_{ij}, \quad {}^t\epsilon_{ij}^p, \quad {}^t\sigma_{ij}, \quad {}^t\alpha_{ij}.$$

Thus the approach can be used for a general form of loading.

Populating and factorizing  $\mathbf{K}$  for each iteration and load step would be expensive. Thus the modified Newton method is employed and  $\mathbf{K}$  is only populated and factorized once:

$${}^{t=0}\mathbf{K}^{(i=1)}\Delta\mathbf{u} = {}^t\mathbf{f}^{(i)} \quad (8.19)$$

By this approach, the tangential stiffness matrix is only obtained once. The procedure works well for proportional loading; however, for a general loading and unloading loop necessitates recalculating the tangential stiffness matrix to account for loading direction. Thus in this fashion the approach is really that of a nonlinear elastic material.

Applying the continuity condition between the elements via the penalty method can cause ill conditioning. Therefore, more weight functions than unknowns were chosen creating an over-determined system of equations that can be solved in the least-squares sense. The advantage of over-determining the system is that additional information (more weight function or test equations) allows the ILPGSM to obtain a converged solution despite the conditioning. This was done by choosing more weight functions than unknowns and thus resulting in more equations. The over-determined, least-squares approach is one approach used with the MLPG [188, 189]. Because the matrix is overdetermined, the QR-decomposition was used to factorize the stiffness matrix. That is for  $\mathbf{K}$  having dimensions  $n \times m$  where  $n > m$ , the matrices  $\mathbf{Q}$  and  $\mathbf{R}$  were determined such that:

$$\mathbf{K} = \mathbf{QR} \quad (8.20)$$

where  $\mathbf{Q}$  is  $n \times n$  matrix and  $\mathbf{R}$  is an  $n \times m$  upper triangular matrix. Letting the top  $m$  rows of  $\mathbf{Q}$  and  $\mathbf{R}$  be  $\tilde{\mathbf{Q}}$  and  $\tilde{\mathbf{R}}$  respectively then the least squares solution to Eq. (8.17) is approximated by:

$$\tilde{\mathbf{R}}\Delta\mathbf{u} = \tilde{\mathbf{Q}}^T ({}^t\mathbf{f}_{(i)}). \quad (8.21)$$

Note because  $\tilde{\mathbf{R}}$  is upper triangular, the global increment  $\Delta \mathbf{u}$  is estimated without the expense of populating and factorizing  $\mathbf{K}$ .

## 8.2 Numerical Results for Elastic Notched Panel

For numerical evaluation an elastic, infinite, plane-stress panel with an elliptical notch was considered. The problem was analyzed by Batra and Zhang [160] for a infinite panel with a circular hole. For sake of comparison, material properties and dimensions were chosen to remain consistent with Batra and Zhang [160]. To that regard the semi-major axis of the notch was specified to be  $r_2 = 0.5$  m and the aspect ratio  $r_2/r_1$  varied. The following isotropic elastic material properties were chosen:  $E = 226.9$  GPA,  $\nu = 0.33$ . An analytic solution for the present problem is well known [190]. While the panel is infinite, only the inner most square was modeled and the traction boundary conditions were applied from the analytic solution so that this solution remains valid. Both normal and shear traction along the top and right edges were imposed from the analytic solution [190]. Remaining consistent with Batra and Zhang [160], a square segment was modeled with  $a = 3$  m as indicated in Fig. 8.2.

The ILPGSM results were obtained using a Sinc mesh size taken to be  $h = 2/N$ . The number of particles along each axis in the Sinc approximation was chosen by setting  $N = 14$ , that is  $n = 29$  Sinc points along each edge.

Contours of displacement are compared for the present method and the analytic solution in Fig. 8.5 for a circular hole ( $a/b = 1$ ). The contours of the ILPGSM results are indistinguishable from those of the analytic solution, indicating the ILPGSM solution provides a very accurate numerical solution for the displacements in the present problem.

Contours of von Mises stress were plotted in Fig. 8.6 for the complete domain and zoomed in near the hole. Note that the contours are almost indistinguishable from those given by the analytic solution. There is some error in the solution near the line  $2 \leq x_1 \leq 2.5$ ,  $x_2 = 0$ .

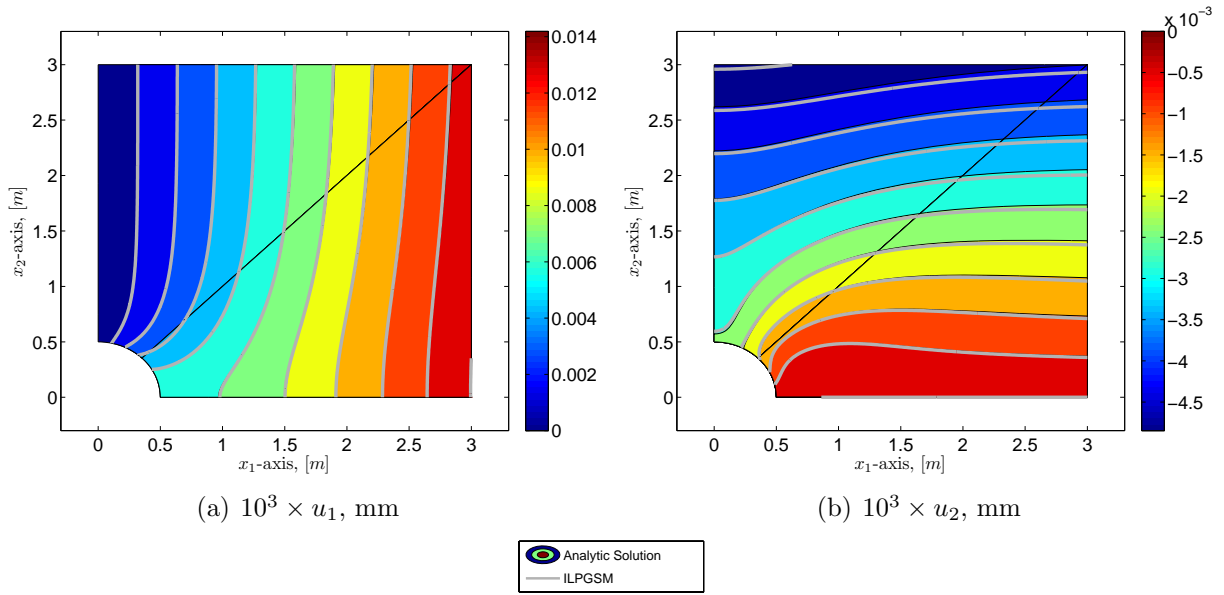


**Figure 8.5.** Displacement contours for a panel with a circular notch by ILPGSM and the analytic solution.

Similar results were obtained for an elliptical hole with aspect ratio of ten ( $r_2/r_1 = 10$ ). The contours of displacement are plotted in Fig. 8.7 and contours of von Mises stress are plotted in Fig. 8.8. For the severe notch, the ILPGSM still performs extremely well. The displacements by the ILPGSM and by the analytic solutions are significantly distinguishable only in the vicinity of  $x_1 = x_2 = 3$ . Recalling the choice to divide the domain along the edge  $x_1 = x_2$ , error in this vicinity may be related to the subdomain division and area mapping. In the vicinity of the substantial notch, the contours by the two solutions are indistinguishable. In general, the ILPGSM solution shows excellent correlation with the analytic solution.

The stress concentration factor in the vicinity of the hole was plotted for the circular hole and a hole with aspect ratio of 10 in Fig. 8.9. In each case, ILPGSM overestimated the stress concentration, predicting stress concentration of 3.2, 12.5, and 24 for the aspect ratio of 1, 5, and 10. Deviation from the analytic solution for the stress concentration obtained by ILPGSM are 7%, 14%, and 14% for aspect ratios of 1, 5, and 10, respectively. The erroneous



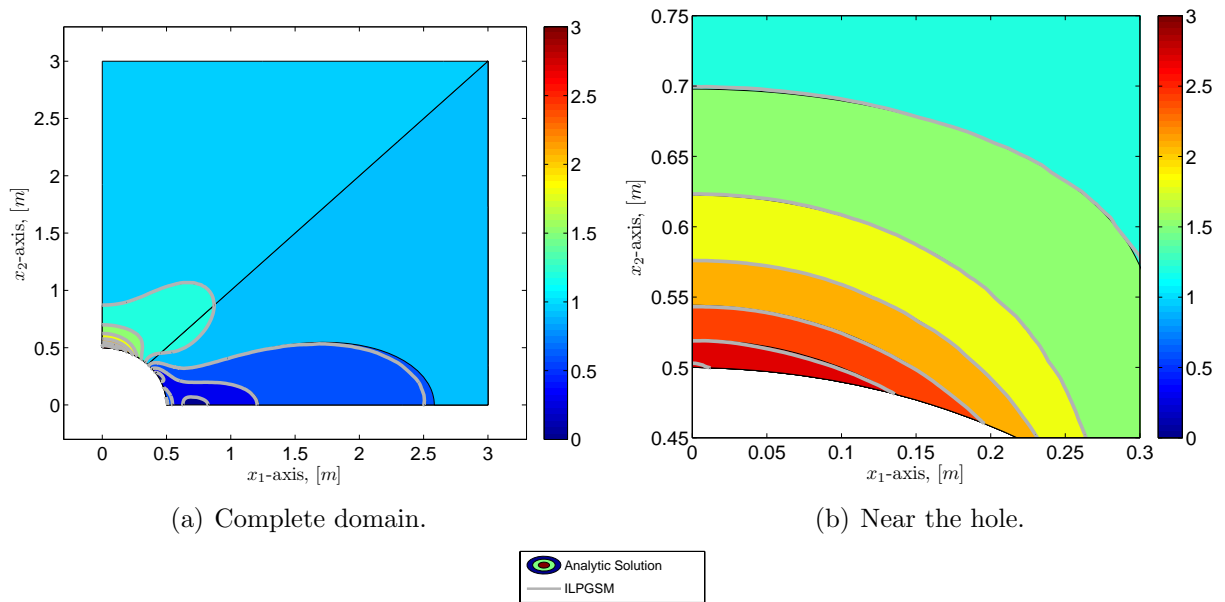


Figure 8.6. Contours of von Mises stress for a panel with a circular notch by ILPGSM and by the analytic solution.

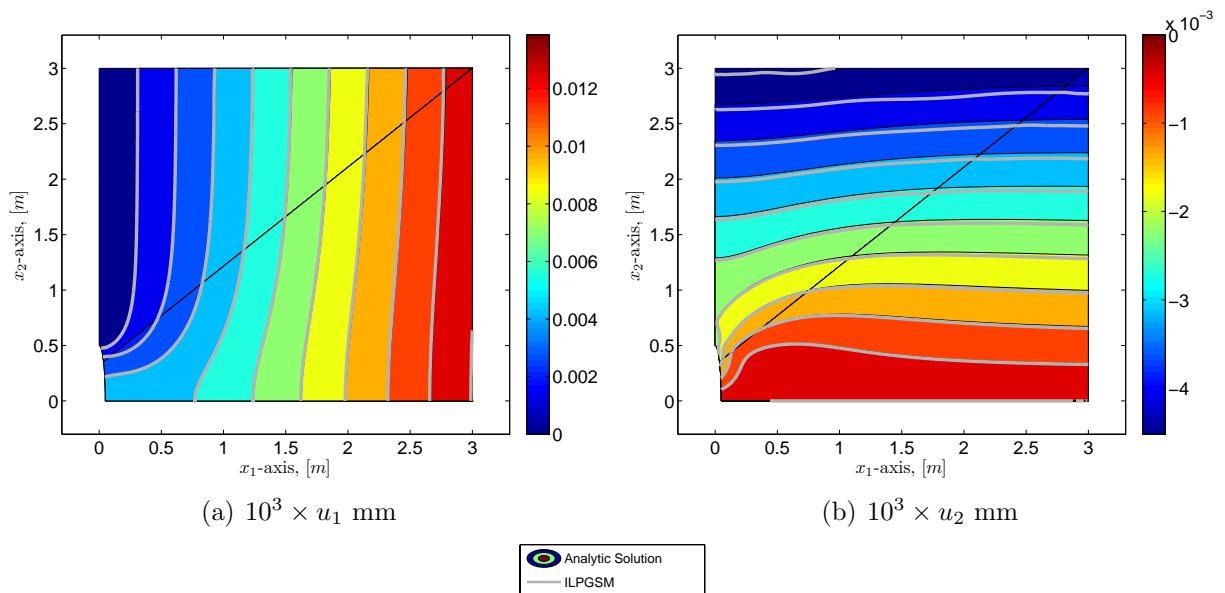
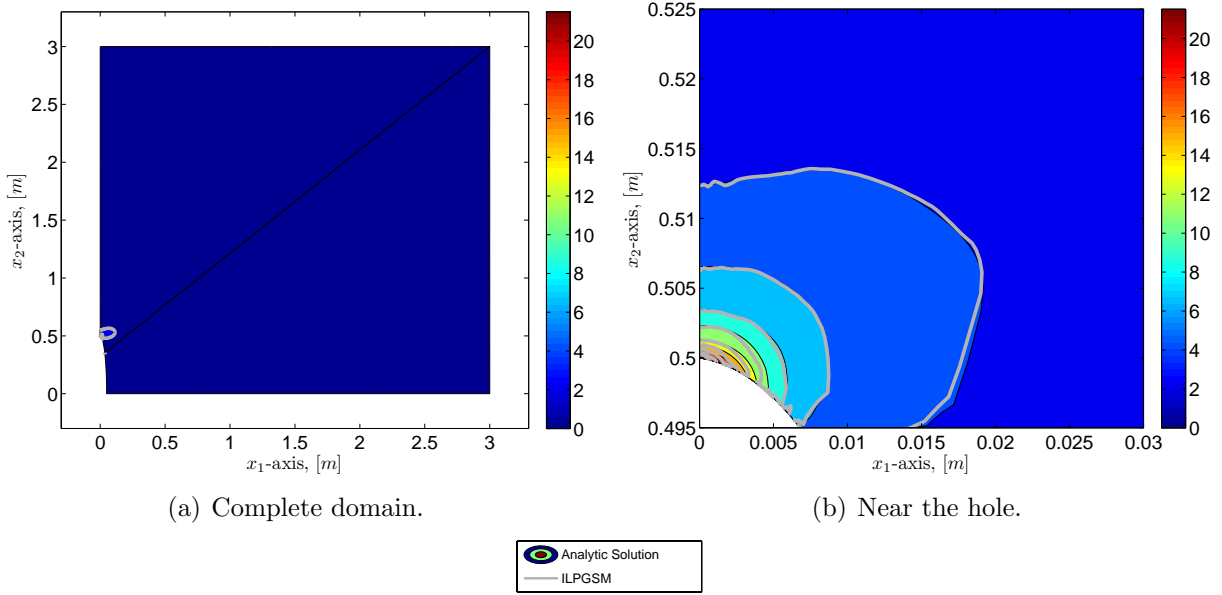


Figure 8.7. Displacement contours for a panel with an elliptical notch with aspect ratio  $r_2/r_1 = 10$  by ILPGSM and the analytic solution.



**Figure 8.8.** Contours of von Mises stress for a panel with an elliptical notch with aspect ratio of 10 by ILPGSM and the analytic solution.

stress predictions in this vicinity could be related to insufficient Sinc point refinement or applying the boundary conditions via the penalty method along the edge  $x_1 = 0$ .

### 8.2.1 J-Integral

The J-integral, a measure of the strain energy release rate, or work per unit fracture surface area may be computed by:

$$\int_{\Gamma} (W n_2 - n_i \sigma_{ij} u_{j,2}) d\Gamma \quad (8.22)$$

where  $W$  is the strain energy density for elastic material and the elastic strain energy density plus the energy dissipation density for an elastic-plastic material under proportional loading. For a line crack in an isotropic homogeneous linear elastic material, the J-integral is path independent and can be related to the mode I stress intensity factor [175, 176] by:

$$J = K_1 \left( \frac{1 - \nu^2}{E} \right) \quad (8.23)$$

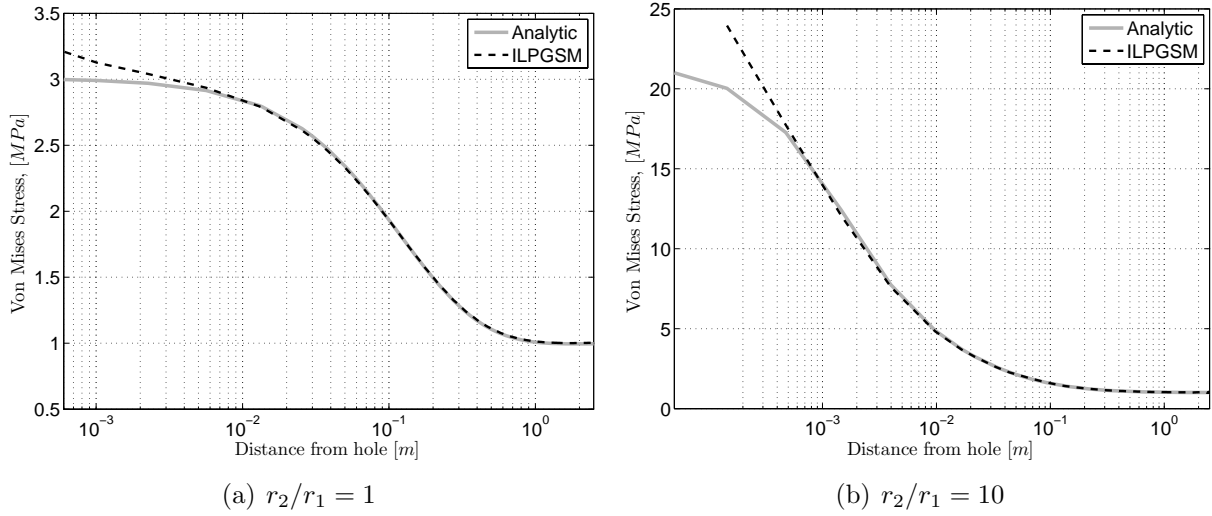


Figure 8.9. Von Mises stress along  $x_1 = 0$  in the vicinity of the hole.

Therefore, computing the J-integral is a critical element of assessing the damage tolerance of a structural member. For an elliptical notch, the J-integral is path independent; however, it is not independent of the beginning and ending points. This is illustrated in Fig. 8.10 below. Paths  $A$  and  $B$  give the same J-integral; however, path  $C$  does not. For the present problem the J-integral was analytically evaluated between the two extreme points along the minor-axis (paths  $A$  and  $B$  in Fig. 8.10) by Livieri and Segala [176]. Accordingly, the J-integral is analytically given by:

$$J = \frac{\sigma_{\text{norm}}^2}{E} \left\{ \frac{2r_2^4}{c(r_2 - r_1)^2} \left[ \frac{cr_1}{r_2^2} + \tan^{-1} \left( \frac{c}{r_1} \right) \right] - 4 \frac{r_2^2 r_1 c}{(r_2 - r_1)^3} \tan^{-1} \left( \frac{c}{r_1} \right) + \frac{r_1 c^4}{(r_2 - r_1)^4} \right\} \quad (8.24)$$

where  $r_2$  is the major-axis,  $r_1$  is the minor-axis and  $c = \sqrt{r_2^2 - r_1^2}$ .

The J-integral was numerically evaluated from the ILPGSM solution by selecting successive paths on which  $\xi$  or  $\eta$  are constant. Three paths were selected and the resulting J-integrals were averaged for the three paths. The standard deviation between the paths was less than 1% for each aspect ratio considered verifying path independence. The paths are shown for an aspect ratio of ten in the  $(x_1, x_2)$  domains in Fig. 8.11. Due to the problem's

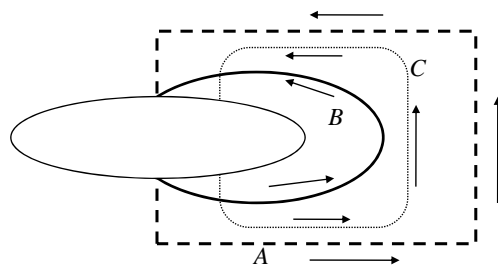


Figure 8.10. Path dependence of J-integral for elliptical hole

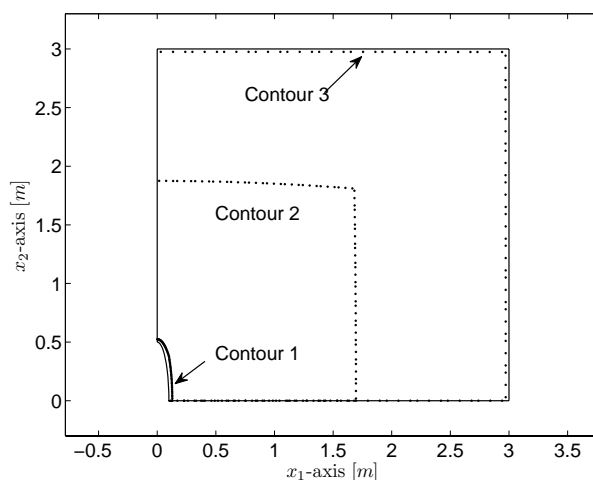
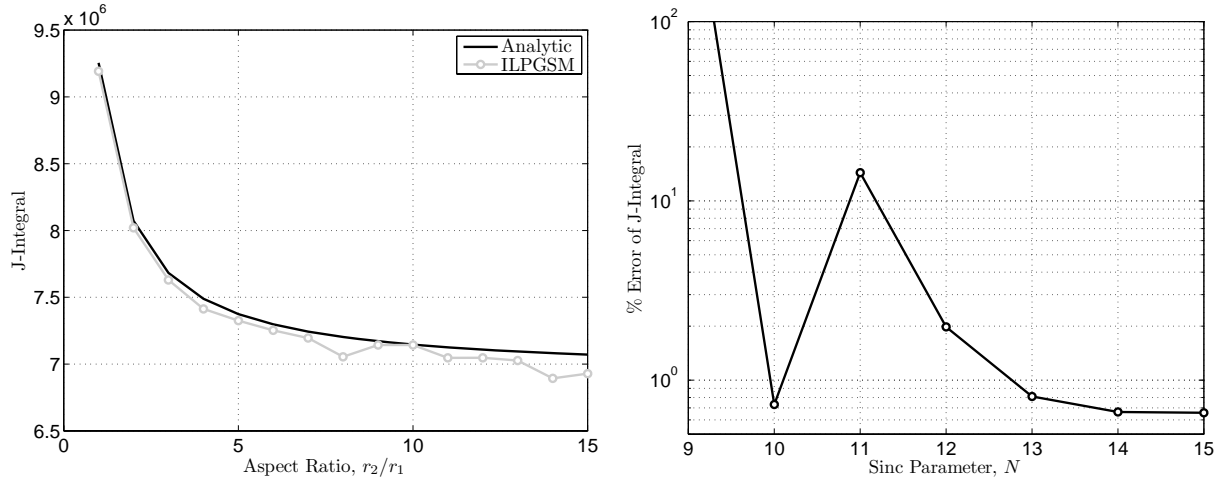


Figure 8.11. Paths on which the J-integral was computed and averaged for the elliptical notch with aspect ratio of 5.

symmetry, it can be shown that the J-integral defined around the whole notch (see Fig. 8.10) is twice that along the contours shown in Fig. 8.11. The numerical results were compared with that from the analytic solution for increasing aspect ratio in Fig. 8.12 using  $N = 15$ . The figure indicates that the J-integral compares well with the analytic solution. However, the results deteriorate with increasing aspect ratio due to increasing severity of the stress concentration.

In Fig. 8.12, the convergence of the J-integral is plotted for increasing number of Sinc points for aspect ratio of five. The result indicates  $N = 15$  (31 Sinc points along each axis in each subdomain) provides a converged solution.



(a) Comparison of J-integral to Analytic Solution      (b) Convergence with increasing  $N$  for  $r_2/r_1 = 5$

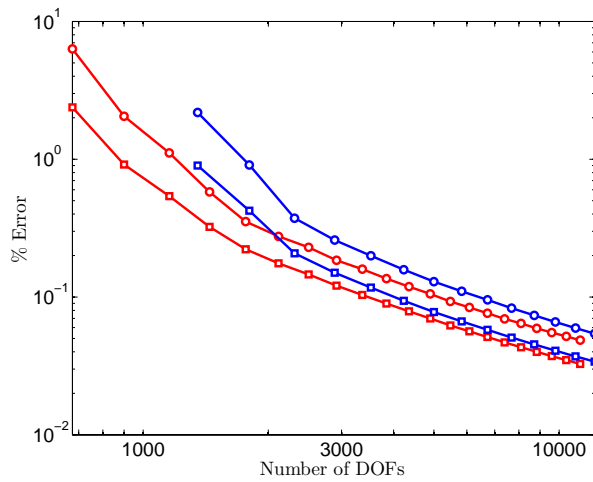
**Figure 8.12.** Comparison of J-integral by ILPGSM with the analytic solution. J-integral given in units of  $N/m$ .

### 8.2.2 Comparison of Additional Domain Decomposition

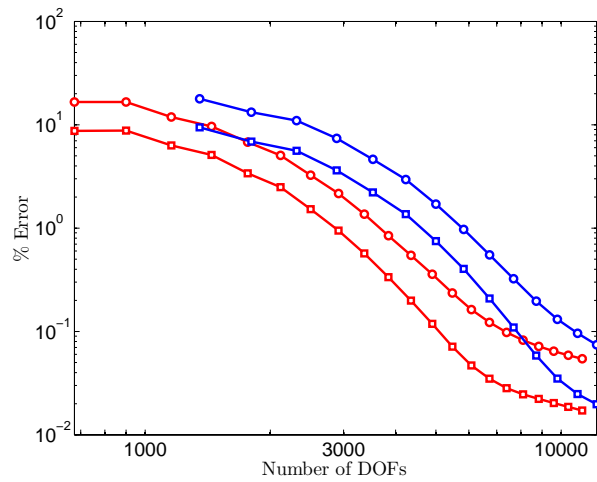
The numerical accuracy of the ILPGSM solution was compared for the infinite panel using two and four subdomains. In Fig. 8.13, the error defined by Eq. (4.7), of the displacements and stresses was plotted against the number of DOF for an elastic panel with a circular notch and elliptical notch with aspect ratio of 5. The figure indicates that the two subdomain decomposition approach is superior to the four subdomain decomposition solution and results in less error in the displacements and stress for equal number of unknowns. This result is somewhat intuitive because the Sinc series converges with increasing number of Sinc points. There are additional unknowns that are introduced as constants of integration. By using more subdomains, the user pays an additional penalty in introducing additional constants of integration which do not contribute to a convergent Sinc series.

The point-wise error of stress  $\sigma_{11}$  defined by:

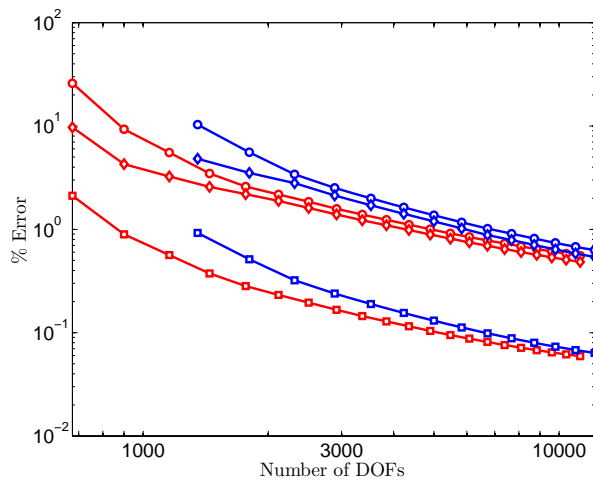
$$\|e\| = \frac{|\sigma_{11_{approx}} - \sigma_{11_{exact}}|}{q_0}, \quad (8.25)$$



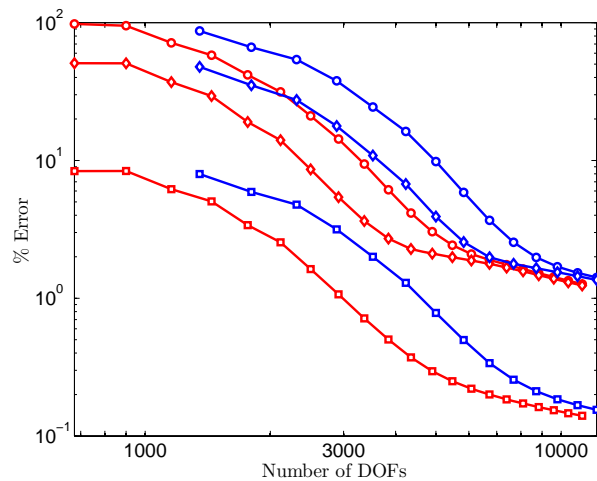
(a) 2 subdomains



(b) 4 subdomains



(c) 2 subdomains



(d) 4 subdomains

Figure 8.13. Comparison of % error in displacement and stresses from ILPGSM with 2 and 4 subdomains.

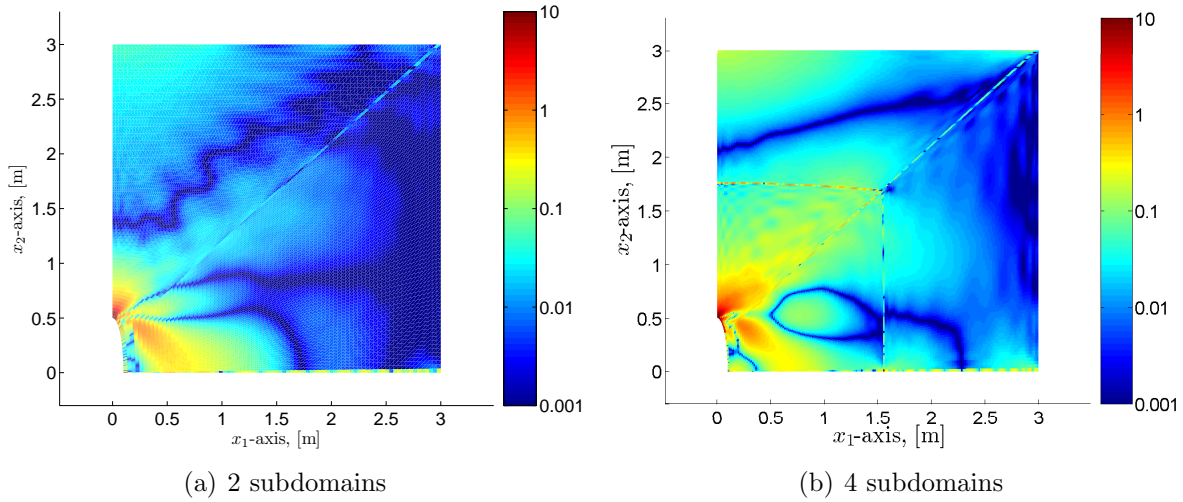


**Figure 8.14.** Comparison of error in stress component,  $\sigma_{11}$  from solution with two and four subdomains. The two subdomain solution had 7,396 DOF and the four subdomain solution had 7,688 DOF.

where  $\sigma_{11_{approx}}$  is the approximate stress and  $\sigma_{11_{exact}}$  is the exact, and where  $q_0$  is the applied far field stress at  $x_1 = \infty$ , was plotted in Fig. 8.14). The solution was obtained with two subdomains and  $N = 20$  and with four subdomains and  $N = 15$ . These two analyses result in similar number of total DOF (7,396 DOF for the two subdomain solution and 7,688 DOF for the four subdomain solution). Both figures indicate that the maximum error occurs in the vicinity of the notch tip ( $x_1 = 0, x_2 = 0.5$ ). However, the solution obtained using two subdomains has far more blue and green areas and the solution obtained using four subdomains exhibits more yellow and red areas over  $0 \leq x_1 \leq 1.5$  and  $0 \leq x_2 \leq 1.5$ . Thus confirming the hypothesis that using a minimum number of subdomains is ideal with this method. Furthermore, the subdomain boundaries exhibit larger error than the interior of each subdomain. This is an artifact of using the penalty method to impose essential boundary conditions.

**Table 8.10. Elastic-plastic material properties for a generic aluminum alloy.**

Properties	Values
$E$ , GPa	70
$\nu$	0.33
$\sigma_y$ , MPa	400
$E_p$ , GPa	1.4

### 8.3 Numerical Results for Elastic-Plastic Notched Panel

Elastic-plastic panels with circular and elliptical notches were studied numerically using the ILPGSM. The panels were assumed to have a bilinear kinematic hardening material law as detailed by Kojić and Bathe [187]. The material properties for a generic aluminum alloy were used. The properties are summarized in Table 8.10.

In each case, the panel had finite dimensions as shown in Fig. 8.2 with  $a = 0.71$  m and  $r_2 = 0.12$  m. Uniform tension was applied to the right edge, and the top surface was free. The symmetry boundary conditions were applied to surfaces  $x_1 = 0$  and  $x_2 = 0$  (see Fig. 8.2). For the panel with a circular notch, the load was increased proportionally from 10 MPa to 340 MPa in steps of 10 MPa. A relative convergence criterion was used to determine convergence of the modified Newton method. Convergence was assumed to occur when the norm of the vector of displacement increments was  $10^{-4}$  times the norm of displacements at the Sinc points. That is:

$$\frac{\|\{\Delta u_1(\xi_i, \eta_j), \Delta u_2(\xi_i, \eta_j)\}\|}{\|\{u_1(\xi_i, \eta_j), u_2(\xi_i, \eta_j)\}\|} < 1 \times 10^{-4} \quad (8.26)$$

where  $i, j = \{-N, -N + 1, \dots, N\}$ . The onset of plasticity was estimated to occur at a load of approximately 130 MPa assuming the panel behaves similarly to the infinite panel.

For a panel with a circular notch, the ILPGSM implemented in MATLAB was used to analyze the problem. The Sinc points were distributed using  $N = 14$  or  $n = 29$  Sinc points along each edge in each subdomain and using a mesh size of  $2/N$ . A total of 1,682



**Table 8.11. L2 norm of displacements between fine and coarse mesh solution for notched elastic-plastic panels.**

Notch Aspect Ratio	# Elements Coarse	# Elements Fine	$e_{u_1}$	$e_{u_2}$
1	2,736	7,002	0.06 %	0.10 %
5	3,077	13,172	0.03 %	0.18 %

Sinc points were used resulting in a system of 4,356 equations in 3,844 unknowns. For this problem, the QR-decomposition using LAPACK took a total of 45 seconds on a single 2.99 GHz processor. For the panel with the elliptical notch, more Sinc points were used. The ILPGSM was implemented in Fortran 90. The Sinc points were distributed using  $N = 20$  or  $n = 41$  Sinc points along each edge in each subdomain and using a mesh size of  $2/N$ . A total of 3,362 Sinc points were used resulting in a system of 8,100 equations in 7,396 unknowns. For this problem, the QR-decomposition using LAPACK took a total of 297 seconds on the same 2.99 GHz processor.

Results were compared with a FEM solution obtained in ABAQUS. The L2 norm of the difference in  $u_1$  and  $u_2$  was computed by Eq. (4.7) for the first load step. The L2 norm of the converged mesh are summarized in Table 8.11. For each mesh, the elements were refined near the notch to obtain the stress concentration more accurately. A total of 7,002 elements were used to mesh the panel with a circular hole and 13,172 elements were used to mesh the panel with an elliptical hole with aspect ratio of five. The von Mises stress was examined to insure that there were no stress peaks occurring in only one element. For the panel with circular notch, the converged FEA mesh with boundary conditions and the ILPGSM Sinc point distribution may be seen in Fig. 8.15.

### 8.3.1 Circular Notch

The maximum  $u_1$  displacement was plotted against the applied tension load in Fig. 8.16. The FEA and ILPGSM solutions are indistinguishable. Note that while the onset of plasticity occurs near 130 MPa applied load, the displacement shows very mild nonlinearity until

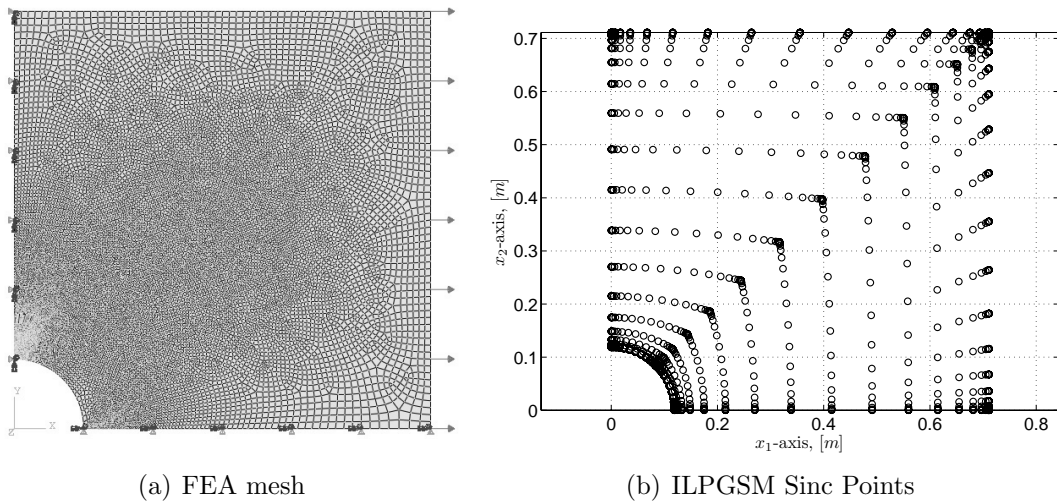


**Figure 8.15.** Converged FEA mesh and ILPGSM Sinc point distribution for elastic-plastic plane-stress panel with circular notch.

approximately 300 MPa applied load. Near 340 MPa the panel becomes fully plastic. The von Mises stress and plastic strain ( $\epsilon_{11}^p$ ) were plotted along the line  $x_1 = 0$  in Fig. 8.17 for load increments  $q = 100, 130, 150, 200, 250, 300,$  and  $340$  MPa. The success of the ILPGSM for capturing the plasticity is apparent. Note that the ILPGSM performs well at capturing the plastic zone size and tip stress results tend to deteriorate. As the plasticity grows, the stress slope discontinuity moves into areas of less densely populated Sinc points (see Fig. 8.15). This results in deterioration of the methods accuracy as evident by slight wiggles in the stress in load step 6 and 7 and in the drop in plastic strain near the hole in steps 6 and 7.

The growth of the plastic zone size was plotted in Fig. 8.18. Note that the two analyses provide similar results. In general, ILPGSM results in larger plastic zone size than does the FEA. In Fig. 8.18(d) there are additional blue contours indicating yielded material. This result is likely because of an insufficient refinement in the Sinc point distribution.

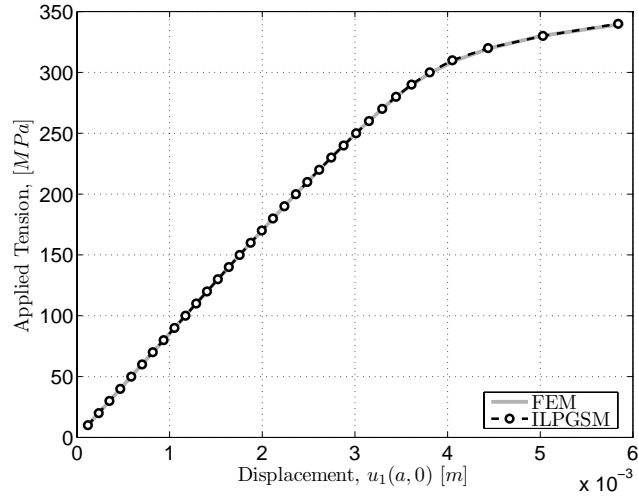


Figure 8.16. Displacement of the point  $(a, 0)$  versus applied tension load. The onset of plasticity occurs at about 130 MPa.

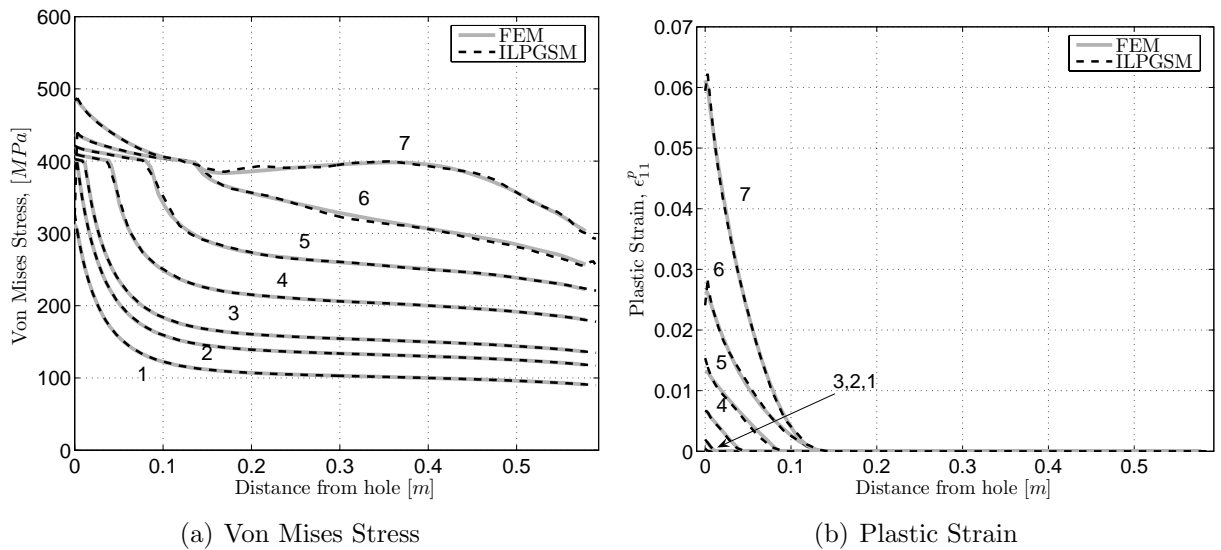


Figure 8.17. Von Mises stress and plastic strain for panel with circular notch. Load step 1 - 100 MPa, 2 - 130 MPa, 3 - 150 MPa, 4 - 200 MPa, 5 - 250 MPa, 6 - 300 MPa and 7 - 340 MPa.

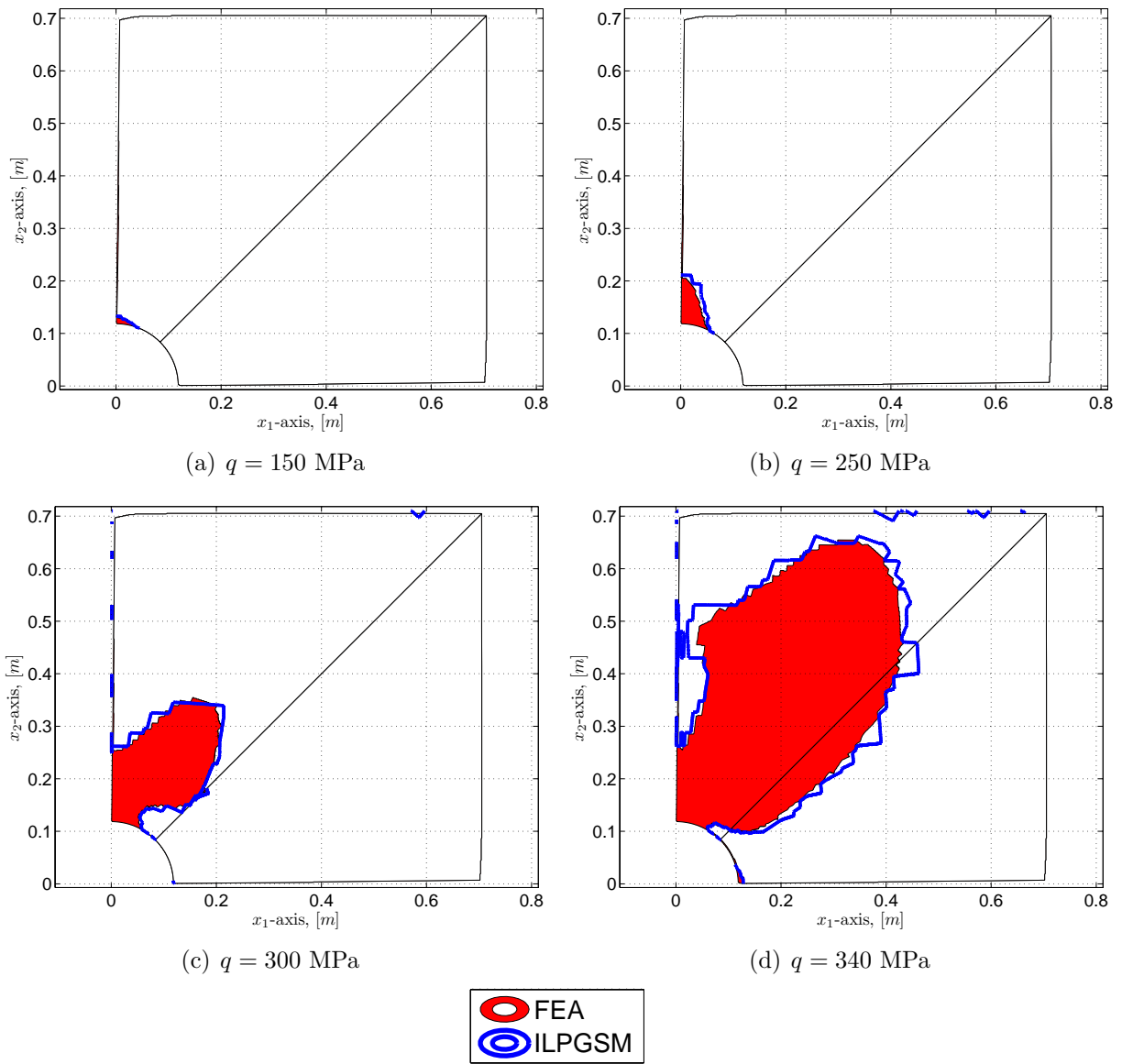
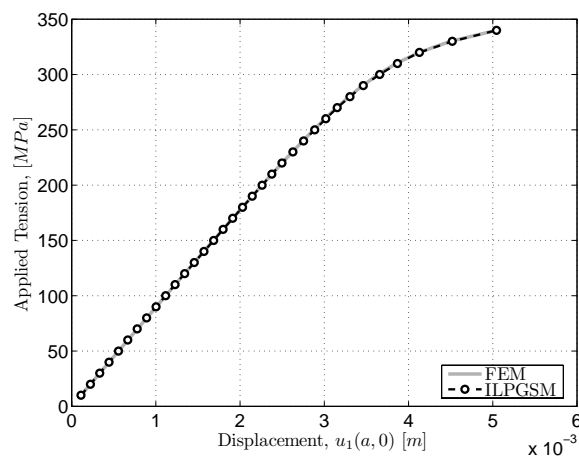


Figure 8.18. Growth of plastic zone with increasing applied load by ILPGSM and FEA. The red and blue contours indicates yielded material from the FEA and ILPGSM respectively.



**Figure 8.19.** Displacement of the point  $(a, 0)$  versus applied tension load. The onset of plasticity occurs at about 36 MPa.

### 8.3.2 Elliptical Notch

The maximum  $u_1$  displacement was plotted against the applied tension load in Fig. 8.19 for a panel with an elliptical notch with aspect ratio of five. The FEA and ILPGSM solutions are indistinguishable. For the elliptical case, the onset of plasticity occurs near 36 MPa applied load; however, the plasticity remains localized until approximately 300 MPa applied load.

The von Mises stress and the plastic strain are plotted in Fig. 8.20. The von Mises stress by the ILPGSM solution and by the FEA solution are nearly indistinguishable. Even plotting with a logarithmic ordinance scale, the FEA and ILPGSM stress appears nearly indistinguishable. The plastic strain is predicted slightly higher by the ILPGSM in the direct vicinity of the hole. Nonetheless, the figure indicates an excellent correlation between the ILPGSM and the FEA solutions.

The growth of the plastic zone size was plotted in Fig. 8.21. The two analyses provide very similar results. The plastic zone size is predicted to be larger in some areas and smaller in others.

Contours of von Mises stress for the panel with an elliptical notch were plotted in Fig. 8.22. Contours of displacements were plotted in Fig. 8.23. In each case, the contours are indis-

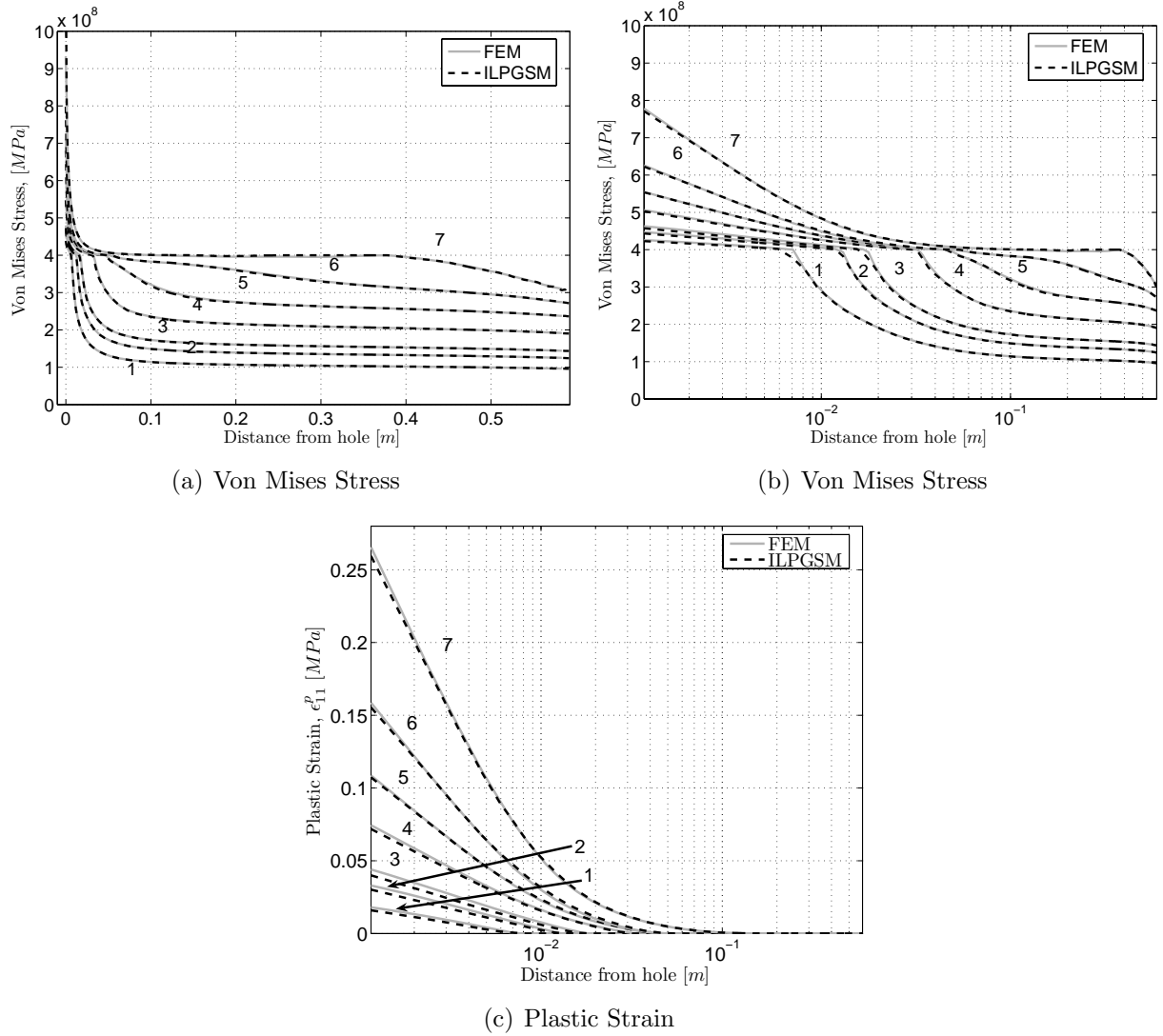


Figure 8.20. Von Mises stress and plastic strain for panel with elliptical notch of aspect ratio of five ( $r_2/r_1 = 5$ ). Load step 1 - 100 MPa, 2 - 130 MPa, 3 - 150 MPa, 4 - 200 MPa, 5 - 250 MPa, 6 - 300 MPa and 7 - 340 MPa.

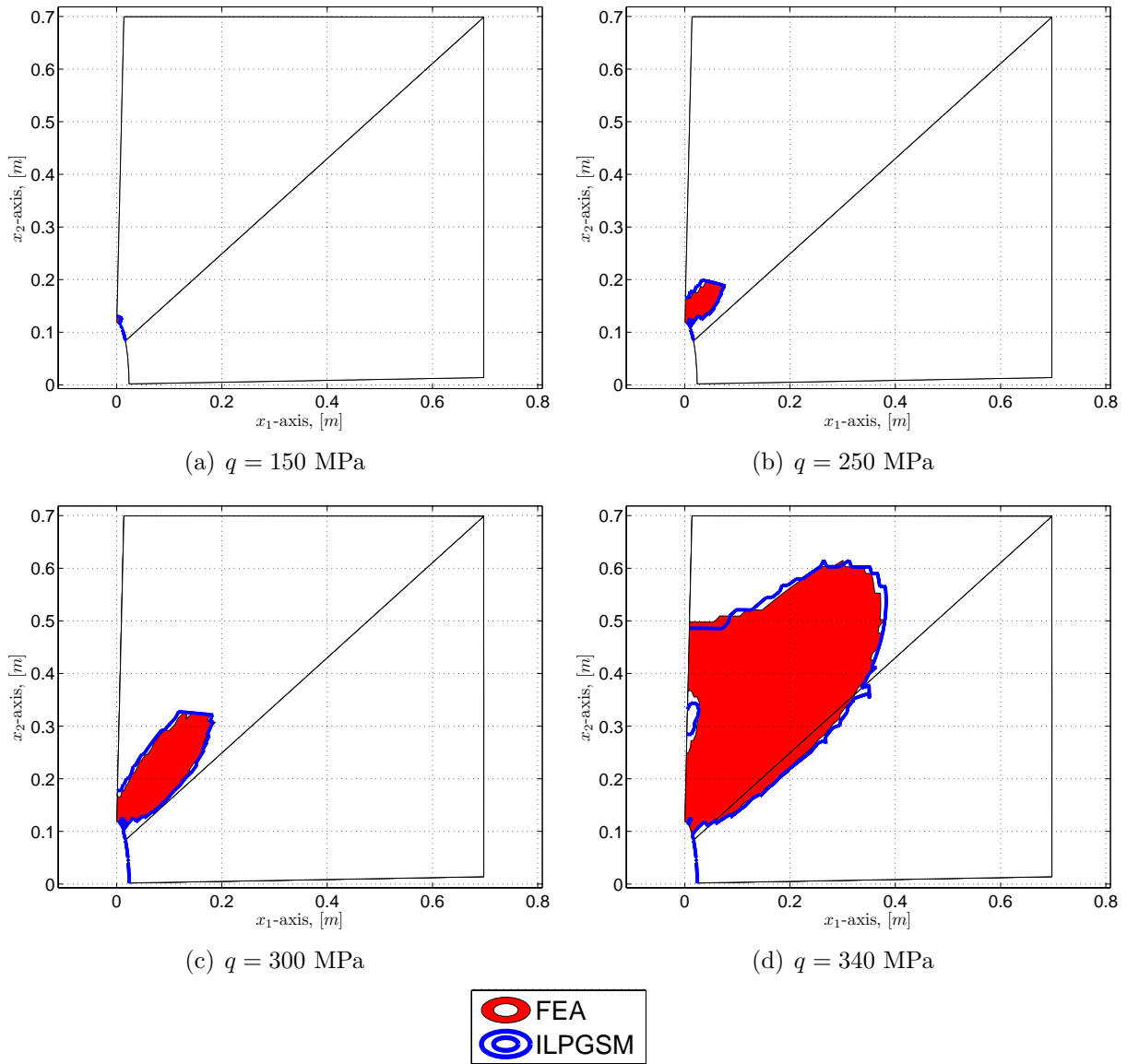


Figure 8.21. Growth of plastic zone with increasing applied load by ILPGSM and FEA for elliptical notch with aspect ratio of five ( $r_2/r_1 = 5$ ). The red and blue contours indicates yielded material from the FEA and ILPGSM respectively.

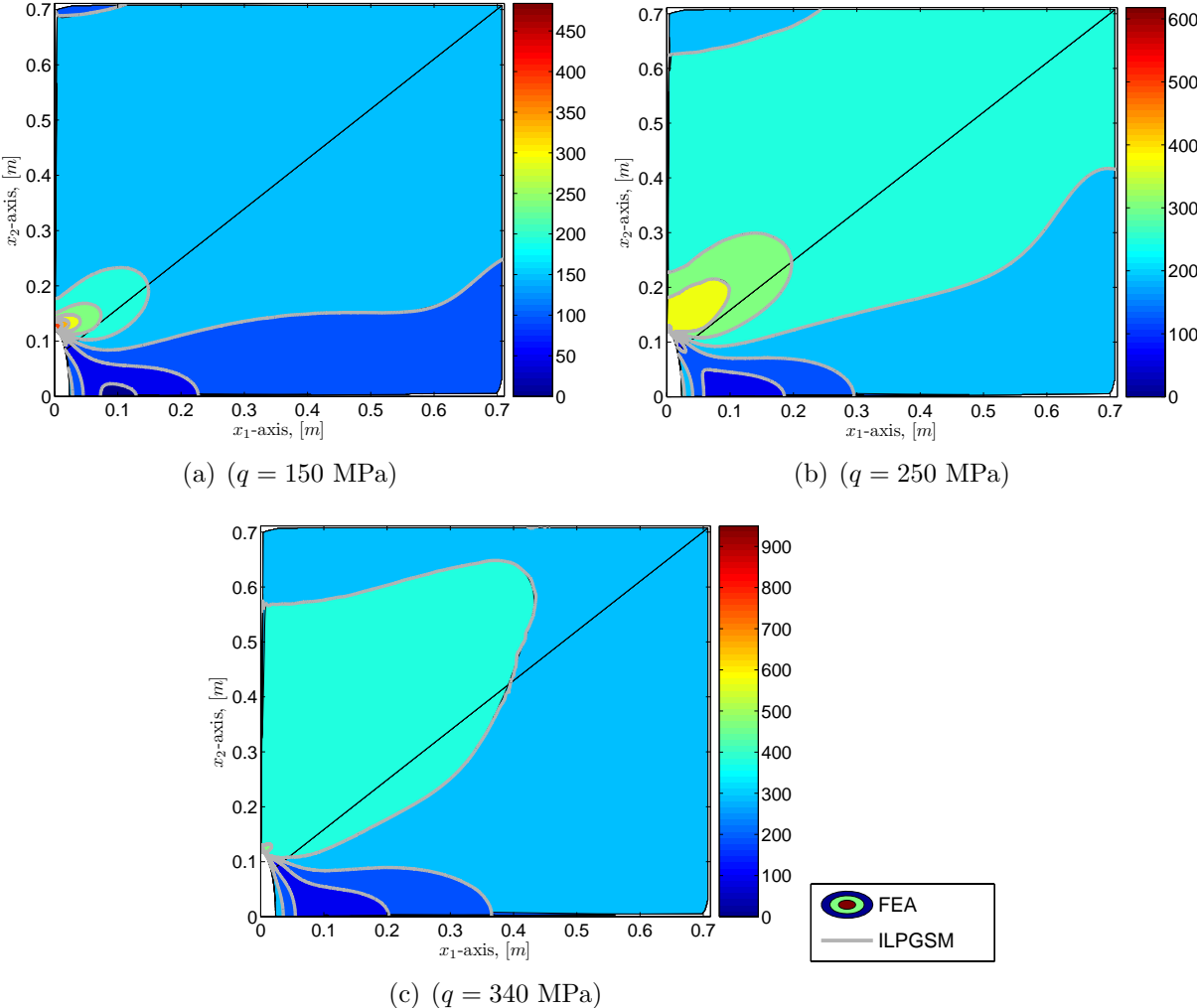


Figure 8.22. Comparison of contours of von Mises stress by ILPGSM and FEA for panel with elliptical hole.

tinguishable from the FEA result. Contours of displacement and von Mises stress for the elastic-plastic panel with a circular notch were plotted in Appendix I. The results were similar to those presented here in the text.

### 8.3.3 J-integral

The J-integral was computed for both the panel with circular hole and elliptical hole. For the ILPGSM results, the J-integral was averaged over the three contours shown in Fig. 8.11.



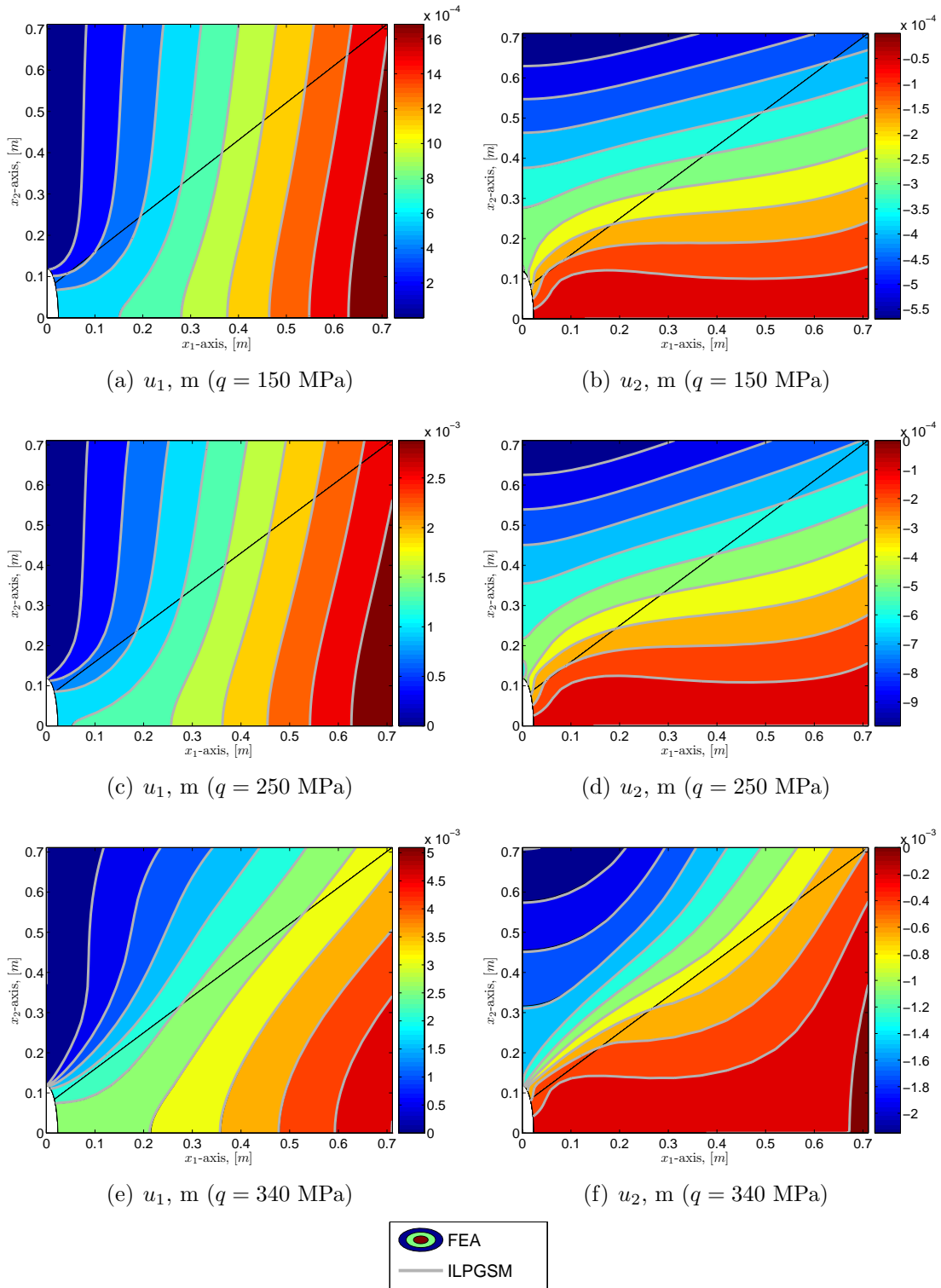
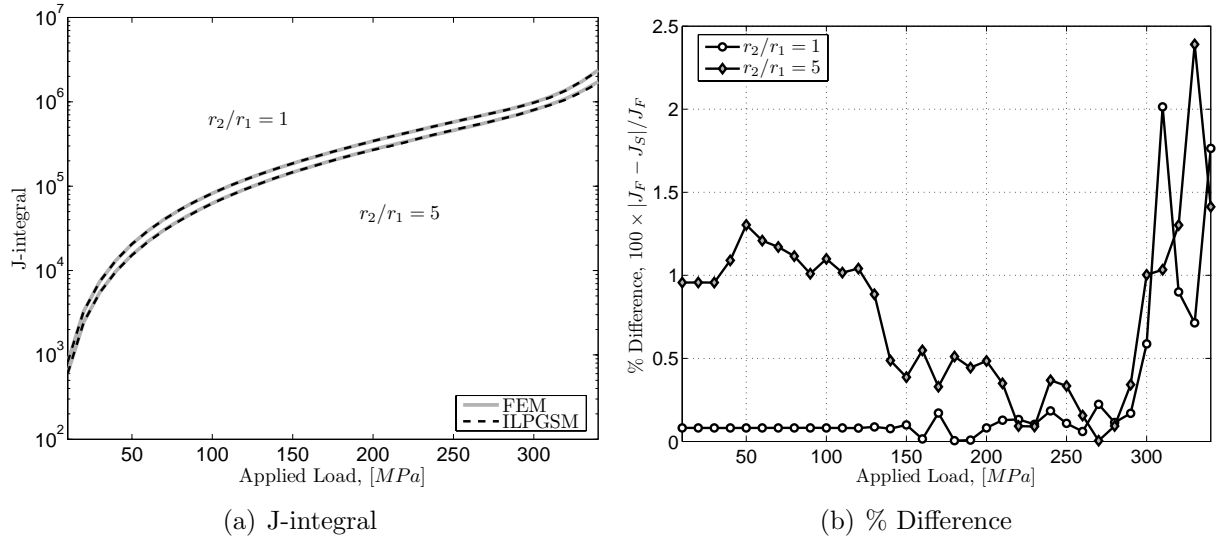


Figure 8.23. Comparison of contours of  $u_1$  and  $u_2$  by ILPGSM and FEA for panel with elliptical hole.



**Figure 8.24.** Comparison of J-integral computed by ILPGSM and ABAQUS FEA. J-integral given in units of  $N/m$ .

Five contours were averaged for the FEA results in ABAQUS. The results are compared in Fig. 8.24. The J-integral is computed within 2% and 2.5% of that by the FEA for the circular and elliptic hole, respectively.

## 8.4 Summary and Conclusions

In this chapter, the ILPGSM was extended for analysis of elastic-plastic materials. Both elastic and elastic-plastic, plane-stress panels with elliptical and circular notches were considered. The results showed that the ILPGSM provides sufficient accuracy for both elastic and elastic-plastic problems. The elastic panel was compared with the analytic solution for the problem [190]. The elastic-plastic problem was compared with a FEA performed in ABAQUS. The results indicate a high level of accuracy for both the linear and nonlinear problems, even with large levels of plastic flow occurring. The accuracy decreases for increasing hole aspect ratio (with the same number of Sinc points), a result which is not surprising because with FE solution more elements are required for a converged solution for the highly elliptic, “crack-like” notch.

## 9 Delamination Analysis using FSDT and a Cohesive Interface Model

In this chapter, the use of the ILPGSM for analysis of delamination in composite materials is examined. Delamination can be a major failure mode in composites and hybrid materials. Interlaminar failures most often originate at free-edges, interlaminar manufacturing defects, or dropped plies [98, 191, 192]. The delaminations result in reduced stiffness and strength and can substantially reduce the integrity of the structural component or result in the ultimate failure of the structure.

There are several approaches that have been developed to model delamination in composites. The earliest stress based criterion for delamination, the quadratic delamination criterion, was developed by Brewer and Lagace and has been used to successfully predict the onset of delamination [61]. Traditional fracture mechanics techniques such as the Virtual Crack Closure Technique (VCCT) have been successfully used to predict delamination growth by many authors [193, 194, 195]. In this technique, the strain energy release rates (or the differential release of strain energy per differential change in crack area) for mode I ( $G_I$ ), mode II ( $G_{II}$ ), and mode III ( $G_{III}$ ) are computed by allowing the interlaminar damage to propagate a small distance  $\Delta a$ . The strain energy release rates are compared with their critical value  $G_{Ic}$ ,  $G_{IIc}$ , and  $G_{IIIc}$  using a mixed mode criterion of some form. Kapania and Wolfe used the VCCT to study delamination buckling in beams and plates by simple one and two dimensional analyses [195]. Recently, Moorthy and Reddy [196] utilized the VCCT with a geometrically nonlinear layer-wise theory to predict strain energy release rates in the presence of delamination. Yang, Chadegani, and Tomblin [197] used the VCCT to study debonding of composite lap joints with thick bond lines.

One of the most widely used analysis methods for debonding and delamination is the cohesive zone modeling technique. To the author's knowledge, the cohesive zone model

(CZM) was first introduced by Barenblatt [198] and Dugdale [199]. The cohesive zone model concept is an indirect application of fracture mechanics. A constitutive law representing the adhesive layer in which the material softens in such a way that the strain energy release rate at crack propagation (no stiffness at the crack tip) is equal to the critical strain energy release rate. To the author's knowledge, Schellekens and de Borst [200] were the first to propose a separate element for the interface material within a FEA.

Interface elements or cohesive finite elements have been used by many authors [201, 202, 203, 204, 205, 206, 207] and are currently provided with most FE packages for performing delamination analysis. The element library in ABAQUS contains both 2D (COH2D4) and 3D (COH3D8) cohesive finite elements [75]. These elements allow both stress (quadratic delamination criterion) and displacement based criteria for damage onset as well as delamination propagation based on the strain energy release rates. There are options to model the cohesive in a continuum sense or as a traction-separation law. If the continuum model is adopted the adhesive layer is modeled using the assigned material properties with finite thickness. If the traction-separation behavior is selected, the adhesive is negligible thin and the tractions are related to the separation gap between the adherents. In either case, the constitutive law has a linear region followed by either an exponential or linear softening region. For a single mode (I) delamination, the traction separation law is illustrated in Fig. 9.1. For mixed mode delamination, the strain energy release rates can be mixed using a power law [218] or by the Benzeggagh and Kenane criterion [208] in which the total energy release rate  $G_T = G_I + G_{II}$  is expressed in terms of the ratio  $G_{II}/G_T$  [209].

The bilinear constitutive relation was used by Camanho and Dávila [207] for analyzing mode I, mode II, and mixed-mode (I + II) delamination growth of a PEEK composite. Several authors have successfully utilized the interface element's bilinear model in ABAQUS to study failure in laminates [210, 211, 212, 213]. Additional cohesive models have been developed. Needleman [214] used a smoothly varying quadratic traction separation law that

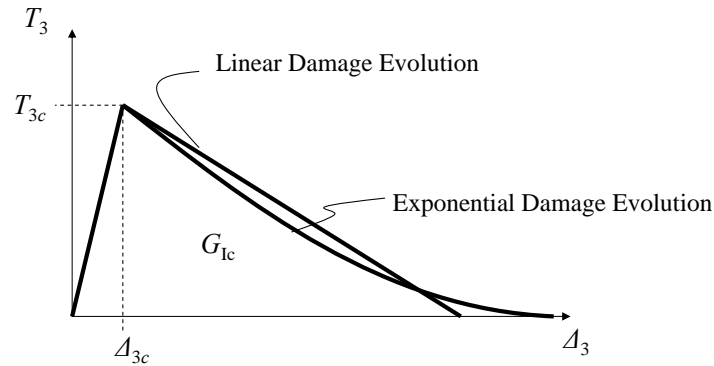


**Figure 9.1.** Cohesive damage evolution laws for traction-separation behavior in ABAQUS.

was derived from an interface potential. Xu and Needleman [215] developed an exponential traction separation law based on the strain energy release rate.

With its implementation into commercial FE packages, the bilinear cohesive model is the most widely used. However, the discontinuity of derivative associated with the bilinear cohesive model can lead to numerical problems or even convergence failure [216]. Goyal, Johnson, and Dávila [60] presented an irreversible exponential constitutive law (see Fig. 9.2). Unlike the bilinear law, the exponential cohesive law has a continuous derivative. The sharp peak is replaced by a smoothly varying continuous one. Rose *et al.* [217] indicated that the exponential law more accurately represents the atomic separation occurring.

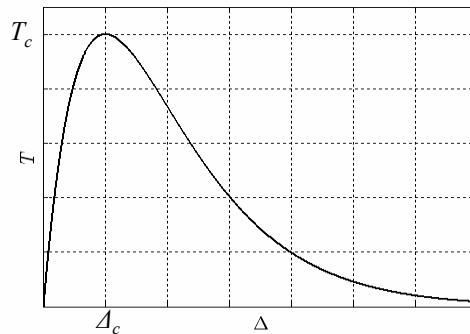


**Figure 9.2.** Exponential cohesive damage evolution laws.

In the present chapter, an approach is developed for using a CZM along with the FSDT to

perform delamination analysis with the ILPGSM. The exponential irreversible constitutive law was utilized along with a 1D analysis with the ILPGSM to solve the 2D delamination of a plane-strain or a plane-stress adhesively bonded specimen. Both mode I and mixed mode (I+II) delamination are considered in this chapter.

Mode I delamination analysis of an adhesively bonded aluminum beam was performed using the ILPGSM. An adaptive Sinc point distribution technique was introduced in which the domain is divided at the delamination front to better take advantage of the biased distribution of Sinc points with the ILPGSM. Furthermore, delamination analysis of a fixed ratio mixed mode (FRMM),  $[0^\circ]_s$ , composite specimen was performed using the adaptive Sinc point distribution. Finally, results were obtained for delamination of a GLARE 3-3/2-0.4 specimen. The GLARE example illustrates how the ILPGSM may be used, along with a 1D analysis and a subsequent through-the-thickness integration to obtain an approximation for the transverse normal and transverse shear stresses. The results demonstrate the accuracy of the proposed method in comparison with results obtained by using 2D plane-stress or plane-strain elements with ABAQUS COH2D4 cohesive elements.

## 9.1 Rate Independent CZM

For the present analysis, the interlaminar interface will be modeled using the traction-separation law postulated by Goyal, Johnson and Dávila [60]. For a detailed description of the formulation, including a proof clearly demonstrating the mixed mode constitutive law satisfies a multi-axial stress criterion for the initiation of delamination and an empirical mixed mode fracture criterion for the progression of delamination, see Goyal, Johnson and Dávila [60]. The most pertinent details of the formulation will be reviewed in this section. For brittle materials and ductile materials under small-scale yielding, the strain energy release rate,  $G$ , is the most appropriate measure for fracture analysis. When the strain energy release rate exceeds the critical value  $G_c$  unstable crack growth occurs. The strain energy

release rate can be calculated from a traction-displacement jump law. For a pure mode I fracture, the strain energy release rate is given by:

$$G_I = \int_0^{\Delta_3} T_3 d\Delta_3 \quad (9.1)$$

where  $G_I$  is the mode I strain energy release rate or the work done by the applied normal traction  $T_3$  and  $\Delta_3$  is the normal separation gap between adherents. The critical mode I strain energy release rate,  $G_{Ic}$ , is obtained from Eq. (9.1) when  $\Delta_3 \rightarrow \infty$  or a complete separation is achieved. By formulating the thin layer of adhesive by a traction-displacement relationship, the integral in Eq. (9.1) may be evaluated.

For delamination onset, a stress based criterion is used. For the constitutive law used by Goyal, Johnson, and Dávila [60], the multi-axial stress criterion was used:

$$\left[ \left( \frac{T_1}{T_{1c}} \right)^\alpha + \left( \frac{T_2}{T_{2c}} \right)^\alpha + \left( \frac{\langle T_3 \rangle}{T_{3c}} \right)^\alpha \right]^{1/\alpha} = 1, \quad (9.2)$$

where  $T_1$  and  $T_2$  are the transverse shear traction components,  $T_3$  is the normal traction component, and  $T_{1c}$ ,  $T_{2c}$ , and  $T_{3c}$  are the critical traction components and the operator  $\langle l \rangle$  is defined by

$$\langle l \rangle = \begin{cases} l, & l > 0 \\ 0, & l \leq 0 \end{cases}. \quad (9.3)$$

In Eq. (9.2),  $\alpha \geq 2$  is a real number that specifies the shape of the failure surface. Note that this criterion reduces to the Quadratic delamination criterion of Brewer and Lagace [61] with the choice of  $\alpha = 2$ .

For mixed-mode delamination growth, the power law proposed by Whitcomb [218],

$$\left( \frac{G_I}{G_{Ic}} \right)^{\alpha/2} + \left( \frac{G_{II}}{G_{IIc}} \right)^{\alpha/2} + \left( \frac{G_{III}}{G_{IIIc}} \right)^{\alpha/2} = 1, \quad (9.4)$$

is used to predict delamination growth. This criterion reduces to the linear fracture criterion of Wu [219] when  $\alpha$  is selected to be 2. The damage propagation models utilized by the CZM in the element libraries of ABAQUS, utilizes a similar approach to mode-mixing. The power law for energy mixing with ABAQUS would be identical to Eq. (9.4). Thus for a the linear fracture criterion of Wu [219], the power should be chosen to be 1. In either case, the delamination onset in ABAQUS utilizes the quadratic delamination criterion [ $\alpha = 2$  in Eq. (9.2)].

The mixed mode, irreversible, exponential traction-separation law [60] can be written as:

$$\begin{Bmatrix} \bar{T}_1 \\ \bar{T}_2 \\ \bar{T}_3 \end{Bmatrix} = \begin{Bmatrix} \bar{\Delta}_1 \\ \bar{\Delta}_2 \\ \bar{\Delta}_3 \end{Bmatrix} \Theta - \begin{Bmatrix} 0 \\ 0 \\ \langle -\bar{\Delta}_3 \rangle \end{Bmatrix} \exp\left(\frac{1 + \kappa |\bar{\Delta}_3|^\beta}{\beta}\right) \quad (9.5)$$

where  $\bar{T}_i = T_i/T_{ic}$ ,  $\bar{\Delta}_i = \Delta_i/\Delta_{ic}$ ,  $\Delta_{ic}$  is defined by the definition of the strain energy release rates such that:

$$\begin{aligned} G_{Ic} &= \int_0^\infty T_3 d\Delta_3 = \psi(\beta) T_{3c} \Delta_{3c}, \\ G_{IIc} &= \int_0^\infty T_1 d\Delta_1 = \psi(\beta) T_{1c} \Delta_{1c}, \\ G_{IIIc} &= \int_0^\infty T_2 d\Delta_2 = \psi(\beta) T_{2c} \Delta_{2c}. \end{aligned} \quad (9.6)$$

The function  $\psi(\beta)$  is defined by:

$$\psi(\beta) = \beta^{(2-\beta)/\beta} \Gamma\left(\frac{2}{\beta}\right) \exp\left(\frac{1}{\beta}\right), \quad (9.7)$$

where  $\Gamma$  is the Euler gamma function [145]. The function  $\Theta$  is defined by:

$$\Theta = \exp\left(\frac{2 - \mu^\beta/d - d}{\beta}\right), \quad (9.8)$$



where the mixed mode parameter  $\mu$  is the coupled normalized displacement jump measure defined by,

$$\mu = (|\bar{\Delta}_1|^\alpha + |\bar{\Delta}_2|^\alpha + \langle \bar{\Delta}_3 \rangle^\alpha)^{1/\alpha} \quad (9.9)$$

and where  $d$  is a damage variable. The damage variable,  $d$ , is always positive and is 1 for an undamaged interface. If load step  $t$  is indicated by a left superscript, then the damage variable  $d$  in load step  $t + \Delta t$  is set by:

$${}^{t+\Delta t}d = \max(1, {}^t d, \mu^\beta). \quad (9.10)$$

For a 2D problem, the traction-separation law has the same form as Eq. (9.5) but taking  $\Delta_2 = 0$  and neglecting the traction component  $T_2$ .

By carefully considering  $d$  as given by Eq. (9.10), the cohesive law is irreversible. The path taken during a loading, unloading, and subsequent loading cycle is plotted in Fig. 9.3.

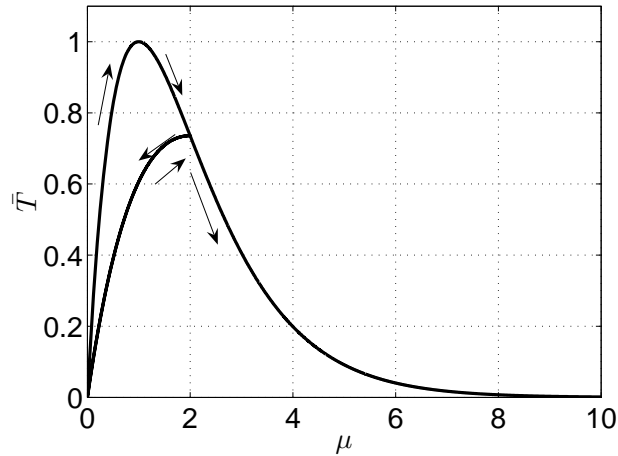


Figure 9.3. Exponential cohesive law through a loading and unloading cycle.

## 9.2 Delamination Kinematics

Consider the 2D delaminated specimen shown in Fig. 9.4. The interlaminar stresses play a critical role in delamination onset and propagation. For a perfectly bonded beam with no crack, the zigzag plate and beam theories have been used to accurately determine interlaminar stresses using through-the-thickness integration of the equilibrium equations of the 3D elasticity theory. However, in the vicinity of a boundary, the kinematics often prevent accurate modeling of the boundary conditions and thus the stresses in this vicinity are erroneous. Furthermore, in the vicinity of a free edge, the so called “free-edge effects” or the localized occurrence of interlaminar stresses in a boundary layer region along the free laminate edges cannot be captured by the traditional ESL plate or beam theories. Naturally, the large interlaminar stresses result in delamination onset and thus are critical to delamination modeling. The layer-wise theories [98] exhibit enough detail in the kinematic definition that there is no such limitation. They have been successfully used to capture the “free-edge effects”, and they can be easily enhanced to incorporate delamination kinematics [220]. For the layer-wise theories, the assumed displacement field (see Fig. 9.5) is given by:

$$u_i = \sum_{I=1}^N U_{iI}(x_1, x_2) \Phi^I(x_3) + \sum_{I=1}^D \mathcal{U}_{iI} H^I(x_3) \quad (9.11)$$

where there are  $N - 1$  layers and  $\Phi^I(x_3)$  is a piecewise linear function such that the displacement is interpolated linearly through the layer thickness. The delamination kinematics are introduced by piecewise constant function  $\mathcal{U}_{iI}$  [ $H^I(x_3)$  is the Heaviside step function]. Note that there can be different number of delamination variables than the number of layer-wise displacement variables.

It should be noted that the layer-wise kinematics of Eq. (9.11) allow each layer to have a different rotation. This feature is critical after the delamination onset occurs. If an equivalent single layer theory were used, the delamination kinematics would require the use

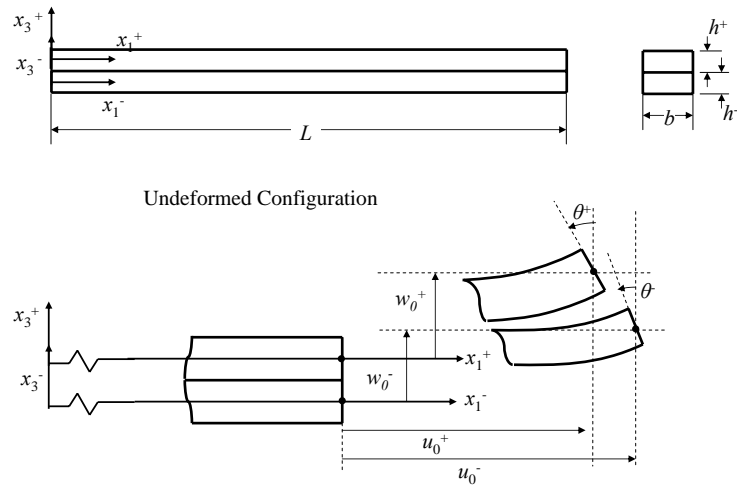


Figure 9.4. Undeformed and deformed geometries of two stacked Timoshenko beams with deformation kinematics indicated.

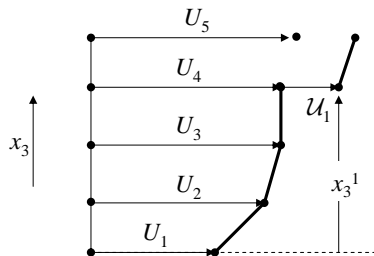


Figure 9.5. Delamination kinematics with layer-wise plate theory.

of enhancement with Heaviside step function for the displacement and rotation variables. Thus the layer-wise theory provides the minimum number of kinematic variables for the delamination kinematics.

For the sake of utility, the present study utilizes the kinematics of stacked Timoshenko beams as shown in Fig. 9.4. The deformation field for each beam is given by:

$$\begin{aligned} U_1(x_1, x_3) &= u_0(x_1) + x_3\theta(x_1) \\ U_3(x_1, x_3) &= w_0(x_1). \end{aligned} \tag{9.12}$$

The deformation field prescribed above would have exactly the same number of kinematic variables as a layer-wise theory with a piecewise linear  $U_1$  displacement and a piecewise constant  $U_3$  displacement through each lamina thickness, and with a new delamination variable  $\mathcal{U}_1$  and  $\mathcal{U}_3$  at each layer interface. However, the present implementation allows the interlaminar stresses through each layer thickness to be calculated by the algorithm used in Chapter 2. Also, a sublaminar may be modeled by an ESL when delamination is not expected to occur between the layers. The strains, and stress resultants can be formulated in the standard fashion for the FSDT.

## 9.3 Equilibrium Formulation for Adhesively Bonded Timoshenko Beams

### 9.3.1 Internal Virtual Work

Consider a laminated beam with two sublaminar layers. The top sublaminar has thickness  $h^+$ . The bottom sublaminar has thickness  $h^-$ . Both sublaminars have length,  $L$  and out-of-plane width,  $b$  as shown in Fig. 9.4. Note in Fig. 9.4, the global coordinate system  $(x_1, x_3)$  was omitted for clarity. The  $x_1$  datum is intuitively taken to be the left edge of the beam ( $x_1^+ = x_1^- = 0$ ). The  $x_3$  datum was placed at the sublaminar interface ( $x_3^+ = -h^+/2$  and

$x_3^- = h^-/2$ ). The assumed displacement profile of each beam is defined on the sublaminar local coordinate system and each has the form given in Eq. (9.12) in the fashion of the FSĐT. Applying the plane-strain assumption,  $\epsilon_2 = \gamma_{12} = \gamma_{23} = 0$ , when  $b \gg h$  or the plane-stress assumption,  $\sigma_{22} = \sigma_{12} = \sigma_{23} = 0$ , when  $b \ll h$ , the internal virtual work can be expressed by

$$\delta\mathcal{W}_{int} = \int_{\Omega} (\sigma_{11}\delta\epsilon_{11} + \sigma_{13}\delta\gamma_{13}) d\Omega \quad (9.13)$$

where  $\Omega$  is the complete laminate volume domain.

Across the interface surface the displacements are discontinuous. Therefore, the principle of virtual work may not be applied to the complete domain. Nonetheless, it may be applied to the individual sublaminar domains. In this case, the traction applied to the top and bottom surface should be explicitly considered. Letting  $\Omega^+$  and  $\Omega^-$  be the domain (volume) of the beam above and below the interface respectively, and letting  $S^+$  and  $S^-$  be the upper and lower interface surfaces respectively, then the total internal virtual work can be expressed by

$$\begin{aligned} \delta\mathcal{W}_{int}^+ &= \int_{\Omega^+} (\sigma_{11}\delta\epsilon_{11} + \sigma_{13}\delta\gamma_{13}) d\Omega^+ + \int_{S^+} (T_1^+\delta U_1^+ + T_3^+\delta U_3^+) dS^+, \\ \delta\mathcal{W}_{int}^- &= \int_{\Omega^-} (\sigma_{11}\delta\epsilon_{11} + \sigma_{13}\delta\gamma_{13}) d\Omega^- + \int_{S^-} (T_1^-\delta U_i^- + T_3^-\delta U_3^-) dS^-, \end{aligned} \quad (9.14)$$

where  $T_1$  is the traction component in the  $x_1$  direction and  $T_3$  is the traction component in the  $x_3$  direction.

It is convenient to express the interface traction which acts on a surface,  $\bar{S}$  that is the mid-surface between the surfaces  $S^+$  and  $S^-$  as shown in Fig. 9.6. The force equilibrium may be expressed by:

$$T_i^+ dS^+ = -T_i^- dS^- = T_i d\bar{S} \quad (9.15)$$

By summing the internal virtual work from the  $\Omega^+$  subdomain and the  $\Omega^-$  subdomain, the following expression for internal virtual work was obtained:

$$\delta\mathcal{W}_{int} = \int_{\Omega} (\sigma_{11}\delta\epsilon_{11} + \sigma_{13}\delta\gamma_{13}) d\Omega + \int_{\bar{S}} [T_1(\delta U_1^+ - \delta U_1^-) + T_3(\delta U_3^+ - \delta U_3^-)] d\bar{S} \quad (9.16)$$

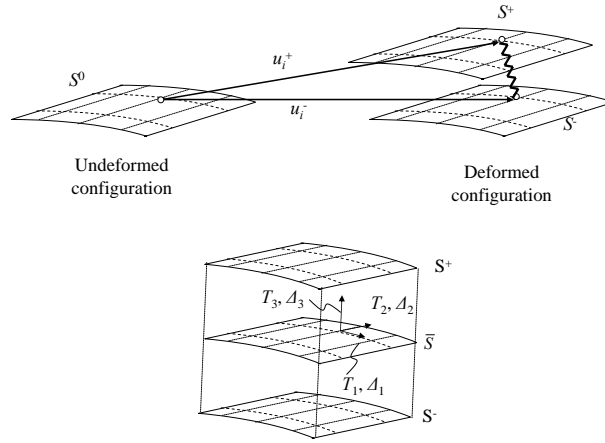


**Figure 9.6.** Deformation of cohesive layer with cohesive mid-surface indicted.

The traction-separation law was formulated in terms of the traction components that are normal and tangential to the interface mid-surface. Therefore, it is more convenient to replace the scalar product of traction components and virtual displacements expressed in the  $x_i$  orthogonal basis with that expressed in the normal and tangential basis,  $\Delta_i$ ,

$$\delta\mathcal{W}_{int} = \int_{\Omega} \sigma_{11}\delta\epsilon_{11} + \sigma_{13}\delta\gamma_{13}d\Omega + \int_{\bar{S}} T_1\delta\Delta_1 + T_3\delta\Delta_3d\bar{S} \quad (9.17)$$

where now  $T_1$  and  $T_3$  represent the tangential and normal (to the mid-surface,  $\bar{S}$ ) traction components respectively as shown in Fig. 9.6

To relate the separation gaps,  $\Delta_i$ , and the displacement components, the orientation of the mid-surface,  $\bar{S}$ , must be known with respect to the undeformed coordinate basis  $(x_1, x_3)$ . Let  $(\bar{x}_1, \bar{x}_3)$  define a point on the interface surface in the deformed coordinate system. This point may be expressed in terms of the kinematic variables and the undeformed coordinates

by:

$$\begin{aligned}\bar{x}_1 &= x_1 + \frac{1}{2} (u_0^+ + z^+ \theta^+ + u_0^- + z^- \theta^-), \\ \bar{x}_3 &= \frac{1}{2} (w_0^+ + w_0^-).\end{aligned}\tag{9.18}$$

If we define the mid-surface displacement gradient tensor,  $g_{ij} = \partial \bar{x}_i / \partial x_j$ , then the normal vector is simply given by:

$$\begin{aligned}\mathbf{r}_3 &= \{g_{13}, g_{33}\}^T \\ \mathbf{r}_3 &= \left\{ \frac{1}{2} (\theta^+ + \theta^-), 1 \right\}^T\end{aligned}\tag{9.19}$$

The tangential vector can be found in a similar manner; however, it is simpler to recognize the out of plane direction should be orthogonal to the  $\mathbf{r}_1$  and  $\mathbf{r}_3$  and thus apply  $\mathbf{r}_1 = \mathbf{r}_2 \times \mathbf{r}_3$ . Therefore, the tangential direction may be written as:

$$\mathbf{r}_1 = \left\{ 1, -\frac{1}{2} (\theta^+ + \theta^-) \right\}^T\tag{9.20}$$

The local orientation vectors  $\mathbf{r}_1$  and  $\mathbf{r}_3$  are normalized by their length ( $\hat{\mathbf{r}}_1 = \mathbf{r}_1 / |\mathbf{r}_1|$  and  $\hat{\mathbf{r}}_3 = \mathbf{r}_3 / |\mathbf{r}_3|$ ) to form a rotation matrix,  $\mathbf{R} = \{\hat{\mathbf{r}}_1, \hat{\mathbf{r}}_3\}$  that relates the local mid-surface coordinate system to the global coordinate system  $(x_1, x_3)$ . In doing so, the tangential and shear displacement jumps may be expressed by:

$$\{\Delta_1, \Delta_3\} = \mathbf{R} \left\{ u_0^+ - \frac{h^+}{2} \theta^+ - u_0^- - \frac{h^-}{2} \theta^-, w_0^+ - w_0^- \right\}^T\tag{9.21}$$

Furthermore, the deformed mid-surface area can be related to the initial mid-surface area by the length of the normal vector:

$$d\bar{S} = |\mathbf{r}_3| dx_2 dx_1\tag{9.22}$$

To illustrate the solution approach with the ILPGSM, we divide the internal virtual work into the following three terms, each of which will be evaluated independently:

$$\begin{aligned}\delta\mathcal{W}^+ &= \int_{\Omega^+} \sigma_{11}^+ \delta\epsilon_{11}^+ + \sigma_{13}^+ \delta\gamma_{13}^+ d\Omega^+, \\ \delta\mathcal{W}^- &= \int_{\Omega^-} \sigma_{11}^- \delta\epsilon_{11}^- + \sigma_{13}^- \delta\gamma_{13}^- d\Omega^-, \\ \delta\mathcal{W}^{coh} &= \int_{\bar{S}} T_1 \delta\Delta_1 + T_3 \delta\Delta_3 d\bar{S}.\end{aligned}\tag{9.23}$$

By substituting the strain definitions into  $\delta\mathcal{W}^+$  and  $\delta\mathcal{W}^-$ , and integrating through the thickness and width, the following expression is obtained in the fashion of the FSdT:

$$\delta\mathcal{W}^{(+/-)} = \int_0^L N_{11} \delta u_{0,1} + M_{11} \theta_{,1} + Q_1 (\delta w_{0,1} + \delta\theta) dx_1,\tag{9.24}$$

where the stress resultants were defined by Eq. (2.6) or Eq. (2.22), and the superscript “+” and “-” have been omitted from all terms. By using the stress resultant-strain relations, the  $\delta\mathcal{W}^{(+/-)}$  may be written as:

$$\begin{aligned}\delta\mathcal{W}^{(+/-)} &= \int_0^L (A_{11} u_{0,1} + B_{11} \theta_{,1}) \delta u_{0,1} + (B_{11} u_{0,1} + D_{11} \theta_{,1}) \delta \theta_{,1} \\ &\quad + (A_{55} w_{0,1} + A_{55} \theta) (\delta w_{0,1} + \delta\theta) dx_1\end{aligned}\tag{9.25}$$

The ILPGSM basis function, Eq. (3.30), can be used to approximate each of the displacement variables and their derivatives. Note however, the basis function is evaluated on the computational domain  $\xi$  which is discretized by the DE transformation. The derivative,  $d\xi/dx_1$ , can be used to translate between the  $\xi$  and physical domain  $x_1$ . Thus the unknown



displacement and rotation quantities are each approximated by:

$$\begin{aligned}
u_0^+(x_1) &= \mathbf{B}(\xi)\mathbf{U}_0^+ & u_{0,1}^+(x_1) &= \frac{d\xi}{dx_1}\mathbf{A}(\xi)\mathbf{U}_0^+ \\
\theta^+(x_1) &= \mathbf{B}(\xi)\boldsymbol{\Theta}^+ & \theta_{,1}^+(x_1) &= \frac{d\xi}{dx_1}\mathbf{A}(\xi)\boldsymbol{\Theta}^+ \\
w_0^+(x_1) &= \mathbf{B}(\xi)\mathbf{w}_0^+ & W_{0,1}^+(x_1) &= \frac{d\xi}{dx_1}\mathbf{A}(\xi)\mathbf{W}_0^+
\end{aligned} \tag{9.26}$$

with similar equations for the lower sublaminates ( $u_0^-$ ,  $\theta^-$ , and  $w_0^-$ ).

Substituting the basis function approximations into the expressions for  $\delta\mathcal{W}^{(+/-)}$  results in the following expression:

$$\begin{aligned}
\delta\mathcal{W}^{(+/-)} &= \int_0^L \left( A_{11} \frac{d\xi}{dx_1} \mathbf{A}(\xi) \mathbf{U}_0 + B_{11} \frac{d\xi}{dx_1} \mathbf{A}(\xi) \boldsymbol{\Theta} \right) \delta u_{0,1} + \left( B_{11} \frac{d\xi}{dx_1} \mathbf{A}(\xi) \mathbf{U}_0 + \right. \\
&\quad \left. D_{11} \frac{d\xi}{dx_1} \mathbf{A}(\xi) \boldsymbol{\Theta} \right) \delta \theta_{,1} + \left( A_{55} \frac{d\xi}{dx_1} \mathbf{A}(\xi) \mathbf{W}_0 + A_{55} \mathbf{B}(\xi) \boldsymbol{\Theta} \right) (\delta w_{0,1} + \delta \theta) dx_1 \tag{9.27}
\end{aligned}$$

To generate the equilibrium equations, the virtual displacement and rotation variables are independently set to be weight function of compact support  $W^I$ .  $W^I$  is defined so that it is nonzero only on the domain  $\xi_{min} < \xi < \xi_{max}$  [see Eq. (7.13)]. Therefore, the domain integrals on  $0 \leq x_1 \leq L$  can be evaluated over the  $I$ th local domain only. By defining the following matrices,

$$\begin{aligned}
\mathbf{K}_{00}^I &= \int_{\xi_{min}}^{\xi_{max}} \mathbf{B}(\xi) W^I(\xi) d\xi \\
\mathbf{K}_{01}^I &= \int_{\xi_{min}}^{\xi_{max}} \mathbf{A}(\xi) W^I(\xi) d\xi \\
\mathbf{K}_{10}^I &= \int_{\xi_{min}}^{\xi_{max}} \mathbf{B}(\xi) \frac{dW^I(\xi)}{d\xi} d\xi \\
\mathbf{K}_{11}^I &= \int_{\xi_{min}}^{\xi_{max}} \mathbf{A}(\xi) \frac{dW^I(\xi)}{d\xi} d\xi
\end{aligned} \tag{9.28}$$

By recognizing that  $dx_1 = (dx_1/d\xi) d\xi$ , then  $\delta\mathcal{W}^{(+/-)}$  results in the following terms:

$$\begin{aligned}\delta\mathcal{W}_{\delta u_0}^{(+/-)} &= A_{11} \frac{d\xi}{dx_1} \mathbf{K}_{11}^I \mathbf{U}_0 + B_{11} \frac{d\xi}{dx_1} \mathbf{K}_{11}^I \Theta \\ \delta\mathcal{W}_{\delta\theta}^{(+/-)} &= B_{11} \frac{d\xi}{dx_1} \mathbf{K}_{11}^I \mathbf{U}_0 + \left( D_{11} \frac{d\xi}{dx_1} \mathbf{K}_{11}^I + A_{55} \frac{1}{d\xi/dx_1} \mathbf{K}_{00}^I \right) \Theta + A_{55} \mathbf{K}_{01}^I \mathbf{W}_0 \\ \delta\mathcal{W}_{\delta w_0}^{(+/-)} &= A_{55} \mathbf{K}_{10}^I \Theta + A_{55} \mathbf{K}_{11}^I \mathbf{W}_0\end{aligned}\quad (9.29)$$

where  $\delta\mathcal{W}_{\delta u_0}^{(+/-)}$ ,  $\delta\mathcal{W}_{\delta\theta}^{(+/-)}$ , and  $\delta\mathcal{W}_{\delta w_0}^{(+/-)}$  are the terms resulting from  $\delta u_0 = W^I$  and  $\delta\theta = \delta w_0 = 0$ ;  $\delta\theta = W^I$  and  $\delta u_0 = \delta w_0 = 0$ ; and  $\delta w_0 = W^I$  and  $\delta\theta = \delta u_0 = 0$ , respectively. The terms  $\delta\mathcal{W}_{\delta u_0}^{(+/-)}$ ,  $\delta\mathcal{W}_{\delta\theta}^{(+/-)}$ , and  $\delta\mathcal{W}_{\delta w_0}^{(+/-)}$  are arranged into a force vector as follows:

$$\mathbf{F}_b^I = \{\delta\mathcal{W}_{\delta u_0}^+, \delta\mathcal{W}_{\delta\theta}^+, \delta\mathcal{W}_{\delta w_0}^+, \delta\mathcal{W}_{\delta u_0}^-, \delta\mathcal{W}_{\delta\theta}^-, \delta\mathcal{W}_{\delta w_0}^-\}^T. \quad (9.30)$$

Next, the term  $\delta\mathcal{W}^{coh}$  is considered. The virtual normal and tangential displacements,  $\delta\Delta_3$  and  $\delta\Delta_1$  can be written in terms of the global unknowns using Eq. (9.21). Performing the integration through out-of-plane width results in

$$\begin{aligned}\delta\mathcal{W}^{coh} &= b \int_0^L T_1(\Delta_1, \Delta_3) \left[ R_{11} \left( \delta u_0^+ - \frac{-h^+}{2} \delta\theta^+ - \delta u_0^- - \frac{h^-}{2} \delta\theta^- \right) + R_{13} (\delta w_0^+ - \delta w_0^-) \right] \\ &+ T_3(\Delta_1, \Delta_3) \left[ R_{31} \left( \delta u_0^+ - \frac{-h^+}{2} \delta\theta^+ - \delta u_0^- - \frac{h^-}{2} \delta\theta^- \right) + R_{33} (\delta w_0^+ - \delta w_0^-) \right] |_{\mathbf{r}_3} dx_1. \quad (9.31)\end{aligned}$$

To generate the equilibrium equations, the virtual displacement and rotation variables are independently set to be weight function of compact support,  $W^I$ . By introducing the following definitions,

$$\begin{aligned}F_1^I &= b \int_{\xi_{min}}^{\xi_{max}} \left[ T_1(\Delta_1, \Delta_3) R_{11} + T_3(\Delta_1, \Delta_3) R_{31} \right] W^I \frac{1}{d\xi/dx_1} d\xi, \\ F_3^I &= b \int_{\xi_{min}}^{\xi_{max}} \left[ T_1(\Delta_1, \Delta_3) R_{13} + T_3(\Delta_1, \Delta_3) R_{33} \right] W^I \frac{1}{d\xi/dx_1} d\xi,\end{aligned}\quad (9.32)$$

then the force vector resulting from  $\delta\mathcal{W}^{coh}$  is determined to be:

$$\begin{aligned}\mathbf{F}_{coh}^I &= \{\delta\mathcal{W}_{u_0^+}^{coh}, \delta\mathcal{W}_{\theta^+}^{coh}, \delta\mathcal{W}_{w_0^+}^{coh}, \delta\mathcal{W}_{u_0^-}^{coh}, \delta\mathcal{W}_{\theta^-}^{coh}, \delta\mathcal{W}_{w_0^-}^{coh}\}^T, \\ \mathbf{F}_{coh}^I &= \{F_1^I, \frac{-h^+}{2}F_1^I, F_3^I, -F_1^I, \frac{-h^-}{2}F_1^I, -F_3^I\}^T.\end{aligned}\quad (9.33)$$

The traction components  $T_1$  and  $T_3$  are nonlinear functions of  $\Delta_1$  and  $\Delta_2$  as described in Section 9.1. Furthermore, the rotation matrix depends on the displacement and rotation variables. Therefore, the Newton-Raphson method should be used to solve the problem in an incremental-iterative fashion. To facilitate this process the displacement and rotation variables are expressed as small increments from the previous iteration:  $(u_0^+)_i = (u_0^+)_i + \Delta u_0^+$  where  $i$  indicates the solution from the previous iteration and  $\Delta u_0^+$  indicates the unknown increment from the iteration  $i$ . Each of the unknowns are incremented in this manner. If the global unknown vector is defined by  $\mathbf{q} = \{(\mathbf{U}_0^+)^T, (\mathbf{\Theta}^+)^T, (\mathbf{W}_0^+)^T, (\mathbf{U}_0^-)^T, (\mathbf{\Theta}^-)^T, (\mathbf{W}_0^-)^T\}^T$ , then  $\delta\mathcal{W}_{int}$  can be approximated by a Taylor series about  $\mathbf{q}_i$ :

$$\delta\mathcal{W}_{int}(\mathbf{q}_i + \Delta\mathbf{q}) = \delta\mathcal{W}_{int}(\mathbf{q}_i) + \Delta\mathbf{q} \left. \frac{\partial\delta\mathcal{W}_{int}}{\partial\mathbf{q}} \right|_{\mathbf{q}_i}. \quad (9.34)$$

The nonlinear equilibrium equations are obtained by  $\delta\mathcal{W}_{int} = \delta\mathcal{W}_{ext}$ . By combining this with Eq. (9.34) and setting each of the virtual displacement and rotations to be weight functions of compact support ( $W^I$ ) in the MLPG fashion, the nonlinear differential equations become a system of linear algebraic equations that can be solved for the unknown increment  $\Delta\mathbf{q}$ . By selecting  $I = \{1, 2, \dots, n_u\}$ , where  $n_u$  is the number of unknowns, a complete system of the form:

$$\mathbf{K}\Delta\mathbf{q} = \mathbf{F} \quad (9.35)$$

is obtained. In Eq. (9.35),  $\mathbf{K}$  is the tangential stiffness matrix and  $\mathbf{F}$  is the load vector.

By defining,

$$\mathbf{K}_{(+/-)}^I = \begin{bmatrix} A_{11} \frac{\partial \xi}{\partial x_1} \mathbf{K}_{11}^I & B_{11} \frac{\partial \xi}{\partial x_1} \mathbf{K}_{11}^I & \mathbf{0} \\ B_{11} \frac{\partial \xi}{\partial x_1} \mathbf{K}_{11}^I & D_{11} \frac{\partial \xi}{\partial x_1} \mathbf{K}_{11}^I + A_{55} \frac{1}{\partial d \xi / \partial x_1} \mathbf{K}_{00}^I & A_{55} \mathbf{K}_{01}^I \\ \mathbf{0} & A_{55} \mathbf{K}_{10}^I & A_{55} \mathbf{K}_{11}^I \end{bmatrix}, \quad (9.36)$$

the contribution to the tangential stiffness matrix resulting from  $\delta \mathcal{W}^{(+/-)}$  is obtained.

Determining the contribution to the tangential stiffness matrix from  $\partial \delta \mathcal{W}^{coh} / \partial \mathbf{q}$  merits some discussion. The rotation components are assumed to be constant with respect to displacement variables. This assumption was used successfully by Goyal, Johnson and Dávila [60], Makhecha [216] and Makhecha *et al.*[66]. To evaluate  $\partial \delta \mathcal{W}^{coh} / \partial \mathbf{q}$  under this assumption only requires determining  $\partial T_1 / \partial \mathbf{q}$  and  $\partial T_3 / \partial \mathbf{q}$  which may be expressed by:

$$\frac{\partial T_i}{\partial \mathbf{q}} = \frac{\partial T_i}{\partial \Delta_1} \frac{\partial \Delta_1}{\partial \mathbf{q}} + \frac{\partial T_i}{\partial \Delta_3} \frac{\partial \Delta_3}{\partial \mathbf{q}}, \quad (9.37)$$

with  $i = \{1, 3\}$ . The derivatives of  $T_i$  can be determined from differentiation of the traction-separation law (see Eq. (69) in Goyal, Johnson, and Dávila [60]):

$$C_{11} = \frac{\partial T_1}{\partial \Delta_1} = \frac{T_1^c}{\Delta_1^c} \left( 1 - \frac{(\bar{\Delta}_1)^2}{\tilde{w} \mu^{\alpha-\beta}} |\bar{\Delta}_1|^{\alpha-2} \right) \Theta, \quad (9.38a)$$

$$C_{12} = \frac{\partial T_1}{\partial \Delta_3} = \frac{T_1^c}{\Delta_3^c} \left( -\frac{\bar{\Delta}_1 \bar{\Delta}_3}{\tilde{w} \mu^{\alpha-\beta}} |\bar{\Delta}_3|^{\alpha-2} \right) \Theta, \quad (9.38b)$$

$$C_{21} = \frac{\partial T_3}{\partial \Delta_1} = \frac{T_3^c}{\Delta_1^c} \left( -\frac{\bar{\Delta}_1 \bar{\Delta}_3}{\tilde{w} \mu^{\alpha-\beta}} |\bar{\Delta}_1|^{\alpha-2} \right) \Theta, \quad (9.38c)$$

$$C_{22} = \frac{\partial T_3}{\partial \Delta_3} = \frac{T_3^c}{\Delta_3^c} \left( 1 - \frac{(\bar{\Delta}_3)^2}{\tilde{w} \mu^{\alpha-\beta}} |\bar{\Delta}_3|^{\alpha-2} \right) \Theta. \quad (9.38d)$$

If  $\Delta_3 < 0$  then the Eq. (9.38d) is not explicitly correct. However, Goyal, Johnson, and Dávila[60] report numerical conditioning problems when the exact derivative is used. For

this reason, the expressions for  $T_3$  in the presence of interpenetration is replaced with a simple linear relationship:

$$T_3 = T_3^c \exp(1/\beta) \bar{\Delta}_3, \quad \Delta_3 < 0, \quad (9.39)$$

the derivative of which is simply:

$$C_{22} = \frac{\partial T_3}{\partial \Delta_3} = T_3^c \frac{\exp(1/\beta)}{\Delta_3^c}. \quad (9.40)$$

By introducing,

$$\bar{C}_{kl} = C_{ij} R_{jk} R_{il} \quad (9.41)$$

and letting

$$\mathbf{K}_{coh}^{(ij)} = \int_{\xi_{min}}^{\xi_{max}} W^I(\xi) \bar{C}_{ij}(\xi) |\mathbf{r}_3| \mathbf{B}(\xi) \frac{1}{d\xi/dx_1} d\xi, \quad (9.42)$$

the contribution to the tangential stiffness matrix of the cohesive layer, resulting from  $\delta \mathcal{W}_{coh}$  is given by:

$$\mathbf{K}_{coh}^I = \begin{bmatrix} \mathbf{K}_{coh}^{(11)} & -\frac{h^+}{2} \mathbf{K}_{coh}^{(11)} & \mathbf{K}_{coh}^{(13)} & -\mathbf{K}_{coh}^{(11)} & -\frac{h^-}{2} \mathbf{K}_{coh}^{(11)} & -\mathbf{K}_{coh}^{(13)} \\ -\frac{h^+}{2} \mathbf{K}_{coh}^{(11)} & \left(\frac{h^+}{2}\right)^2 \mathbf{K}_{coh}^{(11)} & -\frac{h^+}{2} \mathbf{K}_{coh}^{(13)} & \frac{h^+}{2} \mathbf{K}_{coh}^{(11)} & \frac{h^+}{2} \frac{h^-}{2} \mathbf{K}_{coh}^{(11)} & \frac{h^+}{2} \mathbf{K}_{coh}^{(13)} \\ \mathbf{K}_{coh}^{(31)} & -\frac{h^+}{2} \mathbf{K}_{coh}^{(31)} & \mathbf{K}_{coh}^{(33)} & -\mathbf{K}_{coh}^{(31)} & -\frac{h^-}{2} \mathbf{K}_{coh}^{(31)} & -\mathbf{K}_{coh}^{(33)} \\ -\mathbf{K}_{coh}^{(11)} & \frac{h^+}{2} \mathbf{K}_{coh}^{(11)} & -\mathbf{K}_{coh}^{(13)} & \mathbf{K}_{coh}^{(11)} & \frac{h^-}{2} \mathbf{K}_{coh}^{(11)} & \mathbf{K}_{coh}^{(13)} \\ -\frac{h^-}{2} \mathbf{K}_{coh}^{(11)} & \frac{h^-}{2} \frac{h^+}{2} \mathbf{K}_{coh}^{(11)} & -\frac{h^-}{2} \mathbf{K}_{coh}^{(13)} & \frac{h^-}{2} \mathbf{K}_{coh}^{(11)} & \left(\frac{h^-}{2}\right)^2 \mathbf{K}_{coh}^{(11)} & \frac{h^-}{2} \mathbf{K}_{coh}^{(13)} \\ -\mathbf{K}_{coh}^{(31)} & \frac{h^+}{2} \mathbf{K}_{coh}^{(31)} & -\mathbf{K}_{coh}^{(33)} & \mathbf{K}_{coh}^{(31)} & \frac{h^-}{2} \mathbf{K}_{coh}^{(31)} & \mathbf{K}_{coh}^{(33)} \end{bmatrix} \quad (9.43)$$

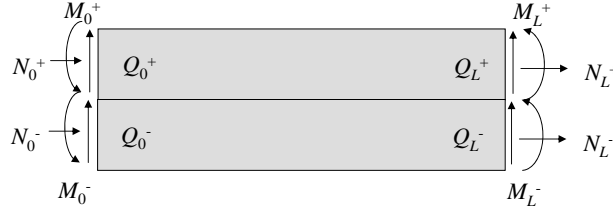


Figure 9.7. Applied forces and moments to top and bottom sublaminates.

### 9.3.2 External Virtual Work

Now consider the external virtual work,  $\delta\mathcal{W}_{ext}$ . Edge loads and moments are considered as shown in Fig. 9.7. The potential of the external work is given by:

$$\begin{aligned} \delta\mathcal{W}_{ext} = & (M_L^+ \delta\theta^+(L) + M_0^+ \delta\theta^+(0) + M_L^- \delta\theta^-(L) + M_0^- \delta\theta^-(0) + Q_L^+ \delta w_0^+(L) + Q_0^+ \delta w_0^+(0) \\ & + Q_L^- \delta w_0^-(L) + Q_0^- \delta w_0^-(0) + N_L^+ \delta u_0^+(L) + N_0^+ \delta u_0^+(0) + N_L^- \delta u_0^-(L) + N_0^- \delta u_0^-(0)) \end{aligned} \quad (9.44)$$

The virtual displacements and rotations are each independently set to  $W^I$ . Because  $W^I$  are functions of compact support, the external virtual work is only nonzero on a subdomain  $I$  which intersects the boundary. By defining:

$$\mathbf{F}_{ext}^I = \begin{cases} W^I(\xi_{-N}) \{N_0^+, M_0^+, Q_0^+, N_0^-, M_0^-, Q_0^-\}^T & \xi_{min} < \xi_{-N} < \xi_{max} \\ W^I(\xi_N) \{N_L^+, M_L^+, Q_L^+, N_L^-, M_L^-, Q_L^-\}^T & \xi_{min} < \xi_N < \xi_{max} \\ \{0, 0, 0, 0, 0, 0\}^T & \xi_{min} > \xi_{-N}, \xi_{max} < \xi_N \end{cases}, \quad (9.45)$$

the external virtual work is fully defined.

The tangential stiffness matrix in the incremental iterative equilibrium, Eq. (9.35), is defined by:

$$\mathbf{K} = \begin{bmatrix} \mathbf{K}_{(+)}^I & \mathbf{0} \\ \mathbf{0} & \mathbf{K}_{(-)}^I \end{bmatrix} + \mathbf{K}_{coh}^I \quad (9.46)$$

Furthermore, the force vector,  $\mathbf{F}$ , is defined by:

$$\mathbf{F} = \mathbf{F}_{ext}^I - \mathbf{F}_{coh}^I - \mathbf{F}_b^I. \quad (9.47)$$

### 9.3.3 Essential Boundary Conditions

To apply the essential boundary conditions, the penalty method and the Lagrange multiplier method were utilized in the present study. The methods were implemented as described in Section 7.2.2. In this chapter, only quasi-static, monotonically increasing loading of the following types are considered: (1) the double cantilever beam (DCB) delamination and (2) the fixed ratio mixed mode (FRMM) delamination (see Fig. 9.8). In each of these cases, the loading is displacement controlled (i.e.  $w$  is specified). Therefore, the applied loads,  $N_0$ ,  $M_0$ ,  $Q_0$ ,  $N_L$ ,  $M_L$ , and  $Q_L$ , are each replaced by either a penalty term or the Lagrange multiplier or zero ( $N_L = M_L = 0$  for the double cantilever beam).

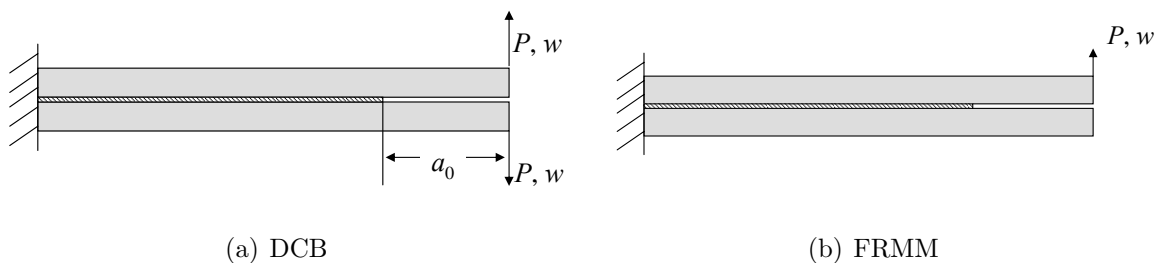


**Figure 9.8.** Loading configurations for (a) double cantilever beam (DCB) and (b) fixed ratio mixed mode (FRMM) delamination.

## 9.4 Mode I Delamination of Adhesively Bonded DCB

To validate the assumptions and implementation of the use of interface elements with 1D analysis, peel delamination of an adhesively bonded aluminum cantilever beam was analyzed using the ILPGSM. The mode I delamination specimen was studied by Makhecha *et al.* [216, 66] using interface finite elements by a user defined element in LS-DYNA with the

exponential irreversible cohesive law of Goyal, Johnson, and Dávila [60]. Results obtained using the ILPGSM implementation are compared against the FEM results of Makhecha and experimental results obtained by Simon in 2004 [221]. Moreover, the ILPGSM results are compared using a CZM in ABAQUS. The adherents were bonded using LESA<sup>3</sup> adhesive. The adherents each had a thickness of  $h = 6.35$  mm and a length of  $L = 203$  mm. The out of plane width was  $b = 25.4$  mm  $\gg h$ . Therefore, the specimen will behaves in a plane-strain manner. An initial delamination length of  $a_0 = 55$  mm was assumed. The material properties for the aluminum alloy are given in Table 9.12. The material properties for the LESA adhesive are given in Table 9.13. These properties were used by Makhecha [216] and Makhecha *et al.* [66].

**Table 9.12. Material properties for aluminum alloy for mode I delamination.**

$E$ [GPa]	$\nu$
69	0.3

**Table 9.13. Material properties for LESA adhesive for mode I delamination.**

$T_{1c}$ [MPa]	$G_{Ic}$ [N/mm]	$\beta$
40	1.6	1

#### 9.4.1 Finite Element Analysis

A FEA was performed for the problem using ABAQUS. A total of 508 2D, plane-strain (CPE4I) elements were used to model each of the aluminum layers (508 along the length and one through the thickness). The adhesive layer was modeled using the COH2D4 cohesive elements. The constitutive behavior of the adhesive elements was modeled using the traction-separation law. The elements had a thickness of 0.01 mm. A total of 508 cohesive elements were used along the length of the adhesive layer. The adhesive mesh and the plane-strain, aluminum mesh were not compatible; however, tie constraints were introduced to attach the

<sup>3</sup>LESA is a product of Dow Adhesive Company



nodes of the top aluminum layer to the top of the cohesive layer. Similarly, tie constraints were used to attach the nodes on the bottom aluminum layer to the bottom of the cohesive layer. The clamped boundary condition was enforced on the right edge by constraining all nodes along the edge against both  $u_1$  and  $u_2$  translational displacement. The ABAQUS finite element mesh may be seen in Fig. 9.9.

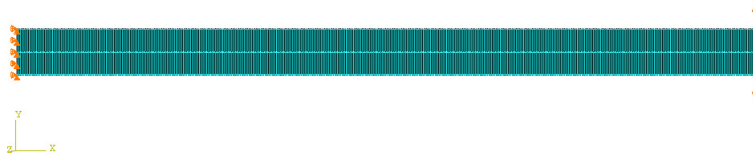


**Figure 9.9.** Finite element mesh for aluminum double cantilever beam with boundary conditions indicated.

### 9.4.2 Numerical Results

The ILPGSM was used to perform delamination analysis of an adhesively bonded aluminum beam. The ILPGSM solution was implemented as described in Section 9.3. The Sinc points were distributed using  $N = 100$  with the Sinc mesh size given by  $h = 2/N$ . Displacement control was used with the Newton-Raphson method. A total of 100 displacement steps were used to apply a maximum tip displacement,  $w_{max} = 4$  mm. The essential boundary conditions ( $u_0^+(0) = u_0^-(0) = \theta^+(0) = \theta^-(0) = w_0^+(0) = w_0^-(0) = 0$ ,  $w_0^+(L) = \bar{w}$ , and  $w_0^-(L) = -\bar{w}$ ) were imposed by the traditional penalty method. A relative convergence

criteria on displacements and rotations at the Sinc points ( $\xi_i$ ) was used as given below:

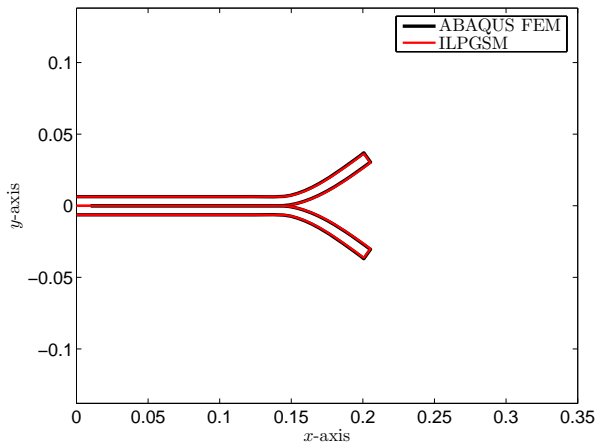
$$\epsilon = \left( \frac{\sum_{i=-N}^N \Delta u_0^+(\xi_i)^2}{\sum_{i=-N}^N u_0^+(\xi_i)^2} + \frac{\sum_{i=-N}^N \Delta w_0^+(\xi_i)^2}{\sum_{i=-N}^N w_0^+(\xi_i)^2} + \frac{\sum_{i=-N}^N \Delta \theta_0^+(\xi_i)^2}{\sum_{i=-N}^N \theta_0^+(\xi_i)^2} + \frac{\sum_{i=-N}^N \Delta u_0^-(\xi_i)^2}{\sum_{i=-N}^N u_0^-(\xi_i)^2} + \frac{\sum_{i=-N}^N \Delta w_0^-(\xi_i)^2}{\sum_{i=-N}^N w_0^-(\xi_i)^2} + \frac{\sum_{i=-N}^N \Delta \theta_0^-(\xi_i)^2}{\sum_{i=-N}^N \theta_0^-(\xi_i)^2} \right)^{1/2} < 1 \times 10^{-4} \quad (9.48)$$

If convergence was not reached in 25 iterations for a given load step  $i$ , the load step size was reduced by half and the nonlinear solution procedure was restarted with the previous converged load step.

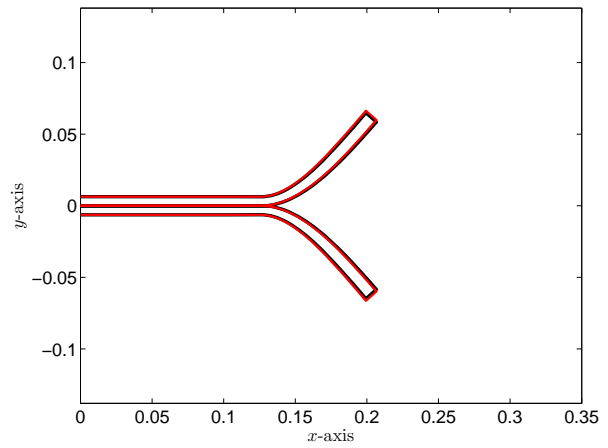
In Fig. 9.10, the shape of the deformed beam was compared as obtained by the ILPGSM solution and that obtained by the ABAQUS FEA. The deformation was plotted for an opening tip displacement of 1, 2, 3, and 4 mm. To better illustrate the deformation, an amplification factor of 3 was applied to the deformation. The deformed shape of the beam is indistinguishable between the two analyses.

In Fig. 9.11, the normal traction in the cohesive zone was plotted for the four load instances. A similar solution was obtained with the ILPGSM and FEA. The negative, traction indicates the interpenetration condition is being enforced.

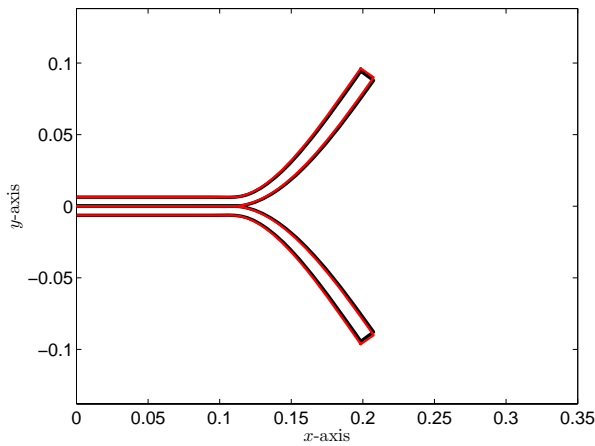
The reaction force history of the applied displacement was plotted in Fig. 9.12. The results are compared with experimental results obtained by Simon [221] and finite element results obtained by Makhecha [216]. The reaction force history obtained by the present FEA was also plotted. The DCB results from the present FEA and the ILPGSM are indistinguishable. Furthermore, there is excellent agreement between the experimental results and the present results.



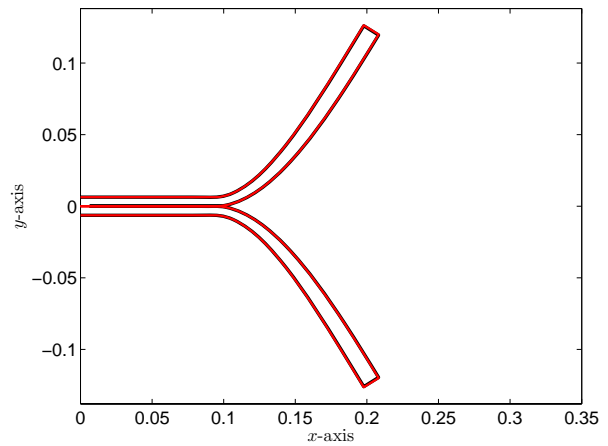
(a) Applied Displacement  $\bar{w} = 1$  mm



(b) Applied Displacement  $\bar{w} = 2$  mm



(c) Applied Displacement  $\bar{w} = 3$  mm



(d) Applied Displacement  $\bar{w} = 4$  mm

**Figure 9.10.** Comparison of deformed shape of aluminum DCB by ILPGSM and ABAQUS plane-strain FEA. An amplification factor of 3 was used to illustrate the results.

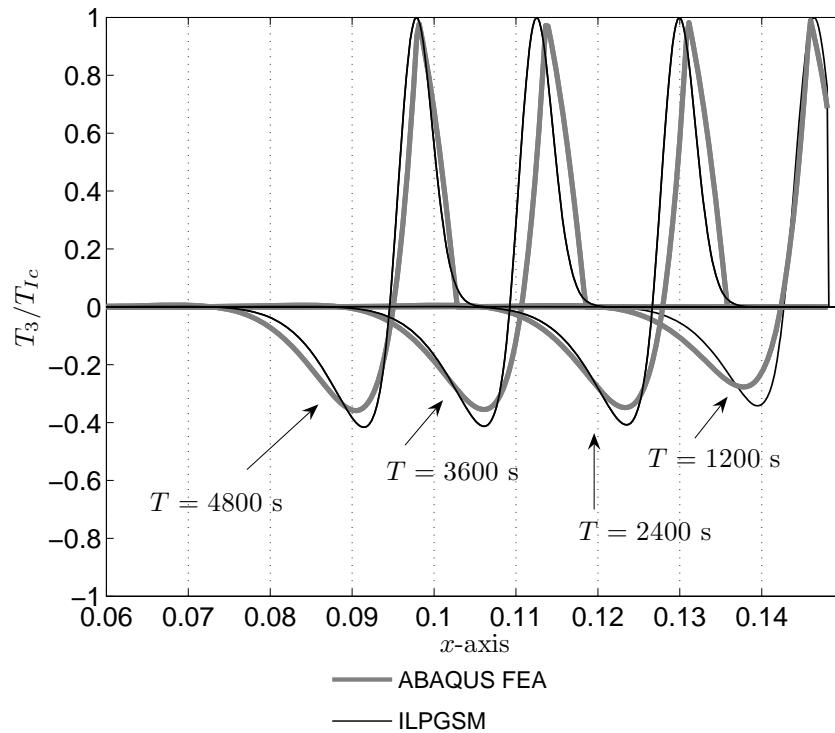


Figure 9.11. Comparison of normal traction in adhesive layer by ABAQUS COH2D4 elements and by ILPGSM with cohesive zone modeling. ( $T = 1,200$  s corresponds to  $\bar{w} = 1$  mm,  $T = 2,400$  s corresponds to  $\bar{w} = 2$  mm,  $T = 3,600$  s corresponds to  $\bar{w} = 3$  mm, and  $T = 4,800$  s corresponds to  $\bar{w} = 4$  mm)

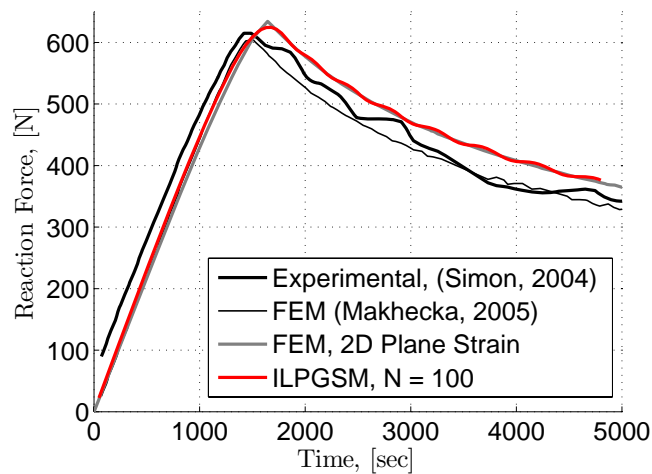


Figure 9.12. Reaction force history for mode I loading of adhesively bonded double cantilever beam.

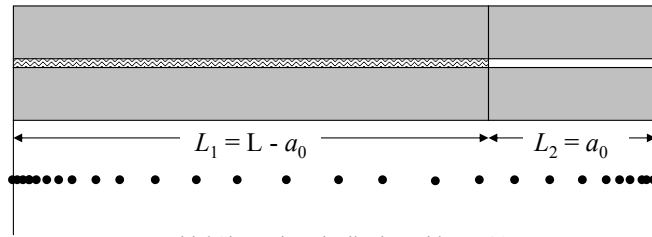
## 9.5 Adaptive Sinc Point Distribution

To more efficiently utilize the ILPGSM for delamination analysis, an adaptive discretization method was developed. This approach is described in the following section.

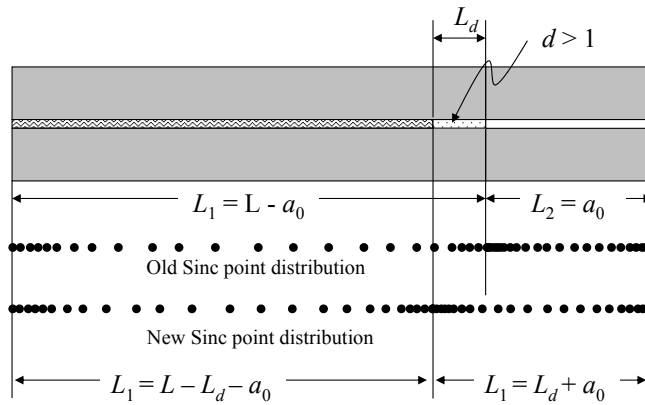
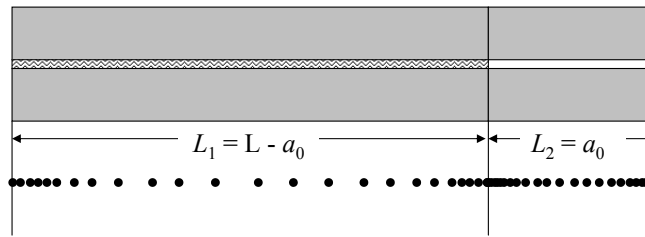
Sinc methods are often implemented for analysis of BVPs with end-point singularities. Moreover, by the DE transformation, the Sinc points are biased toward the edges. This can be seen in Fig. 9.13. This allows the approximated function to change very rapidly over a small distance and thus singularities or near singularities are approximated very well. For delamination analysis the normal and shear tractions within the CZM change very rapidly. When the critical strain energy release rates are small, the spike occurs over a smaller area. Therefore, it can be difficult to approximate this spike without a substantial mesh refinement. For the ILPGSM, when the delamination front is near the center of the beam where the Sinc points are very far apart, the natural distribution of Sinc points is not advantageous for this type of analysis.

If two subdomains were introduced in such a way that the maximum amount of Sinc points occurs in the vicinity of the delamination front, a far more efficient solution could be obtained. To that end, the following adaptive technique was developed. Two subdomains were used as indicated in Fig. 9.13. The adherents and adhesive in each subdomain were modeled as described in Section 9.3. Between the subdomains, the penalty method or Lagrange multiplier method can be used to enforce the continuity condition for the displacements and rotations. Initially, the subdomains are specified such that boundary occurs at the crack tip (subdomain I -  $x \in [0, L - a_0]$ , subdomain II -  $x \in [L - a_0, L]$ ). In this fashion, the large shear and normal traction in the cohesive layer at the crack tip remains within the highly discretized area near the interface.

Following a converged load step,  $i$ , in which damage has occurred, characterized by  $d > 1$  in Eq. (9.10), the Sinc points are redistributed. In the ILPGSM implementation, the damage variable,  $d$ , is tracked at the integration points. In subdomain I, the first integration point



(a) Single Subdomain



(b) Adaptive approach

Figure 9.13. Two-subdomain adaptive Sinc point distribution approach

for which  $d > 1$  is identified. This point constitutes the new subdomain I - subdomain II boundary for the Sinc point distribution to be utilized in the load step,  $i + 1$ .

The tangential stiffness matrix is re-obtained utilizing the current Sinc point distribution and the current Jacobian,  $dx_1/d\xi$  for each of the subdomains. For the single subdomain analysis, the solution from load step  $i$  served as the initial guess for the Newton-Raphson procedure for load step  $i + 1$ . However, because of the adaptive Sinc point distribution and because the unknowns for the ILPGSM do not represent the value of the function at the Sinc points, reconciling the solution from the  $i$ th load step onto the Sinc point distribution of the  $(i + 1)$ th step is not trivial. A complicated reconciliation process may be used to acquire the solution from load step  $i$  in the modified domain to be used as an initial guess for load step  $i + 1$ ; however, doing so would be tedious. For the present analysis, the solution (displacement and rotation unknowns) was simply utilized in its load-step  $i$  form to serve as an initial guess for the load step  $i + 1$ .

The damage variable,  $d$ , at each integration point merits some care. The integration points in load step  $i$  do not correspond physically to integration points in load step  $i + 1$ . However, if the loading cycle includes loading and unloading, the damage variable must be propagated from the previous load step to facilitate the irreversibility of the damage. For the present analysis, linear interpolation between integration points in the previous load step was performed to determine the damage at integration points in the  $i + 1$  Sinc point distribution. While the damage variable is nonlinear between the integration points, using linear interpolation allows the damage variable to be efficiently reconciled between subdomains during the adaptive Sinc point distribution procedure. By choosing a sufficiently small load step, the integration points in  $i$  and  $i + 1$  load steps will be sufficiently close so that the damage is approximated well.

### 9.5.1 Comparison of DCB Results by Adaptive and Standard ILPGSM

To assess the efficiency of the adaptive Sinc point distribution procedure, the aluminum DCB was analyzed using both a single subdomain and the two-subdomain adaptive procedure. In Fig. 9.14, the reaction force history is compared for increasing number of DOF. In Fig. 9.14, the reaction force is plotted against the applied displacement,  $\bar{w}$ . With a single subdomain, the solution was obtained using  $N = 50, 65, 80, 100,$  and  $120$ , resulting in  $618, 798, 978, 1,218,$  and  $1,458$  DOF respectively. For the adaptive approach, the solution was obtained using  $N = 5, 10, 20, 30,$  and  $50$ , resulting in  $156, 276, 516,$  and  $756$  DOF respectively. For each case, the solution was obtained using an initial step size of  $w_{\max}/150$ .

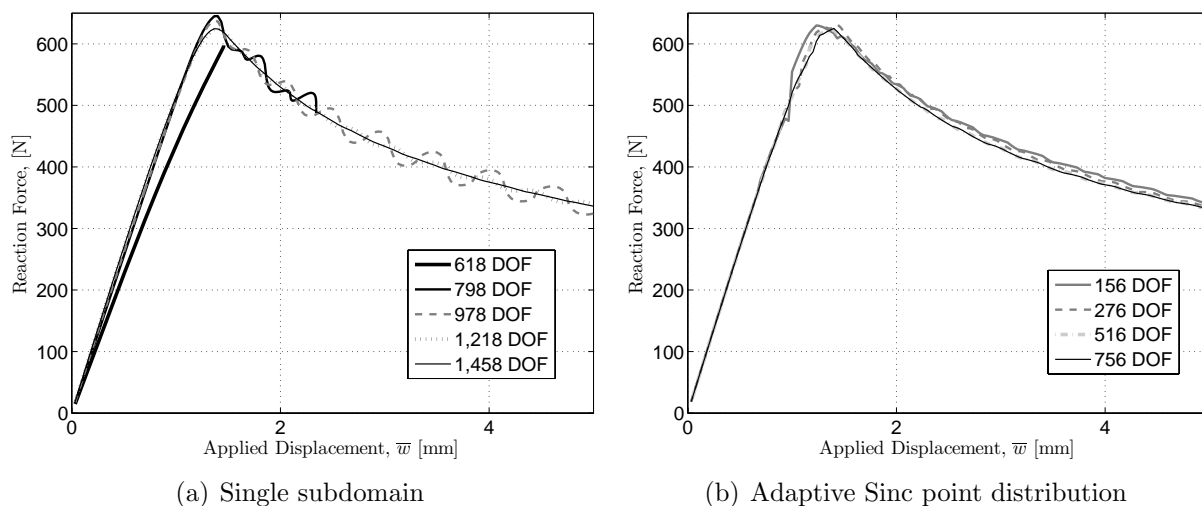


**Figure 9.14.** Reaction force history for the aluminum DCB using the a single Sinc point distribution and using the adaptive Sinc point distribution with two subdomains.

With a single subdomain, the full history was not obtained using 618 and 798 DOF. For these cases, the solution failed to converge, the step size was reduced by half in each failed iteration until the step size was 1% of the original step size. For these two cases (618 and 798 DOF), the solution failed at a applied displacement of 2.91 and 4.69 mm, respectively. When 978 DOF were used ( $N = 80$ ), the full load history was obtained; however, the reaction force was seen to exhibit significant oscillations in the unloading region. With 1,218 and 1,458



**Table 9.14.** Comparison of computational time by the single subdomain and by the two-subdomain adaptive Sinc point distribution procedure for aluminum DCB.

Single		Adaptive	
DOF	Time [sec]	DOF	Time [sec]
618	-*	156	6.5
798	-*	276	10.8
978	184.9	516	20.3
1,218	237.6	756	30.7
1,458	322.4	1,236	62.5

\* Failed to obtain a full history. The step size was reduced to less than 1% of the initial step size.

DOF, a similar solution was obtained, comparable to that obtained with the ABAQUS FEA (see Fig. 9.12).

With the adaptive procedure, there was no trouble obtaining a converged solution for the whole loading history, even with as few as 156 DOF. Furthermore, there are no oscillations in the reaction force history characteristic of the solution from the single subdomain analysis. The solution appears to be converged with as few as 516 DOF, with a similar solution being obtained with 516 and 756 DOF. The reduction in required DOF makes the adaptive procedure a substantial advantage over the single subdomain approach.

In Table 9.14, the computational time elapsed during the entire loading history is compared for the single subdomain and the adaptive procedure. The table indicates that adaptive procedure results in substantially reduced computational time for obtaining a converged solution. The benefit of using the adaptive procedure are not solely the result of reducing the number of DOF. With a single subdomain and 1,218 DOF the analysis took 3.8 times as long as using 1,236 DOF with the adaptive approach. The substantial difference in computational time results from the fact that each load step within the single subdomain solution took more iterations to converge than did the same load step within the adaptive procedure.

To illustrate the benefits of the adaptive approach, the shear force in the top sublaminar

was plotted in Fig. 9.15 at an applied displacement of 2.91 mm. The figure illustrates that the single subdomain solution suffers from the Gibbs phenomenon due to the very large change in shear force in the vicinity of the crack tip. In this region, the shear force transitions from 0 to the applied reaction load. When the crack tip occurs in the interior, the basis function is unable to correctly capture the sharp change in shear force. However, when the transition occurs at the edge of the domain, the basis function captures the transition very well. Sinc methods are often used to study problems with end point singularities because of their ability to capture sharp changes near the edge. The adaptive procedure utilizes this property to capture the sharp change in shear force very accurately with a minimum number of unknowns.

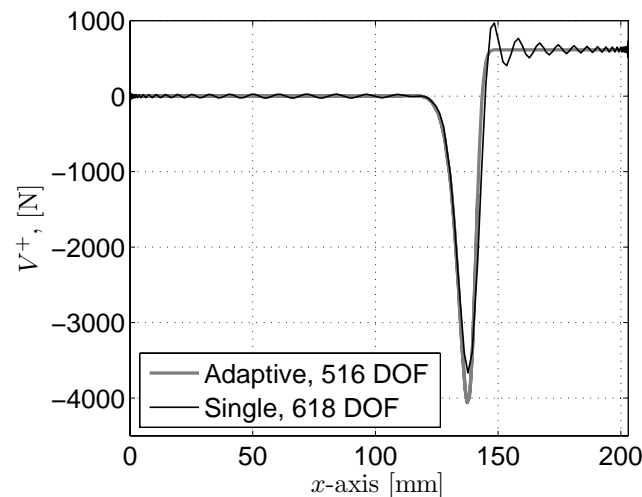


**Figure 9.15.** Shear force in the top sublaminates for single subdomain analysis and adaptive Sinc point distribution.

## 9.6 Fixed-Ratio Mixed Mode Delamination

To test the mixed mode (I+II) capabilities of the beam analysis with ILPGSM, a fixed-ratio mixed mode (FRMM) specimen was considered. The FRMM specimen exhibits mode I and II strain energy release rates with a ratio of  $G_I/G_{II} = 4/3$  and has been studied by many

authors when testing traction-separation laws for use with delamination [72, 222, 60].

### 9.6.1 Numerical Results for FRMM Delamination

A generic composite material was used for the analysis. The material properties for the composite and interface are shown in Table 9.15. These properties were given in Chen *et al.* [72]. Two layers of  $0^\circ$  plys, each with a thickness of 3.1 mm, were used. The beam was taken to be 105 mm long with an out of plane width of 2.4 mm. An initial crack length of 45 mm was used. Because of the chosen dimensions, the plane-stress assumption is applicable. The loading configuration for a FRMM specimen was given in Fig. 9.8.

**Table 9.15. Material properties for composite material for FRMM delamination.**

$E_1$ [GPa]	$E_2$ [GPa]	$G_{13} = G_{12}$	$\nu_{12} = \nu_{23} = \nu_{13}$
130	8	6	0.27

**Table 9.16. Material properties for cohesive layer used for FRMM specimen.**

$T_{1c}$ [MPa]	$T_{2c}$ [MPa]	$G_{Ic}$ [N/mm]	$G_{2c}$ [N/mm]
48	48	0.256	0.856

The present results with the ILPGSM were compared with those obtained by a FEA. The FE mesh was composed of stacked beam elements. Each of the 0 degree lamina were meshed using a total of 2,100 B21 beam elements placed at the mid-surface. The tie constraint [75] was used to attach the beam surfaces at the interface to the adhesive. The adhesive was meshed using 1,200 COH2D4 elements with a thickness of 0.01 mm using the bilinear traction-separation law. The mode mixing was performed using a linear power law so that the interface behaves similarly to the exponential cohesive law implemented for the ILPGSM results [ $\alpha = 2$  in Eqs. (9.2) and (9.4)]. The ILPGSM solution was obtained using the adaptive Sinc point distribution procedure using  $N = 50$  in both subdomains and using a total of 13 Lagrange multipliers to apply the essential boundary conditions and continuity between the subdomains. Therefore, a total of 1,249 DOF resulted.

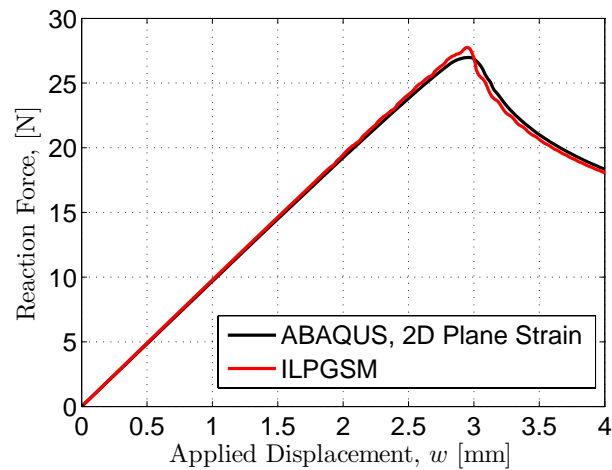


**Figure 9.16.** Reaction force history for a FRMM specimen of a  $[0^\circ]_s$  composite beam. Comparison is made with a 2D plane-strain analysis with ABAQUS cohesive finite elements. The ILPGSM results were obtained using the adaptive Sinc point distribution approach with  $N = 50$  (1,249 DOF).

The reaction force history is plotted against the applied displacement in Fig. 9.16. The figure indicates an excellent correlation between the two analysis techniques confirming the accuracy of the mixed-mode interface model. The deformation and interface traction are plotted in Appendix J and show good correlation between the FEA and ILPGSM solutions.

## 9.7 Delamination of GLARE Specimen

FMLs have recently been introduced by Delft University in order to improve the fatigue performance of aircraft structures [223]. FMLs were developed as an attempt to improve the durability of fiber reinforced polymer laminates (FRPL). In FMLs, the FRPL are protected from the environment by a outer metal layer. Moisture absorption in FRPL has been shown to reduce the laminate strength and stiffness due to matrix plasticization and degradation of the interface between the fiber and matrix material [224, 225]. Unlike FRPL the FML panels can be used in much the same way as aluminum with traditional fixation techniques.

GLARE, a FML composed of alternating layers of glass-reinforced epoxy composite and 2024-T3 aluminum [225] has been successfully used in Airbus A380 [20, 21]. There are

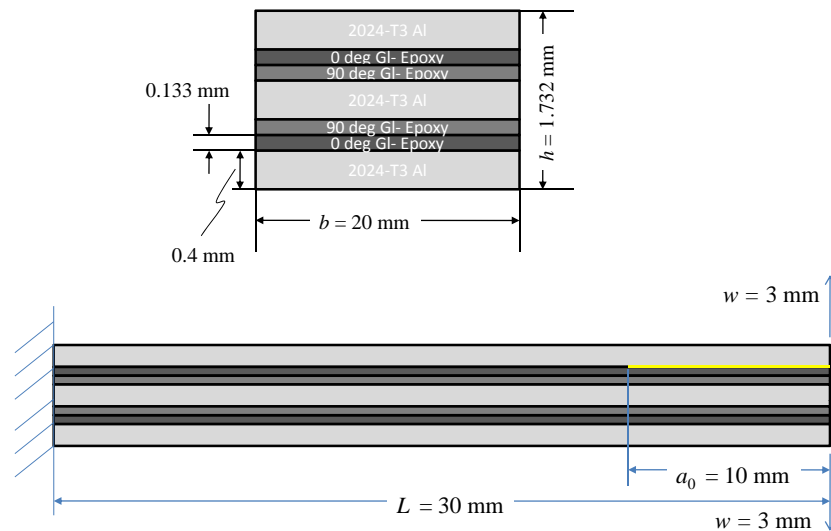


**Figure 9.17.** Layup of GLARE 3-3/2-0.4 with dimensions [1]. The dimensions, loading, and boundary conditions of the plane-strain specimen considered in this analysis are given.

several “grades” of GLARE consisting of various orientations of the glass-epoxy layers. In this section, a GLARE 3-3/2-0.4 [1] which refers to a GLARE specimen with three aluminum layers and two cross-ply glass-epoxy layers was considered. The 2024-T3 aluminum layers have thickness of 0.4 mm each. The complete layup scheme is indicated by

$$[2024 - T3, 0^\circ, 90^\circ, 2024 - T3, 90^\circ, 0^\circ, 2024 - T3].$$

Each unidirectional lamina has thickness of 0.133 mm (see Fig. 9.17).

Numerous studies have been conducted researching the delamination growth due to fatigue in FMLs [226, 227, 228, 229]. Delamination buckling of FMLs has also been a highly studied phenomena [230, 231]. Local delaminations can result in a local buckle of the delaminated layer and cause progressive delamination growth. These initial delaminations can be the result of manufacturing flaws, impact, or excessive stresses in the interface. The delamination growth can reduce the stiffness of the hybrid system potentially resulting in a catastrophic failure. Three-point bending tests by de Jong *et al.* [191] have shown delaminations most

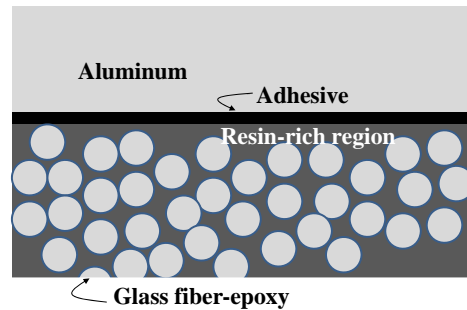


**Figure 9.18.** Illustration of resin-rich region between the aluminum layer and the glass fiber-epoxy in which delamination is expected to occur.

typically result between the outer most aluminum and glass fiber-epoxy layers. While the adhesive bonding between the aluminum and the glass fiber-epoxy layers is excellent, a crack is likely to form in the “resin-rich” region of the  $0^\circ$  glass fiber-epoxy layer as illustrated in Fig. 9.18. Remmers and de Borst [230, 231] used “solid-like” shell elements along with interface elements to study buckling delamination growth of a GLARE-like specimen. These “solid-like” elements [232] are similar to the “continuum shell” elements in ABAQUS [75]. These elements consist of 8 external nodes with linearly varying (through-the-thickness) transverse normal strain.

The total thickness of the seven layer system is only 1.732 mm. A detailed FEA of the GLARE system with each layer modeled with 3D elements would require a large number of elements through the thickness. Furthermore, modeling the delamination analysis in the 3D sense would require a very fine mesh along the width and thickness dimensions. Therefore, stacked plate elements and beam would be more appropriate. When used with interface elements, these theories could be utilized to study the delamination growth in a GLARE member. The traction-separation law could be used to obtain the interlaminar stresses in the interface material. However, obtaining the through-the-lamina-thickness state of stress from the plate elements would require a post-processing technique as discussed in Chapter 2. Using the integrated Sinc methods, however, would supply all the necessary information to obtain the through-the-thickness stress distribution from beam or plate analysis without

the need for a post-processing technique.

To demonstrate the use of the ILPGSM for delamination analysis of a plane-strain GLARE specimen, a  $L = 30$  mm long GLARE panel was considered. The dimensions of the panel are shown in Fig. 9.17. The out-of-plane width was taken to be ( $b = 20$  mm). Because  $b \gg h$ , the plane-strain assumption may be used. An initial delamination of  $a_0 = 10$  mm was assumed to exist between the top aluminum and composite layers as shown in Fig. 9.17. The material properties for the 2024-T3 aluminum and the glass fiber-epoxy composite are given in Table 9.17. The material properties for the interface were taken to be those utilized by Remmers and de Borst [231] and are given in Table 9.18.

**Table 9.17. Material properties for GLARE constituents.**

Material	$E_1$ [GPa]	$E_2$ [GPa]	$G_{13} = G_{12}$	$G_{23}$	$\nu_{12} = \nu_{23} = \nu_{13}$
Aluminum*	72.4	72.4	27.2	27.2	0.3
Glass Fiber-Epoxy†	53.8	17.9	8.96	3.45	0.25

\* Material properties were taken from Ref. [231].

† Material properties were taken from Ref. [98].

**Table 9.18. Material properties for cohesive layer.**

$T_{1c}$ [MPa]	$T_{2c}$ [MPa]	$G_{Ic}$ [N/mm]	$G_{2c}$ [N/mm]
25	50	1.1	1.1

The ILPGSM analysis was performed by modeling the seven-layer laminate by two equivalent single layers using the classical lamination theory to obtain the equivalent monoclinic material. The FSDT was used to analyze each sublaminde as detailed in Section 9.3. The loading (see Fig. 9.17) is that of the DCB with and displacement being applied to the top and bottom sublaminde; however, the asymmetry of the specimen above and below the delamination makes the loading mixed mode. The maximum displacement of 3 mm was applied using 100 equal load steps. The adaptive Sinc point distribution was used with  $N = 60$  on each side of the delamination front. The essential boundary conditions and continuity were imposed using a total of 14 Lagrange multipliers. This resulted in a total of 1,490 DOF.

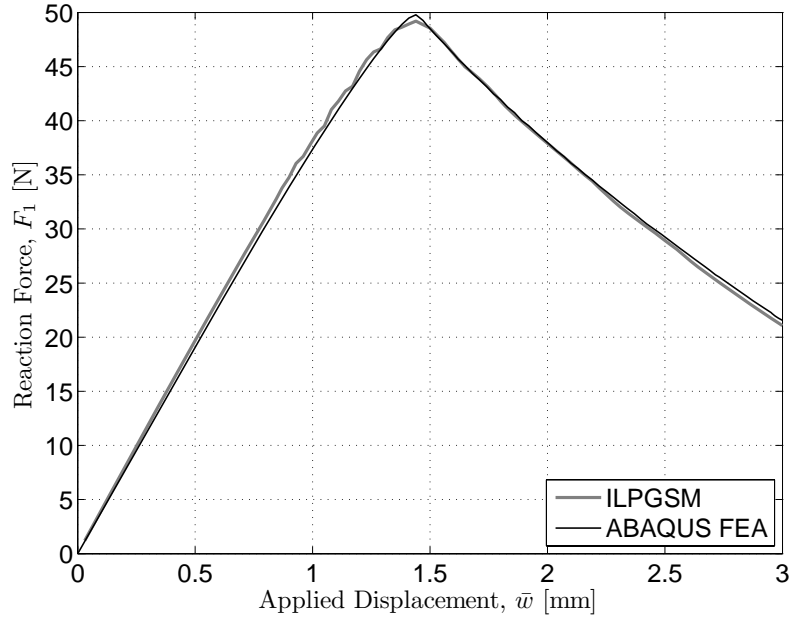
For the sake of comparison, FE results were also obtained with ABAQUS. Each lamina layer was meshed using CPE4I elements. Five elements were used through the thickness of each of the seven layers and 500 elements were used along the length of the specimen. The cohesive layer was meshed using a total of 400 COH2D4 cohesive interface elements. An interface thickness of 0.01 mm was used to model the cohesive. Tie constraints were used to connect each of the seven lamina layers and the cohesive layer to the appropriate surrounding material.

The reaction force histories of the applied loads,  $F_1$  and  $F_2$  are plotted in Fig. 9.19 against the applied tip displacements. The loads  $F_1$  and  $F_2$  correspond to the applied load in the top and bottom sublaminates respectively (see Fig. 9.17). Figure 9.19 indicates an excellent agreement between the FEA and ILPGSM results. The stable delamination growth is approximated well by the ILPGSM solution. The force in the top sublaminate falls steadily with increasing applied displacement; however, the bottom sublaminate retains substantial bending stiffness. The load continues to increase at reduced stiffness throughout the loading history.

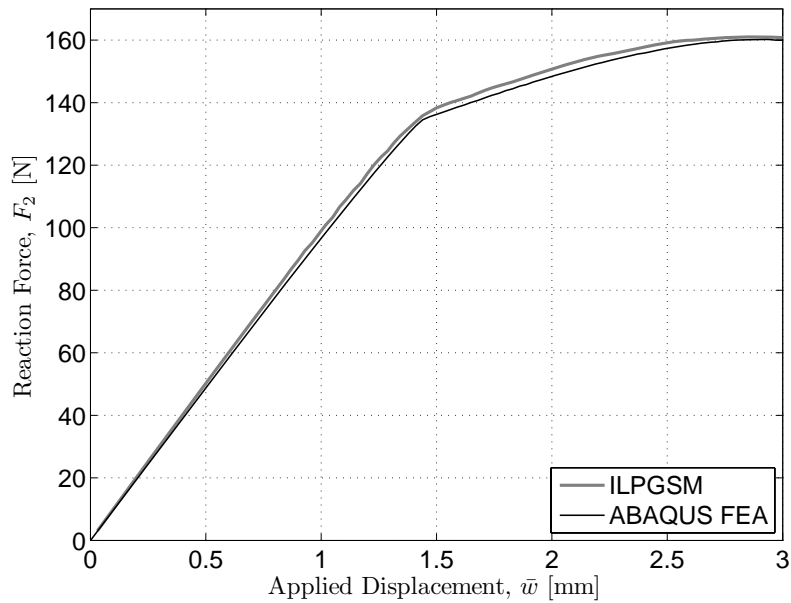
The deformation of the specimen was compared for results from the FEA and ILPGSM solutions in Fig. 9.20. The deformed geometry was plotted at four instances in the load history, 1.0, 2.0, 2.5, and 3.0 mm applied displacement. The figure indicates the deformed geometry is indistinguishable from that by the FEA at each load step. The delamination front appears to track the FEA solution well.

The traction in the cohesive layer was plotted in Fig. 9.21 obtained by the FEA and by the ILPGSM. For the ILPGSM solution, the normal and tangential traction components were rotated into  $(x_1, x_3)$  coordinate system using Eq. (9.21). The tractions were plotted at 1.0, 2.0, 2.5, and 3.0 mm applied displacement. The figure indicates good correlation of interfacial traction components obtain by the two analysis approaches. While there is some discrepancy between the traction components themselves, the location of the crack tip





(a) Top reaction force history



(b) Bottom reaction force history

**Figure 9.19.** Reaction force history of GLARE specimen with 10 mm initial delamination between top aluminum and composite layers. Results were obtained using an ABAQUS plane-strain FEA and ILPGSM with  $N = 60$ .

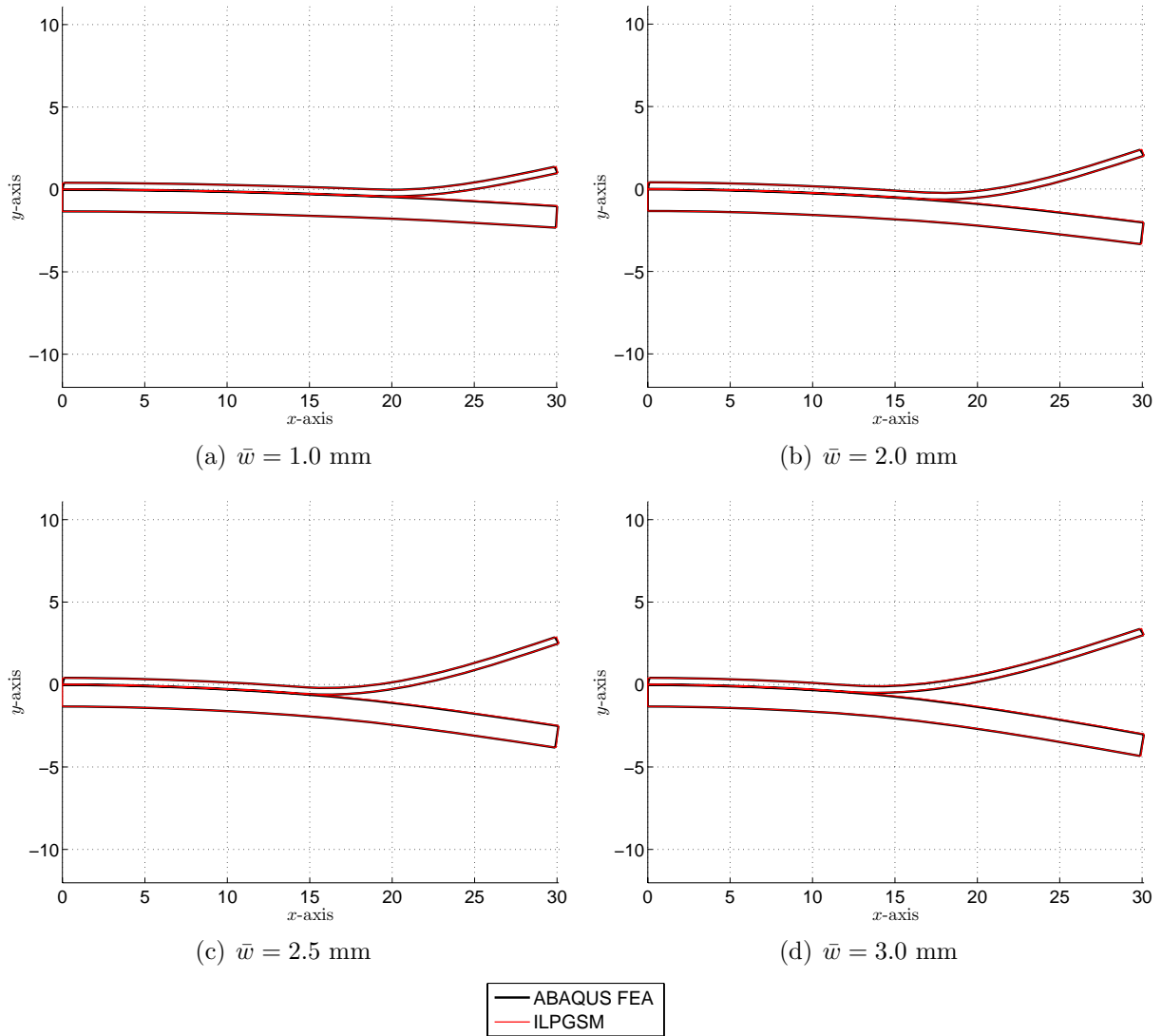


Figure 9.20. Deformation of GLARE specimen with increasing applied opening displacement.

appears to correlate well. In the figure, the normalized effective traction as computed by Eq. (9.2) was plotted. For each increment, the normalized traction for both the FEA and the ILPGSM peaks at 1; however, in front of the peak, the normalized traction is higher for that given by the ILPGSM than that given by the FEA.

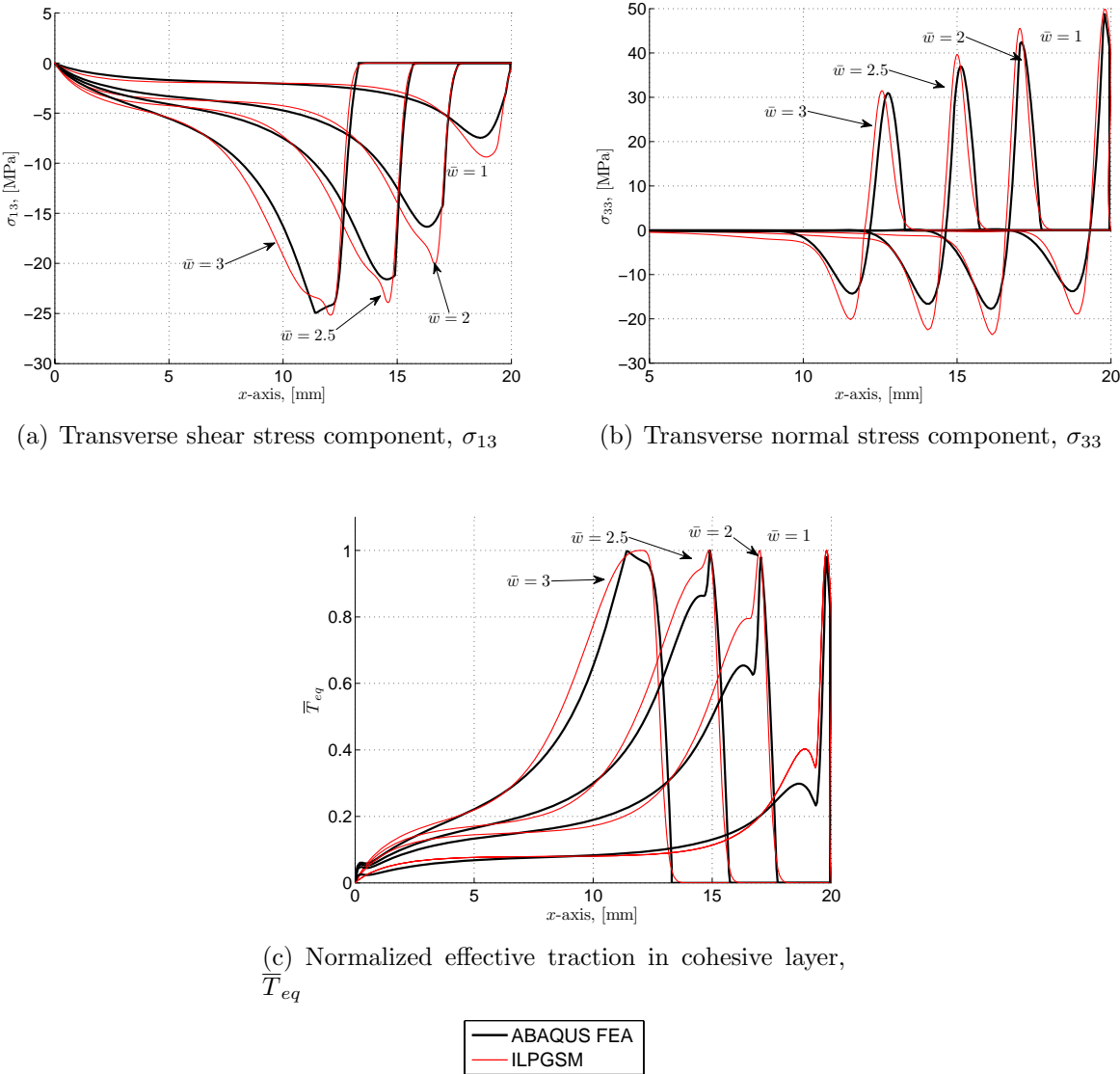


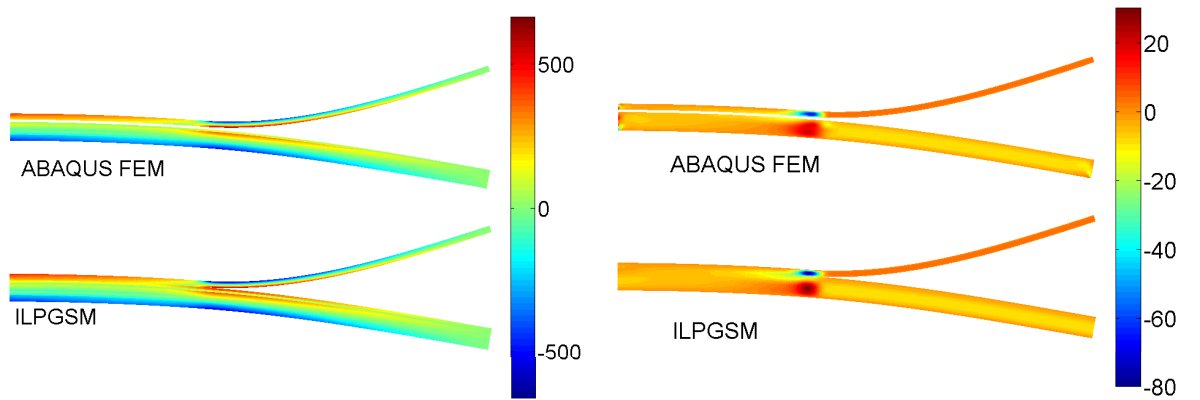
Figure 9.21. Traction components in the cohesive layer between the top aluminum and composite layers in a GLARE 3-3/2-0.4 plane-strain specimen.

The through-the-thickness stresses were also obtained by integration of the equilibrium

equations of the 3D elasticity theory [see Eqs. (2.17) and (2.19)] for each of the two sublaminates at an applied displacement of 3 mm. Fringe plots of the stress distributions are given in Fig. 9.22. The figure indicates that the ILPGSM with the 3D elasticity integration procedure approximates the stresses accurately both qualitatively and quantitatively with the exception of near the boundary. For this case, the clamped condition imposed at the root results in a Poisson pinching of the beam and thus the FEA exhibits stress concentrations in this vicinity. Near the tip where the displacement boundary conditions are imposed, the transverse normal stress from the FEA exhibits a stress concentration at the point of load application; however, the ILPGSM solution assumes  $U_3 = w_0 = \text{constant}$  through the sublaminate thickness. Therefore, it does not contain enough detail to see a similar stress concentration.

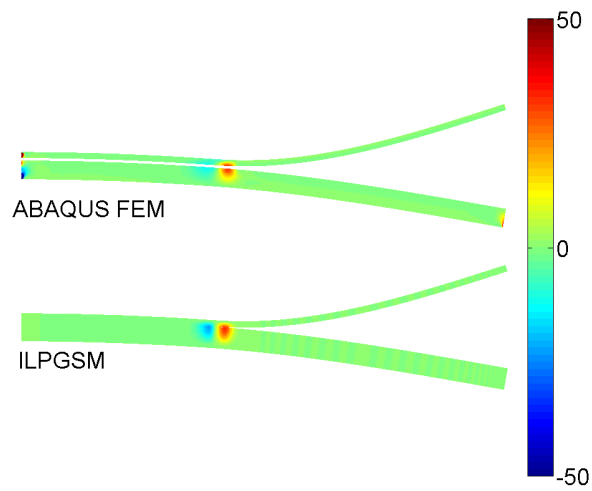
Through-the-thickness distributions of bending stresses at the fixed edge and near the delamination front ( $x = 13$  mm) were plotted in Fig. 9.23. The figure indicates that the bending stresses are very accurately approximated in each of the seven lamina layers. The outer-most aluminum layers experience high stresses. The yield stress of aluminum 2024-T3 is 324 MPa [233]. Thus yielding is expected in the aluminum layers. To include this effect, the through-the-thickness integration to obtain the  $A_{11}$ ,  $B_{11}$ , and  $D_{11}$  should be performed using a nonlinear material model for the aluminum and should be updated in each iteration. Moreover, no fiber or matrix failure of the glass-reinforced epoxy was considered. These effects are beyond the scope of the present analysis. Nonetheless, the accuracy of the bending stresses illustrate how the FSDT can be used to accurately approximate the complicated mechanisms of mixed mode delamination.

The through-the-thickness distribution of transverse shear ( $\sigma_{13}$ ) and transverse normal ( $\sigma_{33}$ ) stresses were plotted in Fig. 9.24 at  $x = 12.5$ ,  $13.0$ , and  $13.5$  mm. While there is some discrepancy between the results at  $x = 13.0$  mm, there is good correlation of the transverse shear and transverse normal stresses by the two analyses at both  $x = 12.5$  and  $x = 13.5$



(a) Fringe plots bending stress,  $\sigma_{11}$  (MPa)

(b) Fringe plots of transverse shear stress,  $\sigma_{13}$  (MPa)



(c) Fringe plots of transverse normal stress,  $\sigma_{33}$  (MPa)

Figure 9.22. Fringe plots of stress in a GLARE 3-3/2-0.4 beam with an applied load of 3 mm.

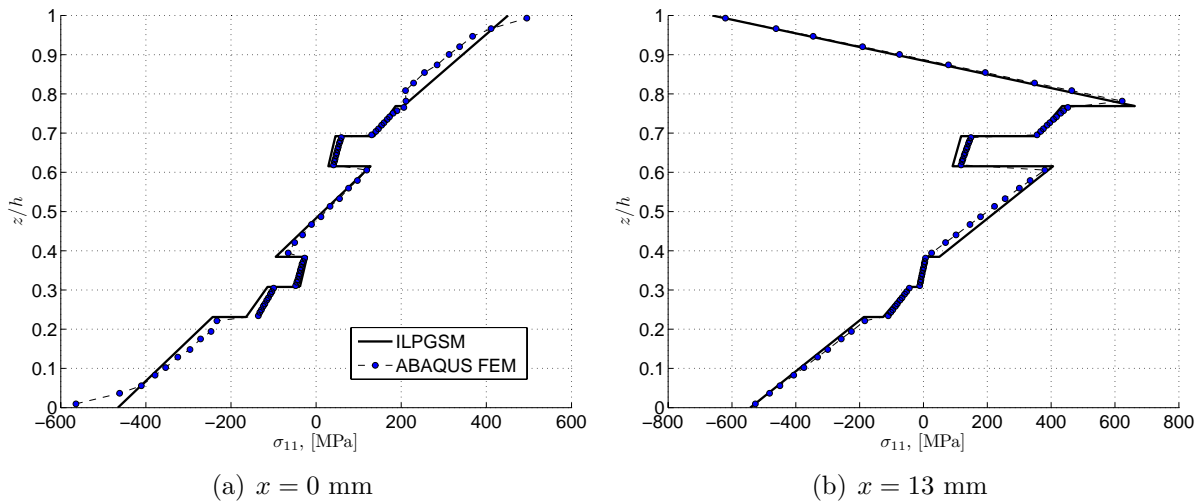
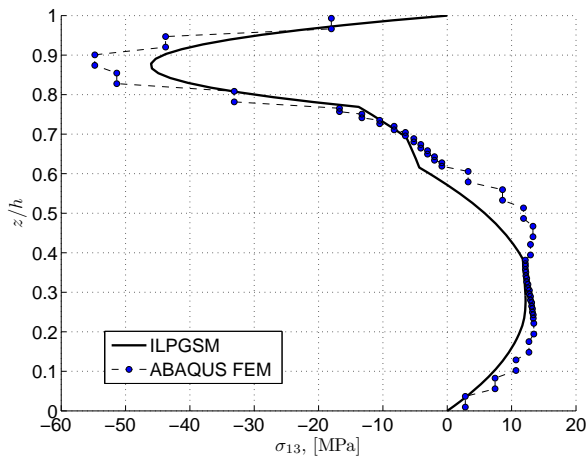


**Figure 9.23.** Through-the-thickness distributions of bending stress in GLARE 3-3/2-0.4 plane-strain specimen with applied displacements of 3.0 mm.

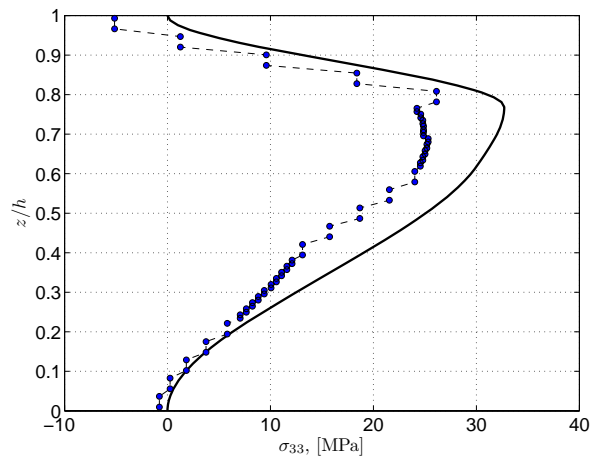
mm. The discrepancy seen at  $x = 13.0$  is the result of the sharp changes that occur in the vicinity of the delamination front. Moreover, it should be noted that the FEA results indicate more elements are needed to obtain accurate stresses through the thickness. Nonetheless, the through-the-thickness distributions of transverse normal and transverse shear stresses at  $x = 12.5$  and  $13.5$  mm obtained by the ILPGSM show excellent correlation compared with those by the 2D FEA.

## 9.8 Summary and Conclusions

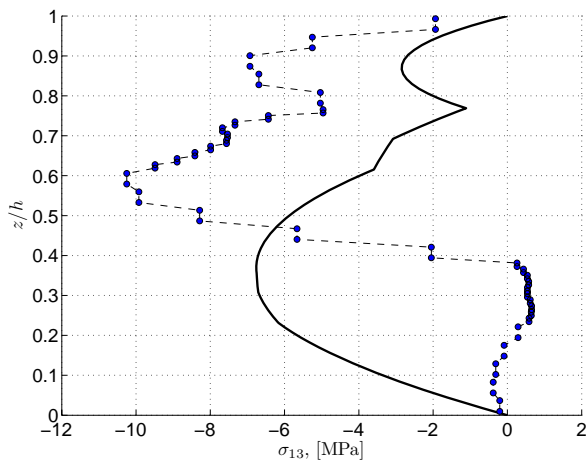
The ILPGSM was used with an irreversible exponential traction-separation constitutive law for modeling mode I and mixed mode delamination of an adhesively bonded aluminum and hybrid plane-strain and plane-stress structural specimen. The FSDT was used to model the specimen both above and below the delamination with the sublaminates interfaces coupled to each other through the CZM. Along with the plane-strain or plane-stress assumption, the analysis is performed by solving a 1D nonlinear BVP with the ILPGSM. Through-the-sublaminates-thickness distributions of interlaminar stresses were obtained using integration



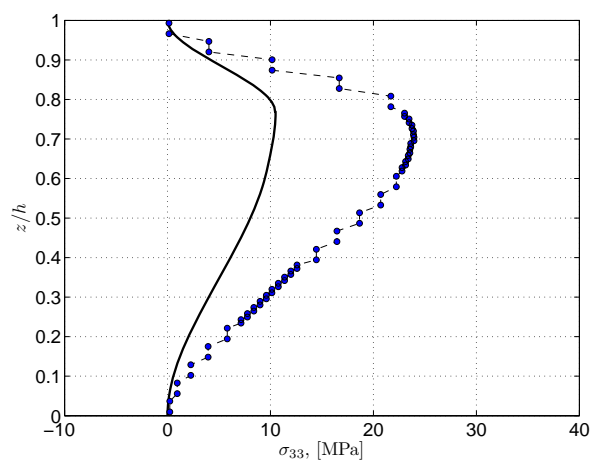
(a)  $x = 12.5$  mm



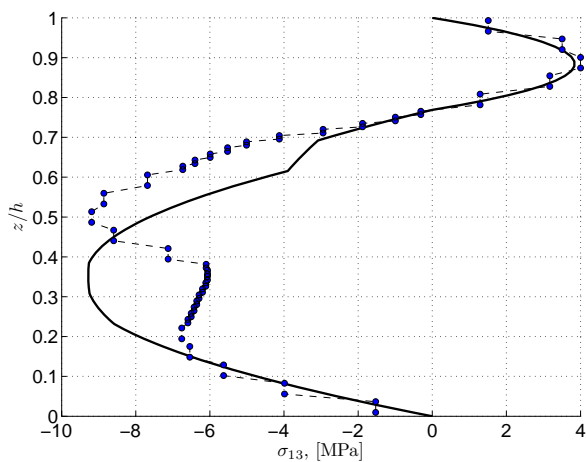
(b)  $x = 12.5$  mm



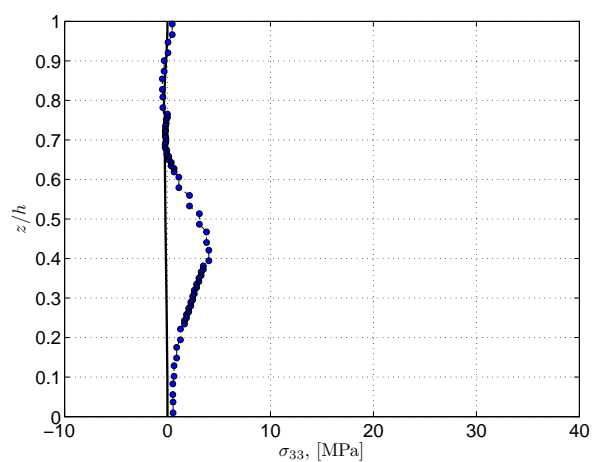
(c)  $x = 13$  mm



(d)  $x = 13$  mm



(e)  $x = 13.5$  mm



(f)  $x = 13.5$  mm

Figure 9.24. Through-the-thickness distributions of transverse shear and transverse normal stress in GLARE 3-3/2-0.4 plane-strain specimen with applied displacements of 3.0 mm.

of the equilibrium equations of 3D elasticity.

Mode I delamination analysis of an adhesively bonded aluminum beam was performed using the ILPGSM. The results indicated excellent correlation between the ILPGSM results and the FEM results obtained using cohesive elements in ABAQUS. The results were also compared with experimental results [221]. The ILPGSM results and FEA results correlated well with the experimental results.

An adaptive Sinc point distribution technique was introduced in which the domain is divided at the delamination front. The domain divide slides as the delamination propagates. Because the Sinc points, distributed by the DE transformation, are biased toward the boundary in the ILPGSM, the adaptive Sinc point distribution allows an accurate solution to be obtained with far fewer Sinc points than when a single subdomain is utilized. The adaptive Sinc point distribution easily overcomes the Gibbs phenomenon seen with a single subdomain.

Mixed-mode delamination analysis of a FRMM,  $[0^\circ]_s$  composite specimen was performed using the adaptive Sinc point distribution. The results compare well with a similar solution obtained using the FEA.

Finally, results were obtained for delamination of a GLARE 3-3/2-0.4 specimen using the ILPGSM with the adaptive Sinc point distribution technique. The results correlate well with similar results obtained using a plane-strain FEA. Interlaminar stresses through the thickness of the specimen were obtained from the ILPGSM results by integrating the equilibrium equations of 3D elasticity through the thickness. These results correlate well with the FEA analysis.



## 10 Concluding Remarks and Future Work

The scope of this dissertation was to examine the feasibility of the integrated Sinc methods as practical tools for analysis of composite and hybrid systems of adhesively bonded materials and enhance their capabilities as an analysis tools. To that end, a substantial amount of work has been conducted to advance the SIHD method and the ILPGSM for analysis of composite materials.

The SIHD method was implemented for solving 1D and 2D BVPs. An alternative symmetric approach for applying the boundary conditions was introduced. The method was implemented for analysis of a 1D graphite-epoxy composite Timoshenko beam problem and 2D analysis of a classical laminated plate problem. The results indicated that the SIHD method with the alternative boundary condition approach performs better than the original SIHD method. The displacements and stresses, including interlaminar stresses were compared with those by an analytic solution of the Timoshenko beam and classical laminated plate and indicated excellent accuracy and convergence properties. The results clearly demonstrated that the higher-order derivatives of strain found by this method were accurate.

The interlaminar stresses obtained by the SIHD method was also compared with those obtained by an approximate solution of 3D elasticity for fiber-matrix laminates and functionally graded composites. Results for interlaminar stresses from the Bickford beam theory [134] and the Timoshenko beam theory compared well against those from 3D elasticity except in the vicinity of the edges where 3D edge effects are present. For the functionally graded composite, the numerical indefinite integration by DE transformation was used to integrate and obtain the interlaminar stresses. To improve the interlaminar stresses, the refined zigzag and HOSNDT were considered with the SIHD method. It was concluded that for laminates with large variations of shear moduli, the Timoshenko beam theory and HOSNDT were less accurate than the refined zigzag theory.

A novel integrated Sinc method named the Integrated Local Petrov-Galerkin Sinc Method

was developed. The method utilized the integrated Sinc basis function but was based on the MLPG for domain decomposition. The method easily handles 2D problems on non-rectangular domains. This method was used to analyze an elastic-plastic panel with a hole and to study delamination in adhesively bonded beams with an irreversible cohesive law. These problems are both nonlinear in nature and can exhibit very large stress concentrations. The results indicated that the ILPGSM performs very well for these type of problems, particularly when a stress concentration is located near the boundary where the Sinc points are highly concentrated.

### **10.1 Merits and Demerits of the ILPGSM and SIHD methods**

Like any numerical method, the integrated Sinc methods each have their merits and demerits. These methods were developed under the thought that by using integration as a process rather than differentiation, the resulting solution will be more accurate. The present results have shown that a high level of accuracy and a high convergence rate is obtainable with both the ILPGSM and the SIHD method. The results in Chapter 7 indicated that the ILPGSM is generally more accurate than the SIHD method. Furthermore, the results have shown that the integrated Sinc basis function is very good at capturing large variations and even nearly singular behavior near the edges. The additional accuracy of higher-order derivatives of strains for composite plate and beam analysis, allows this method to be used as a one-step approach for determining interlaminar stresses.

The SIHD method can be very efficient if the Sinc points are used as the collocation points. The “kernel” matrix,  $k_{ij}$  in Eq. (4.4), is independent of the geometry and depends only on the parameters  $N$  and  $\alpha$ . Thus these matrices can be stored in a library and recalled upon use. This process makes the method very efficient. In contrast, the ILPGSM requires evaluating the basis function at many integration points in order to integrate over the subdomains in the local weak form. Therefore, the ILPGSM is more expensive than the

SIHD. In general, both the ILPGSM and SIHD are slow compared with the FEM. While the FEM benefits from a sparse stiffness matrix, the integrated Sinc methods have a fully or nearly-fully populated stiffness matrix, with each of the unknowns contributing to the value of the function at a given point. This property makes the matrix factorization much more expensive than FEM and requires much more memory for the same number of DOF. For a large problem, the advantage of a sparse stiffness matrix is a substantial advantage and thus makes a fully populated stiffness matrix a substantial demerit for the integrated Sinc methods.

Furthermore, the highly continuous nature of the integrated Sinc methods can be advantageous and results in higher accuracy for a continuous solution. However, for a discontinuous or nearly discontinuous function, particularly when these discontinuities lie toward the center of the domain the Gibbs phenomenon can result which can substantially reduce the accuracy. For a nonlinear problem using the iterative approach, the oscillations can result in convergence failures. In Chapter 9, this demerit was overcome by dividing the domain at the delamination front. However, without knowledge of the location of the discontinuity or without the ability to divide the domain at the discontinuity, the Gibbs phenomenon could be a substantial demerit for the method.

Additionally, the basis function is constructed from the value of the highest-order derivative at the Sinc points and constants of integration that relate the indefinite integral to the specific anti-derivative. These constants represent the value of the lower-order derivatives and unknown function at a location  $\xi = 0$ . The lower-order derivatives may vary from the highest-order derivatives by several orders of magnitude. Thus the unknowns could easily have very different orders of magnitude. Without proper scaling, this could lead to poor numerical conditioning of the stiffness matrix. As a result small inaccuracies in the stiffness matrix or force vector could result in large changes to the unknowns. In nonlinear problems, this could lead to convergence issues. While difficulties that could be directly related to this

nature have not been encountered within the work of this dissertation, it is a foreseeable demerit of the integrated Sinc methods.

In the meshless literature, the key advantage these methods hold over the FEM is that element connectivity is not needed [162]. With a connected FE mesh, the elements can become distorted necessitating re-meshing. The integrated Sinc methods share this disadvantage. The Sinc point must lie on a rectangular grid. Thus constructing a complicated domain requires subdivisions like the two subdomains used to represent the panel with a hole in Chapter 8. Thus for some analyses, these subdomains can become distorted resulting in large errors.

## 10.2 Potential Improvement to the Basis Function

The basis function implemented in the present work was the result of careful consideration of the work of Li and Wu [122] with the modifications described in Chapter 4. In Chapter 4, it was shown that by the transformation from the  $x \in [a, b]$  domain to the  $\xi \in [\xi_{-N}, \xi_N]$  domain for a 1D problem, greater accuracy could be obtained and the solution accuracy depends less on the selection of the mesh size  $h$ .

Consider interpolation of a function  $y = 5$  by the Sinc series. The interpolation was performed and is shown in Fig. 10.1. Note that the approximation suffers highly from the Gibbs phenomenon. The Sinc series should approach zero on edges of each of each end to avoid this kind of oscillation. These oscillations become less severe as the number of Sinc points is increased. Through the DE integration process, these oscillations are smoothed and so that the current basis function can overcome these oscillations and still produce highly accurate results. If the offsets were removed from the approximated function so that the Sinc series approximation was used to approximate a function  $y(x)$  on the domain  $x \in [a, b]$  such that  $y(a) = y(b) = 0$  then the approximation would be highly accurate and free from the Gibbs phenomenon. To that end a new basis function was developed.

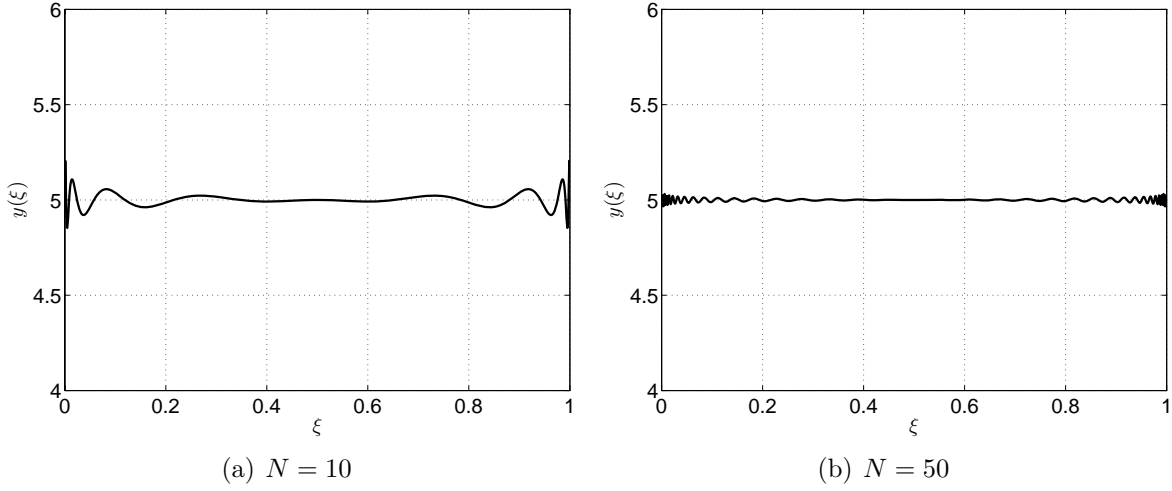


**Figure 10.1.** Gibbs phenomenon associated with Sinc approximation for a function  $y = 5$ .

Let  $y(\xi)$  be an arbitrary function defined on the domain  $\xi \in [0, 1]$ . Let the function  $\tilde{y}(\xi)$  be defined by:

$$\tilde{y}(\xi) = y(\xi) - y(\xi_{-N}) - [y(\xi_N) - y(\xi_{-N})]\xi. \quad (10.1)$$

Now the function  $\tilde{y}(\xi)$  will have a value of zero at  $\xi = 0$  and  $\xi = 1$ . The function  $\tilde{y}(\xi)$  can be approximated by a Sinc series as given in Eq. (3.4). Accordingly,  $y(\xi)$  can be written as:

$$y(\xi) = y(0) + [y(1) - y(\xi_0)]\xi + \sum_{j=-N}^N \tilde{y}_j \text{sinc}[(\pi/h)(\phi(\xi) - jh)] \quad (10.2)$$

where  $\phi$  is the DE transformation as given in Eq. (3.5). If this philosophy were to be used with the numerical indefinite integration process as a basis function, then  $y$  would be a higher-order derivative. Assume we wish to approximate the function  $f''(\xi)$  by a basis function similar to that defined in Section 3.3.2. Then  $f''(\xi)$  can be written by Eq. (10.2):

$$f''(\xi) = f''(0) + [f''(1) - f''(\xi_0)]\xi + \sum_{j=-N}^N \tilde{f}_j'' \text{sinc}[(\pi/h)(\phi(\xi) - jh)] \quad (10.3)$$

where  $f''(0)$ ,  $f''(1)$ , and  $\tilde{f}_j'' = \tilde{f}''(\xi_j)$  are unknowns. Applying the Eq. (3.12), the first

derivative can be written as:

$$\begin{aligned}
 f'(\xi) &= C_1 + f''(0)\xi + \frac{[f''(1) - f''(\xi_0)]\xi^2}{2} + h \sum_{j=-N}^N \tilde{f}_j'' \psi'(jh) \left( \frac{1}{2} + \frac{1}{\pi} \text{Si}(\pi\phi(\xi)/h - \pi j) \right), \\
 f'(\xi) &= C_1 + f''(0)\xi + \frac{[f''(1) - f''(\xi_0)]\xi^2}{2} + h \sum_{j=-N}^N \tilde{f}_j'' T_1(\xi, j)
 \end{aligned} \tag{10.4}$$

For the basis functions presented in Chapter 3, the function  $T_1(\xi, j)$  would be approximated using the Sinc approximation and integrated. However, the function  $T_1(\xi, j)$  does not have the property  $T_1(1, j) = 0$ . Therefore, such an approach would introduce the oscillations and decrease the accuracy of the method. To overcome this issue,  $T_1(1, j)$  is removed. Rewrite  $f'(\xi)$  in the following fashion:

$$\begin{aligned}
 f'(\xi) &= C_1 + f''(0)\xi + \frac{[f''(1) - f''(\xi_0)]\xi^2}{2} \\
 &\quad + \sum_{j=-N}^N \tilde{f}_j'' [T_1(\xi, j) - T_1(1, j)\xi] + \sum_{j=-N}^N \tilde{f}_j [T_1(1, j)\xi] \tag{10.5}
 \end{aligned}$$

Now let:

$$\begin{aligned}
 \tilde{T}_1(\xi, j) &= T_1(\xi, j) - T_1(1, j)\xi \\
 \tilde{T}_1(\xi, j) &= h\psi'(jh) \left[ \left( \frac{1}{2} + \frac{1}{\pi} \text{Si}(\pi\phi(\xi)/h - \pi j) \right) - \left( \frac{1}{2} + \frac{1}{\pi} \text{Si}(\pi(N - j)) \right) \xi \right] \tag{10.6}
 \end{aligned}$$

Next the Sinc series approximation can be used on the term:

$$g_1(\xi) = \sum_{j=-N}^N \tilde{f}_j'' [T_1(\xi, j) - T_1(1, j)\xi] \tag{10.7}$$

To do so, it is evaluated at each of the Sinc points yielding:

$$g_1(\xi) \approx \sum_{j=-N}^N \sum_{i=-N}^N \tilde{f}_j'' [T_1(i, j) - T_1(1, j)\xi_i] \text{sinc}[(\pi/h)(\phi(\xi) - ih)] \quad (10.8)$$

Now applying Eq. (3.12) and analytically integrating the polynomials terms in Eq. (10.4), the function  $f(\xi)$  can be approximated by:

$$f(\xi) = C_2 + C_1\xi + f''(0)\frac{\xi^2}{2} + \frac{\xi^2}{2} \sum_{j=-N}^N \tilde{f}_j T_1(1, j) + \frac{[f''(1) - f''(\xi_0)]\xi^3}{6} \\ + \sum_{j=-N}^N \sum_{i=-N}^N T_1(\xi, i) \tilde{f}_j'' [T_1(i, j) - T_1(1, j)\xi_i]. \quad (10.9)$$

An analogous procedure in 2D could be quite cumbersome. First, insuring that the function approximated by a scalar product of Sinc series has zero value along the lines  $\xi = 0$ ,  $\eta = 0$ ,  $\xi = 1$ , and  $\eta = 1$  is certainly not a trivial process like in the 1D case presented in this section. Secondly, removing the value of the anti-derivative along the lines  $\xi = 1$  and  $\eta = 1$  at each step of the process would also be a substantial task.

To demonstrate the improved accuracy of the basis function presented above over that given in Chapter 3 the following simple 1D BVP was considered using the SIHD method:

$$f''(x) = \sin(\pi x) + 1000x^2 + x + 1000, \quad x \in (0, 1), \\ f(0) = 0, \quad f(1) = 0, \quad (10.10)$$

the solution of which is given by:

$$f(x) = -\frac{\sin(\pi x)}{\pi^2} + \frac{250x^4}{3} + \frac{x^3}{6} + 500x^2 - \frac{1167}{2}x, \quad x \in [0, 1], \quad (10.11)$$

The accuracy of SIHD with the present basis function is compared against the accuracy of the basis function given in Chapter 3 in Fig. 10.2. While both basis functions have similar

convergence rates initially, the present basis function continues to improve much after the previous basis function exhibits diminishing returns.

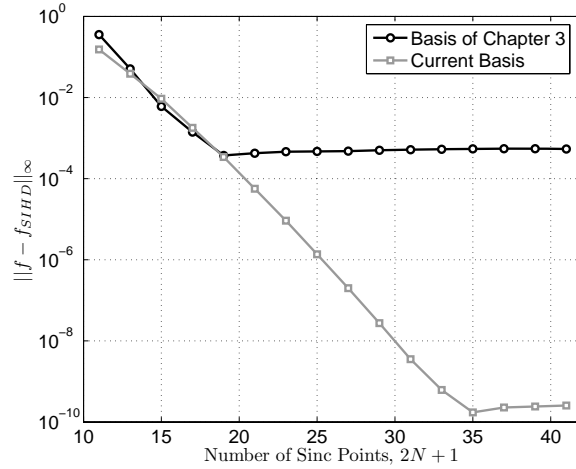


**Figure 10.2.** Comparison of basis function presented in Chapter 3 and basis function developed in this chapter for simple 1D BVP. Results were obtained using  $\alpha = 2.0$ .

The numerical error as a function of  $x$  was plotted in Fig. 10.3 for  $N = 10$  or a total of 21 Sinc points. The figure indicates that the basis function of Chapter 3 has high error near  $x = 1$ . While the present basis function has nearly zero error at  $x = 1$ . The error at  $x = 1$  results from the additive effect of applying the Sinc approximation with nonzero value at its ends.

There is certainly some advantage to exploring the basis function presented in this chapter. However, to implement this basis function in a meaningful manner, a 2D analog to Eqs. (10.2 - 10.9) is needed.

### 10.3 FE Smoothing by the Integrated Basis

While meshless methods have become popular in academic circles, the maturity of the FEM is a key advantage over these methods and over the integrated Sinc methods studied in this dissertation. While the integrated Sinc methods have been shown to work very well for obtaining interlaminar stresses from beam or plate analyses, using these methods for



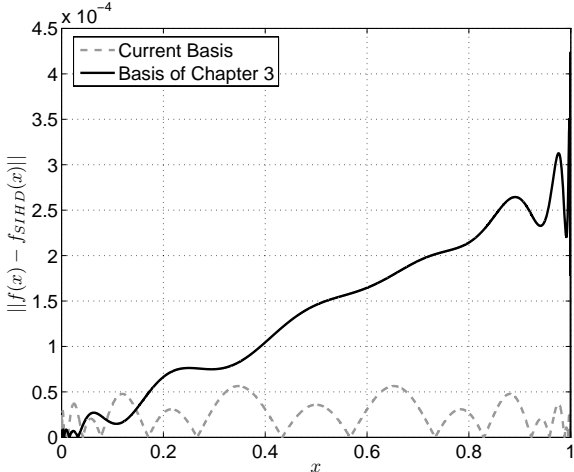


Figure 10.3. Pointwise numerical error in  $f(x)$  found by SIHD with  $N = 10$  or 21 Sinc points over the domain.

studying a realistic problem would be quite difficult. It is this reason that many authors have focused on using post-processing algorithms to “smooth” the results from a FEA. While the ILPGSM and SIHD method can only easily be used for simple beams and plates, the FEA has been used for years for analysis of general complex structures. Nonetheless, the basis function of the integrated Sinc method could potentially be used as the basis of a smoothing algorithm such as that developed by Tessler and Riggs [106]. The results from the FEA of a complex structure could be broken up into rectangular patches which may stretch over larger areas of the FE mesh (see Fig. 10.4).

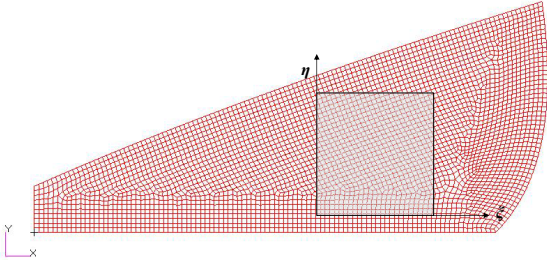


Figure 10.4. Patch over which FE results could be smoothed with the integrated Sinc basis to obtain the interlaminar stresses through the thickness of a composite shell element.

Over these patches, the integrated Sinc basis function could be fit to the FEM data in

the following manner. Assume that a FE solution of a structure using plate elements was conducted. The FE solution resulted in obtaining  $u_i$  and  $\theta_i$  which are the nodal displacements and rotations at the point  $x_i$  on the finite rectangular patch ( $i = \{1, 2\}$ ). The integrated Sinc basis function is fit to the FE data by minimizing the following functional:

$$\Pi = \frac{1}{2} \sum_{i=1}^2 \left[ (u_i - \tilde{u}_i)^2 + (\theta_i - \tilde{\theta}_i)^2 \right] \quad (10.12)$$

where  $\tilde{u}_i$  and  $\tilde{\theta}_i$  are approximated by the integrated Sinc basis function. This could be done in a collocation fashion where the FE nodes are the collocation points or using the Sinc points such as with the SIHD method. Because the integrated Sinc basis function is used, the higher-order derivatives needed to perform the through the thickness integration to obtain the transverse normal and transverse shear stresses are given by the basis function.

Additional work should be conducted to assess the accuracy of the above smoothing procedure in comparison with other post-processing techniques [102, 103, 104, 105, 106] with results obtained by commercial FE software.

## 10.4 Dynamic Analysis with integrated Sinc methods

There is still a substantial amount of work that can be done toward the maturation of the integrated Sinc methods. To the authors knowledge, no authors have investigated the use of this type of method for solving dynamic problems. Abdella, Yu, and Kucuk [234] used the Sinc Galerkin method for analyzing a 1D, dynamic, elastic-plastic rod; however, no application of either the ILPGSM or the SIHD method has been conducted for dynamic analysis. While an application of this nature is perhaps straight forward, there are some lingering questions that can only be addressed with such a study.

For a bar of elastic material with unit area, fixed at one end, and struck by a force  $p(t)$ ,

the initial-BVP is expressed by:

$$\begin{aligned}\rho\ddot{u}(x, t) &= Eu''(x, t), \\ u(x, 0) &= 0, \quad \dot{u}(x, 0) = 0, \\ u(L, 0) &= 0, \quad Eu'(0, t) = p(t),\end{aligned}\tag{10.13}$$

where dotted variables implies differentiation with respect to  $t$ , a prime implies differentiation with respect to  $x$ ,  $\rho$  is the density,  $E$  is the Young's Modulus, and  $L$  is the rod's length. Following the approach of the ILPGSM, the BVP can be discretized using the basis function and results in the following expression:

$$\rho \int_0^L W^I(x) \mathbf{B}(x) \ddot{\mathbf{U}}(t) dx + E \int_0^L W^{I'}(x) \mathbf{A}(x) \mathbf{U}(t) dx = W^I p(t) \Big|_{x=0},\tag{10.14}$$

where  $W^I$  is a weight function of compact support, the unknowns are denoted by vector  $\mathbf{U}$ , and the basis function Eq. (3.30) were used for  $\mathbf{B}(x)$  and  $\mathbf{A}(x)$ . By selecting equal number of equations as unknowns, Eq. (10.14) becomes:

$$\mathbf{M}\ddot{\mathbf{U}}(t) + \mathbf{K}\mathbf{U}(t) = \mathbf{f}.\tag{10.15}$$

To discretize the temporal domain, the Newmark family of algorithms could be used [98, 234]. The FEM has the benefit of being able to lump the mass matrix and utilize an explicit algorithm. While no work has been done to verify whether a lumped mass matrix could be obtained with the present method, it seems implausible. The mass matrix for this method would be fully populated and there is no guarantee that it is diagonal dominate. Moreover, the unknowns related to the constants of integration are of a completely different nature than those relating to the highest-order derivative at the Sinc points. It would be a substantial study to explore the use of the Newmark family of algorithms for this

problem.

For the wave problem given above, the question arises as to whether the basis function can successfully approximate a wave in the interior of the bar. It was shown in Chapter 9, that when the delamination is near the center of the domain the sharp change in shear force can introduce oscillations relating to Gibbs phenomenon. For the present problem, a similar issue could arise for some types of excitations (ex. a square wave).

Moreover, for a Newmark algorithm that is conditionally stable, the stable time step should be found. The stable time step is dependent on the eigenvalues of the unforced system [Eq. (10.15) with  $\mathbf{f} = \mathbf{0}$ ]. Thus to find the stable time step the eigenvalue problem:

$$-\omega^2 \mathbf{M}\mathbf{U}(t) + \mathbf{K}\mathbf{U}(t) = \mathbf{0}, \quad (10.16)$$

should be solved. For the FEM, the stiffness matrix and mass matrix are positive definite so the eigenvalues will be real and positive. For the present method, whether or not the stiffness matrix and mass matrix are positive definite has not been verified.

Moreover, with the FEM, the stable time step can be computed from the eigenvalues of the smallest element within the mesh. This is a distinct advantage over obtaining the complete set of eigenvalues. Furthermore, it is known that as the element size decreases, the maximum eigenvalue increases and thus the maximum stable-time step decreases. For the integrated Sinc methods, the Sinc point spacing at the edges is very small. Thus it seems reasonable for the stable-time step to be very small as well, and perhaps even unacceptably small. The behavior of the ILPGSM and SIHD methods for obtaining eigenvalues needs to be thoroughly studied to understand the feasibility of these methods for dynamic problems.

## 10.5 Final Remarks

While the work of this dissertation has shown that the present method is very interesting and can be beneficial in some applications, a monumental shift in industry and academia from the FEM to the ILPGSM or SIHD is unlikely. The maturity of the FEM is unmatched. Nonetheless, the process of numerical indefinite integration by DE transformation has been proved to be an excellent tool and works quite well as a basis function for a numerical method.

## Bibliography

- [1] Alderliesten, R. C. and Homan, J. J., “Fatigue and Damage Tolerance Issues of GLARE in Aircraft Structures,” *International Journal of Fatigue*, Vol. 28, No. 10, 2006, pp. 1116 – 1123, The Third International Conference on Fatigue of Composites.
- [2] Kromm, F. X., Quenisset, J. M., Harry, R., and Lorriot, T., “An Example of Multimaterial Design,” *Advanced Engineering Materials*, Vol. 4, 2002, pp. 371–374.
- [3] Bindumadhavan, P. N., Wah, H. K., and Prabhakar, O., “Assessment of Particle-Matrix Debonding in Particulate Metal Matrix Composites Using Ultrasonic Velocity Measurements,” *Materials Science and Engineering A*, Vol. 323, No. 1-2, 2002, pp. 42 – 51.
- [4] Mat, M. D. and Aldas, K., “Experimental and Numerical Investigation of Effect of Particle Size on Particle Distribution in Particulate Metal Matrix Composites,” *Applied Mathematics and Computation*, Vol. 177, No. 1, 2006, pp. 300 – 307.
- [5] Tong, W. and Ravichandran, G., “Effective Elastic Moduli and Characterization of a Particulate Metal-Matrix Composite with Damaged Particles,” *Composites Science and Technology*, Vol. 52, No. 2, 1994, pp. 247 – 252.
- [6] Liu, X. and Hu, G., “A Continuum Micromechanical Theory of Overall Plasticity for Particulate Composites Including Particle Size Effect,” *International Journal of Plasticity*, Vol. 21, No. 4, 2005, pp. 777 – 799.
- [7] Doel, T. J. A., Loretto, M. H., and Bowen, P., “Mechanical Properties of Aluminium-Based Particulate Metal-Matrix Composites,” *Composites*, Vol. 24, No. 3, 1993, pp. 270 – 275.

- [8] Ma, H., Hu, G., and Huang, Z., “A Micromechanical Method for Particulate Composites with Finite Particle Concentration,” *Mechanics of Materials*, Vol. 36, No. 4, 2004, pp. 359 – 368.
- [9] Styles, M., Compston, P., and Kalyanasundaram, S., “The Effect of Core Thickness on the Flexural Behaviour of Aluminium Foam Sandwich Structures,” *Composite Structures*, Vol. 80, No. 4, 2007, pp. 532 – 538.
- [10] Radford, D. D., McShane, G. J., Deshpande, V. S., and Fleck, N. A., “The Response of Clamped Sandwich Plates with Metallic Foam Cores to Simulated Blast Loading,” *International Journal of Solids and Structures*, Vol. 43, No. 7-8, 2006, pp. 2243 – 2259.
- [11] Kesler, O. and Gibson, L. J., “Size Effects in Metallic Foam Core Sandwich Beams,” *Materials Science and Engineering A*, Vol. 326, No. 2, 2002, pp. 228 – 234.
- [12] Crupi, V. and Montanini, R., “Aluminium Foam Sandwiches Collapse Modes Under Static and Dynamic Three-Point Bending,” *International Journal of Impact Engineering*, Vol. 34, No. 3, 2007, pp. 509 – 521.
- [13] Corigliano, A., Rizzi, E., and Papa, E., “Experimental Characterization and Numerical Simulations of a Syntactic-Foam/Glass-Fibre Composite Sandwich,” *Composites Science and Technology*, Vol. 60, No. 11, 2000, pp. 2169 – 2180.
- [14] Avils, F. and Aguilar-Montero, M., “Mechanical Degradation of Foam-Cored Sandwich Materials Exposed to High Moisture,” *Composite Structures*, Vol. 92, No. 1, 2010, pp. 122 – 129.
- [15] Chang, P.-Y., Yeh, P.-C., and Yang, J.-M., “Fatigue Crack Initiation in Hybrid Boron/Glass/Aluminum Fiber Metal Laminates,” *Materials Science and Engineering: A*, Vol. 496, No. 1-2, 2008, pp. 273 – 280.

- [16] Corts, P. and Cantwell, W. J., “The Prediction of Tensile Failure in Titanium-Based Thermoplastic Fibre-Metal Laminates,” *Composites Science and Technology*, Vol. 66, No. 13, 2006, pp. 2306 – 2316.
- [17] Roebroeks, G. H. J. J., “Fibre-Metal Laminates: Recent Developments and Applications,” *International Journal of Fatigue*, Vol. 16, No. 1, 1994, pp. 33 – 42.
- [18] Vlot, A., *GLARE, History of the Development of a New Aircraft Material*, Kluwer Academic, Dordrecht, The Netherlands, 2001.
- [19] Vlot, A. and Gunnink, J. W., *Fibre Metal Laminates, an Introduction*, Kluwer Academic, Dordrecht, The Netherlands, 2001.
- [20] Forster, E., Clay, S., Holzwarth, R., Pratt, D., and Paul, D., “Flight Vehicle Composite Structures,” *The 26th Congress of International Council of the Aeronautical Sciences (ICAS) including 8th AIAA Aviation Technology, Integration, and Ope, Anchorage, Alaska, AIAA-2008-8976.*, Sep. 14-19, 2008.
- [21] Alderliesten, R. C. and Benedictus, R., “Fiber/Metal Composite Technology for Future Primary Aircraft Structures,” *Journal of Aircraft*, AIAA, Vol. 45, 2008, pp. 1182–1189.
- [22] Ray, S. S. and Okamoto, M., “Polymer/Layered Silicate Nanocomposites: A Review from Preparation to Processing,” *Progress in Polymer Science*, Vol. 28, No. 11, 2003, pp. 1539 – 1641.
- [23] Pavlidou, S. and Papaspyrides, C. D., “A Review on Polymer-Layered Silicate Nanocomposites,” *Progress in Polymer Science*, Vol. 33, No. 12, 2008, pp. 1119 – 1198.



- [24] Ma, J., Bilotti, E., Peijs, T., and Darr, J. A., "Preparation of Polypropylene/Sepiolite Nanocomposites Using Supercritical CO<sub>2</sub> Assisted Mixing," *European Polymer Journal*, Vol. 43, No. 12, 2007, pp. 4931 – 4939.
- [25] Kuila, T., Srivastava, S. K., Bhowmick, A. K., and Saxena, A. K., "Thermoplastic Polyolefin Based Polymer-Blend-Layered Double Hydroxide Nanocomposites," *Composites Science and Technology*, Vol. 68, No. 15-16, 2008, pp. 3234 – 3239.
- [26] Zhao, C., Qin, H., Gong, F., Feng, M., Zhang, S., and Yang, M., "Mechanical, Thermal and Flammability Properties of Polyethylene/Clay Nanocomposites," *Polymer Degradation and Stability*, Vol. 87, No. 1, 2005, pp. 183 – 189.
- [27] Rogers, C. W., "Advanced Composite Material Application to Aircraft Structures," *Journal of Aircraft*, AIAA, Vol. 5, No. 3, May-June 1968, pp. 311–316.
- [28] Paul, D. and Pratt, D., "History of Flight Vehicle Structures 1903-1990," *Journal of Aircraft*, Vol. 41, No. 5, 2004, pp. 969–977, doi: 10.2514/1.4036.
- [29] Soni, S. R., "A Comparative Study of Failure Envelopes in Composite Laminates," *Journal of Reinforced Plastic Composites*, Vol. 2, 1983, pp. 40–62.
- [30] Owen, M. J. and Rice, D. I., "Biaxial Strength Behaviour of Glass-Reinforced Polyester Resins," *Composite Materials: Testing and Design, 6th Conference, ASTM STP 787*, 1982, pp. 124–144.
- [31] Chamis, C. C., "Failure Criteria for Filamentary Composites." *Testing and Design, ASTM STP 460*, 1969, pp. 336–460.
- [32] Sandhu, R. S., "A Survey of Failure Theories of Isotropic and Anisotropic Materials," *AFFDL-TR-72-71, AD756889, Air Force Flight Dynamics Laboratory, Wright-Patterson Air Force Base, Ohio, USA, 1972.*

- [33] Tsai, S. W., “A Survey of Macroscopic Failure Criteria for Composites Materials,” *Journal of Reinforced Plastic Composites*, Vol. 3, 1984, pp. 40–62.
- [34] Tsai, S. W., *Composite Design*, Think Composites, Dayton, OH, 4th ed., 1988.
- [35] Hinton, M. J. and Soden, P. D., “Predicting Failure in Composite Laminates: The Background to the Exercise,” *Composites Science and Technology*, Vol. 58, No. 7, 1998, pp. 1001.
- [36] Liu, K.-S. and Tsai, S. W., “A Progressive Quadratic Failure Criterion for a Laminate,” *Composites Science and Technology*, Vol. 58, 1998, pp. 1023–1032.
- [37] Bogetti, T. A., Hoppel, C. P. R., Harik, V. M., Newill, J. F., and Burns, B. P., “Predicting the Nonlinear Response and Progressive Failure of Composite Laminates,” *Failure Criteria in Fibre-Reinforced-Polymer Composites*, edited by M. J. Hinton, A. S. Kaddour, and P. D. Soden, Elsevier, Oxford, 2004, pp. 402 – 428.
- [38] Kuraishi, A., Tsai, S. W., and Liu, K. K. S., “A Progressive Quadratic Failure Criterion, Part B,” *Failure Criteria in Fibre-Reinforced-Polymer Composites*, edited by M. J. Hinton, A. S. Kaddour, and P. D. Soden, Elsevier, Oxford, 2004, pp. 903 – 921.
- [39] Soden, P. D., Hinton, M. J., and Kaddour, A. S., “A Comparison of the Predictive Capabilities of Current Failure Theories for Composite Laminates,” *Composites Science and Technology*, Vol. 58, 1998, pp. 1225–1254.
- [40] Hinton, M. J., Kaddour, A. S., and Soden, P. D., “The World-Wide Failure Exercise: Its Origin, Concept and Content,” *Failure Criteria in Fibre-Reinforced-Polymer Composites*, edited by M. J. Hinton, A. S. Kaddour, and P. D. Soden, Elsevier, Oxford, 2004, pp. 2 – 28.

- [41] Hinton, M. J., Kaddour, A. S., and Soden, P. D., editors, *Failure Criteria in Fibre-Reinforced-Polymer Composites: The World-Wide Failure Exercise*, Elsevier Ltd, 2004.
- [42] Cox, H. L., “The Elasticity and Strength of Paper and Other Fibrous Materials,” *British Journal of Applied Physics*, Vol. 3, 1952, pp. 72–79.
- [43] Rosen, B. W., *Fiber Composite Materials*, American Society of Metals, 1964.
- [44] Hedgepeth, J. M. and Van Dyke, P., “Local Stress Concentrations in Imperfect Filamentary Composite Materials,” *Journal of Composite Materials*, Vol. 1, 1967, pp. 294–309.
- [45] Batdorf, S. B., “Tensile Strength of Unidirectional Reinforced Composites–I,” *Journal of Reinforced Plastics and Composites*, Vol. 1, 1982, pp. 153–176.
- [46] Hahn, H. T. and Williams, J. G., “Compression Failure Mechanisms in Unidirectional Composites,” Tech. Rep. NASA-TM-8583, National Aeronautics and Space Administration, Hampton, VA, August 1984.
- [47] Budiansky, B. and Fleck, N. A., “Compressive Failure of Fibre Composites,” *Journal of Mechanics and Physics of Solids*, Vol. 41, No. 1, 1993, pp. 183–211.
- [48] Boniface, L. and Ogin, S., “Application of the Paris Equation to the Fatigue Growth of Transverse Ply Cracks,” *Journal of Composite Materials*, Vol. 23, 1989, pp. 735–754.
- [49] Highsmith, A. and Reifsnider, K., “Stiffness Reduction Mechanism in Composite Laminates,” *Damage in Composite Materials ASTM STP 775*, 1982, pp. 103–117.

- [50] Wang, A., Kishore, N., and Li, C., “Crack Development in Graphite-Epoxy Cross-Ply Laminates Under Uniaxial Tension,” *Composite Science Technology*, Vol. 24, 1985, pp. 1–31.
- [51] Takeda, N. and Ogihara, S., “In Situ Observation and Probabilistic Prediction of Microscopic Failure Processes in CFRP Cross-Ply Laminates,” *Composites Science and Technology*, Vol. 52, 1994, pp. 183–195.
- [52] Ogihara, S., Takeda, N., and Kobayashi, A., “Experimental Characterization of Microscopic Failure Process Under Quasi-Static Tension in Interleaved and Toughness-Improved CFRP Cross-Ply Laminates,” *Composite Science Technology*, Vol. 57, 1997, pp. 267–275.
- [53] Adolfsson, E. and Gudmundson, P., “Matrix Crack Initiation and Progression in Composite Laminates Subjected to Bending and Extension,” *International Journal of Solids and Structures*, Vol. 36, 1999, pp. 3131–3169.
- [54] Yalvac, S., Yats, L., and Wetters, D., “Transverse Ply Cracking in Toughened and Untoughened Graphite/Epoxy and Graphite/Polycyanate Crossply Laminates,” *Journal of Composite Materials*, Vol. 25, 1991, pp. 1653–1667.
- [55] Liu, S. and Nairn, J., “The Formation and Propagation of Matrix Microcracks in Cross-Ply Laminates During Static Loading,” *Journal of Reinforced Plastic Composites*, Vol. 11, 1992, pp. 158–178.
- [56] Nairn, J. and Hu, S., “Matrix Microcracking,” *Damage Mechanics of Composite Materials*, edited by R. Talreja, Elsevier Science, Amsterdam, 1994, pp. 187–243.
- [57] Reifsnider, K., “Some Fundamental Aspects of the Fatigue and Fracture Response of Composite Materials,” *14th Annual Meeting of Society of Engineering Science*, Vol. 14-16, Bethlehem, PA, November 1977, pp. 373–384.

- [58] Dharani, L. and Tang, H., “Micromechanics Characterization of Sublaminar Damage,” *International Journal of Fracture*, Vol. 46, 1990, pp. 123–140.
- [59] Hashin, Z., “Analysis of Cracked Laminates: A Variational Approach,” *Mechanics of Materials*, Vol. 4, 1985, pp. 121–136.
- [60] Goyal, V. K., Johnson, E. R., and Dávila, C. G., “Irreversible Constitutive Law for Modeling the Delamination Process Using Interfacial Surface Discontinuities,” *Composite Structures*, Vol. 65, 2004, pp. 289–305.
- [61] Brewer, J. C. and Lagace, P. A., “Quadratic Stress Criterion for Initiation of Delamination,” *Journal of Composite Materials*, Vol. 22, No. 12, 1988, pp. 1141–1155, DOI: 10.1177/002199838802201205.
- [62] Hou, J. P., Petrinic, N., and Ruiz, C., “A Delamination Criterion for Laminated Composites Under Low-Velocity Impact,” *Composites Science and Technology*, Vol. 61, No. 14, 2001, pp. 2069 – 2074.
- [63] Hou, J. P., Petrinic, N., Ruiz, C., and Hallett, S. R., “Prediction of Impact Damage in Composite Plates,” *Composites Science and Technology*, Vol. 60, No. 2, 2000, pp. 273 – 281.
- [64] Chang, F.-K. and Chang, K.-Y., “A Progressive Damage Model for Laminated Composites Containing Stress Concentrations,” *Journal of Composite Materials*, Vol. 21, 1987, pp. 834–855.
- [65] Batra, R. C. and Hassan, N. M., “Blast Resistance of Unidirectional Fiber Reinforced Composites,” *Composites Part B: Engineering*, Vol. 39, No. 3, April 2008, pp. 513–536.

- [66] Makhecha, D. P., Kapania, R. K., Johnson, E. R., and Dillard, D. A., “Dynamic Fracture Analysis of Adhesively Bonded Joints Using Explicit Methods,” *AIAA Journal*, Vol. 45, 2007, pp. 2778–2784.
- [67] Allix, O., Ladeveze, P., and Corigliano, A., “Damage Analysis of Interlaminar Fracture Specimens.” *Composite Structures*, Vol. 31, 1995, pp. 66–74.
- [68] Allix, O. and Corigliano, A., “Modelling and Simulation of Crack Propagation in Mixed-Modes Interlaminar Fracture Specimens,” *International Journal of Fracture*, Vol. 77, 1996, pp. 111–140.
- [69] Schellekens, J. C. J. and de Borst, R., “A Nonlinear Finite-Element Approach for the Analysis of Mode-I Free Edge Delamination in Composites,” *International Journal of Solids and Structures*, Vol. 30, No. 9, 1993, pp. 1239–1253.
- [70] Chaboche, J. L., Girard, R., and Schaff, A., “Numerical Analysis of Composite Systems by Using Interphase/Interface Models.” *Computational Mechanics*, Vol. 20, 1997, pp. 3–11.
- [71] Mi, U., Crisfield, M. A., and Davies, G. A. O., “Progressive Delamination Using Interface Elements,” *Journal of Composite Materials*, Vol. 32, 1998, pp. 1246–1272.
- [72] Chen, J., Crisfield, M. A., Kinloch, A. J., Busso, E. P., Matthews, F. L., and Qiu, Y., “Predicting Progressive Delamination of Composite Material Specimens Via Interface Elements,” *Mechanics of Composite Materials and Structures*, Vol. 6, 1999, pp. 301–17.
- [73] Alfano, G. and Crisfield, M. A., “Finite Element Interface Models for the Delamination Analysis of Laminated Composites: Mechanical and Computational Issues,” *International Journal of Numerical Methods in Engineering*, Vol. 77, No. 2, 2001, pp. 111–170.

- [74] Reddy Jr, E. D., Mello, F. J., and Guess, T. R., “Modeling the Initiation and Growth of Delaminations in Composite Structures,” *Journal of Composite Materials*, Vol. 31, 1997, pp. 812–831.
- [75] Dassault Systèmes, Providence, RI, *ABAQUS/Standard User’s Manual*, version 6.7 ed., 2007, <http://esm.vt.edu/v6.7>.
- [76] ANSYS, Inc., Cannonsburg, PA, *ANSYS Elements Reference*, 10th ed., 2005.
- [77] Corporation, M., *MD Nastran R2.1 Quick Reference Guide*, MSC, Santa Ana, CA, 2007, [www.mscsoftware.com](http://www.mscsoftware.com).
- [78] Livermore Software Technology Corporation, Livermore, CA, *LS-DYNA Keywords User’s Manual*, version 971/release 4 ed., June 2009.
- [79] Cherradi, N., Kawasaki, A., and Gasik, M., “Worldwide Trends in Functional Gradient Materials Research and Development,” *Composites Engineering*, Vol. 4, No. 8, 1994, pp. 883–894.
- [80] Oh, S.-Y., Librescu, L., and Song, O., “Vibration of Turbomachinery Rotating Blades Made-Up of Functionally Graded Materials and Operating in a High Temperature Field,” *Acta Mechanica*, Vol. 166, No. 1, Dec. 2003, pp. 69–87.
- [81] Fazelzadeh, S. A. and Hosseini, M., “Aerothermoelastic Behavior of Supersonic Rotating Thin-Walled Beams Made of Functionally Graded Materials,” *Journal of Fluids and Structures*, Vol. 23, No. 8, 2007, pp. 1251 – 1264.
- [82] Batra, R. C. and Jin, J., “Natural Frequencies of a Functionally Graded Anisotropic Rectangular Plate,” *Journal of Sound and Vibration*, Vol. 282, No. 1-2, 2005, pp. 509 – 516.

- [83] Hafley, R. A., Taminger, K. M. B., and Bird, R. K., "Electron Beam Freeform Fabrication in the Space Environment," *45th AIAA Aerospace Sciences Meeting and Exhibit*, Reno, NV, January 8 - 11, 2007, AIAA 2007-1154.
- [84] Yoon, J. W., Bray, G. H., Valente, R. A. F., and Childs, T. E. R., "Buckling Analysis for an Integrally Stiffened Panel Structure with a Friction Stir Weld," *Thin-Walled Structures*, Vol. 47, No. 12, 2009, pp. 1608 – 1622.
- [85] Kapania, R. K., Li, J., and Kapoor, H., "Optimal Design of Unitized Panels with Curvilinear Stiffeners," *AIAA 5th Aviation, Technology, Integration, and Operations Conference (ATIO)/16th Lighter-than-Air and Balloon Systems Conference*, Hyatt Regency Crystal City, Arlington, VA, September 26-28, 2005.
- [86] Gurav, S. P. and Kapania, R. K., "Development of Framework for the Design Optimization of Unitized Structures," *50th AIAA/ASME/ASCE/AHS/ASC Structures, Structural Dynamics, and Materials Conference*, Palm Springs, CA, May 4-7, 2009, AIAA-2009-2186.
- [87] Mulani, S. B., Li, J., Joshi, P., and Kapania, R. K., "Optimization of Stiffened Electron Beam Freeform Fabrication (EBF3) Panels Using Response Surface Approaches," *48th AIAA/ASME/ASCE/AHS/ASC Structures, Structural Dynamics, and Materials Conference*, Honolulu, Hi, April 23-26, 2007, AIAA 2007-1901.
- [88] Joshi, P., Kapania, R. K., Gurav, S. P., and Mulani, S., "Design Optimization for Minimum Sound Radiation from Point-Excited Curvilinearly Stiffened Panel," *50th AIAA/ASME/ASCE/AHS/ASC Structures, Structural Dynamics, and Materials Conference*, Palm Springs, CA, May 4-7, 2009, AIAA-2009-2649.



- [89] Kapania, R. K. and Raciti, S., "Recent Advances in Analysis of Laminated Beams and Plates, Part I: Shear Effects and Buckling," *AIAA Journal*, Vol. 27, No. 7, 1989, pp. 923–935.
- [90] Kant, T. and Swaminathan, K., "Estimation of Transverse/Interlaminar Stresses in Laminated Composites - A Selective Review and Survey of Current Developments," *Composite Structures*, Vol. 49, No. 1, 2000, pp. 65–75.
- [91] Vlasov, B. F., "On One Case of Bending of Rectangular Thick Plates," *Vestnik Moskovskogo Universiteta. Seriià Matematika, Mekhaniki, Astronomii, Fiziki, Khimii*, Vol. 2, No. 2, 1957, pp. 25–34.
- [92] Pagano, N. J., "Exact Solution for Composite Laminates in Cylindrical Bending," *Journal of Composite Materials*, Vol. 3, No. 3, 1969, pp. 398–411.
- [93] Pagano, N. J. and Hatfield, S. J., "Elastic Behavior of Multilayered Bidirectional Composites," *AIAA Journal*, Vol. 10, No. 7, 1972, pp. 931–933.
- [94] Srinivas, S. and Rao, A. K., "Bending, Vibration and Buckling of Simply Supported Thick Orthotropic Rectangular Plates and Laminates," *International Journal of Solids and Structures*, Vol. 6, 1970, pp. 1463–1481.
- [95] Srinivas, S., Joga Rao, C. V., and Rao, A. K., "An Exact Analysis for Vibration of Simply-Supported Homogeneous and Laminated Thick Rectangular Plates," *Journal of Sound and Vibration*, Vol. 12, No. 2, 1970, pp. 187–199.
- [96] Srinivas, S. and Rao, A. K., "Flexure of Thick Rectangular Plates," *Journal of Applied Mechanics*, Vol. 40, No. 1, 1973, pp. 298–299.
- [97] Vel, S. and Batra, R. C., "Analytical Solutions for Rectangular Thick Laminated Plates Subjected to Arbitrary Boundary Conditions," *AIAA Journal*, Vol. 37, No. 11, 1999, pp. 1464–1473.

- [98] Reddy, J. N., *Mechanics of Laminated Composite Plates – Theory and Analysis*, CRC Press, 2004.
- [99] Kim, J. Y. and Hong, C. S., “Three-Dimensional Finite Element Analysis of Interlaminar Stresses in Thick Composite Laminates,” *Computers and Structures*, Vol. 40, No. 6, 1991, pp. 1395–1404.
- [100] Reddy, J. N., “A Simple Higher-Order Theory for Laminated Composite Plates,” *Journal of Applied Mechanics*, Vol. 51, 1984, pp. 745–752.
- [101] Goyal, V. K. and Kapania, R. K., “A Shear-Deformable Beam Element for the Analysis of Laminated Composites,” *Finite Elements in Analysis and Design*, Vol. 43, No. 6, 2007, pp. 463–477.
- [102] Lajczok, M. R., “New Approach in the Determination of Interlaminar Shear Stresses from the Results of MSC/NASTRAN,” *Computers and Structures*, Vol. 24, No. 4, 1986, pp. 651–656.
- [103] Byun, C. and Kapania, R. K., “Prediction of Interlaminar Stresses in Laminated Plates Using Global Orthogonal Interpolation Polynomials,” *AIAA Journal*, Vol. 30, No. 11, 1992, pp. 2740–2749.
- [104] Lee, K. and Lee, S. W., “A Postprocessing Approach to Determine Transverse Stresses in Geometrically Nonlinear Composite and Sandwich Structures,” *Journal of Composite Materials*, Vol. 37, No. 24, 2003, pp. 2207–2224.
- [105] Roos, R., Kress, G., and Ermanni, P., “A Post-Processing Method for Interlaminar Normal Stresses in Doubly Curved Laminates,” *Composite Structures*, Vol. 81, No. 3, 2007, pp. 463–470.

- [106] Tessler, A. and Riggs, H. R., “Accurate Interlaminar Stress Recovery from Finite Element Analysis,” Tech. Rep. NASA-TM-109149, National Aeronautics and Space Administration, Hampton, VA, September 1994.
- [107] Tessler, A., Riggs, H. R., Freese, C. E., and Cook, G. M., “An Improved Variational Method for Finite Element Stress Recovery and A Posteriori Error Estimation,” *Computer Methods in Applied Mechanics and Engineering*, Vol. 155, No. 1-2, 1998, pp. 15 – 30.
- [108] Lund, J. and Bowers, K. L., *Sinc Methods for Quadrature and Differential Equations*, SIAM, Philadelphia, 1992.
- [109] Wu, X., Li, C., and Kong, W., “A Sinc-Collocation Method with Boundary Treatment for Two-Dimensional Elliptic Boundary Value Problems,” *Journal of Computational and Applied Mathematics*, Vol. 196, 2006, pp. 58 – 69.
- [110] Narasimhan, S., Majdalani, J., and Stenger, F., “A First Step in Applying the Sinc Collocation Method to the Nonlinear Navier-Stokes Equations,” *Numerical Heat Transfer, Part B: Fundamentals: An International Journal of Computation and Methodology*, Vol. 41, No. 5, 2002, pp. 447–462.
- [111] Smith, R., Bogar, G., Bowers, K., and Lund, J., “The Sinc-Galerkin Method for Fourth-Order Differential Equations,” *SIAM Journal of Numerical Analysis*, Vol. 28, 1991, pp. 760–788.
- [112] El-Gamel, M. and Zayed, A. I., “Sinc-Galerkin Method for Solving Nonlinear Boundary-Value Problems,” *Computers and Mathematics with Applications*, Vol. 48, No. 9, 2004, pp. 1285–1298.

- [113] El-Gamel, M., “A Comparison Between the Sinc-Galerkin and the Modified Decomposition Methods for Solving Two-Point Boundary-Value Problems,” *Journal of Computational Physics*, Vol. 223, No. 1, 2007, pp. 369–383.
- [114] El-Gamel, M., “Comparison of the Solutions Obtained by Adomian’s Decomposition and Wavelet-Galerkin Methods of Boundary-Value Problems,” *Applied Mathematics and Computation*, Vol. 186, No. 1, 2007, pp. 652–664.
- [115] Al-Khaled, K., “Theory and Computation in Singular Boundary Value Problems,” *Chaos, Solitons, and Fractals*, Vol. 33, 2007, pp. 678–684.
- [116] He, J.-H., “Homotopy Perturbation Technique,” *Computer Methods in Applied Mechanics and Engineering*, Vol. 178, No. 3, 1999, pp. 257–262.
- [117] He, J.-H., “Homotopy Perturbation Method: A New Nonlinear Analytical Technique,” *Applied Mathematics and Computation*, Vol. 135, No. 1, 2003, pp. 73 – 79.
- [118] El-Gamel, M., “Sinc and the Numerical Solution of Fifth-Order Boundary Value Problems,” *Applied Mathematics and Computation*, Vol. 69, No. 2, 2006, pp. 1417–1433.
- [119] Mai-Duy, N. and Tran-Cong, T., “Approximation of Function and its Derivatives Using Radial Basis Function Networks,” *Applied Mathematical Modelling*, Vol. 27, No. 3, March 2003, pp. 197–220.
- [120] Mai-Duy, N. and Tran-Cong, T., “Numerical Solution of Differential Equations Using Multiquadric Radial Basis Function Networks,” *Neural Networks*, Vol. 14, 2001, pp. 185–199.

- [121] Wu, X. and Ren, Y., “Differential Quadrature Method Based on the Highest Derivative and its Applications,” *Journal of Computational and Applied Mathematics*, Vol. 205, No. 1, Aug. 2007, pp. 239–250.
- [122] Li, C. and Wu, X., “Numerical Solution of Differential Equations Using Sinc Method Based on the Interpolation of the Highest Derivatives,” *Applied Mathematical Modeling*, Vol. 31, No. 1, 2007, pp. 1–9.
- [123] Mai-Duy, N. and Tanner, R. I., “A Spectral Collocation Method Based on Integrated Chebyshev Polynomials for Two-Dimensional Biharmonic Boundary-Value Problems,” *Journal of Computational and Applied Mathematics*, Vol. 201, No. 1, April 2007, pp. 30–47.
- [124] Mai-Duy, N. and Tran-Cong, T., “An Integrated-RBF Technique Based on Galerkin Formulation for Elliptic Differential Equations,” *Engineering Analysis with Boundary Elements*, Vol. 33, No. 2, February 2009, pp. 191–199.
- [125] Bellman, R. E. and Casti, J., “Differential Quadrature and Long Term Integration,” *Journal of Mathematical Analysis and Applications*, Vol. 34, 1971, pp. 235–238.
- [126] Striz, A. G., Jang, S. K., and Bert, C. W., “Nonlinear Bending Analysis of Thin Circular Plates by Differential Quadrature,” *Thin-Walled Structures*, Vol. 6, No. 1, 1988, pp. 51–62.
- [127] Bert, C. W., Xinwei, W., and Striz, A. G., “Differential Quadrature for Static and Free Vibration Analyses of Anisotropic Plates,” *International Journal of Solids and Structures*, Vol. 30, No. 13, 1993, pp. 1737–1744.
- [128] Wang, X., Bert, C. W., and Striz, A. G., “Differential Quadrature Analysis of Deflection, Buckling, and Free Vibration of Beams and Rectangular Plates,” *Computers and Structures*, Vol. 48, No. 3, Aug. 1993, pp. 473–479.

- [129] Kang, K., Bert, C. W., and Striz, A. G., “Vibration Analysis of Shear Deformable Circular Arches by the Differential Quadrature Method,” *Journal of Sound and Vibration*, Vol. 183, No. 2, June 1995, pp. 353–360.
- [130] Kang, K. J., Bert, C. W., and Striz, A. G., “Vibration and Buckling Analysis of Circular Arches Using DQM,” *Computers and Structures*, Vol. 60, No. 1, July 1996, pp. 49–57.
- [131] Liu, X. and Wu, X., “Differential Quadrature Trefftz Method for Irregular Plate Problems,” *Engineering Analysis with Boundary Elements*, Vol. 33, No. 3, 2009, pp. 363 – 367.
- [132] Chen, W., Yu, Y., and Wang, X., “Reducing the Computational Requirements of the Differential Quadrature Method,” *Numerical Methods for Partial Differential Equations*, Vol. 12, No. 5, 1996, pp. 565–577.
- [133] Muhammad, M. and Mori, M., “Double Exponential Formulas for Numerical Indefinite Integration,” *Journal of Computational and Applied Mathematics*, Vol. 161, No. 4, 2003, pp. 431–448.
- [134] Bickford, W. B., “A Consistent Higher Order Beam Theory,” *Developments in Theoretical and Applied Mechanics, SECTAM*, Vol. 11, April 1982, pp. 137–150.
- [135] Batra, R. C., “Higher-Order Shear and Normal Deformable Theory for Functionally Graded Incompressible Linear Elastic Plates,” *Thin-Walled Structures*, Vol. 45, No. 12, Dec. 2007, pp. 974–982.
- [136] Tessler, A., Di Sciuva, M., and Gherlone, M., “Refinement of Timoshenko Beam Theory for Composite and Sandwich Beams Using Zigzag Kinematics,” Tech. Rep. NASA-TP-2007-215086, National Aeronautics and Space Administration, Hampton, VA, November 2007.

- [137] Batra, R. C. and Zhang, G. M., “Symmetric Smoothed Particle Hydrodynamics (SSPH) Method and its Application to Elastic Problems,” *Computational Mechanics*, Vol. 43, 2009, pp. 321–340, DOI 10.1007/s00466-008-0308-9.
- [138] Phan, N. D. and Reddy, J. N., “Analysis of Laminated Composite Plates Using a Higher-Order Shear Deformation Theory,” *International Journal for Numerical Methods in Engineering*, Vol. 21, No. 12, 1984, pp. 2201–2219.
- [139] Sugihara, M., “Double Exponential Transformation in the Sinc-Collocation Method for Two-Point Boundary Value Problems,” *Journal of Computational and Applied Mathematics*, Vol. 149, 2002, pp. 239–250.
- [140] Sugihara, M. and Matsuo, T., “Recent Developments of the Sinc Numerical Methods,” *Journal of Computational and Applied Mathematics*, Vol. 164 - 165, No. 1, 2004, pp. 673–689.
- [141] Takahasi, H. and Mori, M., “Double Exponential Formulas for Numerical Integration,” *Publications of the Research Institute for Mathematical Sciences, Kyoto Univ.*, Vol. 9, No. 3, 1974, pp. 721–741.
- [142] Muhammad, M., Nurmuhammad, A., Mori, M., and Sugihara, M., “Numerical Solution of Integral Equations by Means of the Sinc Collocation Method Based on the Double Exponential Transformation,” *Journal of Computational and Applied Mathematics*, Vol. 177, No. 2, 2005, pp. 269–286.
- [143] Mori, M., “Discovery of the Double Exponential Transformation and its Developments,” *Publications of the Research Institute for Mathematical Sciences, Kyoto Univ.*, Vol. 41, No. 4, 2005, pp. 897–935.

- [144] Mori, M. and Sugihara, M., “The Double-Exponential Transformation in Numerical Analysis,” *Journal of Computational and Applied Mathematics*, Vol. 127, No. 1, 2001, pp. 287–296.
- [145] Abramowitz, M. and Stegun, I. A., editors, *Handbook of Mathematical Functions with Formulas, Graphs, and Mathematical Tables*, 9th printing., Dover, New York, 1972.
- [146] MacLeod, A. J., “Rational Approximations, Software and Test Methods for Sine and Cosine Integrals,” *Numerical Algorithms*, Vol. 12, No. 2, 1996, pp. 259–272.
- [147] Mori, T. and Tanaka, K., “Average Stress in Matrix and Average Elastic Energy of Materials with Misfitting Inclusions,” *Acta Metallurgica*, Vol. 21, No. 5, 1973, pp. 571–574.
- [148] Ferreira, A. J. M., Batra, R. C., Roque, C. M. C., Qian, L. F., and Martins, P. A. L. S., “Static Analysis of Functionally Graded Plates Using Third-Order Shear Deformation Theory and a Meshless Method,” *Composite Structures*, Vol. 69, No. 4, 2005, pp. 449–457.
- [149] Ferreira, A. J. M., Batra, R. C., Roque, C. M. C., Qian, L. F., and Jorge, R. M. N., “Natural Frequencies of Functionally Graded Plates by a Meshless Method,” *Composite Structures*, Vol. 75, No. 1–4, 2006, pp. 593–600.
- [150] Zenkour, A. M., “A Comprehensive Analysis of Functionally Graded Sandwich Plates: Part 1 - Deflection and Stresses,” *International Journal of Solids and Structures*, Vol. 42, No. 18–19, 2005, pp. 5224–5242.
- [151] Batra, R. C. and Vidoli, S., “Higher Order Piezoelectric Plate Theory Derived from a Three-Dimensional Variational Principle,” *AIAA Journal*, Vol. 40, No. 1, 2002, pp. 91–104.



- [152] Xiao, J. R., Batra, R. C., Gilhooley, D. F., Gillespie, Jr., J. W., and McCarthy, M. A., “Analysis of Thick Plates by Using a Higher-Order Shear and Normal Deformable Plate Theory and MLPG Method with Radial Basis Functions,” *Computer Methods in Applied Mechanics and Engineering*, Vol. 196, No. 4-6, Jan. 2007, pp. 979–987.
- [153] Xiao, J. R., Gilhooley, D. F., Batra, R. C., Gillespie Jr., J. W., and McCarthy, M. A., “Analysis of Thick Composite Laminates Using a Higher-Order Shear and Normal Deformable Plate Theory (HOSNDPT) and a Meshless Method,” *Composites Part B: Engineering*, Vol. 39, No. 2, March 2008, pp. 414–427.
- [154] Qian, L. F., Batra, R. C., and Chen, L. M., “Static and Dynamic Deformations of Thick Functionally Graded Elastic Plates by Using Higher-Order Shear and Normal Deformable Plate Theory and Meshless Local Petrov-Galerkin Method,” *Composites Part B: Engineering*, Vol. 35, No. 6-8, 2004, pp. 685–697.
- [155] Tessler, A., Di Sciuva, M., and Gherlone, M., “A Refined Zigzag Beam Theory for Composite and Sandwich Beams,” *Journal of Composite Materials*, Vol. 43, No. 9, 2009, pp. 1051–1081.
- [156] Di Sciuva, M., “An Improved Shear-Deformation Theory for Moderately Thick Multilayered Anisotropic Shells and Plates,” *Journal of Applied Mechanics*, Vol. 54, 1987, pp. 589–596.
- [157] Murakami, H., “Laminated Composite Plate Theory with Improved In-plane Responses,” *Journal of Applied Mechanics*, Vol. 53, 1986, pp. 661–666.
- [158] Averill, R. C., “Static and Dynamic Response of Moderately Thick Laminated Beams with Damage,” *Composites Engineering*, Vol. 4, No. 4, 1994, pp. 381–395.

- [159] Tessler, A., Di Sciuva, M., and Gherlone, M., “Refined Zigzag Theory for Laminated Composite and Sandwich Plates,” Tech. Rep. NASA-TP-2009-215561, National Aeronautics and Space Administration, Hampton, VA, January 2009.
- [160] Batra, R. C. and Zhang, G., “SSPH Basis Functions for Meshless Methods, and Comparison of Solutions with Strong and Weak Formulations,” *Computational Mechanics*, Vol. 41, No. 4, March 2008, pp. 527–545.
- [161] Atluri, S. N. and Shen, S., “The Meshless Local Petrov-Galerkin (MLPG) Method: A Simple and Less-Costly Alternative to the Finite Element and Boundary Element Methods,” *Computer Modeling in Engineering and Sciences*, Vol. 3, 2002, pp. 11–51.
- [162] Nguyen, V. P., Rabczuk, T., Bordas, S., and Duflo, M., “Meshless Methods: A Review and Computer Implementation Aspects,” *Mathematics and Computers in Simulation*, Vol. 79, No. 3, December 2008, pp. 763–813.
- [163] Atluri, S. N. and Shen, S., “The Basis of Meshless Domain Discretization: The Meshless Local Petrov-Galerkin (MLPG) Method,” *Advances in Computational Mathematics*, Vol. 23, No. 1, July 2005, pp. 73–93.
- [164] Irons, B. M., “Engineering Applications of Numerical Integration in Stiffness Methods,” *AIAA Journal*, Vol. 4, No. 11, 1966, pp. 2035–2037.
- [165] Cook, R. D., *Concepts and Applications of Finite Element Analysis*, Wiley, New York, 2nd ed., 1981.
- [166] Batra, R. C. and Zhang, G. M., “Modified Smoothed Particle Hydrodynamics (MSPH) Basis Functions for Meshless Methods, and their Application to Axisymmetric Taylor Impact Test,” *Journal of Computational Physics*, Vol. 227, No. 3, Jan. 2008, pp. 1962–1981.

- [167] Sarra, S. A., “Integrated Multiquadric Radial Basis Function Approximation Methods,” *Computers and Mathematics with Applications*, Vol. 51, No. 8, April 2006, pp. 1283–1296.
- [168] Zhu, T. and Atluri, S. N., “A Modified Collocation Method and a Penalty Formulation for Enforcing the Essential Boundary Conditions in the Element Free Galerkin Method,” *Computational Mechanics*, Vol. 21, No. 3, April 1998, pp. 211–222.
- [169] Pereira, E. M. B. R. and Freitas, J. A. T., “A hybrid-Mixed Finite Element Model Based on Legendre Polynomials for Reissner-Mindlin Plates,” *Computer Methods in Applied Mechanics and Engineering*, Vol. 136, No. 1-2, 1996, pp. 111 – 126.
- [170] Pereira, E. M. B. R. and Freitas, J. A. T., “A Mixed-Hybrid Finite Element Model Based on Orthogonal Functions,” *International Journal for Numerical Methods in Engineering*, Vol. 39, No. 8, 1996, pp. 1295–1312.
- [171] Timoshenko, S. P. and Goodier, J. N., *Theory of Elasticity*, McGraw-Hill, New York, 3rd ed., 1970.
- [172] Newman, J. C., James, M. A., and Zerbst, U., “A Review of the CTOA/CTOD Fracture Criterion,” *Engineering Fracture Mechanics*, Vol. 70, No. 3-4, 2003, pp. 371 – 385.
- [173] Rice, J. R., “A Path Independent Integral and the Approximate Analysis of Strain Concentration by Notches and Cracks.” *ASME Journal of Applied Mechanics*, Vol. 35, 1968, pp. 379–386.
- [174] Dowling, N. E., *Mechanical Behavior of Materials*, Prentice Hall, 3rd ed., 2007.

- [175] Livieri, P., “A New Path Independent Integral Applied to Notched Components under Mode-I Loadings,” *International Journal of Fracture*, Vol. 123, No. 3, Oct. 2003, pp. 107–125.
- [176] Livieri, P., “Use of J-Integral to Predict Static Failures in Sharp V-Notches and Rounded U-Notches,” *Engineering Fracture Mechanics*, Vol. 75, No. 7, May 2008, pp. 1779–1793.
- [177] Berto, F. and Lazzarin, P., “Relationships Between J-integral and the Strain Energy Evaluated in a Finite Volume Surrounding the Tip of Sharp and Blunt V-Notches,” *International Journal of Solids and Structures*, Vol. 44, No. 14-15, July 2007, pp. 4621–4645.
- [178] Kuang, J. H. and Chen, Y. C., “The values of J-integral within the plastic zone,” *Engineering Fracture Mechanics*, Vol. 55, No. 6, 1996, pp. 869 – 881.
- [179] Batra, R. C. and Love, B. M., “Crack Propagation Due to Brittle and Ductile Failures in Microporous Thermoelastoviscoplastic Functionally Graded Materials,” *Engineering Fracture Mechanics*, Vol. 72, No. 12, 2005, pp. 1954 – 1979, International Conference of Heterogeneous Material Mechanics, Chongqing University and Yangtze River/Three Gorges, China, June 21-26, 2004.
- [180] Faleskog, J. and Nordlund, P., “Near-Tip Field Characterization and J-Integral Evaluation for Nonproportional Loads,” *International Journal of Solids and Structures*, Vol. 31, No. 1, 1994, pp. 1 – 26.
- [181] Blackburn, W., “Path Independent Integrals to Predict Onset of Crack Instability in an Elastic Plastic Material,” *International Journal of Fracture*, Vol. 8, No. 3, Sept. 1972, pp. 343–346.

- [182] Simha, N. K., Fischer, F. D., Shan, G. X., Chen, C. R., and Kolednik, O., “J-Integral and Crack Driving Force in Elastic-Plastic Materials,” *Journal of the Mechanics and Physics of Solids*, Vol. 56, No. 9, 2008, pp. 2876 – 2895.
- [183] Gu, Y. T., Wang, Q. X., Lam, K. Y., and Dai, K. Y., “A Pseudo-Elastic Local Meshless Method for Analysis of Material Nonlinear Problems in Solids,” *Engineering Analysis with Boundary Elements*, Vol. 31, No. 9, 2007, pp. 771 – 782.
- [184] Ma, J., Xin, X. J., and Krishnaswami, P., “Elastoplastic Meshless Integral Method,” *Computer Methods in Applied Mechanics and Engineering*, Vol. 197, No. 51-52, 2008, pp. 4774 – 4788.
- [185] Zhang, Y. Y. and Chen, L., “Impact Simulation Using Simplified Meshless Method,” *International Journal of Impact Engineering*, Vol. 36, No. 5, 2009, pp. 651 – 658.
- [186] Reddy, J. N., *An Introduction to the Finite Element Method*, McGraw-Hill Science Engineering, 3rd ed., 2004.
- [187] Kojic, M. and Bathe, K.-J., *Inelastic Analysis of Solids and Structures (Computational Fluid and Solid Mechanics)*, Springer, 1st ed., December 2004.
- [188] Schaback, R., “Why Does MLPG Work?” *Keynote Lecture in ICCES 07*, Göttingen, 2006.
- [189] Schaback, R., “Recovery of Functions from Weak Data Using Unsymmetric Meshless Kernel-Based Methods,” *Applied Numerical Mathematics*, Vol. 58, No. 5, 2008, pp. 726 – 741.
- [190] Muskhelishvili, N. I., *Some Basic Problems of the Mathematical Theory of Elasticity: Fundamental Equations, Plane Theory of Elasticity, Torsion and Bending*, Springer, 4th ed., 1954.

- [191] de Jong T. W., E., K., and J., S., *Fibre Metal Laminates, an Introduction.*, chap. 22, Kluwer Academic Publishers, 2001, pp. 337–353, Vlot, A. and Gunnink, J. W. (ed.).
- [192] Makhecha, D. P., Kapania, R. K., Johnson, E. R., Dillard, D. A., Jacob, G. C., and Starbuck, J. M., “Rate-Dependent Cohesive Zone Modeling of Unstable Crack Growth in an Epoxy Adhesive,” *Mechanics of Advanced Materials and Structures*, Vol. 16, No. 1, 2009, pp. 12–19.
- [193] Rybicki, E. F. and Kanninen, M. F., “A Finite Element Calculation of Stress Intensity Factors by a Modified Crack Closure Integral,” *Engineering Fracture Mechanics*, Vol. 9, 1977, pp. 931–938.
- [194] Raju, I. S., “Calculation of Strain-Energy Release Rates with Higher Order and Singular Finite Elements,” *Engineering Fracture Mechanics*, Vol. 28, 1987, pp. 251–274.
- [195] Kapania, R. K. and Wolfe, D. R., “Delamination Buckling and Growth in Axially Loaded Beam-Plate,” *Structures, Structural Dynamics and Materials Conference, 28th (Technical Papers. Part 1 (A87-33551 14-39))*. New York, American Institute of Aeronautics and Astronautics), No. AIAA-1987-878, Monterey, CA, 1987, pp. 766–775.
- [196] Moorthy, C. M. D. and Reddy, J. N., “Recovery of Interlaminar Stresses and Strain Energy Release Rates in Composite Laminates,” *Finite Elements in Analysis and Design*, Vol. 33, No. 1, 1999, pp. 1 – 27.
- [197] Yang, C., Chadegani, A., and Tomblin, J. S., “Strain Energy Release Rate Determination of Prescribed Cracks in Adhesively-Bonded Single-Lap Composite Joints with Thick Bondlines,” *Composites Part B: Engineering*, Vol. 39, No. 5, 2008, pp. 863–873.

- [198] Barenblatt, G. I., “The Formation of Equilibrium Cracks During Brittle Fracture. General Ideas and Hypothesis. Axisymmetrical Cracks,” *Journal of Applied Mathematics and Mechanics*, Vol. 23, 1959, pp. 434–444.
- [199] Dugdale, D. S., “Yielding of Steel Sheets Containing Slits,” *Journal of the Mechanics and Physics of Solids*, Vol. 8, No. 2, 1960, pp. 100–104.
- [200] Schellekens, J. C. J. and de Borst, R., “A Nonlinear Finite Element Approach for the Analysis of Mode-I Free Edge Delamination in Composites,” *International Journal of Solids and Structures*, Vol. 30, 1993, pp. 1239–1253.
- [201] Feraren, P. and Jensen, H. M., “Cohesive Zone Modelling of Interface Fracture Near Flaws in Adhesive Joints,” *Engineering Fracture Mechanics*, Vol. 71, No. 15, 2004, pp. 2125 – 2142.
- [202] Jin, Z.-H. and Sun, C., “Cohesive Zone Modeling of Interface Fracture in Elastic Bi-Materials,” *Engineering Fracture Mechanics*, Vol. 72, No. 12, 2005, pp. 1805 – 1817, International Conference of Heterogeneous Material Mechanics, Chongqing University and Yangtze River/Three Gorges, China, June 21-26, 2004.
- [203] Jin, Z.-H. and Sun, C., “A Comparison of Cohesive Zone Modeling and Classical Fracture Mechanics Based on Near Tip Stress Field,” *International Journal of Solids and Structures*, Vol. 43, No. 5, 2006, pp. 1047 – 1060.
- [204] Lorenzis, L. D. and Zavarise, G., “Cohesive Zone Modeling of Interfacial Stresses in Plated Beams,” *International Journal of Solids and Structures*, Vol. 46, No. 24, 2009, pp. 4181 – 4191.
- [205] Sun, C. and Jin, Z.-H., “Modeling of Composite Fracture using Cohesive Zone and Bridging Models,” *Composites Science and Technology*, Vol. 66, No. 10, 2006, pp. 1297 – 1302.

- [206] Zhang, Z. J. and Paulino, G. H., “Cohesive zone modeling of dynamic failure in homogeneous and functionally graded materials,” *International Journal of Plasticity*, Vol. 21, No. 6, 2005, pp. 1195 – 1254, Plasticity of Multiphase Materials.
- [207] Camanho, P. P. and Dávila, C. G., “Mixed-Mode Decohesion Finite Elements for the Simulation of Delamination in Composite Materials,” Tech. Rep. NASA-TM-2002-211737, National Aeronautics and Space Administration, Hampton, VA, June 2002.
- [208] Benzeggagh, M. L. and Kenane, M., “Measurement of Mixed-Mode Delamination Fracture Toughness of Unidirectional Glass/Epoxy Composites with Mixed-Mode Bending Apparatus,” *Composites Science and Technology*, Vol. 56, No. 4, 1996, pp. 439 – 449.
- [209] Marat-Mendes, R. M. and Freitas, M. M., “Failure Criteria for Mixed Mode Delamination in Glass Fibre Epoxy Composites,” *Composite Structures*, Vol. 92, No. 9, 2010, pp. 2292 – 2298, Fifteenth International Conference on Composite Structures.
- [210] Chen, J., Crisfield, M., Kinloch, A. J., Busso, E. P., Matthews, F. L., and Qiu, Y., “Predicting Progressive Delamination of Composite Material Specimens via Interface Elements,” *Mechanics of Advanced Materials and Structures*, Vol. 6, No. 4, 1999, pp. 301–317.
- [211] Chen, J., Ravey, E., Hallett, S., Wisnom, M., and Grassi, M., “Prediction of Delamination in Braided Composite T-Piece Specimens,” *Composites Science and Technology*, Vol. 69, No. 14, 2009, pp. 2363 – 2367, The Sixteenth International Conference on Composite Materials with Regular Papers.



- [212] Guiamatsia, I., Ankersen, J. K., Davies, G. A. O., and Iannucci, L., “Decohesion Finite Element with Enriched Basis Functions for Delamination,” *Composites Science and Technology*, Vol. 69, No. 15-16, 2009, pp. 2616 – 2624.
- [213] Turon, A., Camanho, P. P., Costa, J., and Renart, J., “Accurate Simulation of Delamination Growth under Mixed-Mode Loading Using Cohesive Elements: Definition of Interlaminar Strengths and Elastic Stiffness,” *Composite Structures*, Vol. 92, No. 8, 2010, pp. 1857 – 1864.
- [214] Needleman, A., “A Continuum Model for Void Nucleation by Inclusion Debonding,” *Journal of Applied Mechanics*, Vol. 54, No. 3, 1987, pp. 525–531.
- [215] Xu, X.-P. and Needleman, A., “Numerical Simulations of Fast Crack Growth in Brittle Solids,” *Journal of the Mechanics and Physics of Solids*, Vol. 42, No. 9, 1994, pp. 1397 – 1434.
- [216] Makhecha, D. P., *Dynamic Fracture of Adhesively Bonded Composite Structures Using Cohesive Zone Models*, Ph.D. thesis, Virginia Polytechnic Institute and State University, Blacksburg, VA, 2005.
- [217] Rose, J. H., Ferrante, J., and Smith, R. J., “Universal Binding Energy Curves for Metals and Bimetallic Interfaces,” *Physical Review Letters*, Vol. 47, 1981, pp. 675–678.
- [218] Whitcomb, J. D., “Analysis of Instability-Related Growth of a Through Width Delamination,” Tech. Rep. NASA-TM-86301, National Aeronautics and Space Administration, Hampton, VA, September 1984.
- [219] Wu, E. M. and Reuter Jr, R. C., “Crack Extension in Fibreglass Reinforced Plastics,” Tech. Rep. 275, Department of Theoretical and Applied Mechanics, Illinois University, Feb 1965.

- [220] Robbins, D. H. and Reddy, J. N., “The Effects of Kinematic Assumption on Computed Strain Energy Release Rates for Delaminated Composite Plates,” *Mathematical Modelling and Scientific Computing*, Vol. 1, No. 1,2, 1993, pp. 50–66.
- [221] Simon, J. C., *Response and Failure of Adhesively Bonded Automotive Composite Structures under Impact Loads*, Master’s thesis, Virginia Polytechnic Institute and State University, Blacksburg, VA, 2004.
- [222] Pantano, A. and Averill, R. C., “A Mesh-Independent Interface Technology for Simulation of Mixed-Mode Delamination Growth,” *International Journal of Solids and Structures*, Vol. 41, No. 14, 2004, pp. 3809 – 3831.
- [223] Vogelesang, L. B., Schijve, J., and Fredell, R., “Fibre-Metal Laminates: Damage Tolerant Aerospace Materials,” *Case Studies in Manufacturing with Advanced Materials*, Vol. 2, 1995, pp. 253–271.
- [224] Costa, M. L., Almeida, S. F. M., and Rezende, M. C., “Strength of Hygrothermally Conditioned Polymer Composites with Voids,” *Journal of Composite Materials*, Vol. 39, 2005, pp. 1943–1961.
- [225] Botelho, E. C., Almeida, R. S., Pardini, L. C., and Rezende, M. C., “Elastic Properties of Hygrothermally Conditioned GLARE Laminate,” *International Journal of Engineering Science*, Vol. 45, No. 1, 2007, pp. 163 – 172.
- [226] Khan, S. U., Alderliesten, R. C., and Benedictus, R., “Delamination Growth in Fibre Metal Laminates under Variable Amplitude Loading,” *Composites Science and Technology*, Vol. 69, No. 15-16, 2009, pp. 2604 – 2615.
- [227] Alderliesten, R. C., Hagenbeek, M., Homan, J. J., Hooijmeijer, P. A., de Vries, T. J., and Vermeeren, C. A. J. R., “Fatigue and Damage Tolerance of Glare,” *Applied Composite Materials*, Vol. 10, No. 4, July 2003, pp. 223–242.

- [228] Papakyriacou, M., Schijve, J., and Stanzl-Tschegg, S. E., “Fatigue Crack Growth Behaviour of Fibre-Metal Laminate GLARE-1 and Metal Laminate 7475 with Different Blunt Notches,” *Fatigue and Fracture of Engineering Materials and Structures*, Vol. 20, No. 11, 1997, pp. 1573–1584, DOI: 10.1111/j.1460-2695.1997.tb01512.x.
- [229] Chlupov, A., Heger, J., and Vaek, A., “Fatigue Crack Initiation and Early Growth in GLARE 3 Fiber-metal Laminate Subjected to Mixed Tensile and Bending Loading,” *Acta Polytechnica*, Vol. 4, 2001, pp. 33–36.
- [230] Remmers, J. J. C. and de Borst, R., “Delamination Buckling of Fibre-Metal Laminates,” *Composites Science and Technology*, Vol. 61, No. 15, 2001, pp. 2207 – 2213.
- [231] Remmers, J. J. C. and de Borst, R., “Delamination Buckling of Fibre-Metal Laminates Under Compressive and Shear Loadings,” *43rd AIAA/ASME/ASCE/AHS/ASC Structures, Structural Dynamics, and Materials Conference*, No. AIAA-2002-1730, Denver, CO, 22-25 April 2002.
- [232] Parisch, H., “A Continuum-Based Shell Theory for Non-Linear Applications,” *International Journal for Numerical Methods in Engineering*, Vol. 38, No. 11, 1995, pp. 1855–1883.
- [233] “Military Handbook: Metallic Materials and Elements for Aerospace Vehicle Structures,” Tech. Rep. MIL-HDBK-5H, Department of Defense, December 1998, Avail: <http://www.grantadesign.com/userarea/mil/mil5.htm>.
- [234] Abdella, K., Yu, X., and Kucuk, I., “Application of the Sinc Method to a Dynamic Elasto-Plastic Problem,” *Journal of Computational and Applied Mathematics*, Vol. 223, No. 2, 2009, pp. 626–645.

# Appendices

## A Fourth-Order Basis Function in 2D Classical Plate

For the 2D classical plate problem, the scalar product of Sinc series with DE transformation was used to approximate  $\partial^8 W(\xi, \eta)/\partial \xi^4 \partial \eta^4$

$$\frac{\partial^8 W(\xi, \eta)}{\partial \xi^4 \partial \eta^4} = \sum_{i=-N}^N \sum_{j=-N}^N T_1(\xi, i) T_1(\eta, j) \frac{\partial^8 W(\xi_i, \eta_j)}{\partial \xi^4 \partial \eta^4} \quad (\text{A.17})$$

where  $T_1(\xi, i)$  is given by Eq. (3.16). The lower-order derivative and unknown function are found by integration of Eq. (A.17). The process is quite tedious; however the result is critical.

For the present problem, the full list of lower-order derivatives are given by:

$$\begin{aligned} \frac{\partial^7 W(\xi, \eta)}{\partial \xi^3 \partial \eta^4} &= T_2(\xi, k) T_1(\eta, l) \frac{\partial^8 W(\xi_k, \eta_l)}{\partial \xi^4 \partial \eta^4} + T_1(\eta, l) \frac{\partial^7 W(0, \eta_l)}{\partial \xi^3 \partial \eta^4} \\ \frac{\partial^7 W(\xi, \eta)}{\partial \xi^4 \partial \eta^3} &= T_1(\xi, k) T_2(\eta, l) \frac{\partial^8 W(\xi_k, \eta_l)}{\partial \xi^4 \partial \eta^4} + T_1(\xi, k) \frac{\partial^7 W(\xi_k, 0)}{\partial \xi^4 \partial \eta^3} \\ \frac{\partial^6 W(\xi, \eta)}{\partial \xi^3 \partial \eta^3} &= T_2(\xi, k) T_2(\eta, l) \frac{\partial^8 W(\xi_k, \eta_l)}{\partial \xi^4 \partial \eta^4} + T_2(\eta, l) \frac{\partial^7 W(0, \eta_l)}{\partial \xi^3 \partial \eta^4} + T_2(\xi, k) \frac{\partial^7 W(\xi_k, 0)}{\partial \xi^4 \partial \eta^3} + \frac{\partial^6 W(0, 0)}{\partial \xi^3 \partial \eta^3} \\ \frac{\partial^6 W(\xi, \eta)}{\partial \xi^4 \partial \eta^2} &= T_1(\xi, k) T_3(\eta, l) \frac{\partial^8 W(\xi_k, \eta_l)}{\partial \xi^4 \partial \eta^4} + T_1(\xi, k) \frac{\partial^7 W(\xi_k, 0)}{\partial \xi^4 \partial \eta^3} \eta + T_1(\xi, k) \frac{\partial^6 W(\xi_k, 0)}{\partial \xi^4 \partial \eta^2} \\ \frac{\partial^6 W(\xi, \eta)}{\partial \xi^2 \partial \eta^4} &= T_3(\xi, k) T_1(\eta, l) \frac{\partial^8 W(\xi_k, \eta_l)}{\partial \xi^4 \partial \eta^4} + T_1(\eta, l) \frac{\partial^7 W(0, \eta_l)}{\partial \xi^3 \partial \eta^4} \xi + T_1(\eta, l) \frac{\partial^6 W(0, \eta_l)}{\partial \xi^2 \partial \eta^4} \\ \frac{\partial^5 W(\xi, \eta)}{\partial \xi^4 \partial \eta} &= T_1(\xi, k) T_4(\eta, l) \frac{\partial^8 W(\xi_k, \eta_l)}{\partial \xi^4 \partial \eta^4} + T_1(\xi, k) \frac{\partial^7 W(\xi_k, 0)}{\partial \xi^4 \partial \eta^3} \frac{\eta^2}{2} \\ &\quad + T_1(\xi, k) \frac{\partial^6 W(\xi_k, 0)}{\partial \xi^4 \partial \eta^2} \eta + T_1(\xi, k) \frac{\partial^5 W(\xi_k, 0)}{\partial \xi^4 \partial \eta} \end{aligned}$$

$$\begin{aligned} \frac{\partial^5 W(\xi, \eta)}{\partial \xi^3 \partial \eta^2} &= T_2(\xi, k) T_3(\eta, l) \frac{\partial^8 W(\xi_k, \eta_l)}{\partial \xi^4 \partial \eta^4} + T_3(\eta, l) \frac{\partial^7 W(0, \eta_l)}{\partial \xi^3 \partial \eta^4} \\ &\quad + T_2(\xi, k) \frac{\partial^7 W(\xi_k, 0)}{\partial \xi^4 \partial \eta^3} \eta + T_2(\xi, k) \frac{\partial^6 W(\xi_k, 0)}{\partial \xi^4 \partial \eta^2} + \frac{\partial^6 W(0, 0)}{\partial \xi^3 \partial \eta^3} \eta + \frac{\partial^5 W(0, 0)}{\partial \xi^3 \partial \eta^2} \end{aligned}$$

$$\begin{aligned} \frac{\partial^5 W(\xi, \eta)}{\partial \xi^2 \partial \eta^3} &= T_3(\xi, k) T_2(\eta, l) \frac{\partial^8 W(\xi_k, \eta_l)}{\partial \xi^4 \partial \eta^4} + T_2(\eta, l) \frac{\partial^7 W(0, \eta_l)}{\partial \xi^3 \partial \eta^4} \xi + T_3(\xi, k) \frac{\partial^7 W(\xi_k, 0)}{\partial \xi^4 \partial \eta^3} \\ &\quad + T_2(\eta, l) \frac{\partial^6 W(0, \eta_l)}{\partial \xi^2 \partial \eta^4} + \frac{\partial^6 W(0, 0)}{\partial \xi^3 \partial \eta^3} \xi + \frac{\partial^5 W(0, 0)}{\partial \xi^2 \partial \eta^3} \end{aligned}$$

$$\begin{aligned} \frac{\partial^5 W(\xi, \eta)}{\partial \xi \partial \eta^4} &= T_4(\xi, k) T_1(\eta, l) \frac{\partial^8 W(\xi_k, \eta_l)}{\partial \xi^4 \partial \eta^4} + T_1(\eta, l) \frac{\partial^7 W(0, \eta_l)}{\partial \xi^3 \partial \eta^4} \frac{\xi^2}{2} + T_1(\eta, l) \frac{\partial^6 W(0, \eta_l)}{\partial \xi^2 \partial \eta^4} \xi \\ &\quad + T_1(\eta, l) \frac{\partial^5 W(0, \eta_l)}{\partial \xi \partial \eta^4} \end{aligned}$$

$$\begin{aligned} \frac{\partial^4 W(\xi, \eta)}{\partial \xi^4} &= T_1(\xi, k) T_5(\eta, l) \frac{\partial^8 W(\xi_k, \eta_l)}{\partial \xi^4 \partial \eta^4} + T_1(\xi, k) \frac{\partial^7 W(\xi_k, 0)}{\partial \xi^4 \partial \eta^3} \frac{\eta^3}{6} + T_1(\xi, k) \frac{\partial^6 W(\xi_k, 0)}{\partial \xi^4 \partial \eta^2} \frac{\eta^2}{2} \\ &\quad + T_1(\xi, k) \frac{\partial^5 W(\xi_k, 0)}{\partial \xi^4 \partial \eta} \eta + T_1(\xi, k) \frac{\partial^4 W(\xi_k, 0)}{\partial \xi^4} \end{aligned}$$

$$\begin{aligned} \frac{\partial^4 W(\xi, \eta)}{\partial \xi^3 \partial \eta} &= T_2(\xi, k) T_4(\eta, l) \frac{\partial^8 W(\xi_k, \eta_l)}{\partial \xi^4 \partial \eta^4} + T_4(\eta, l) \frac{\partial^7 W(0, \eta_l)}{\partial \xi^3 \partial \eta^4} + T_2(\xi, k) \frac{\partial^7 W(\xi_k, 0)}{\partial \xi^4 \partial \eta^3} \frac{\eta^2}{2} \\ &\quad + T_2(\xi, k) \frac{\partial^6 W(\xi_k, 0)}{\partial \xi^4 \partial \eta^2} \eta + T_2(\xi, k) \frac{\partial^5 W(\xi_k, 0)}{\partial \xi^4 \partial \eta} + \frac{\partial^6 W(0, 0)}{\partial \xi^3 \partial \eta^3} \frac{\eta^2}{2} \\ &\quad + \frac{\partial^5 W(0, 0)}{\partial \xi^3 \partial \eta^2} \eta + \frac{\partial^4 W(0, 0)}{\partial \xi^3 \partial \eta} \end{aligned}$$

$$\begin{aligned} \frac{\partial^4 W(\xi, \eta)}{\partial \xi^2 \partial \eta^2} &= T_3(\xi, k) T_3(\eta, l) \frac{\partial^8 W(\xi_k, \eta_l)}{\partial \xi^4 \partial \eta^4} + T_3(\eta, l) \frac{\partial^7 W(0, \eta_l)}{\partial \xi^3 \partial \eta^4} \xi + T_3(\xi, k) \frac{\partial^7 W(\xi_k, 0)}{\partial \xi^4 \partial \eta^3} \eta \\ &+ T_3(\eta, l) \frac{\partial^6 W(0, \eta_l)}{\partial \xi^2 \partial \eta^4} + T_3(\xi, k) \frac{\partial^6 W(\xi_k, 0)}{\partial \xi^4 \partial \eta^2} + \frac{\partial^6 W(0, 0)}{\partial \xi^3 \partial \eta^3} \xi \eta + \frac{\partial^5 W(0, 0)}{\partial \xi^2 \partial \eta^3} \eta \\ &+ \frac{\partial^5 W(0, 0)}{\partial \xi^3 \partial \eta^2} \xi + \frac{\partial^4 W(0, 0)}{\partial \xi^2 \partial \eta^2} \end{aligned}$$

$$\begin{aligned} \frac{\partial^4 W(\xi, \eta)}{\partial \xi \partial \eta^3} &= T_4(\xi, k) T_2(\eta, l) \frac{\partial^8 W(\xi_k, \eta_l)}{\partial \xi^4 \partial \eta^4} + T_2(\eta, l) \frac{\partial^7 W(0, \eta_l)}{\partial \xi^3 \partial \eta^4} \frac{\xi^2}{2} + T_4(\xi, k) \frac{\partial^7 W(\xi_k, 0)}{\partial \xi^4 \partial \eta^3} \\ &+ T_2(\eta, l) \frac{\partial^6 W(0, \eta_l)}{\partial \xi^2 \partial \eta^4} \xi + T_2(\eta, l) \frac{\partial^5 W(0, \eta_l)}{\partial \xi \partial \eta^4} + \frac{\partial^6 W(0, 0)}{\partial \xi^3 \partial \eta^3} \frac{\xi^2}{2} \\ &+ \frac{\partial^5 W(0, 0)}{\partial \xi^2 \partial \eta^3} \xi + \frac{\partial^4 W(0, 0)}{\partial \xi \partial \eta^3} \end{aligned}$$

$$\begin{aligned} \frac{\partial^4 W(\xi, \eta)}{\partial \eta^4} &= T_5(\xi, k) T_1(\eta, l) \frac{\partial^8 W(\xi_k, \eta_l)}{\partial \xi^4 \partial \eta^4} + T_1(\eta, l) \frac{\partial^7 W(0, \eta_l)}{\partial \xi^3 \partial \eta^4} \frac{\xi^3}{6} + T_1(\eta, l) \frac{\partial^6 W(0, \eta_l)}{\partial \xi^2 \partial \eta^4} \frac{\xi^2}{2} \\ &+ T_1(\eta, l) \frac{\partial^5 W(0, \eta_l)}{\partial \xi \partial \eta^4} \xi + T_1(\eta, l) \frac{\partial^4 W(0, \eta_l)}{\partial \eta^4} \end{aligned}$$

$$\begin{aligned} \frac{\partial^3 W(\xi, \eta)}{\partial \xi^3} &= T_2(\xi, k) T_5(\eta, l) \frac{\partial^8 W(\xi_k, \eta_l)}{\partial \xi^4 \partial \eta^4} + T_5(\eta, l) \frac{\partial^7 W(0, \eta_l)}{\partial \xi^3 \partial \eta^4} + T_2(\xi, k) \frac{\partial^7 W(\xi_k, 0)}{\partial \xi^4 \partial \eta^3} \frac{\eta^3}{6} \\ &+ T_2(\xi, k) \frac{\partial^6 W(\xi_k, 0)}{\partial \xi^4 \partial \eta^2} \frac{\eta^2}{2} + T_2(\xi, k) \frac{\partial^5 W(\xi_k, 0)}{\partial \xi^4 \partial \eta} \eta + T_2(\xi, k) \frac{\partial^4 W(\xi_k, 0)}{\partial \xi^4} + \frac{\partial^6 W(0, 0)}{\partial \xi^3 \partial \eta^3} \frac{\eta^3}{6} \\ &+ \frac{\partial^5 W(0, 0)}{\partial \xi^3 \partial \eta^2} \frac{\eta^2}{2} + \frac{\partial^4 W(0, 0)}{\partial \xi^3 \partial \eta} \eta + \frac{\partial^3 W(0, 0)}{\partial \xi^3} \end{aligned}$$

$$\begin{aligned} \frac{\partial^3 W(\xi, \eta)}{\partial \xi^2 \partial \eta} &= T_3(\xi, k) T_4(\eta, l) \frac{\partial^8 W(\xi_k, \eta_l)}{\partial \xi^4 \partial \eta^4} + T_4(\eta, l) \frac{\partial^7 W(0, \eta_l)}{\partial \xi^3 \partial \eta^4} \xi + T_3(\xi, k) \frac{\partial^7 W(\xi_k, 0)}{\partial \xi^4 \partial \eta^3} \frac{\eta^2}{2} \\ &+ T_4(\eta, l) \frac{\partial^6 W(0, \eta_l)}{\partial \xi^2 \partial \eta^4} + T_3(\xi, k) \frac{\partial^6 W(\xi_k, 0)}{\partial \xi^4 \partial \eta^2} \eta + T_3(\xi, k) \frac{\partial^5 W(\xi_k, 0)}{\partial \xi^4 \partial \eta} + \frac{\partial^6 W(0, 0)}{\partial \xi^3 \partial \eta^3} \frac{\xi \eta^2}{2} \\ &+ \frac{\partial^5 W(0, 0)}{\partial \xi^2 \partial \eta^3} \frac{\eta^2}{2} + \frac{\partial^5 W(0, 0)}{\partial \xi^3 \partial \eta^2} \xi \eta + \frac{\partial^4 W(0, 0)}{\partial \xi^2 \partial \eta^2} \eta + \frac{\partial^4 W(0, 0)}{\partial \xi^3 \partial \eta} \xi + \frac{\partial^3 W(0, 0)}{\partial \xi^2 \partial \eta} \end{aligned}$$

$$\begin{aligned} \frac{\partial^3 W(\xi, \eta)}{\partial \xi \partial \eta^2} &= T_4(\xi, k) T_3(\eta, l) \frac{\partial^8 W(\xi_k, \eta_l)}{\partial \xi^4 \partial \eta^4} + T_3(\eta, l) \frac{\partial^7 W(0, \eta_l) \xi^2}{\partial \xi^3 \partial \eta^4} + T_4(\xi, k) \frac{\partial^7 W(\xi_k, 0)}{\partial \xi^4 \partial \eta^3} \eta \\ &+ T_3(\eta, l) \frac{\partial^6 W(0, \eta_l)}{\partial \xi^2 \partial \eta^4} \xi + T_4(\xi, k) \frac{\partial^6 W(\xi_k, 0)}{\partial \xi^4 \partial \eta^2} + T_3(\eta, l) \frac{\partial^5 W(0, \eta_l)}{\partial \xi \partial \eta^4} + \frac{\partial^6 W(0, 0) \xi^2 \eta}{\partial \xi^3 \partial \eta^3} \frac{1}{2} \\ &+ \frac{\partial^5 W(0, 0)}{\partial \xi^2 \partial \eta^3} \xi \eta + \frac{\partial^5 W(0, 0) \xi^2}{\partial \xi^3 \partial \eta^2} \frac{1}{2} + \frac{\partial^4 W(0, 0)}{\partial \xi^2 \partial \eta^2} \xi + \frac{\partial^4 W(0, 0)}{\partial \xi \partial \eta^3} \eta + \frac{\partial^3 W(0, 0)}{\partial \xi \partial \eta^2} \end{aligned}$$

$$\begin{aligned} \frac{\partial^3 W(\xi, \eta)}{\partial \eta^3} &= T_5(\xi, k) T_2(\eta, l) \frac{\partial^8 W(\xi_k, \eta_l)}{\partial \xi^4 \partial \eta^4} + T_2(\eta, l) \frac{\partial^7 W(0, \eta_l) \xi^3}{\partial \xi^3 \partial \eta^4} + T_5(\xi, k) \frac{\partial^7 W(\xi_k, 0)}{\partial \xi^4 \partial \eta^3} \\ &+ T_2(\eta, l) \frac{\partial^6 W(0, \eta_l) \xi^2}{\partial \xi^2 \partial \eta^4} \frac{1}{2} + T_2(\eta, l) \frac{\partial^5 W(0, \eta_l)}{\partial \xi \partial \eta^4} \xi + T_2(\eta, l) \frac{\partial^4 W(0, \eta_l)}{\partial \eta^4} + \frac{\partial^6 W(0, 0) \xi^3}{\partial \xi^3 \partial \eta^3} \frac{1}{6} \\ &+ \frac{\partial^5 W(0, 0) \xi^2}{\partial \xi^2 \partial \eta^3} \frac{1}{2} + \frac{\partial^4 W(0, 0)}{\partial \xi \partial \eta^3} \xi + \frac{\partial^3 W(0, 0)}{\partial \eta^3} \end{aligned}$$

$$\begin{aligned} \frac{\partial^2 W(\xi, \eta)}{\partial \xi^2} &= T_3(\xi, k) T_5(\eta, l) \frac{\partial^8 W(\xi_k, \eta_l)}{\partial \xi^4 \partial \eta^4} + T_5(\eta, l) \frac{\partial^7 W(0, \eta_l)}{\partial \xi^3 \partial \eta^4} \xi + T_3(\xi, k) \frac{\partial^7 W(\xi_k, 0) \eta^3}{\partial \xi^4 \partial \eta^3} \frac{1}{6} \\ &+ T_5(\eta, l) \frac{\partial^6 W(0, \eta_l)}{\partial \xi^2 \partial \eta^4} + T_3(\xi, k) \frac{\partial^6 W(\xi_k, 0) \eta^2}{\partial \xi^4 \partial \eta^2} \frac{1}{2} + T_3(\xi, k) \frac{\partial^5 W(\xi_k, 0)}{\partial \xi^4 \partial \eta} \eta \\ &+ T_3(\xi, k) \frac{\partial^4 W(\xi_k, 0)}{\partial \xi^4} + \frac{\partial^6 W(0, 0) \xi \eta^3}{\partial \xi^3 \partial \eta^3} \frac{1}{6} + \frac{\partial^5 W(0, 0) \eta^3}{\partial \xi^2 \partial \eta^3} \frac{1}{6} + \frac{\partial^5 W(0, 0) \xi \eta^2}{\partial \xi^3 \partial \eta^2} \frac{1}{2} \\ &+ \frac{\partial^4 W(0, 0) \eta^2}{\partial \xi^2 \partial \eta^2} \frac{1}{2} + \frac{\partial^4 W(0, 0)}{\partial \xi^3 \partial \eta} \xi \eta + \frac{\partial^3 W(0, 0)}{\partial \xi^2 \partial \eta} \eta + \frac{\partial^3 W(0, 0)}{\partial \xi^3} \xi + \frac{\partial^2 W(0, 0)}{\partial \xi^2} \end{aligned}$$

$$\begin{aligned} \frac{\partial^2 W(\xi, \eta)}{\partial \xi \partial \eta} &= T_4(\xi, k) T_4(\eta, l) \frac{\partial^8 W(\xi_k, \eta_l)}{\partial \xi^4 \partial \eta^4} + T_4(\eta, l) \frac{\partial^7 W(0, \eta_l) \xi^2}{\partial \xi^3 \partial \eta^4} \frac{1}{2} + T_4(\xi, k) \frac{\partial^7 W(\xi_k, 0) \eta^2}{\partial \xi^4 \partial \eta^3} \frac{1}{2} \\ &+ T_4(\eta, l) \frac{\partial^6 W(0, \eta_l)}{\partial \xi^2 \partial \eta^4} \xi + T_4(\xi, k) \frac{\partial^6 W(\xi_k, 0)}{\partial \xi^4 \partial \eta^2} \eta + T_4(\eta, l) \frac{\partial^5 W(0, \eta_l)}{\partial \xi \partial \eta^4} + T_4(\xi, k) \frac{\partial^5 W(\xi_k, 0)}{\partial \xi^4 \partial \eta} \\ &+ \frac{\partial^6 W(0, 0) \xi^2 \eta^2}{\partial \xi^3 \partial \eta^3} \frac{1}{4} + \frac{\partial^5 W(0, 0) \xi \eta^2}{\partial \xi^2 \partial \eta^3} \frac{1}{2} + \frac{\partial^5 W(0, 0) \xi^2 \eta}{\partial \xi^3 \partial \eta^2} \frac{1}{2} + \frac{\partial^4 W(0, 0)}{\partial \xi^2 \partial \eta^2} \xi \eta + \frac{\partial^4 W(0, 0) \eta^2}{\partial \xi \partial \eta^3} \frac{1}{2} \\ &+ \frac{\partial^4 W(0, 0) \xi^2}{\partial \xi^3 \partial \eta} \frac{1}{2} + \frac{\partial^3 W(0, 0)}{\partial \xi^2 \partial \eta} \xi + \frac{\partial^3 W(0, 0)}{\partial \xi \partial \eta^2} \eta + \frac{\partial^2 W(0, 0)}{\partial \xi \partial \eta} \end{aligned}$$

$$\begin{aligned} \frac{\partial^2 W(\xi, \eta)}{\partial \eta^2} &= T_5(\xi, k)T_3(\eta, l) \frac{\partial^8 W(\xi_k, \eta_l)}{\partial \xi^4 \partial \eta^4} + T_3(\eta, l) \frac{\partial^7 W(0, \eta_l) \xi^3}{\partial \xi^3 \partial \eta^4} + T_5(\xi, k) \frac{\partial^7 W(\xi_k, 0)}{\partial \xi^4 \partial \eta^3} \eta \\ &+ T_3(\eta, l) \frac{\partial^6 W(0, \eta_l) \xi^2}{\partial \xi^2 \partial \eta^4} + T_5(\xi, k) \frac{\partial^6 W(\xi_k, 0)}{\partial \xi^4 \partial \eta^2} + T_3(\eta, l) \frac{\partial^5 W(0, \eta_l)}{\partial \xi \partial \eta^4} \xi + T_3(\eta, l) \frac{\partial^4 W(0, \eta_l)}{\partial \eta^4} \\ &+ \frac{\partial^6 W(0, 0) \xi^3 \eta}{\partial \xi^3 \partial \eta^3} + \frac{\partial^5 W(0, 0) \xi^2 \eta}{\partial \xi^2 \partial \eta^3} + \frac{\partial^5 W(0, 0) \xi^3}{\partial \xi^3 \partial \eta^2} + \frac{\partial^4 W(0, 0) \xi^2}{\partial \xi^2 \partial \eta^2} \\ &+ \frac{\partial^4 W(0, 0)}{\partial \xi \partial \eta^3} \xi \eta + \frac{\partial^3 W(0, 0)}{\partial \xi \partial \eta^2} \xi + \frac{\partial^3 W(0, 0)}{\partial \eta^3} \eta + \frac{\partial^2 W(0, 0)}{\partial \eta^2} \end{aligned}$$

$$\begin{aligned} \frac{\partial W(\xi, \eta)}{\partial \xi} &= T_4(\xi, k)T_5(\eta, l) \frac{\partial^8 W(\xi_k, \eta_l)}{\partial \xi^4 \partial \eta^4} + T_5(\eta, l) \frac{\partial^7 W(0, \eta_l) \xi^2}{\partial \xi^3 \partial \eta^4} + T_4(\xi, k) \frac{\partial^7 W(\xi_k, 0) \eta^3}{\partial \xi^4 \partial \eta^3} \\ &+ T_5(\eta, l) \frac{\partial^6 W(0, \eta_l) \xi}{\partial \xi^2 \partial \eta^4} + T_4(\xi, k) \frac{\partial^6 W(\xi_k, 0) \eta^2}{\partial \xi^4 \partial \eta^2} + T_5(\eta, l) \frac{\partial^5 W(0, \eta_l)}{\partial \xi \partial \eta^4} + T_4(\xi, k) \frac{\partial^5 W(\xi_k, 0)}{\partial \xi^4 \partial \eta} \eta \\ &+ T_4(\xi, k) \frac{\partial^4 W(\xi_k, 0)}{\partial \xi^4} + \frac{\partial^6 W(0, 0) \xi^2 \eta^3}{\partial \xi^3 \partial \eta^3} + \frac{\partial^5 W(0, 0) \xi \eta^3}{\partial \xi^2 \partial \eta^3} + \frac{\partial^5 W(0, 0) \xi^2 \eta^2}{\partial \xi^3 \partial \eta^2} \\ &+ \frac{\partial^4 W(0, 0) \xi \eta^2}{\partial \xi^2 \partial \eta^2} + \frac{\partial^4 W(0, 0) \eta^3}{\partial \xi \partial \eta^3} + \frac{\partial^4 W(0, 0) \xi^2 \eta}{\partial \xi^3 \partial \eta} + \frac{\partial^3 W(0, 0)}{\partial \xi^2 \partial \eta} \xi \eta \\ &+ \frac{\partial^3 W(0, 0) \eta^2}{\partial \xi \partial \eta^2} + \frac{\partial^3 W(0, 0) \xi^2}{\partial \xi^3} + \frac{\partial^2 W(0, 0)}{\partial \xi^2} \xi + \frac{\partial^2 W(0, 0)}{\partial \xi \partial \eta} \eta + \frac{\partial W(0, 0)}{\partial \xi} \end{aligned}$$

$$\begin{aligned} \frac{\partial W(\xi, \eta)}{\partial \eta} &= T_5(\xi, k)T_4(\eta, l) \frac{\partial^8 W(\xi_k, \eta_l)}{\partial \xi^4 \partial \eta^4} + T_4(\eta, l) \frac{\partial^7 W(0, \eta_l) \xi^3}{\partial \xi^3 \partial \eta^4} + T_5(\xi, k) \frac{\partial^7 W(\xi_k, 0) \eta^2}{\partial \xi^4 \partial \eta^3} \\ &+ T_4(\eta, l) \frac{\partial^6 W(0, \eta_l) \xi^2}{\partial \xi^2 \partial \eta^4} + T_5(\xi, k) \frac{\partial^6 W(\xi_k, 0)}{\partial \xi^4 \partial \eta^2} \eta + T_4(\eta, l) \frac{\partial^5 W(0, \eta_l)}{\partial \xi \partial \eta^4} \xi \\ &+ T_5(\xi, k) \frac{\partial^5 W(\xi_k, 0)}{\partial \xi^4 \partial \eta} + T_4(\eta, l) \frac{\partial^4 W(0, \eta_l)}{\partial \eta^4} + \frac{\partial^6 W(0, 0) \xi^3 \eta^2}{\partial \xi^3 \partial \eta^3} + \frac{\partial^5 W(0, 0) \xi^2 \eta^2}{\partial \xi^2 \partial \eta^3} \\ &+ \frac{\partial^5 W(0, 0) \xi^3 \eta}{\partial \xi^3 \partial \eta^2} + \frac{\partial^4 W(0, 0) \xi^2 \eta}{\partial \xi^2 \partial \eta^2} + \frac{\partial^4 W(0, 0) \xi \eta^2}{\partial \xi \partial \eta^3} + \frac{\partial^4 W(0, 0) \xi^3}{\partial \xi^3 \partial \eta} \\ &+ \frac{\partial^3 W(0, 0) \xi^2}{\partial \xi^2 \partial \eta} + \frac{\partial^3 W(0, 0)}{\partial \xi \partial \eta^2} \xi \eta + \frac{\partial^3 W(0, 0) \eta^2}{\partial \eta^3} \\ &+ \frac{\partial^2 W(0, 0)}{\partial \eta^2} \eta + \frac{\partial^2 W(0, 0)}{\partial \xi \partial \eta} \xi + \frac{\partial W(0, 0)}{\partial \eta} \end{aligned}$$



$$\begin{aligned}
 W(\xi, \eta) = & T_5(\xi, k)T_5(\eta, l) \frac{\partial^8 W(\xi_k, \eta_l)}{\partial \xi^4 \partial \eta^4} + T_5(\eta, l) \frac{\partial^7 W(0, \eta_l) \xi^3}{\partial \xi^3 \partial \eta^4} + T_5(\xi, k) \frac{\partial^7 W(\xi_k, 0) \eta^3}{\partial \xi^4 \partial \eta^3} \\
 & + T_5(\eta, l) \frac{\partial^6 W(0, \eta_l) \xi^2}{\partial \xi^2 \partial \eta^4} + T_5(\xi, k) \frac{\partial^6 W(\xi_k, 0) \eta^2}{\partial \xi^4 \partial \eta^2} + T_5(\eta, l) \frac{\partial^5 W(0, \eta_l) \xi}{\partial \xi \partial \eta^4} \\
 & + T_5(\xi, k) \frac{\partial^5 W(\xi_k, 0)}{\partial \xi^4 \partial \eta} \eta + T_5(\eta, l) \frac{\partial^4 W(0, \eta_l)}{\partial \eta^4} + T_5(\xi, k) \frac{\partial^4 W(\xi_k, 0)}{\partial \xi^4} \\
 & + \frac{\partial^6 W(0, 0) \xi^3 \eta^3}{\partial \xi^3 \partial \eta^3} \frac{1}{36} + \frac{\partial^5 W(0, 0) \xi^2 \eta^3}{\partial \xi^2 \partial \eta^3} \frac{1}{12} + \frac{\partial^5 W(0, 0) \xi^3 \eta^2}{\partial \xi^3 \partial \eta^2} \frac{1}{12} + \frac{\partial^4 W(0, 0) \xi^2 \eta^2}{\partial \xi^2 \partial \eta^2} \frac{1}{4} \\
 & + \frac{\partial^4 W(0, 0) \xi \eta^3}{\partial \xi \partial \eta^3} \frac{1}{6} + \frac{\partial^4 W(0, 0) \xi^3 \eta}{\partial \xi^3 \partial \eta} \frac{1}{6} + \frac{\partial^3 W(0, 0) \xi^2 \eta}{\partial \xi^2 \partial \eta} \frac{1}{2} + \frac{\partial^3 W(0, 0) \xi \eta^2}{\partial \xi \partial \eta^2} \frac{1}{2} \\
 & + \frac{\partial^3 W(0, 0) \eta^3}{\partial \eta^3} \frac{1}{6} + \frac{\partial^3 W(0, 0) \xi^3}{\partial \xi^3} \frac{1}{6} + \frac{\partial^2 W(0, 0) \xi^2}{\partial \xi^2} \frac{1}{2} + \frac{\partial^2 W(0, 0) \eta^2}{\partial \eta^2} \frac{1}{2} \\
 & + \frac{\partial^2 W(0, 0)}{\partial \xi \partial \eta} \xi \eta + \frac{\partial W(0, 0)}{\partial \xi} \xi + \frac{\partial W(0, 0)}{\partial \eta} \eta + W(0, 0)
 \end{aligned}$$

Note that repetition of  $l$  and  $k$  implies summation from  $-N$  to  $N$ ,  $T_2(\xi, j)$  was defined in Eq. (3.17),  $T_3(\xi, j)$  was defined in Eq. (3.31) and the following additional definitions are introduced:

$$\begin{aligned}
 T_4(\xi, j) = & \psi'(jh)h^3 \sum_{i=-N}^N \sum_{k=-N}^N \psi'(ih)\psi'(kh) \left[ \frac{1}{2} + \frac{1}{\pi} \text{Si} \left( \frac{\pi\phi(\xi)}{h} - \pi i \right) \right] \\
 & \times \left[ \frac{1}{2} + \frac{1}{\pi} \text{Si}(\pi(i - k)) \right] \left[ \frac{1}{2} + \frac{1}{\pi} \text{Si}(\pi(k - j)) \right], \quad (\text{A.18})
 \end{aligned}$$

$$\begin{aligned}
 T_5(\xi, j) = & \psi'(jh)h^4 \sum_{i=-N}^N \sum_{k=-N}^N \sum_{l=-N}^N \psi'(ih)\psi'(kh)\psi'(lh) \left[ \frac{1}{2} + \frac{1}{\pi} \text{Si} \left( \frac{\pi\phi(\xi)}{h} - \pi i \right) \right] \\
 & \times \left[ \frac{1}{2} + \frac{1}{\pi} \text{Si}(\pi(i - k)) \right] \left[ \frac{1}{2} + \frac{1}{\pi} \text{Si}(\pi(k - l)) \right] \left[ \frac{1}{2} + \frac{1}{\pi} \text{Si}(\pi(l - j)) \right]. \quad (\text{A.19})
 \end{aligned}$$

The full list of unknowns were given in Table 4.2. For the SIHD method, if only the value at the Sinc points are desired then the  $T$  functions can be replaced by the appropriate multiplication of inner products of  $k_{ij}$  with itself, where  $k_{ij}$  was defined in Eq. (4.4).

$$(T_5(\xi_i, j) = k_{ik}k_{kl}k_{lm}k_{mj})$$

## B Governing Equations of ESL Beam Theories

Governing equations for the beam theories are derived from the principle of virtual work.

That is

$$\int_{\Omega} [\sigma_{xx}\delta\epsilon_{xx} + \sigma_{xz}\delta\gamma_{xz}] dV = \int_{\partial\Omega} f_z\delta w dA, \quad (\text{B.20})$$

where  $f_z$  is the surface traction in the  $z$  direction. Substituting the reduced stress-strain relation and integrating through the thickness and across through the width, results in the following relation:

$$b \left[ \int_0^L N_{xx}\delta\epsilon_{xx}^{(0)} + M_{xx}\delta\epsilon_{xx}^{(1)} + P_{xx}\delta\epsilon_{xx}^{(3)} + Q_x\delta\gamma_{xz}^{(0)} + R_x\delta\gamma_{xz}^{(2)} dx \right] = b = b \int_0^L f_z\delta w dx.$$

Now by simplifying and substituting the strain-displacement relations, the governing equations for a symmetrically laminated Bickford beam theory are obtained as:

$$\frac{d\bar{Q}_x}{dx} + c_1 \frac{d^2 P_{xx}}{dx^2} + q = 0, \quad \text{and} \quad \frac{d\bar{M}_{xx}}{dx} - \bar{Q}_x = 0,$$

where the stress resultants  $Q_x$ ,  $R_x$ ,  $P_{xx}$ , were defined in Eq. 2.6,  $\bar{Q}_x = Q_x - 3c_1 R_x$ ,  $\bar{M}_{xx} = M_{xx} - c_1 P_{xx}$ ,  $c_1 = 4/3h^2$ , and

$$q = \int_{-b/2}^{b/2} f_z dy. \quad (\text{B.21})$$

The primary variables are  $w_0$ ,  $dw_0/dx$ , and  $\phi_x$ . The corresponding secondary variables are  $V_x$ ,  $P_{xx}$ , and  $\bar{M}_{xx}$ , where  $V_x = c_1 dP_{xx}/dx + \bar{Q}_x$ . If we substitute the stress resultant-strain relations, Eqs. (2.7 - 2.8), and the strain-displacement relations and simplify we obtain:

$$\begin{aligned} T_1 \frac{d\phi_x}{dx} + T_2 \frac{d^2 w_0}{dx^2} + T_3 \frac{d^4 w_0}{dx^4} &= -q, \\ T_4 \phi_x + T_5 \frac{d^2 \phi_x}{dx^2} + T_6 \frac{dw_0}{dx} + T_7 \frac{d^3 w_0}{dx^3} &= 0, \end{aligned}$$

where

$$\begin{aligned}
 T_1 &= \frac{(D_{11}^* - c_1 F_{11}^*)(\bar{A}S_{55}^*)}{\bar{D}_{11}^*}, \quad T_2 = \frac{3c_1(D_{11}^* - c_1 F_{11}^*)(-DS_{55}^* + 3c_1 FS_{55}^*)}{\bar{D}_{11}^*}, \quad T_3 = \frac{c_1^2(F_{11}^{*2} - D_{11}^* H_{11}^*)}{\bar{D}_{11}^*}, \\
 T_4 &= -\bar{A}S_{55}^*, \quad T_5 = \bar{D}_{11}^*, \quad T_6 = 3c_1 DS_{55}^* - 9c_1^2 FS_{55}^*, \quad T_7 = c_1^2 H_{11}^* - c_1 F_{11}^*, \\
 \bar{A}S_{55}^* &= AS_{55}^* - 6c_1 DS_{55}^* + 9c_1^2 FS_{55}^*, \quad \bar{D}_{11}^* = A_{11}^* - 2c_1 D_{11}^* + c_1^2 F_{11}^*.
 \end{aligned}$$

The boundary conditions at a simply-supported end,  $x = x_0$ , are  $w_0(x_0) = 0$ ,  $\bar{M}_{xx}(x_0) = 0$  and  $P_{xx}(x_0) = 0$ . For a rigidly clamped end at  $x = x_0$ , the boundary conditions are  $w_0(x_0) = 0$ ,  $dw_0/dx(x_0) = 0$ , and  $\phi_x(x_0) = 0$ . For a free-end at  $x = x_0$ , the boundary conditions are  $V_x(x_0) = 0$ ,  $\bar{M}_{xx}(x_0) = 0$ , and  $P_{xx}(x_0) = 0$ .

The governing equations for a symmetrically laminated Timoshenko beam were given in [98] to be

$$\frac{dQ_x}{dx} + q = 0, \quad \text{and} \quad \frac{dM_{xx}}{dx} - Q_x = 0,$$

with  $Q_x$  and  $M_{xx}$  defined in Eq. (2.6). The primary variables are  $w_0$  and  $\phi_x$ . The corresponding secondary variables are  $Q_x$  and  $M_{xx}$ . If the stress resultant-strain relations and the strain-displacement relations are substituted into the governing equations the result is

$$\begin{aligned}
 AS_{55}^* K \left( \frac{d\phi_x}{dx} + \frac{d^2 w_0}{dx^2} \right) &= -q, \\
 D_{11}^* \frac{d^2 \phi_x}{dx^2} - AS_{55}^* K \left( \phi_x + \frac{dw_0}{dx} \right) &= 0.
 \end{aligned}$$

The boundary conditions at a simply-supported end,  $x = x_0$ , are  $w_0(x_0) = 0$  and  $\bar{M}_{xx}(x_0) = 0$ . For a rigidly clamped end at  $x = x_0$ , the boundary conditions are  $w_0(x_0) = 0$  and  $\phi_x(x_0) = 0$ . For a free-end at  $x = x_0$ , the boundary conditions are  $Q_x(x_0) = 0$  and  $\bar{M}_{xx}(x_0) = 0$ .

## C Solving the Bickford Beam Problem using SIHD

An approximate solution may be obtained for a Bickford beam using the SIHD method. First, select  $n = 2N + 1$  collocation points on  $\xi \in (0, 1)$  by the DE transformation. For a mesh-size  $h$ , select collocation points by

$$\xi_j = \psi(jh) = \frac{1}{2} \tanh\left(\frac{\pi}{2} \sinh(jh)\right) + \frac{1}{2} \text{ for } j = \{-N, -N + 1, \dots, N - 1, N\} \quad (\text{C.22})$$

The domain  $x \in [0, L]$  is transformed to  $\xi \in (\xi_{-N}, \xi_N)$  by the linear transformation,

$$\xi = \frac{x - L}{\xi_N - \xi_{-N}} + \xi_{-N}. \quad (\text{C.23})$$

Accordingly, the governing equations become

$$\begin{aligned} T_1 \frac{d\phi_x(\xi)}{d\xi} \frac{d\xi}{dx} + T_2 \frac{d^2 w_0(\xi)}{d\xi^2} \left(\frac{d\xi}{dx}\right)^2 + T_3 \frac{d^4 w_0(\xi)}{d\xi^4} \left(\frac{d\xi}{dx}\right)^4 &= -q, \\ T_4 \phi_x(\xi) + T_5 \frac{d^2 \phi_x(\xi)}{d\xi^2} \left(\frac{d\xi}{dx}\right)^2 + T_6 \frac{dw_0(\xi)}{d\xi} \frac{d\xi}{dx} + T_7 \frac{d^3 w_0(\xi)}{d\xi^3} \left(\frac{d\xi}{dx}\right)^3 &= 0. \end{aligned}$$

Now assuming

$$\frac{d^4 w_0(\xi_j)}{d\xi^4} \text{ and } \frac{d^2 \phi_x(\xi_j)}{d\xi^2}$$

are known for  $j = \{-N, -N + 1, \dots, N - 1, N\}$ , then the lower-order derivatives and primary functions employing the DE integration scheme can easily be written. The lower-order

derivatives and primary functions are given by

$$\begin{aligned}
 \frac{d^3 w_0(x(\xi_i))}{d\xi^3} &= k_{ij} \frac{d^4 w_0(\xi_j)}{d\xi^4} + C_0, \\
 \frac{d^2 w_0(x(\xi_i))}{d\xi^2} &= k_{il} k_{lj} \frac{d^4 w_0(\xi_j)}{d\xi^4} + C_0 \xi_i + C_1, \\
 \frac{d w_0(x(\xi_i))}{d\xi} &= k_{im} k_{ml} k_{lj} \frac{d^4 w_0(\xi_j)}{d\xi^4} + \frac{C_0 \xi_i^2}{2} + C_1 \xi_i + C_2, \\
 w_0(x(\xi_i)) &= k_{in} k_{nm} k_{ml} k_{lj} \frac{d^4 w_0(\xi_j)}{d\xi^4} + \frac{C_0 \xi_i^3}{6} + \frac{C_1 \xi_i^2}{2} + C_2 \xi_i + C_3, \\
 \frac{d\phi_x(x(\xi_i))}{d\xi} &= k_{ij} \frac{d^2 \phi_x(\xi_j)}{d\xi^2} + C_4, \\
 \phi_x(x(\xi_i)) &= k_{il} k_{lj} \frac{d^2 \phi_x(\xi_j)}{d\xi^2} + C_4 \xi_i + C_5.
 \end{aligned}$$

Now let  $\{u\} = \{C_0, C_2, C_3, C_4, C_5, \{w_{-N,N}^{(iv)}\}, \{\phi''_{-N,N}\}\}^T$  be the  $(2n+6) \times 1$  global unknown vector with

$$\{w_{-N,N}^{(iv)}\} = \left\{ \frac{d^4 w_0(\xi_{-N})}{dx^4}, \frac{d^4 w_0(\xi_{-N+1})}{dx^4}, \dots, \frac{d^4 w_0(\xi_{N-1})}{dx^4}, \frac{d^4 w_0(\xi_N)}{dx^4} \right\} \quad (\text{C.24})$$

and with

$$\{\phi''_{-N,N}\} = \left\{ \frac{d^2 \phi_x(\xi_{-N})}{dx^2}, \frac{d^2 \phi_x(\xi_{-N+1})}{dx^2}, \dots, \frac{d^2 \phi_x(\xi_{N-1})}{dx^2}, \frac{d^2 \phi_x(\xi_N)}{dx^2} \right\}. \quad (\text{C.25})$$

Furthermore, let

$$\begin{aligned}
 \mathbf{E}_1 &= [0_{6 \times n}, I_n, 0_{n \times n}], \\
 \mathbf{A}_1 &= [1_{n \times 1}, 0_{n \times 5}, k_{ij}, 0_{n \times n}], \\
 \mathbf{B}_1 &= [\xi_i, 1_{n \times 1}, 0_{n \times 4}, g_{ij}, 0_{n \times n}], \\
 \mathbf{C}_1 &= [\xi_i^2/2, \xi_i, 1_{n \times 1}, 0_{n \times 3}, f_{ij}, 0_{n \times n}], \\
 \mathbf{D}_1 &= [\xi_i^3/6, \xi_i^2/2, \xi_i, 1_{n \times 1}, 0_{n \times 2}, e_{ij}, 0_{n \times n}], \\
 \mathbf{E}_2 &= [0_{6 \times n}, 0_{n \times n}, I_n], \\
 \mathbf{A}_2 &= [0_{n \times 4}, 1_{n \times 1}, 0_{n \times 1}, 0_{n \times n}, k_{ij}], \\
 \mathbf{B}_2 &= [0_{n \times 4}, \xi_i, 1_{n \times 1}, 0_{n \times n}, g_{ij}]
 \end{aligned}$$

where  $n = 2N + 1$ ,  $k_{ij}$  is the  $n \times n$  sub-matrix of integration weights as computed from Eq. (4.4),  $g_{ij} = k_{il}k_{lj}$  is  $n \times n$ ,  $f_{ij} = k_{im}k_{ml}k_{lj}$  is  $n \times n$ ,  $e_{ij} = k_{in}k_{nm}k_{ml}k_{lj}$  is  $n \times n$ ,  $\xi_i$  is an  $n \times 1$  sub-matrix of Sinc points,  $I_n$  is the  $n \times n$  identity matrix, and with sub-matrices of zeros and ones with indicated dimensions. Note that  $\mathbf{E}_1$ ,  $\mathbf{E}_2$ ,  $\mathbf{A}_1$ ,  $\mathbf{A}_2$ ,  $\mathbf{B}_1$ ,  $\mathbf{B}_2$ ,  $\mathbf{C}_1$ , and  $\mathbf{D}_1$  each have dimension of  $n \times (2n + 6)$ .

With these definitions, the highest-order derivatives, the lower-order derivatives, and the unknown functions,  $w$  and  $\phi_x$ , can be written in terms a linear expression for the global

unknown  $\mathbf{u}$ :

$$\begin{aligned}
 \{w_{-N,N}^{(iv)}\}^T &= \mathbf{E}_1 \mathbf{u}, \\
 \{w_{-N,N}'''\}^T &= \mathbf{A}_1 \mathbf{u}, \\
 \{w_{-N,N}''\}^T &= \mathbf{B}_1 \mathbf{u}, \\
 \{w_{-N,N}'\}^T &= \mathbf{C}_1 \mathbf{u}, \\
 \{w_{-N,N}\}^T &= \mathbf{D}_1 \mathbf{u}, \\
 \{\phi_{-N,N}''\}^T &= \mathbf{E}_2 \mathbf{u}, \\
 \{\phi_{-N,N}'\}^T &= \mathbf{A}_2 \mathbf{u}, \\
 \{\phi_{-N,N}\}^T &= \mathbf{B}_2 \mathbf{u},
 \end{aligned} \tag{C.26}$$

where  $\{w_{-N,N}\}$ ,  $\{w'_{-N,N}\}$ ,  $\{w''_{-N,N}\}$ ,  $\{w'''_{-N,N}\}$ ,  $\{\phi_{-N,N}\}$ , and  $\{\phi'_{-N,N}\}$  are  $1 \times n$  row matrices of the respective variable derivative at each of the  $2N + 1$  Sinc points. However, these represent derivatives  $d/d\xi$  and not  $d/dx$ . The derivatives with respect to  $x$  are obtained by multiplying by the appropriate power of  $d\xi/dx$ .

The governing equations are imposed at each Sinc point by applying,

$$\begin{aligned}
 \left[ T_1 \mathbf{A}_2 \frac{d\xi}{dx} + T_2 \mathbf{B}_1 \left( \frac{d\xi}{dx} \right)^2 + T_3 \mathbf{E}_1 \left( \frac{d\xi}{dx} \right)^4 \right] \mathbf{u} &= -\mathbf{q}, \\
 \left[ T_4 \mathbf{B}_2 + T_5 \mathbf{E}_2 \left( \frac{d\xi}{dx} \right)^2 + T_6 \mathbf{C}_1 \frac{d\xi}{dx} + T_7 \mathbf{A}_1 \left( \frac{d\xi}{dx} \right)^3 \right] \mathbf{u} &= \mathbf{0}_{1 \times n},
 \end{aligned}$$

where  $\mathbf{q} = \{q(\xi_{-N}), q(\xi_{-N+1}), \dots, q(\xi_{N-1}), q(\xi_N)\}^T$ .

The boundary conditions were imposed at the Sinc points  $\xi_{-N}$  and  $\xi_N$ . For the simple-support, the conditions  $w_0(x) = 0$ ,  $\bar{M}_{xx}(x) = 0$ , and  $P_{xx}(x) = 0$  were imposed for  $x = x(\xi_{-N}) = 0$  and  $x = x(\xi_N) = L$  in the following manner. First, the stress resultants are

expressed in terms of the primary variables by:

$$\begin{aligned}\bar{M}_{xx} &= \bar{D}_{11}^* \frac{d\phi_x}{d\xi} \frac{d\xi}{dx} + (c_1^2 H_{11}^* - c_1 F_{11}) \frac{d^2 w_0}{d\xi^2} \left( \frac{d\xi}{dx} \right)^2, \\ P_{xx} &= F_{11}^* \frac{d\phi_x}{d\xi} \frac{d\xi}{dx} - c_1 H_{11}^* \left( \frac{d\phi_x}{d\xi} \frac{d\xi}{dx} + \frac{d^2 w_0}{d\xi^2} \left( \frac{d\xi}{dx} \right)^2 \right),\end{aligned}$$

where  $\bar{D}_{11}^*$ ,  $\bar{F}_{11}^*$ , and  $\bar{H}_{11}^*$  are stiffnesses that relate the strains and stress resultants. The overbar indicates the stiffnesses were plane-stress reduced (see Chapter 2) and the stars indicate applying the assumption that the stress resultants  $M_{yy}$ ,  $M_{xy}$ ,  $P_{yy}$ , and  $P_{xy}$  vanish for beams. Introducing the definitions  $\{l_0\} = \{1, \mathbf{0}_{1 \times (n-1)}\}$  and  $\{l_L\} = \{\mathbf{0}_{1 \times (n-1)}, 1\}$ , the boundary conditions are expressed in terms of the global unknown vector  $\mathbf{u}$ . For the simply-supported condition on both ends, that is:

$$\begin{aligned}w_0(0) : \{l_0\} \mathbf{D}_1 \mathbf{u} &= 0, \\ \bar{M}_{xx}(0) : \{l_0\} \left[ \bar{D}_{11}^* \mathbf{A}_2 \frac{d\xi}{dx} + (c_1^2 H_{11}^* - c_1 F_{11}) \mathbf{B}_1 \left( \frac{d\xi}{dx} \right)^2 \right] \mathbf{u} &= 0, \\ P_{xx}(0) : \{l_0\} \left[ F_{11}^* \mathbf{A}_2 \frac{d\xi}{dx} - c_1 H_{11}^* \left( \mathbf{A}_2 \frac{d\xi}{dx} + \mathbf{B}_1 \left( \frac{d\xi}{dx} \right)^2 \right) \right] \mathbf{u} &= 0, \\ w_0(L) : \{l_L\} \mathbf{D}_1 \mathbf{u} &= 0, \\ \bar{M}_{xx}(L) : \{l_L\} \left[ \bar{D}_{11}^* \mathbf{A}_2 \frac{d\xi}{dx} + (c_1^2 H_{11}^* - c_1 F_{11}) \mathbf{B}_1 \left( \frac{d\xi}{dx} \right)^2 \right] \mathbf{u} &= 0, \\ P_{xx}(L) : \{l_L\} \left[ F_{11}^* \mathbf{A}_2 \frac{d\xi}{dx} - c_1 H_{11}^* \left( \mathbf{A}_2 \frac{d\xi}{dx} + \mathbf{B}_1 \left( \frac{d\xi}{dx} \right)^2 \right) \right] \mathbf{u} &= 0.\end{aligned}$$



The complete system of  $2n + 6$  equations in  $2n + 6$  unknowns is expressed by,

$$\begin{bmatrix} T_1 \mathbf{A}_2 \frac{d\xi}{dx} + T_2 \mathbf{B}_1 \left(\frac{d\xi}{dx}\right)^2 + T_3 \mathbf{E}_1 \left(\frac{d\xi}{dx}\right)^4 \\ T_4 \mathbf{B}_2 + T_5 \mathbf{E}_2 \left(\frac{d\xi}{dx}\right)^2 + T_6 \mathbf{C}_1 \frac{d\xi}{dx} + T_7 \mathbf{A}_1 \left(\frac{d\xi}{dx}\right)^3 \\ \{l_0\} \mathbf{D}_1 \\ \{l_0\} \left[ \bar{D}_{11}^* \mathbf{A}_2 \frac{d\xi}{dx} + (c_1^2 H_{11}^* - c_1 F_{11}) \mathbf{B}_1 \left(\frac{d\xi}{dx}\right)^2 \right] \\ \{l_0\} \left[ F_{11}^* \mathbf{A}_2 \frac{d\xi}{dx} - c_1 H_{11}^* \left( \mathbf{A}_2 \frac{d\xi}{dx} + \mathbf{B}_1 \left(\frac{d\xi}{dx}\right)^2 \right) \right] \\ \{l_L\} \mathbf{D}_1 \\ \{l_L\} \left[ \bar{D}_{11}^* \mathbf{A}_2 \frac{d\xi}{dx} + (c_1^2 H_{11}^* - c_1 F_{11}) \mathbf{B}_1 \left(\frac{d\xi}{dx}\right)^2 \right] \\ \{l_L\} \left[ F_{11}^* \mathbf{A}_2 \frac{d\xi}{dx} - c_1 H_{11}^* \left( \mathbf{A}_2 \frac{d\xi}{dx} + \mathbf{B}_1 \left(\frac{d\xi}{dx}\right)^2 \right) \right] \end{bmatrix} \mathbf{u} = \begin{bmatrix} -\mathbf{q} \\ \mathbf{0}_{1 \times n}, \\ 0 \\ 0 \\ 0 \\ 0 \\ 0 \\ 0 \end{bmatrix}. \quad (\text{C.27})$$

With  $\mathbf{u}$  the highest-order derivatives, the lower-order derivatives, and the primary function at each of the Sinc point is known by Eq. (C.26). The value is known at any location across the beam by interpolating using the basis function. The ease with which the higher-order derivatives are computed makes SIHD an attractive tool for interlaminar stress computation.

## **D Analytic solution for the tapered bar problem.**

The analytic solution of the BVP of a tapered axial bar under a body force with an area variation  $a(x) = (1 - x + \delta)/(1 + \delta)$  may be obtained simply by integration of the governing differential equation. The approach is as follows. First perform indefinite integration on both sides:

$$\begin{aligned}\int ([a(x)u_{,1}(x)]_{,1} + 1) dx &= C_1, \\ a(x)u_{,1}(x) + x &= C_1.\end{aligned}$$

Rearranging and performing indefinite integration again:

$$\begin{aligned}\int u_{,1}(x) dx &= \int \frac{C_1 - x}{a(x)} dx + C_2, \\ u(x) &= \int \frac{C_1 - x}{a(x)} dx + C_2\end{aligned}$$

The integration was performed using Mathematica for the given area distribution. The constants  $C_1$  and  $C_2$  were obtained by imposing the boundary conditions  $u(0) = 0$  and  $u(1) = 0$ .

## E Mixed Finite Element Formulation

The mixed FEs implemented in Chapter 7 uses Lagrange interpolation polynomials as shape functions to approximate both displacements and stress components independently. These are approximated by

$$\begin{aligned} u_1 &= \mathbf{N}(\xi, \eta)\mathbf{U}_1, & u_2 &= \mathbf{N}(\xi, \eta)\mathbf{U}_2 & \sigma_{11} &= \bar{Q}_{11}\mathbf{N}(\xi, \eta)\mathbf{S}_{11}, \\ \sigma_{22} &= \bar{Q}_{11}\mathbf{N}(\xi, \eta)\mathbf{S}_{22}, & \sigma_{12} &= \bar{Q}_{11}\mathbf{N}(\xi, \eta)\mathbf{S}_{12} \end{aligned} \quad (\text{E.28})$$

where  $\mathbf{N}(\xi, \eta)$  is a matrix of element shape functions which interpolate the nodal displacements and stresses,  $\mathbf{U}_i$  and  $\mathbf{S}_{ij}$ . The plane-stress reduced stiffness,  $\bar{Q}_{11}$  was used to normalize the nodal stresses. The present implementation uses four-node elements with the following shape functions:

$$\mathbf{N}(\xi, \eta) = \left\{ \begin{array}{cccc} \frac{(\xi + 1)(\eta + 1)}{4} & \frac{(\xi - 1)(\eta + 1)}{-4} & \frac{(\xi - 1)(\eta - 1)}{4} & \frac{(\xi + 1)(\eta - 1)}{-4} \end{array} \right\}, \quad (\text{E.29})$$

where the element nodes are identified in Fig. E.1.

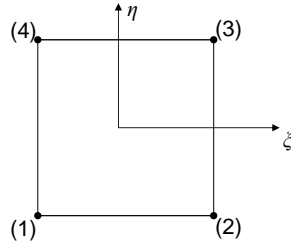


**Figure E.1.** Four node FE used in both the displacement based  $C^0$  and the mixed FEM with node numbering convention indicated.

The following functional was used to obtain the stiffness matrix:

$$\begin{aligned} \int_{\Omega} \sigma_{11}\delta\epsilon_{11} + \sigma_{22}\delta\epsilon_{22} + \sigma_{12}\delta\gamma_{12} + \delta\sigma_{11}(\sigma_{11} - \bar{Q}_{11}\epsilon_{11} - \bar{Q}_{12}\epsilon_{22}) \\ + \delta\sigma_{22}(\sigma_{22} - \bar{Q}_{12}\epsilon_{11} - \bar{Q}_{22}\epsilon_{22}) + \delta\sigma_{12}(\sigma_{12} - \bar{Q}_{66}\gamma_{12})d\Omega = \int_{\Gamma} t_1\delta u_1 + t_2\delta u_2d\Gamma \end{aligned} \quad (\text{E.30})$$

where  $\epsilon_{ij}$  is expressed in terms of displacements,  $u_1$  and  $u_2$ . If the element degree of freedom are arranged such that  $\mathbf{u} = \{\mathbf{U}_1^T, \mathbf{U}_2^T, \mathbf{S}_{11}^T, \mathbf{S}_{12}^T, \mathbf{S}_{22}^T\}^T$ , then the element stiffness matrix is given by:

$$\mathbf{K}_{ele} = \begin{bmatrix} \mathbf{0} & \mathbf{0} & Q_{11}\mathbf{K}_{x1} & Q_{11}\mathbf{K}_{y1} & \mathbf{0} \\ \mathbf{0} & \mathbf{0} & \mathbf{0} & Q_{11}\mathbf{K}_{x1} & Q_{11}\mathbf{K}_{y1} \\ -Q_{11}K_{1x} & -Q_{12}K_{1y} & Q_{11}\mathbf{K}_{11} & \mathbf{0} & \mathbf{0} \\ -Q_{66}K_{1y} & -Q_{66}K_{1x} & \mathbf{0} & Q_{11}\mathbf{K}_{11} & \mathbf{0} \\ -Q_{12}K_{1x} & -Q_{22}K_{1y} & \mathbf{0} & \mathbf{0} & Q_{11}\mathbf{K}_{11} \end{bmatrix} \quad (\text{E.31})$$

with the following matrices definitions:

$$\begin{aligned} \mathbf{K}_{11} &= \int_{-1}^{-1} \int_{-1}^{-1} N_i(\xi, \eta) N_j(\xi, \eta) |J| d\xi d\eta \\ \mathbf{K}_{x1} &= \int_{-1}^{-1} \int_{-1}^{-1} N_{i,x}(\xi, \eta) N_j(\xi, \eta) |J| d\xi d\eta \\ \mathbf{K}_{y1} &= \int_{-1}^{-1} \int_{-1}^{-1} N_{i,y}(\xi, \eta) N_j(\xi, \eta) |J| d\xi d\eta \end{aligned} \quad (\text{E.32})$$

and with  $i, j = 1, 2, \dots, 4$ ,  $\mathbf{K}_{1x} = \mathbf{K}_{x1}^T$  and  $\mathbf{K}_{1y} = \mathbf{K}_{y1}^T$ . The elemental load vector is given by:

$$\mathbf{F}_{ele} = \{\mathbf{F}_u, \mathbf{F}_v, \mathbf{0}, \mathbf{0}, \mathbf{0}\}^T \quad (\text{E.33})$$

where

$$\begin{aligned} \mathbf{F}_u &= \int_{\Gamma} t_1 \mathbf{N} d\Gamma \\ \mathbf{F}_v &= \int_{\Gamma} t_2 \mathbf{N} d\Gamma \end{aligned} \quad (\text{E.34})$$

For the present implementation, the elements were integrated using Gauss quadrature with two integration points on the  $\xi$  and  $\eta$  axis of the element.

## F Analytical Solution for Infinite Elliptical Panel

Consider the panel geometry shown in Fig. F.1. A uniform tension is applied at  $x_1 = \pm\infty$ . Along the top and bottom surfaces, the tractions vanish at infinity. Using the methodology of Muskhelishvili [190], the problem is solved in the complex plane  $z = x_1 + ix_2$ . The stresses and displacements can be written in terms of stress functions,  $\phi(z)$  and  $\psi(z)$  by employing a conformal mapping that maps an ellipse onto a unit circle. Let the conformal mapping be given by:

$$z = \omega(\zeta) = R \left( \zeta + \frac{m}{\zeta} \right) \quad (\text{F.35})$$

where  $R = (a + b)/2$  and  $m = a/R - 1$ . Note that the points  $z = a$  and  $z = bi$  map to  $\zeta = 1$  and  $\zeta = i$  respectively. Given the stress functions  $\phi$  and  $\psi$ , the stresses and displacements may be found by:

$$\sigma_{22} + \sigma_{11} = 4\text{Re}[\phi'(\zeta)/\omega'(\zeta)] \quad (\text{F.36})$$

$$\sigma_{22} - \sigma_{11} + 2i\sigma_{12} = 2\{\overline{\omega(\zeta)}[\phi'(\zeta)/\omega'(\zeta)]' + \psi'(\zeta)\}/\omega'(\zeta) \quad (\text{F.37})$$

$$2\mu(u_1 + iu_2) = \kappa\phi(\zeta) - \omega(\zeta)\overline{\phi'(\zeta)}/\overline{\omega'(\zeta)} - \overline{\psi(\zeta)} \quad (\text{F.38})$$

where  $\mu = E/[2(1 + \nu)]$  and  $\kappa = (3 - \nu)/(1 + \nu)$ .

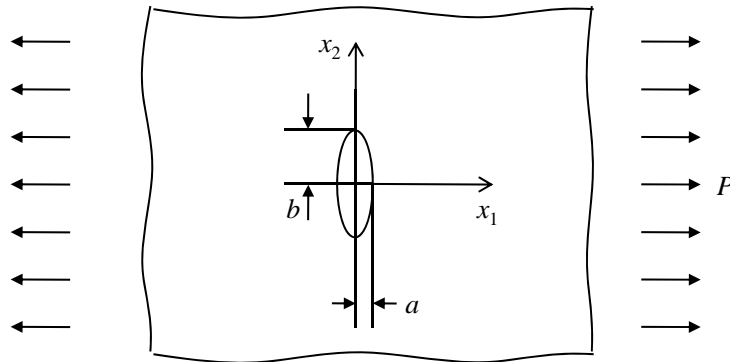


**Figure F.1.** Geometry definition form infinite tensioned panel with elliptic notch.

The present problem is solved by choosing the stress functions as

$$\begin{aligned}\phi(\zeta) &= \frac{PR}{4} \left( \zeta + \frac{(2-m)}{\zeta} \right), \\ \psi(\zeta) &= -\frac{PR}{2} \left( \zeta + \frac{1}{m\zeta} - \frac{(1+m^2)(1-m)\zeta}{m(\zeta^2-m)} \right).\end{aligned}\tag{F.39}$$

## **G Stress Integration Procedure for Perfectly Plastic and Kinematic Hardening Materials**

The stress integration procedure implemented for the elastic-plastic material follows the procedure outlined by Kojić and Bathe [187]. The procedure is reviewed below for the case of plane stress with kinematic hardening.

The present and previous loading step are indicated by left superscript of “ $t + \Delta t$ ” and “ $t$ ” respectively. At each integration point, the following variables are known: the total strain in the present load step, the plastic strain in the previous load step, the stress tensor in the previous load step, and the back-stress at the previous load increment.

$$\boxed{{}^{t+\Delta t}\epsilon_{ij}, \quad {}^t\epsilon_{ij}^p, \quad {}^t\sigma_{ij}, \quad {}^t\alpha_{ij}}$$

The unknowns are: the total stress in the present load step, the plastic strain in the current load step, the back-stress tensor in the current load step, and the tangential, plane-stress reduced stiffness matrix at the current load step.

$$\boxed{{}^{t+\Delta t}\sigma_{ij}, \quad {}^{t+\Delta t}\epsilon_{ij}^p, \quad {}^{t+\Delta t}\alpha_{ij}, \quad {}^{t+\Delta t}\bar{C}_{ij}}$$

However, if the Modified Newton’s method is used the tangential, plane-stress reduced stiffness matrix is not necessary (first step is in the elastic régime).

The deviatoric stress is defined as  $S_{ij} = \sigma_{ij} - (1/3)\sigma_{kk}\delta_{ij}$  and is important to metal plasticity because of the assumption that plastic flow is incompressible. Under the plane-stress assumption, the nonzero transverse normal ( $S_{33}$ ) component can be found by:

$$S_{33} = -S_{11} - S_{22} \tag{G.40}$$

From the deviatoric stress, the back stress is removed:

$$\hat{S}_{ij} = S_{ij} - \alpha_{ij}. \quad (\text{G.41})$$

The hatted deviatoric stress components are called the stress radius components because a scalar product of these components forms the yield surface. The yield surface for a von Mises kinematic hardening material under the plane stress assumption is:

$$f_y = \frac{3}{2} \left( \hat{S}_{11}^2 + \hat{S}_{22}^2 + \hat{S}_{33}^2 + 2\hat{S}_{12}^2 \right) - \sigma_y^2 \quad (\text{G.42})$$

where  $\sigma_y$  is the one-dimensional yield stress of the material. Yielding is expected to occur when  $f_y > 0$ . Obtaining  $S_{ij}$ , however, requires knowledge of the stress which is unknown prior to determining whether yielding is occurring.

The minimum possible value of  $f_y$  would be to assume yielding is not occurring in the present step. Therefore, calculating  $S_{ij}$  assuming no plastic deformation can be used to determine if plastic flow occurs in the present load step. The assumption that the present step is free from plastic deformation is indicated by right superscript “E” for elastic. The deviatoric stress can be found from the known quantities while operating under the present assumption:

$$\begin{Bmatrix} S_{11}^E \\ S_{22}^E \\ S_{12}^E \end{Bmatrix} = \hat{\mathbf{C}} \left( \begin{Bmatrix} {}^{t+\Delta t}\epsilon_{11} \\ {}^{t+\Delta t}\epsilon_{22} \\ {}^{t+\Delta t}\epsilon_{12} \end{Bmatrix} - \begin{Bmatrix} {}^t\epsilon_{11}^p \\ {}^t\epsilon_{22}^p \\ {}^t\epsilon_{12}^p \end{Bmatrix} \right) \quad (\text{G.43})$$

where

$$\hat{\mathbf{C}} = \frac{E}{3(1-\nu^2)} \begin{bmatrix} 2-\nu & (2\nu-1) & 0 \\ (2\nu-1) & 2-\nu & 0 \\ 0 & 0 & \frac{6G(1-\nu^2)}{E} \end{bmatrix} \quad (\text{G.44})$$

With Eq. (G.41), the yield surface given in Eq. (G.42) may be evaluated. If  $f_y > 0$ ,



plastic flow **is** occurring in the present step. If the yield surface indicates no yielding has occurred, the strain increment is known ( $\Delta\epsilon_{ij}^p = 0$ ). Thus the plastic strain in the present increment is simply that of the previous load increment,  ${}^{t+\Delta t}\epsilon_{ij}^p = {}^t\epsilon_{ij}^p$ . The back-stress remains unchanged. Therefore, the stress can be computed by

$${}^{t+\Delta t}\sigma_{ij} = C_{ijkl}^E ({}^{t+\Delta t}\epsilon_{kl} - {}^{t+\Delta t}\epsilon_{kl}^p). \quad (\text{G.45})$$

If the plastic flow is occurring, the plastic strain increment  $\Delta\epsilon_{ij}^p$  must be obtained. The general procedure is to express Eq. (G.42) in terms of a single variable and solve  $f_y = 0$ . To that end, the deviatoric stress is expressed in terms of the plastic strains by:

$${}^{t+\Delta t}\hat{\mathbf{S}} = \hat{\mathbf{C}} ({}^{t+\Delta t}\mathbf{e} - {}^t\mathbf{e}^p - \Delta\mathbf{e}^p) - {}^t\mathbf{a} - \Delta\mathbf{a} \quad (\text{G.46})$$

where  $\hat{\mathbf{S}} = \{\hat{S}_{11}, \hat{S}_{22}, \hat{S}_{12}\}$ ,  $\mathbf{e} = \{\epsilon_{11}, \epsilon_{22}, \epsilon_{12}\}$ ,  $\mathbf{e}^p = \{\epsilon_{11}^p, \epsilon_{22}^p, \epsilon_{12}^p\}$  and  $\mathbf{a} = \{\alpha_{11}, \alpha_{22}, \alpha_{12}\}$ .

By the Prandtl-Reuss equations,[187] the increment on plastic strains can be expressed by:

$$\Delta\mathbf{e}^p = \Delta\lambda\hat{\mathbf{S}} \quad (\text{G.47})$$

where  $\lambda$  is a scalar proportionality factor between the plastic strain and deviatoric stress and  $\Delta\lambda$  represents its increment. Similarly, the increment on back stress is given by the Prager's hardening rule [187] for a bilinear, kinematic hardening material:

$$\Delta\mathbf{a} = \frac{2E_p}{3}\Delta\mathbf{e}^p = \frac{2E_p}{3}\Delta\lambda\hat{\mathbf{S}} \quad (\text{G.48})$$

Note that  $E_p$  is a material property defined by  $E_p = \partial\sigma/\partial\epsilon^p$  for uniaxial yielding.

With Eqs. (G.47) and (G.48), Eq. (G.46) may be written in terms of a single variable

$\Delta\lambda$ . Solving for the stress radius components,  $\hat{\mathbf{S}}$ , yields:

$${}^{t+\Delta t}\hat{\mathbf{S}} = \left[ \mathbf{I} \left( 1 + \frac{2E_p}{3} \Delta\lambda \right) + \Delta\lambda \hat{\mathbf{C}} \right]^{-1} \left[ \hat{\mathbf{C}} ({}^{t+\Delta t}\mathbf{e} - {}^t\mathbf{e}^p) - {}^t\mathbf{a} \right] \quad (\text{G.49})$$

The transverse normal stress radius component can be found from Eq. (G.40). Note that the stress radius  $f_y$  is a nonlinear function of a single parameter  $\Delta\lambda$ . To solve  $f_y$  by Newton's method, the Jacobian is needed but it can be found by chain-rule differentiation.

$$\begin{aligned} \frac{\partial f_y}{\partial \Delta\lambda} &= \frac{\partial f_y}{\partial \hat{S}_{11}} \frac{\partial \hat{S}_{11}}{\partial \Delta\lambda} + \frac{\partial f_y}{\partial \hat{S}_{22}} \frac{\partial \hat{S}_{22}}{\partial \Delta\lambda} + \frac{\partial f_y}{\partial \hat{S}_{12}} \frac{\partial \hat{S}_{12}}{\partial \Delta\lambda} + \frac{\partial f_y}{\partial \hat{S}_{33}} \frac{\partial \hat{S}_{33}}{\partial \Delta\lambda} + \frac{\partial f_y}{\partial \hat{S}_{33}} \frac{\partial \hat{S}_{11}}{\partial \Delta\lambda} + \frac{\partial f_y}{\partial \hat{S}_{33}} \frac{\partial \hat{S}_{22}}{\partial \Delta\lambda} \\ &= \frac{3}{2} \left[ 2\hat{S}_{11} \frac{\partial \hat{S}_{11}}{\partial \Delta\lambda} + 2\hat{S}_{22} \frac{\partial \hat{S}_{22}}{\partial \Delta\lambda} + 4\hat{S}_{12} \frac{\partial \hat{S}_{12}}{\partial \Delta\lambda} + 2\hat{S}_{33} \left( \frac{\partial \hat{S}_{33}}{\partial \hat{S}_{11}} \frac{\partial \hat{S}_{11}}{\partial \Delta\lambda} + \frac{\partial \hat{S}_{33}}{\partial \hat{S}_{22}} \frac{\partial \hat{S}_{22}}{\partial \Delta\lambda} \right) \right] \end{aligned} \quad (\text{G.50})$$

where:

$$\begin{aligned} \frac{\partial \hat{S}_{33}}{\partial \hat{S}_{11}} &= \frac{\partial \hat{S}_{33}}{\partial \hat{S}_{22}} = -1 \\ \frac{\partial \hat{\mathbf{S}}}{\partial \Delta\lambda} &= \left[ \mathbf{I} \left( 1 + \frac{2E_p}{3} \Delta\lambda \right) + \Delta\lambda \hat{\mathbf{C}} \right]^{-1} \left[ - \left( \mathbf{I} \frac{2E_p}{3} + \hat{\mathbf{C}} \right) \hat{\mathbf{S}} \right] \end{aligned} \quad (\text{G.51})$$

Therefore,  $\Delta\lambda$  may be obtained and thus the plastic strain increment is given by Eq. (G.47) and the back stress is given by Eq. (G.48). The stress components can be computed from the deviatoric stress by:

$${}^{t+\Delta t}\sigma_{ij} = {}^{t+\Delta t}\hat{S}_{ij} + {}^{t+\Delta t}\alpha_{ij} + K\delta_{ij} \left[ {}^{t+\Delta t}\epsilon_{11} + {}^{t+\Delta t}\epsilon_{22} + \frac{-\nu}{1-\nu} ({}^{t+\Delta t}\epsilon_{11} + {}^{t+\Delta t}\epsilon_{22}) \right] \quad (\text{G.52})$$

where  $K$  is the material bulk modulus.

The plane-stress reduced stiffness matrix is defined by:

$${}^{t+\Delta t}\bar{C}_{ijkl} = \frac{\partial \sigma_{ij}}{\delta \epsilon_{kl}} \quad (\text{G.53})$$

which may be expressed in terms of the unknowns; however, because the modified Newton's method was used, the tangential stiffness tensor was not developed. The linear elastic stiffness tensor was used to develop the initial  $\mathbf{K}$  matrix in Eq. (8.17). The elastic stiffness matrix was retained to avoid additional factorization.

## Practical aspects of stress integration

Solving Eq. (G.42) at each integration point inside a loop could be computationally expensive. Therefore, the Newton's method approach for finding  $\Delta\lambda$  was vectorized so that it would take strains at all integration points and output the stresses at all integration points. The vectorization is mostly straight forward; however, the approach for solving Eq. (G.42) at each integration point should be discussed. Let left subscript “ $(i)$ ” denote quantities at integration point  $i$  and let  $\mathbf{f}_y = \{(1)f_y, (2)f_y, \dots, (N_i)f_y\}$ ,  $\Delta\Lambda = \{(1)\Delta\lambda, (2)\Delta\lambda, \dots, (N_i)\Delta\lambda\}$ , and:

$$\mathbf{F}_{,\Delta\lambda} = \begin{bmatrix} \left(\frac{\partial f_y}{(1)\partial\Delta\lambda}\right)^{-1} & 0 & 0 & 0 \\ 0 & \left(\frac{\partial f_y}{(2)\partial\Delta\lambda}\right)^{-1} & 0 & 0 \\ 0 & 0 & \ddots & 0 \\ 0 & 0 & 0 & \left(\frac{\partial f_y}{(N_i)\partial\Delta\lambda}\right)^{-1} \end{bmatrix} \quad (\text{G.54})$$

Then the  $\Delta\Lambda$  can be incremented for all integration points by:

$$\Delta\Lambda^{(i)} = \Delta\Lambda^{(i-1)} - \mathbf{F}_{,\Delta\lambda}\mathbf{f}_y^{(i-1)} \quad (\text{G.55})$$

The present study used the following convergence criteria:

$$\frac{\|\mathbf{f}_y\|}{\sigma_y^2} < \epsilon_{abs} \quad (\text{G.56})$$

where the  $\epsilon_{abs} = 1 \times 10^{-5}$  was used to verify convergence.

Naturally, it is important to choose a reasonable starting point for each  $\Delta\lambda$ . For the fully three-dimensional state of stress, the yield function is linear and therefore can be solved in closed form. For that case, the closed form solution of  $\Delta\lambda$  was given by Kojić and Bathe[187]:

$$\Delta\lambda = \frac{3(\hat{\sigma}^E - \sigma_y)}{2\sigma_y(3G + E_p)} \quad (\text{G.57})$$

with

$$\hat{\sigma}^E = \sqrt{\frac{3}{2}\hat{S}_{ij}^E\hat{S}_{ij}^E}. \quad (\text{G.58})$$

While Eq. (G.57) does not satisfy the yield surface for the plane-stress case, it was used as the initial guess for the iterative approach.

## H Additional Numerical Results for Elastic, Plane-stress Panels with Elliptical Notches

Contours of displacements and stresses were plotted for a plane-stress member with an elliptical notch of section 8.2. The panel with an elliptical notch that had an aspect ratio of five. The stress concentration along the edge  $x_1 = 0$  and in the vicinity of the hole was also plotted.

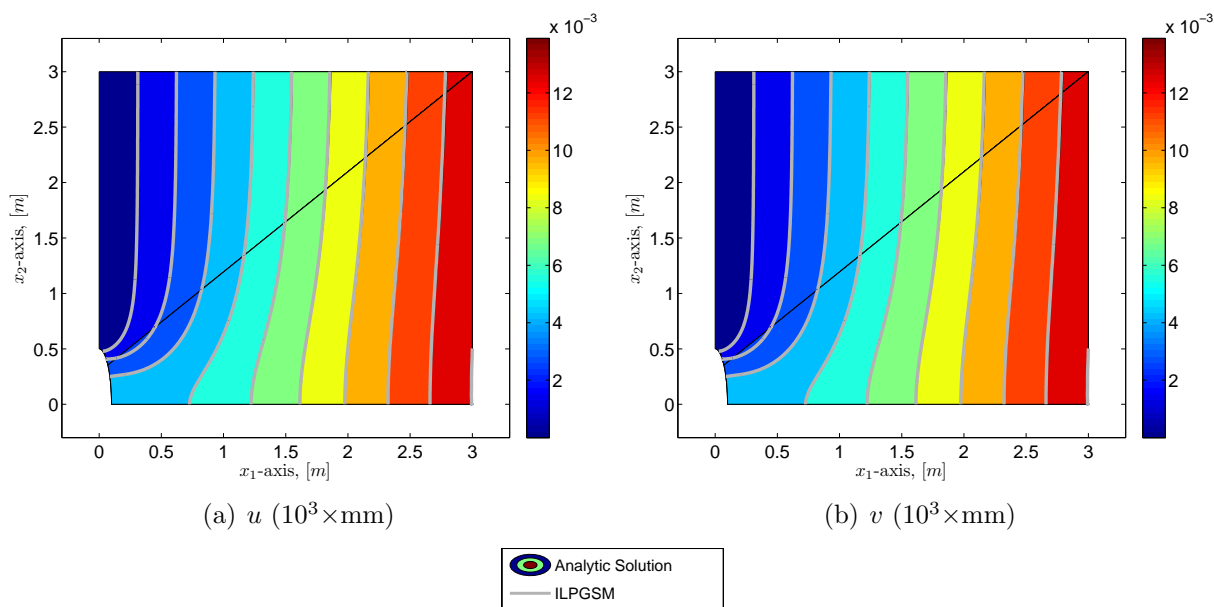


**Figure H.1.** Displacement contours for a panel with a elliptical notch with aspect ratio  $r_2/r_1 = 5$  by ILPGSM.

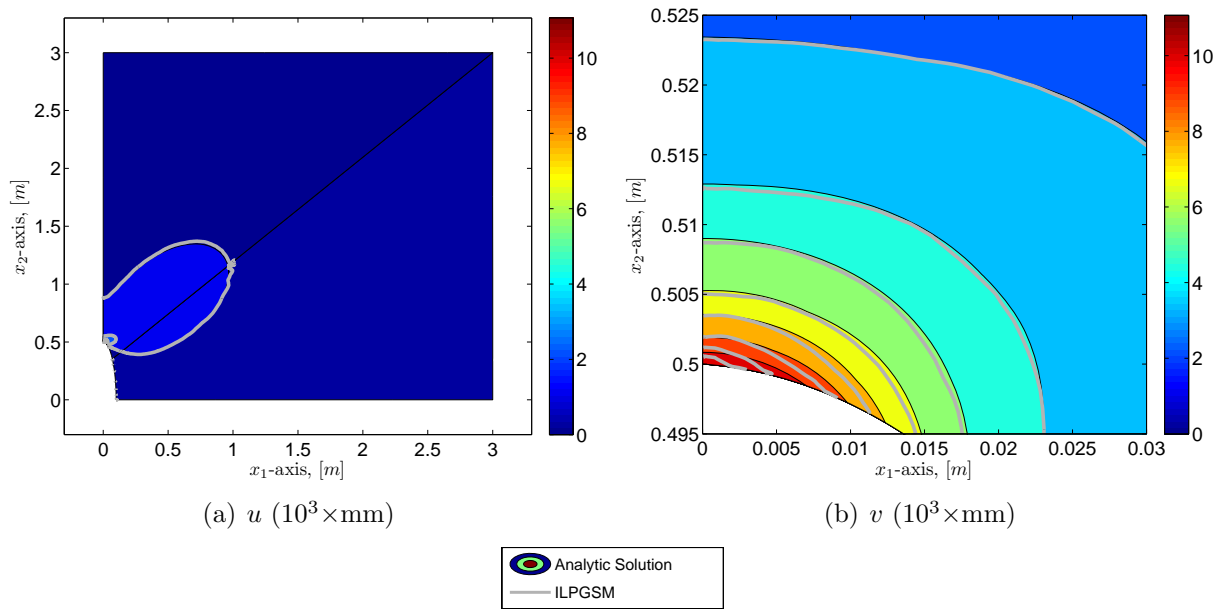


Figure H.2. Contours of Von Mises stress for a panel with an elliptical notch with aspect ratio of 5.

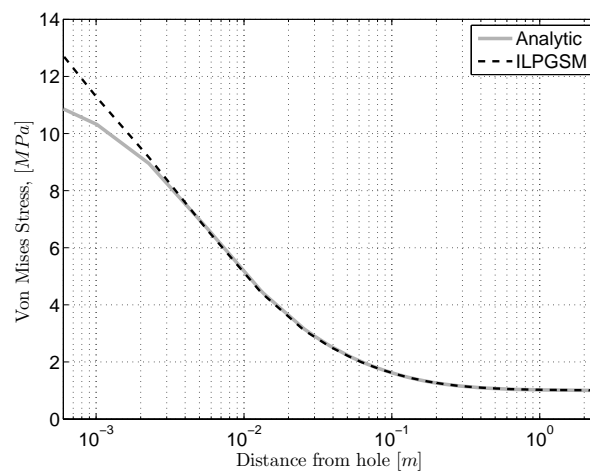
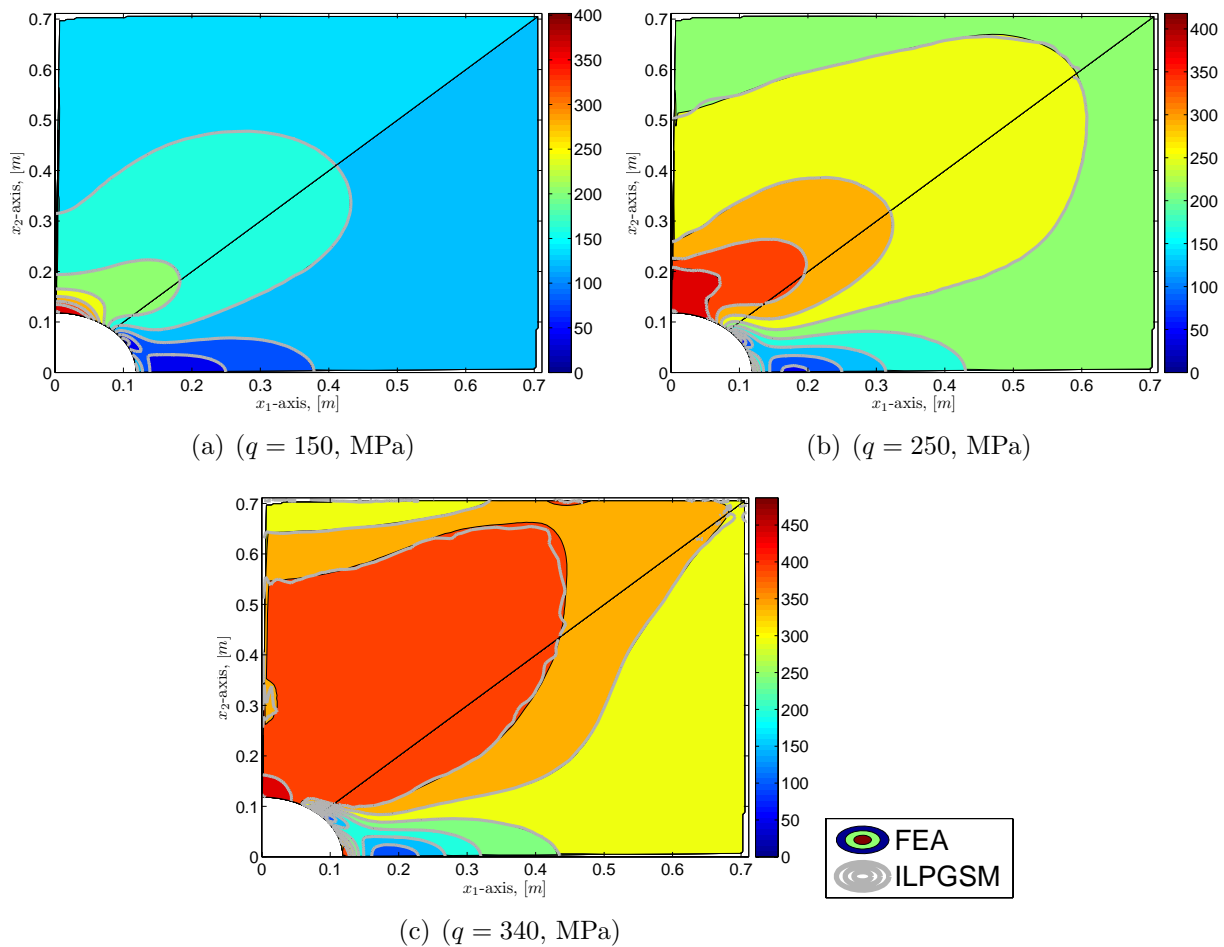


Figure H.3. Von Mises stress along  $x_1 = 0$  in the vicinity of the hole for aspect ratio of 5.; the analytic solution being valid for infinite domain.

## I Additional Numerical Results for Elastic-plastic, Plane-stress Panels with Circular and Elliptical Notches.

Contours of Von-Mises stress for the elastic-plastic notched members of Section 8.3 with a circular notch were plotted in Fig. I.1. Contours of displacements were plotted in Fig. I.2.



**Figure I.1.** Comparison of contours of Von Mises stress by ILPGSM and FEA for panel with circular hole.

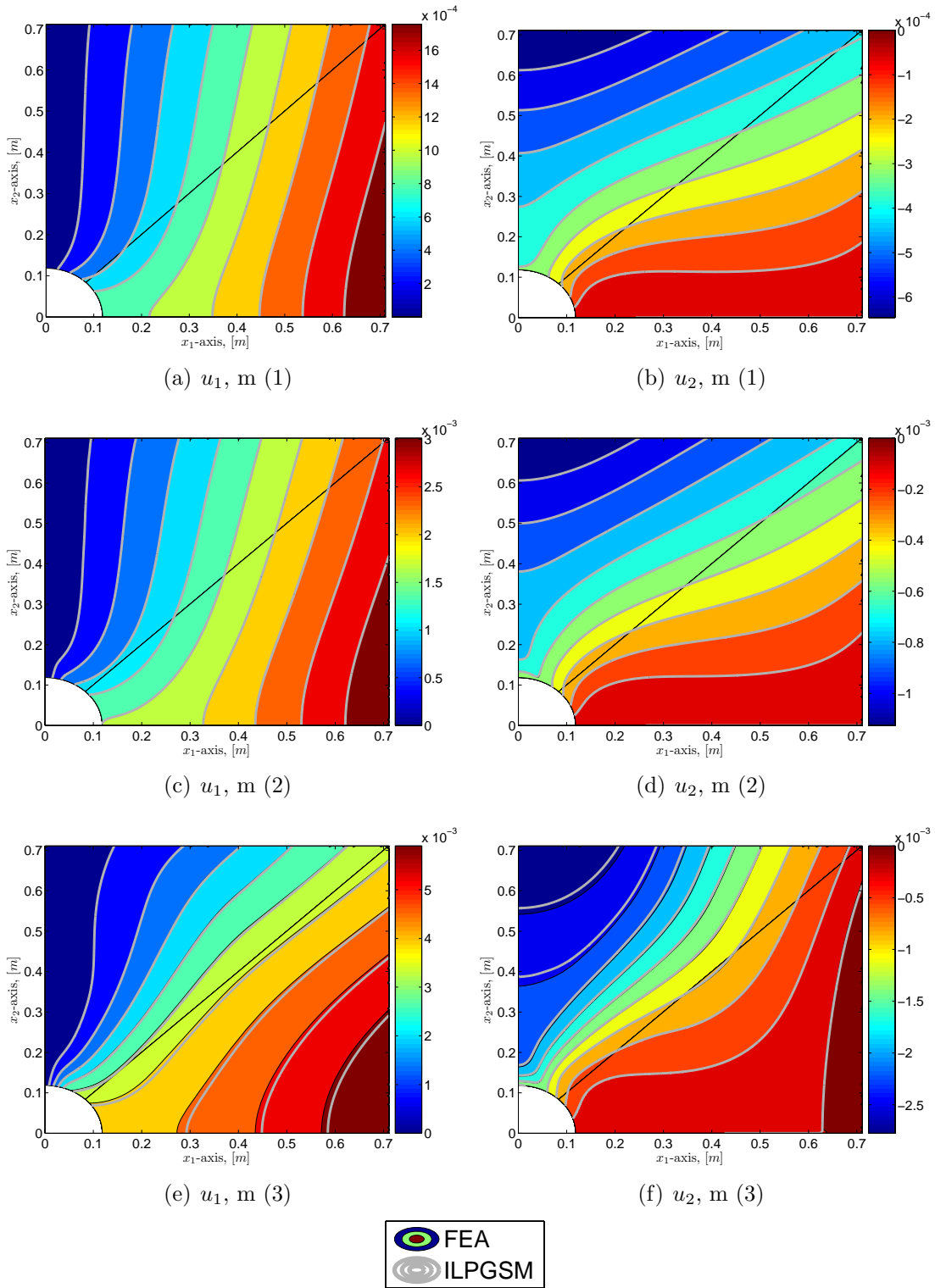


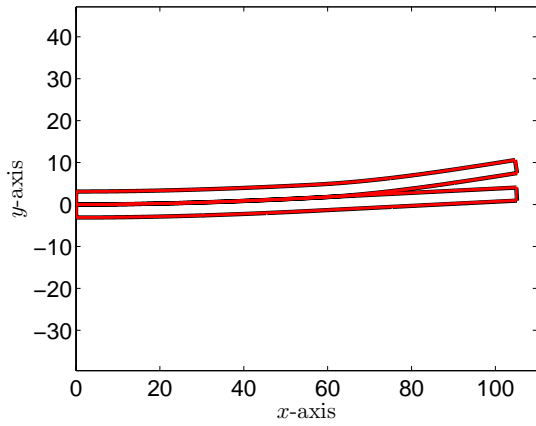
Figure I.2. Comparison of contours of  $u_1$  and  $u_2$  by ILPGSM and FEA for panel with circular hole. (1- 150 MPa, 2-250 MPa, 3 - 340 MPa applied load)



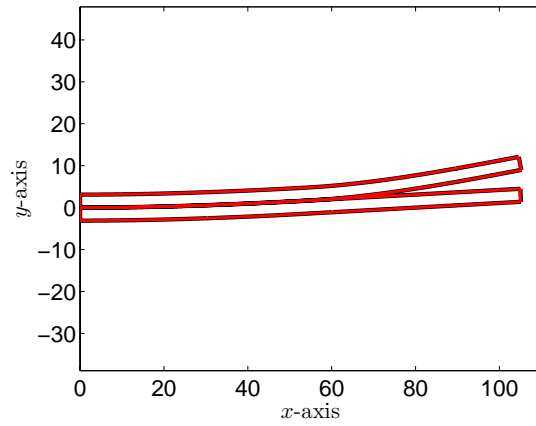
## **J Additional Numerical Results for the Fixed Ratio Mixed Mode Composite Specimen**

The deformation of a fixed-ratio mixed mode (FRMM) composite beam specimen obtained by the ILPGSM and FEA solutions is compared in Fig. J.1 for  $\bar{w} = 2.5, 3.0, 3.5,$  and  $4.0$  mm. To better illustrate the deformation, the deformation was amplified by a factor of 3. The FEA and ILPGSM results are indistinguishable indicating good correlation between the two analyses.

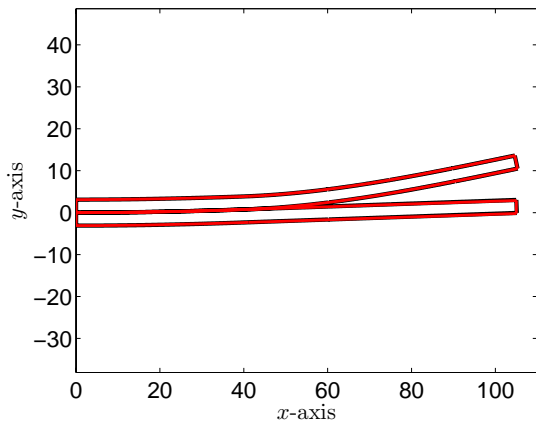
The traction within the cohesive interface are plotted in Fig. J.2. The tangential and normal stress components from the irreversible exponential traction-separation law were rotated into the  $(x_1, x_3)$  components ( $\sigma_{13}$  and  $\sigma_{33}$ ) using Eq. (9.21). Figure J.2 indicate good correlation between the FEA and ILPGSM solutions. The delamination crack front obtained by the FEA lags that of the ILPGSM. Moreover, the FEA solution indicates higher shear stress than the ILPGSM does. The ILPGSM results are otherwise excellent in comparison with the those obtained by the FEA.



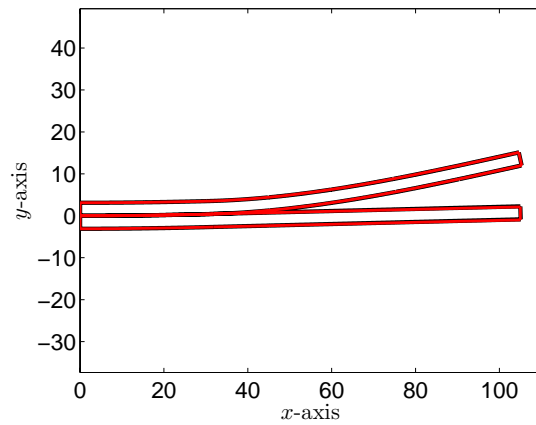
(a) Applied Displacement  $\bar{w} = 2.5$  mm



(b) Applied Displacement  $\bar{w} = 3$  mm



(c) Applied Displacement  $\bar{w} = 3.5$  mm



(d) Applied Displacement  $\bar{w} = 4$  mm



**Figure J.1.** Comparison of deformed shape of a  $[0]_s$  FRMM composite specimen obtained by the ILPGSM and a FEA. The deformation is shown utilizing an amplification factor of 3.

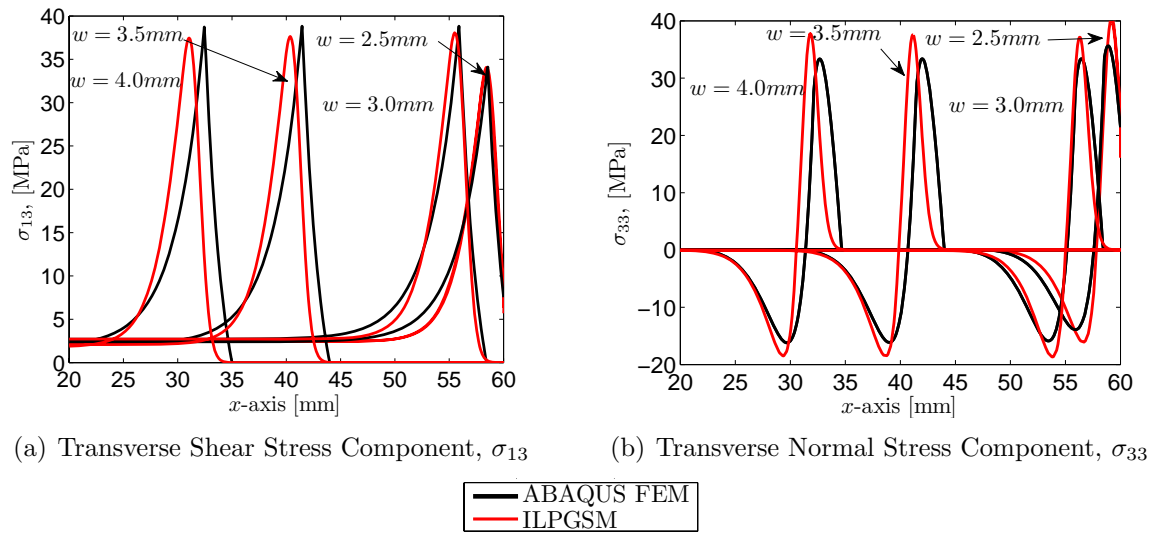


**Figure J.2.** Comparison of traction components in the cohesive layer of a  $[0]_s$  FRMM composite specimen by ILPGSM and a FEA.